Optimal Control Theory Techniques for Nitrogen Vacancy Ensembles

by

Madelaine Susan Zoritza Liddy

A thesis
presented to the University of Waterloo
in fulfillment of the
thesis requirement for the degree of
Doctor of Philosophy
in
Electrical and Computer Engineering (Quantum Information)

Waterloo, Ontario, Canada, 2022

Examining Committee Membership

The following served on the Examining Committee for this thesis. The decision of the Examining Committee is by majority vote.

External Examiner:	Dr. Ronald Walsworth Founding Director, Quantum Technology Center Minta Martin Professor Dept. of Physics Dept. of Electrical and Computer Engineering University of Maryland
Supervisor(s):	Dr. David G. Cory Professor, Dept. of Chemistry, University of Waterloo Dr. Guo-Xing Miao Associate Professor, Dept. of Electrical and Computer Engineering, University of Waterloo
Internal Member:	Dr. Christopher Wilson Deputy Director, Institute for Quantum Computing Professor, Dept. of Electrical and Computer Engineering, University of Waterloo
Internal Member:	Dr. Michal Bajcsy Associate Professor, Dept. of Electrical and Computer Engineering, University of Waterloo
Internal-External Member:	Dr. Shirley Tang Associate Dean of Science, Research, Professor, Dept. of Chemistry, University of Waterloo

Author's Declaration

I hereby declare that I am the sole author of this thesis. This is a true copy of the thesis, including any required final revisions, as accepted by my examiners.

I understand that my thesis may be made electronically available to the public.

Abstract

Nitrogen Vacancy (NV) centers have been used for many quantum sensing and navigation based applications. A diamond NV sensor with enhanced sensitivity through an ensemble measurement, and the ability to coherently and independently control each of the four defect orientations provides an efficient building block for these applications. Use of all orientations in the ensemble, naturally aligned perfectly in the crystal, increases the information content compared to using only one orientation. Selective control of each orientation allows for vector quantities to be explored in parallel, reducing measurement times. Optimal Control Theory (OCT) techniques, implemented with helical microwave control fields allow for both of these to be achieved in a setup that is compatible with a future compact sensing device. This thesis details the theory, build, and implementation of OCT control with NV ensembles, laying the ground work for such future devices.

The first part of this thesis introduces some general applications of NV ensembles and presents current solutions for controlling all four orientations. This is followed by a brief introduction to the Nitrogen Vacancy center, including the energy level and Hamiltonians relevant to this work. The main body consists of three parts. The first part develops a generalized Hamiltonian model dependent on both the orientation and microwave control field configuration for any NV orientation in three single crystal diamonds. This model is then integrated with OCT pulses, and simulates key examples to show its applications across (100), (110) and (111) single crystal diamonds with the same experimental configuration for both collective and selective control over all four NV orientations. Second, the thesis details the design, build and characterization of the experimental apparatus required for measuring ensembles of NV centers and to implement the necessary microwave controls for OCT experiments. The last part consists of a set of characterization experiments to learn the spin dynamics of NV ensembles and collect the necessary parameters needed to implement OCT pulses. This is followed by a demonstration of selective transitions with OCT pulses that optimize over the four orientations in a (100) diamond, in the absence of a static magnetic field, and removing the geometric constraint of the active NV ensembles located relative to the microwave microstrips.

Acknowledgements

I know this section is usually reserved for thanking those that have helped me along the way, but I thought I'd do things a bit differently. I thought I would just take a paragraph or two, and introduce myself (and yes, I am aware this will be publicly available); but I would be remised if I couldn't add a bit of my character into this 262 page work.

So hello! I am Madelaine. I am an animal loving, food enthusiast, music obsessed, 30 year old autistic person. My hobbies include singing in the local Grandphilharmonic Choir and playing the piano. My other loves are powerlifting, snowboarding, reading, baking, gardening and watching movies.

I genuinely enjoy research. Everyday, I get to make up problems and then figure out the answers. It's not without frustration, heartbreak or questioning my very being, but I'm sure if whoever is reading this is in research, they understand why it's all worth it.

Now that I've explained a bit about myself, let's talk about this degree. It contained the highest highs and the lowest lows, as I imagine is common with most graduate students. I'd like to stay away from the lowest lows; don't really want to ruin the mood. The highest highs wouldn't have been possible without all the folks who helped me along the way.

First to my supervisors, thank you to David and Guo-Xing for giving me the opportunity to pursue this degree, and giving me this time to play, tinker and learn about a broad range of topics. Not many students are given the ability to study such a broad range of topics as I have, and are encouraged to pursue whatever it is that they find interesting. Who knew that when I sat down to my introductory Quantum Mechanics class ten years ago, with David as the course instructor that I'd end up here.

When you've been in and out of a lab group for ten years through an undergrad internship, senior design project, and grad school, you come across a few people. Thank you to all in Cory group who I have crossed paths with. To Dusan, going through undergrad and grad school together; thank you for being side by side with me and for being my riddle buddy. To George, I am so happy we're neighbours both in and out of the lab. You and Ali are such a great set of friends to have, I am so grateful to you both. To Ian, thank you for being my guide to NVs while I was just starting out. To Chris and Andrew, thank you for being my private theorist tutors.

To Julia and Rahul, thank you for always being a positive addition to whatever space you're in. To Kent, Saba and Holger, our hallway chats were such a nice way to break up the day and remind me there is life outside my lab doors. To Yonatan, you were such a valuable asset to me during a time when I really needed help. Thank you for being my sanity check, for making sure I (mostly) didn't spiral down obsessive loops, for pushing me and being endlessly patient with me. To Troy, my steadfast cheerleader. Your constant optimism helped me turn my near weekly meltdowns of "My results are terrible! I'm quitting" to "Hey...okay...this is good! Now I know the next step!". To Peter, thank you for being such a positive influence, teaching me about all things electronics and also how to be happy with my work. To Don, Sara and Carly, thank you for keeping us all in check and everything running, I love our chats. Last, to Maryam. Your kindness and life advice helped me get through day to day, week to week, month to month and to the end of this degree. I could not have asked for a better office mate.

I cannot finish these acknowledgements without mentioning my time spent at the Hanson Lab in TU Delft. What a phenomenal time I had there, exploring a completely different application of NV centers, seeing a different part of the world and making many new friends along the way. Thank you to everyone at TU Delft for making me feel so at home, especially to Ronald Hanson for opening his group to me and making me feel accepted from day one. To Marko Lončar, I am so happy I was able to reconnect with you and have some fun working on fabrication together! To Julia, Lizanne, Suzanne, Peter, Norbert, James, Nodar and to Stefan, my cleanroom partner in crime, I am so grateful for the time we spent together. It was truly a pleasure to get to know all of you, work together and thank you for being so welcoming to me!

To Emma, who helped me make this thesis a reality, I thank you for our weekly meetings! You go so far beyond your duties as a writing coach, your weekly pep talks helped me more than you know. To my coaches Casey, Craig, Dan and Tracy, thank you for keeping me moving, teaching me how to breath and letting me take out my stress on the barbell. To Renate, the wellness counsellor in Electrical Engineering, your guidance helped me through my time at home during the lockdown. To Dr. Kim Dawson, thank you for challenging me to decide if I even wanted to finish the degree, and when I did, helping me get there, piece by piece. To Jeff Casello, thank you for truly caring about the students at UW, for encouraging me to pursue a formal mental health diagnosis, and that there is nothing to be ashamed of for doing so.

To my family and friends. I truly feel like this has been a team effort and I am so so lucky to have a support group like this. There is just not enough space for me to write all the names out, but I hope you know who you are. From everyone encouraging me, laughing with me, crying with me when I was sad, yelling with me when I was angry and celebrating with me when I was happy. I love and thank all of you from the bottom of my heart.

My family has always been a huge support to me, and there really isn't enough space for me to write how much they have helped me through life and school since day one. Daily phone calls even when we live thousands of kilometers away with words of encouragement were of plenty. To AJ, I'll save all of my gushy words for our vows.

The best way to describe my parents undying enthusiasm is to describe the answer my Dad said when I asked if he'd like to attend my defense. He said "wild horses couldn't keep him away". To my Mom, I couldn't sum it up any better than crediting her with the first figure of this thesis.

Dedication

To the Hermiones of the world; never stop putting your hand up.

Table of Contents

List of Tables

List of Figures

List of Abbreviations

AOM acousto-optic modulator 89–92, 110, 111, 113, 114, 117, 121, 124, 129, 130

APD avalanche photo diode 85, 108

AWG arbitrary waveform generator 34, 36, 45, 46, 131–133, 135, 137, 139, 157, 215

CW continuous wave 6, 130, 137, 143–145, 154, 156, 157

DOF depth of field 103, 104

FWHM full width half maximum 146, 155

GRAPE gradient ascent pulse engineering 20, 44, 212

HWP half wave plate 89, 90, 92, 93, 127, 130, 152

IF intermediate frequency 137, 138

ISC inter-system crossing 12, 13

LO local oscillator 137, 138

NV nitrogen vacancy 1–3, 5, 6, 10, 14, 16, 20, 22, 24, 32, 39, 43, 44, 48, 56, 60, 62, 66, 69, 73, 76, 80, 83, 85, 89, 92, 95, 106, 109, 118, 129, 131, 137, 143, 148, 160, 167, 171, 175, 179, 196, 208, 225

OCT optimal control theory 1, 2, 4–6, 20, 22, 39, 44, 48, 66, 131, 142, 143, 154, 175, 178, 198, 199, 204, 206–208, 212, 218, 224, 225

ODMR optically-detected magnetic resonance 6, 137, 143–145, 154

P.A.S principle axis system 12, 15, 16, 18, 19, 21, 24, 28–30, 32, 43, 148, 150, 151, 202, 211, 213

PBS polarizing beam splitter 85, 89, 90, 111, 113, 127–130

QWP quarter wave plate 90, 113, 127, 130

RF radio frequency 137, 138

SMF single mode fiber 92, 93, 109, 112, 119, 120, 122, 127

TTL transistor-transistor logic 135, 157

ZFS zero field splitting 12, 14, 22, 32, 35, 147

Chapter 1

Introduction

1.1 Thesis Goals

The main goal of this thesis is to use circularly-polarized microwaves in the absence of a static magnetic field to implement optimal control theory (OCT) pulses for all four orientations in an ensemble of nitrogen vacancy (NV) centers in bulk single crystal diamond. The geometric constraint of the location of the NVs relative to the microwave control field has also been removed. Demonstrating this control allows for NV ensembles to be used for sensing vector quantities in a variety of applications. Performing collective control for all four NV orientations, increases the number of useful centers in the ensemble, boosting the signal to noise ratio by four times. Selective control of the four NV orientations allows for more accurate magnetic field sensing compared to using just one or two orientations. OCT control in the absence of a magnetic field with a helical microwave source enables both of these operations removing some hardware constraints like requiring multiple microwave frequencies to control the NV centers, or requiring a specific location of NV centers relative to the microwave source.

First, the theory of designing and simulations of OCT pulses for NV ensembles in single crystal diamond will be described, including a generalized Hamiltonian model for any NV orientation in the (100), (110) and (111) diamond. Following this, a detailed description for the design, build and characterization of the experimental setup suitable for implementing NV ensemble experiments with helical microwaves is provided. Last, characterization experiments for NV ensembles are completed, followed by a demonstration of OCT experiments, showing collective control of four orientations in the (100) diamond.

1.2 Thesis Outline

Chapter one of this thesis will introduce the attraction of NV centers and give a brief overview of the state of ensemble work with NV centers. It will motivate the use of circularly polarized microwaves for NV ensembles, and show the application for vector magnetometry with NV ensembles and where OCT control of NV ensembles may benefit these applications including a proposal for a chemical sensing device with NV ensembles.

Chapter two will introduce the NV center in single crystal diamond, its energy level structure and ground state Hamiltonian. It will also provide a description of each of the four NV orientations in single crystal diamond in the common lab frame for three typically used diamonds in NV experiments. For NV ensemble work, it is critical to have a good understanding of the physical space the NV centers occupy within a single crystal diamond.

Chapter three introduces the general control Hamiltonian used for any single NV and then expands to NV ensembles using the same microwave configuration. Following this, it will detail the control capabilities of optimal control theory pulses for NV ensembles, simulated for the (100), (110) and (111) diamond orientations. Several key examples will be shown for either collective targets operation for all NVs or selective control on each of the four orientations.

Chapter four describes the necessary experimental configuration to achieve the OCT experiments outlined in chapter three. It details the optical and microwave configuration required for NV ensemble experiments. It will first describe the general layout and function of each module of the design, and follow by characterizing and testing the function of the design independent of the NV measurements.

Chapter five demonstrates several experiments conducted to learn the spin dynamics of NV ensembles in a (100) diamond. It then uses the parameters collected through several experiments to implement OCT experiments with helical control on NV ensembles.

Chapter six discusses the next steps and future applications of quantum sensing using ensembles of NV centers in a single crystal diamond, and expansion of experimental testing to other diamond orientations beyond the (100) diamond.

1.3 Attraction and Applications of NV ensembles

NV centers are highly useful quantum centers, most notably for their ability to be used at room temperature, sensitivity to external magnetic fields, optical initialization and optical read out schemes, [59]. As a colour center in a diamond, it benefits from the thermally and mechanically stable lattice, chemically inert environment and biocompatibility, [1]. This expands the applications of NV centers for imaging small magnetic fields, [91], DC and AC magnetic field sensing [1, 10], sensing crystal strain in the diamond lattice, [70, 71], and use of its photon emissions for quantum internet nodes [85], to name a few. This is by no means a complete list, but is meant to display the versatility of applications of the NV center.

The NV center is one of many lattice defects in the diamond crystal. It is created by substituting one carbon with a nitrogen and removing an adjacent carbon to create a vacancy site, [64, 59]. The bond between the nitrogen and vacancy may be found pointing to any of the four vertices of the characteristic tetrahedral lattice shape within a single crystal diamond, giving four NV orientations, [59]. Under normal growth conditions in a single crystal diamond, the distribution of the orientations are uniform, [82].

Ensembles of NV centers have improved sensitivity to magnetic fields compared to using a single center as the sensitivity is proportional to $\sqrt{N}$ where N is the number of useful centers, [59, 91, 113]. However, using ensembles of NV centers does not come without its challenges compared to using a single NV center. Increasing the density of NV centers in the crystal in turn creates other unwanted lattice defects such as sole substitutional Nitrogen (P1 centers), and adds more crystal strain in the diamond, and temperature dependence; both limiting the coherence of NV centers [3, 14, 24, 101]. The lifetime of the NVs have also been shown to be dependent on the alignment of an external static magnetic field with the principle axis of the NV center, [55, 101]. Naturally, as the volume of NVs of interest is increased, the homogeneity of the microwave field would vary enough over all centers to influence the control of the ensemble, [125].

Many experiments have focused on enhancing the properties of NV ensembles, including lifetimes, through improved growth conditions of diamond crystals, [8, 13, 21, 30, 39, 45, 74]. There has also been work in improving the collection efficiency of NV ensembles through fabricating structures out of diamond or collecting on the side of the crystal, [58, 74].

The most notable piece to consider with the use of NV ensembles are their orientations within the diamond crystal lattice. As the diamond crystal lattice is a tetrahedral structure, the NV may be found in one of four orientations, its principle axis pointing towards one of the four vertices. This presents a challenge as both the optical and microwave control fields are sensitivity to the projection onto the principle axis of the NV orientation.

Control over all four orientations enhances the sensing capabilities of NV ensembles, by increasing the number of useful centers within the NV volume by up to four times. Additionally, selective control over each of the four orientations is very useful in vector magnetometry. There has already been work demonstrating use of all four orientations for vector magnetometry, by sequentially or simultaneously controlling all centers with multiple microwave frequencies, [120, 123]. These techniques have also been used for detecting both magnetic field and temperature simultaneously, [97].

This thesis will present the use of OCT techniques to use all four orientations of NVs in the ensemble. This is not the first attempt at using OCT methods for NV ensembles, OCT has been used to develop pulses robust to the hyperfine coupling to the Nitrogen nuclear spin, [86]. As well, a thorough review on OCT works for Nitrogen-Vacancy Centers was published recently, [89]. OCT pulses are also not the only solution for improving the control, with composite and other advanced pulse sequences having been demonstrated for NV ensembles, [78, 118, 129]. This thesis presents a general model for NV ensembles in the (100), (110) or (111) oriented diamond and demonstrate OCT pulses in the (100) diamond.

1.4 Addressing Selective Transitions with Helical Microwave Sources

In this thesis, circularly polarized (helical) microwaves are used to study the behaviour of the NV ensembles, and to demonstrate the OCT controls simulated in chapter three and implemented in chapter five. Use of OCT controls expands the capabilities of selective single transitions in the NV ground state without the use of an additional static magnetic field. The ground state of the NV center is a triplet state, with the states $|0\rangle$ and $|\pm1\rangle$ split by a zero field splitting, [64]. In the absence of a static magnetic field, the $|\pm1\rangle$ states are degenerate, [64]. A convenient way to address the single transitions between the $|0\rangle$ and $|+1\rangle$ or $|-1\rangle$ states is to add a static magnetic field to split the degeneracy between the $|\pm1\rangle$ states, [1, 10]. A linear microwave source on resonance with either the $|+1\rangle$ or $|-1\rangle$ state will selectively address each transition from the ground state zero. As the other transition is so far off resonance from the selected one, it is very unlikely it will be populated.

While the $|\pm1\rangle$ states are degenerate, they are sensitive to the polarization of the incoming microwave field. Using circularly polarized microwaves as the microwave source allows for selective transitions between the $|0\rangle$ and $|+1\rangle$ or $|-1\rangle$ to be achieved in the absence of a static magnetic field. Demonstrating selective transitions between the ground states of the NV in the absence of adding a static magnetic field with circular polarization has been shown in a few works for both single NVs and ensembles of NV centers, [6, 60, 77, 121, 122, 127, 128].

Two linearly polarized sources are used to create circularly polarized microwaves, by changing the relative phase between the two channels. The most simple designs for achieving circularly polarized microwave controls use two [60, 77, 128] or four [122] parallel microstrips, or two perpendicular microstrips [6]. Optimization of these designs with a ring structure, parallel lines or crossed microstrips are shown in [121].

Using circular polarization to address the selective transitions has its advantage over using a static magnetic field and linearly polarized microwave source. Using circularly polarized microwave sources increases the Rabi oscillation frequency and contrast for the same comparative linear source strength, [122]. Circularly polarized microwaves pave the wave for zero-field magnetometry devices with NV centers, [60, 127, 128]. This thesis will demonstrate selective transitions for an ensemble of NV centers using circularly polarized microwave sources from two parallel microstrips.

1.5 Vector Magnetometry with NV ensembles

The successful implementation of OCT controls for NV ensembles expands the already impressive range of applications for NV ensembles, in particular their use for vector magnetometry. The applications of using NV ensembles for vector magnetometry have been demonstrated in many works, [34, 51, 57, 61, 75, 83, 103, 108, 109]. They have also been used to image 2D magnetic fields, [83, 103], bacteria and molecules attached to the surface, [34, 51, 57, 75], and magnetic fields for integrated circuits, [108, 109] to list some examples.

NV ensembles are a wonderful medium for detecting vector quantities because they have four orientations in the single crystal diamond. Magnetic fields may be reconstructed by measuring the projection of the field on each one of these four orientations, [66, 93, 107, 112, 119, 126]. The most simple method to measure a vector quantity is through a optically-detected magnetic resonance (ODMR)-continuous wave (CW) measurement. In the absence of an external magnetic field, the $|\pm 1\rangle$ ground states of the NV are degenerate. Adding an external field splits these levels proportional to the strength of the external field projected along the NVs' principle axis. As the same field will project differently onto the four principle axes of the NVs within a single crystal diamond, the Cartesian coordinates of the external field may be re-constructed using the measurements from each orientation, [66, 93].

Enhancements to this scheme for both DC and AC field sensing, involve pulsed ODMR, pulse quantum filtration, Ramsey fringe and Hahn echo experiments, [38, 53, 112, 119, 126]. Other improvements to vector magnetometry with NV ensembles acquire the signal from the four orientations of the NVs simultaneously rather than sequentially, reducing the length of experiment by four times and also boosting the sensitivity, [53, 93].

Much of the advancement in simultaneous detection of all four orientations is owed to using multiple microwave frequencies to address the resonant frequency of each of the four axis of NVs with the addition of a static field, [93, 119]. Along a different vein, other work has focused on growing the NV ensemble along one axis, so there is only one of four orientations present allowing the field to be reconstructed, [107]. OCT control of NV ensembles not only allows for simultaneous control of all four orientations, but also allows for selective control of each orientation, further illustrated in the following section.

1.6 Chemical Sensing with NV Ensembles

The material properties of diamonds make them an excellent medium for chemical sensing. Even without incorporating NV centers, diamonds have been used as an alternative to glass based substrates for chemical sensing, desired for their mechanical and chemical stability, outperforming other materials.

As the growth process of CVD diamond typically involves the use of methane and hydrogen gases, this results in a hydrophobic, hydrogen terminated surface. Having an inert hydrogen surface prevents unintended bonding of other chemical species to the surface allowing for more specific functionalization. Additionally, the hydrophobic surface prevents unwanted water build up, which in turn prevents hydrolysis of the desired functionalized groups, allowing diamond based sensors to be used for longer periods of time compared with other more hydrophilic materials. Last, a lack of water on the surface prevents the functionalized groups from bonding together with Van der Waals forces, reducing their potential to bond with the desired target molecules, [20, 87, 102].

Diamonds have been functionalized with many different schemes for biological or chemical sensing, [20, 102, 116]. One such scheme is to alter the surface to be terminated with a carboxyl group, expanding the options for attaching other functional chemical species to be sensed, [105].

Incorporation of NV centers as the chemical sensing scheme further expands diamonds' chemical sensing capabilities. Use of NVs for chemical and biological sensing has already been demonstrated in numerous works. This has been shown and is not limited to, sensing and transferring the polarization of the NV centers to nuclear species on the surface of the diamond [7, 16, 25, 33, 40, 65], sensing biological tissues, neural action potential and small molecules [11, 48, 105], and sensing surface bacteria and molecules, [34, 51, 57, 75].

A proposal for one such chemical sensing scheme is outlined in figure 1.1. There are many options for sensing chemical species on the surface of diamonds, this is merely an example to illustrate the adaptability of diamond based sensors, and how they may be enhanced with the inclusion of OCT protocols for controlling ensembles of NV centers.

Consider an ensemble of NV centers uniformly distributed throughout a bulk single crystal diamond. The figure shows the four orientations of NV, with their principle axes highlighted with the vector. Below the diamond are two parallel microwave microstrips used for the control of the NV ground state **(black rectangles)**. On the surface of the diamond, are an array of DNA aptamers (single stranded DNA) **(black lines)**, with a Gadolinium (Gd) particle attached to one end **(blue circle)**. Gd is a spin-$\frac{7}{2}$ particle, commonly used in a few NV sensing schemes, [50, 105]. DNA aptamers are designed to have preferential binding to target molecules, [79]. As the aptamer is capable of conformation change, it will wrap around the target molecule **(green star)** when the target is within close proximity of the aptamer. In doing so, this changes the distance of the Gd particle relative to the NV centers within the diamond. In this sensing scheme, it is this distance change (Δd) that is being detected by the NV centers. This may be done in a binary case of detecting an extended or collapsed aptamer. The adaptability may also be seen in this case, as a simple way to change the target molecule being sensed is to simply change the DNA aptamer attached to the surface of the diamond.

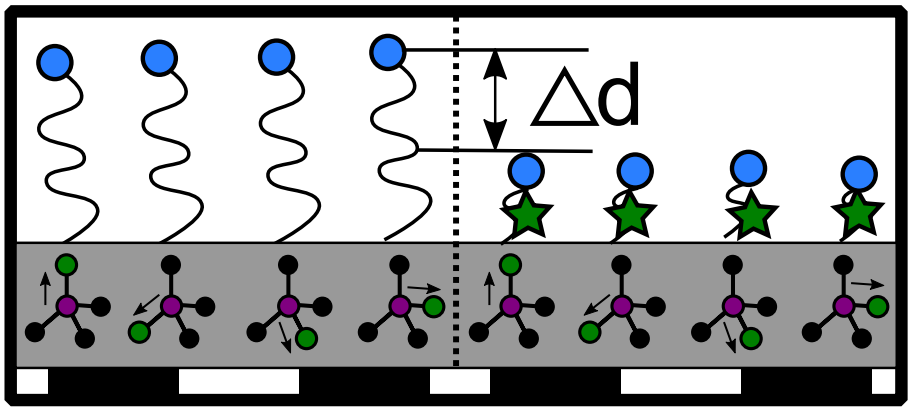

Figure 1.1: A proposed scheme for chemical sensing with OCT. In this protocol, a bulk single diamond contains an ensemble of NV centers. Their principle axes are indicated with the black vector. DNA aptamers are attached to the surface, each terminated with a Gd particle **(blue circle)**. As DNA aptamers are sensitive to target molecules **(green star)**, they will undergo a conformational change in its presence, changing the distance of the Gd particle relative to the NV ensemble. OCT pulses sourced with helical microwaves enable the use of all four NV orientations, enhancing the ability to detect this distance change (Δd). OCT enables this scheme to be easily adaptable to other sensing protocols and applications without changing the experimental setup.

NV ensembles increase the sensitivity to magnetic fields, an attractive quality for chemical sensing protocols. As NV centers have principle axis systems orienting in four possible directions, the control of all four orientations is non-trivial. Some experimental setups circumvent using all four orientations by suppressing the signal of all but one orientation by changing the incoming optical polarization, [5, 110]. In other cases, there has been an effort in growing diamond crystals which preferentially grow NV centers, reducing the number of orientations, [35, 82, 107].

Increasing the control of the NV ensemble from one orientation to all four orientations expands the experimental applications and enhances existing schemes. In the above example, controlling all four orientations simultaneously and having them behave as one collective qubit, increases the signal by four times, compared to only using one orientation. For more complex protocols, selective operations on each of the four orientations allows for multiplexing through sequential or simultaneous measurements.

As previously discussed, there are schemes involving multiple microwave frequencies to control all four orientations, but this comes at a cost of adding complexity to the experimental setup. OCT techniques offer a solution to controlling all four orientations while keeping with a modest setup design which is easily adaptable to future portable chemical sensing devices.

To maintain this compact design, the OCT controls are implemented with two parallel microstrips, represented in the figure above. Using two independently controlled microstrips provides a helical microwave source, enabling access to single transitions of the ground state without the use of an external magnetic field. Access to these single transitions has been demonstrated previously, but in these cases great care was taken to position the NV ensemble where the use of circularly polarized microwaves would be at the greatest advantage. The ensemble was at a specific height and in the middle between the two microstrips, [60, 77, 128]. In this thesis, selective transitions are demonstrated for an arbitrary position of the active NV ensemble away from the microstrips enabled by OCT controls, allowing for a more generalized device fabrication and chemical sensing schemes.

The following chapters will detail the theory for designing optimal control theory pulses, building an experimental setup suitable for NV ensemble measurements and last, a demonstration of NV ensembles experiments including an implementation of OCT experiments.

Chapter 2

Nitrogen Vacancy Centers in Diamond

This chapter will introduce the nitrogen vacancy (NV) center, giving a brief description of the main aspects of the energy level structure. Addressing first the optical transitions for initialization and readout, and then the microwave transitions for ground state control. Following this, the ground state Hamiltonian will be introduced, and address which aspects are important for this work. Last, a visualization of the NV center in the diamond lattice unit cell, and further expanding this to how the four orientations of NV center reside in the common lab frame for three diamond crystals will be presented.

2.1 The Energy Level Structure of the NV Center

The NV center is a common lattice defect in the diamond crystal. It is formed by substituting a carbon with a nitrogen, and removing an adjacent carbon to form a vacant lattice site (vacancy), [92]. The NV center may be in a NV^0 or NV^-, the difference between them being the absence or presence of an electron in the vacancy, [30]. The NV^0 and NV^- can be easily differentiated as they differ in spin. The electronic ground state of the NV^0 center is an effective spin-$\frac{1}{2}$ particle, while the NV^- center is an effective spin-1 particle, [9, 12, 67]. In addition, the NV^- center has a spin-state dependent optical initialization and read-out scheme while the NV^0 does not, [9, 12, 67]. In this thesis, the NV^- is the center being studied, and will be referred to as an NV center for simplicity.

In the lattice, the two unpaired electrons from the Nitrogen, three unpaired electrons from the surrounding Carbon atoms, and the electron in the vacancy combine to form the effective electronic spin-1 ground and excited states of the NV^- center, [67, 92] . There are also two singlet states present, which are not directly accessible through optical transitions.

A simplified version of the energy structure of the NV center is shown in figure 2.1. The NV center contains two regimes of transitions, optical and microwave. The optical transitions are used to initialize and readout the state of the NV center, while the microwave transitions control the ground state, [59, 67, 92].

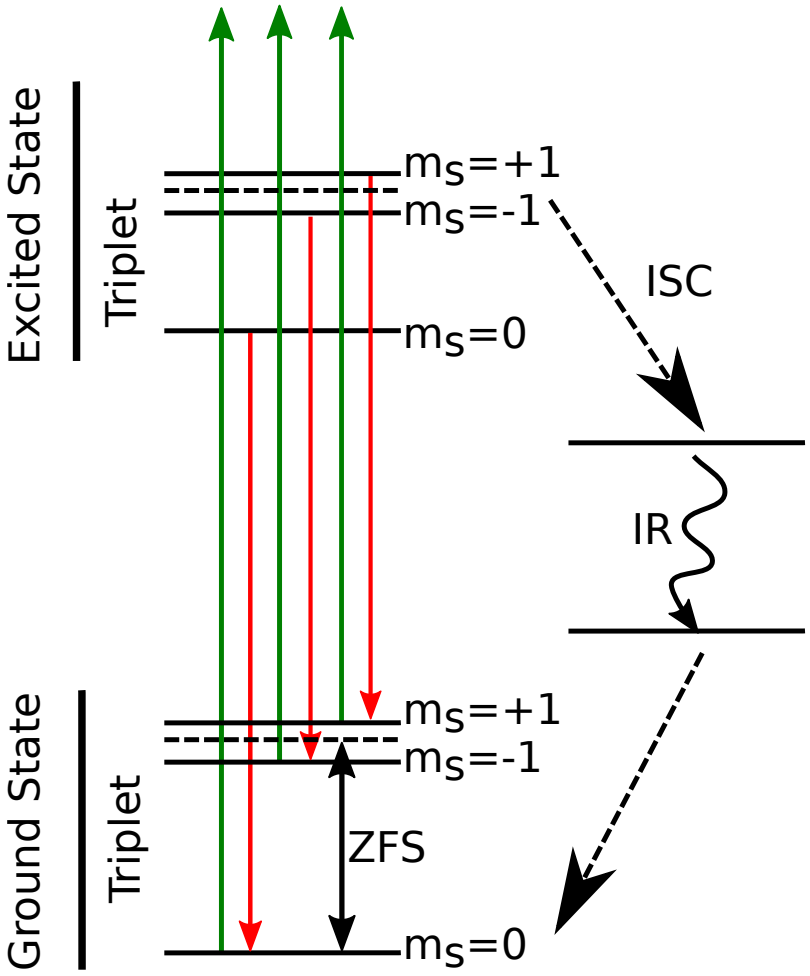

Figure 2.1: The NV Energy Level Structure with main states and transitions. Both the ground and excited states have single and triplet states. The zero field splitting (ZFS) in the ground state permanently splits the $|0\rangle$ and $|\pm1\rangle$ states. The ZFS (2.87 GHz) lies along the principle axis system (P.A.S); also the quantization axis of the NV. An external magnetic field induces a Zeeman splitting on the $|\pm1\rangle$ state, lifting the degeneracy proportional to the strength of the field projected onto the P.A.S. The NV center may be excited and controlled using a combination of optical and microwave transitions. The optical transitions initialize and readout, while the microwave transitions control the ground state energy levels. At room temperature, green light excites off resonantly from the ground state beyond the excited state to a vibronic band, which quickly decays to the excited state in a spin conversing transition. When exciting from the $|0\rangle$ ground state, all spins return to the ground $|0\rangle$ state, releasing a red photon, in a cycle of 13 ns. However, when excited from the $|\pm1\rangle$ ground state, through inter-system crossing (ISC) promoted by spin-orbit coupling, the excited $|\pm1\rangle$ states have a $\approx \frac{1}{3}$ chance of decaying to the singlet states. The singlet states have a delayed decay of $\approx$ 300 ns back to the $|0\rangle$ state, making on average less photons emitted when decaying from the $|\pm1\rangle$ excited state than the $|0\rangle$ state. This allows for optical readout of the NV center ground state, as the $|0\rangle$ state give on average more red photons than the $|\pm1\rangle$ states, known as the bright and dark states. There is a release of infrared (IR) light (1042 nm) released during the singlet state transitions, an alternative method of detection, [2, 29].

To excite the optical transitions of the NV at room temperature, a green laser is applied off resonantly at 532 nm (563 THz) which excites from the ground state to a vibronic state located above the excited state of the NV. There is a fast decay from the vibronic state to the excited state of the NV center, resulting in a spin conserving optical transition from the ground to the excited state. On the decay from the excited state to the ground state, the NV releases a red photon in a range from $\approx$600 nm to 750 nm, in another spin-conversing transition.

There are three spin states, $|0\rangle, |+1\rangle, |-1\rangle$, in the ground state of the NV center. In the absence of a magnetic field, the $|\pm1\rangle$ states are degenerate, and separated from the $|0\rangle$ state by 2.87 GHz, the ZFS. The ZFS lies along the principle axis system of the NV. When a static magnetic field is applied, the portion which lies along the P.A.S of the NV splits the degeneracy of the $|\pm1\rangle$ states, proportional to the strength of the external field.

To control the ground state population of the NV center, microwaves are applied at 2.87 GHz in the absence of a magnetic field. The frequency of the microwaves are changed in the presence of a magnetic field to lie on resonance with either the $|+1\rangle$ or $|-1\rangle$ state to achieve select transitions between the $|0\rangle$ and $|+1\rangle$ or $|-1\rangle$.

Optical transitions may not only be used to initialize the NV but to readout the ground state as well. The ground state of the NV is read-out by comparing the intensity of red photons released from the $|0\rangle$ and $|\pm1\rangle$ states. When the NV is excited from the $|0\rangle$ state, the state will transfer from the ground to the excited $|0\rangle$ state, and then relax back to the ground state, releasing a red photon, in a lifecycle of 13 ns, [42, 67, 92].

If microwaves are applied to populate the $|\pm1\rangle$ state and the NV is excited from here, the state will reach the $|\pm1\rangle$ excited state. In this case, there are multiple pathways for decay to the $|0\rangle$ ground state. In roughly $\approx 2/3$ of the transitions, the states will decay back to the $|\pm1\rangle$ in the ground state, releasing a red photon, followed by a fast vibronic decay back to the $|0\rangle$ state. However, the remaining $\approx 1/3$ of the time, the states will travel to the singlet states by way of ISC from spin-orbital coupling [90]. Once in the excited singlet state, there is a decay to the ground singlet state, with a release of an infra-red photon (1042 nm), and then an eventual decay back to the ground state $|0\rangle$ once again. The transition from the singlet to the ground state $|0\rangle$ is delayed by 300 ns, [42, 67]. Due to the alternative pathway which does not release a red photon on decay and the extended lifecycle of the delayed transition back to $|0\rangle$, the average amount of red photons emitted from the $|\pm1\rangle$ excited state compared to the $|0\rangle$ state is less. Optical readout is achieved by the intensity of red-photons being released from the NV center, with the $|0\rangle$ state being the bright state and the $|\pm1\rangle$ states being the dark states, [4].

NVs are initialized to the $|0\rangle$ ground state with a continuous pumping of the laser. All pathways, whether by a continuous excitation of the $|0\rangle$ state, or by the spin-conserving and fast vibronic decay of the $|\pm1\rangle$ states, or by the ISC path, all eventually lead back to the ground state $|0\rangle$. Thus just simply leaving the green laser on for some initialization time, populates the $|0\rangle$ state and initializes the NV.

The energy level of the NV describes both the optical and microwave transitions for the NV center. The optical transitions initialize and are used to readout the ground state, while the microwave transitions control of the ground state. Having provided a description of the energy level of the NV center, the ground state Hamiltonian may now be described.

2.2 The NV Center Ground State Hamiltonian

The Hamiltonian of the NV center describes the dynamics of the ground state, including the relationships within the NV center and may include interactions with nearby spins in the diamond lattice, and the conditions on the lattice itself. Equation 2.1 shows the Hamiltonian which describes the ground state energy levels for an NV center. Recalling the contribution of the three electrons from the neighbouring Carbons, two from the Nitrogen and the last from the electron found in the void combine to form an effective spin-1 particle, for an NV^-, [26, 56, 81, 88].

$$\begin{aligned}\mathcal{H} &= \Delta S_z^2 + E(S_x^2 - S_y^2) + \gamma_e \vec{B} \cdot \vec{S} + \gamma_N \vec{B} \cdot \vec{I_N} \\ &+ \gamma_C \vec{B} \cdot \vec{I_C} - A_N \vec{S} \cdot \vec{I_N} - A_C \vec{S} \cdot \vec{I_C} + Q I_{Nz}^2\end{aligned} \tag{2.1}$$

The zero field splitting (ZFS), (ΔS_z^2), is a permanent splitting in the ground state of NV, with a magnitude of 2.87 GHz, [56, 81]. There is a transverse zero field splitting component as well $E(S_x^2 - S_y^2)$, but unless lattice conditions in the diamond crystal are outside normal conditions, for example, large amounts of non-axial strain is present, this term is often neglected [92].

The ground $|\pm 1\rangle$ states are degenerate in the absence of a magnetic field, but in the presence of a static magnetic field, will split, according to a Zeeman interaction, shown as the $\gamma_e \vec{B} \cdot \vec{S}$.

The nuclear spin of the nitrogen, with its most common isotope being N^{14} (99.6% abundance) also contributes a nuclear spin-1, and is sensitive to the presence of an external magnetic field, as seen with the $\gamma_N \vec{B} \cdot \vec{I_N}$ term, [22, 47]. It is possible the nitrogen isotope be an N^{15} (3.4% abundance), which contributes only a spin-$\frac{1}{2}$ nuclear spin, also sensitive to an external magnetic field, [22]

There is a hyperfine splitting between the electron and nitrogen nuclear spin, $A_N \vec{S} \cdot \vec{I_N}$, with axial strength of 2.3 MHz and transverse strength of 2.1 MHz, [81, 88, 117]. Additionally, as the N^{14} nuclear spin is larger than spin $\frac{1}{2}$, there is a nuclear quadropolar term $Q I_{Nz}^2$ (-5.04 MHz), [81, 88].

The NV center is not the only spin particle found within a diamond lattice. While the diamond lattice consists of mostly carbon-12 atom (spin-0), there are also carbon-13 (spin-$\frac{1}{2}$) at 1.1% natural abundance [30]. As such, there may be a hyperfine interaction with the carbon-13 nuclear spin as well, included in the $A_C\vec{S}\cdot\vec{I_C}$ term, and the zeeman term, $\gamma_C\vec{B}\cdot\vec{I_C}$, for the nuclear carbon-13 [15, 22, 42, 88]. There are many additional lattice defects involving one or multiple substitutional atoms, [92]. These contribute to the overall spin bath of the diamond lattice, but the details of these are beyond the scope of this thesis.

The experiments performed in this work are in zero applied field, and in a low strain crystal so the Hamiltonian reduces to ΔS_z^2. As it lies along the P.A.S of the NV center, this term in real space has one of four orientations. The following section will show a visualization of the P.A.S. of each of the four orientations of NV center in the crystal lattice.

2.3 Nitrogen Vacancy Centers in the Single Crystal Lattice

Now that the energy level and Hamiltonian for the NV center have been defined, a visualization of the center in the diamond unit cell is provided. Following this, a figure of each of the four NV centers in three common diamond crystals are shown in the common lab frame.

Figure 2.2 shows the basic structure of the NV center within the diamond unit cell. The diamond unit cell is a face centered cubic lattice structure, with a total of 8 Carbon atoms, [54, 95]. The figure displays the nitrogen **(red)** and vacancy **(blue)** for each of the four possible orientations within the unit cell. The bond between the nitrogen and the vacancy form the P.A.S of the NV center, thus with four orientations, there would be four directions of the P.A.S within the crystal, [92] .

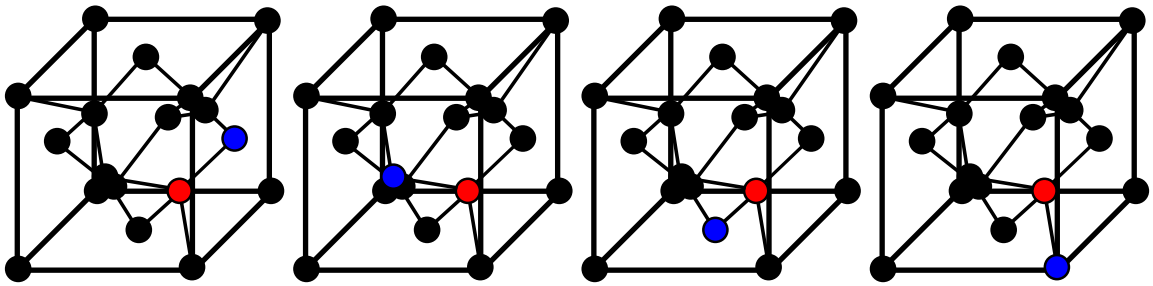

Figure 2.2: Four orientations of an NV center in a diamond lattice unit cell. An NV Center is formed by replacing a carbon atom **(black)** in a unit cell of a diamond with a nitrogen **(red)**, and removing an adjacent carbon to create a vacancy **(blue)**. The vector between the nitrogen and vacancy forms the P.A.S of the NV Center. As the Nitrogen and Vacancy may replace any pair of Carbon atoms in the lattice, there may be four orientations of the NV center and therefore four P.A.S. within a diamond crystal.

The NV center is an sp_3 hybridized structure, with each of the four P.A.S oriented, 109.471° relative to each other, [26, 32]. It should also be noted that the position of the Nitrogen and Vacancy may also be swapped, and so the negatives of these orientations are also possible. Only the four oriented listed here will be used, as the eight are a reflection of the two sets of four. Within the crystal frame, the NV bonds are labelled as (1,1,1), (-1,-1,1), (-1,1,-1), and (1,-1,-1), [82].

NV experiments focus on three main diamond single crystal cuts; (100), (110), and (111), each useful for different applications, [32, 54, 82]. The name (100), (110), and (111) refers to the vector perpendicular to the face of the diamond crystal. While the relative angle between each of the NV orientations within the crystal has not changed as the crystal structure does not differ between the (100), (110) and (111) diamonds, the relative angle between the NV and the face of the diamond does change. In this thesis, the model and simulations were developed for the (100), (110) and (111) orientations, and experiments performed on the (100) diamond.

Visualizing NV Centers in the common lab frame

It is important to consider the orientation of each NV center within the common lab frame. As the control Hamiltonian is defined by coordinates in the lab frame, and projects uniquely onto each of the NVs, an understanding of their orientations in the lab frame is critical. Figure 2.3 shows the four orientations of NV centers within the (100), (110) and (111) diamonds, where the surface of the diamond lies along the xy plane. The "z" axis represent each of the (100), (110) and (111) vectors, perpendicular to the face of the diamond, and is also in line with gravity in the lab frame. As the z-vector of the diamond crystal has been placed inline with the "z" axis in the lab frame, this figure represents the orientation of the NV centers in the lab frame.

Recall that the diamond lattice between each of the (100), (110) and (111) crystals are the same, thus the orientation between each of the NV centers does not change within the crystal structure. What is different is the vector defining the face of the diamond, which in turn changes the orientation of the NV centers relative to the surface, as is being reflected in the figure.

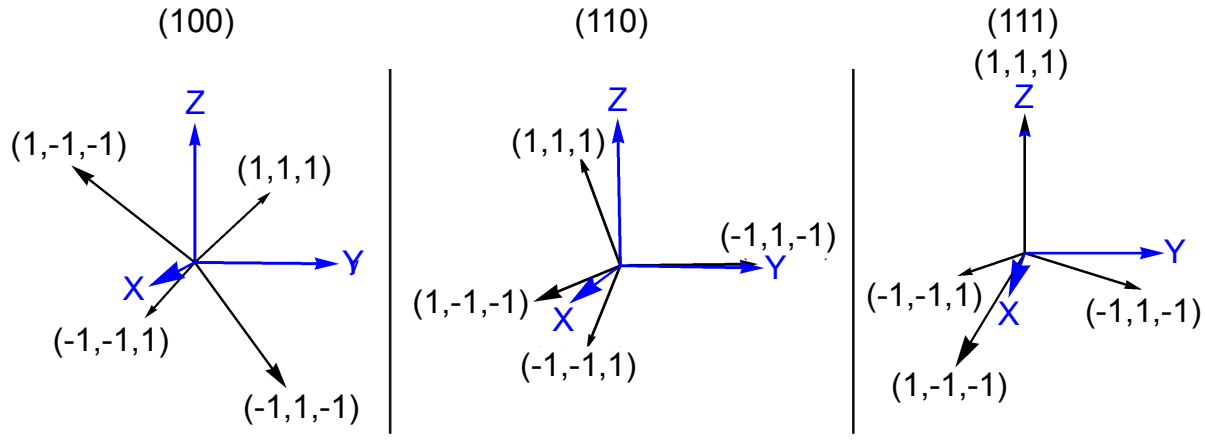

Figure 2.3: Recalling that there are three single crystal diamond orientations commonly used for NV experiments, labelled, (100), (110) and (111). The four NV geometries within each single crystal diamond change relative to the surface of the diamond. The figure shows the NV P.A.S relative to the surface of the (100), (110) and (111) diamond, which has been placed inline with the lab frame. The "x", "y" and "z" axis here are represented in the lab frame, with the surface of the diamond lying along the xy plane, and the (100), (110) and (111) axes pointing along the "z" axis (along gravity) in the lab frame.

Looking at each orientation more closely, the (100) diamond has the NVs symmetrical about the xy-plane, with the (1,-1,-1) and (1,1,1) orientations oriented 54° above the xy plane, and the (-1,1,-1) and (-1,-1,1) oriented 54° below the xy plane. In addition to symmetry about the xy plane, there is also symmetry about the "z" axis, having the (1,1,1) and (-1,1,-1) rotated a positive 54° from the "z" axis and the (1,-1,-1) and (-1,-1,1) being a negative 54° from the "z" axis. The procedure to solve for these angles will be shown in chapter three (section 3.1.2), but are summarized here to gain an intuition. With respect to the surface of the diamond, this is the most symmetrical orientation the NVs may be presented as they are split equally about the "z" axis and xy plane. This symmetry will be advantageous for ensemble control of the NV centers.

The (110) crystal has the (1,-1,-1) and (-1,1,-1) NVs lying along the xy plane, oriented 109° apart on this plane. The (1,1,1) and (1,-1,-1) lie 35° and 144°, off the "z" axis, notably also separated by 109°. Recall that 109° is the bond angle for an sp_3 hybridized structure.

The (111) crystal is unique from the other two in that the "z" axis in the lab frame, "z" axis of the crystal frame and the "z" axis of the (1,1,1) NV all lie along the same vector. The other three NV orientations lie 109° away from the "z" axis. The (111) diamond is the easiest to visualize as the characteristic sp_3 hybridized structure, because one of the P.A.S points in the positive z-direction. It is important to remember all three crystal orientations have this same structure, they are simply rotated relative to the crystal's face.

This chapter provided the description of the energy level, ground state Hamiltonian and a good visual representation for the orientations of the NV centers in the lab frame for each of the three crystals being studied. Chapter three will now provide the procedure of how to rotate the NV centers from their native frame dictated by their P.A.S to the crystal frame and subsequently to the lab frame, so as to arrive at the figure shown in this chapter. Following this, each of these three crystal structures will be explored in detail to arrive at the control Hamiltonian used to create the control parameters for optimal control theory pulses.

Chapter 3

Optimal Control Theory Techniques for NV Center Ensembles

Chapter two described the energy level structure, ground state Hamiltonian and concluded with a visualization of each nitrogen vacancy (NV) center in the common lab frame. In this chapter, the control Hamiltonian for each orientation will be described so OCT pulses may be designed for NV ensembles. It will then show key examples of optimal control theory (OCT) pulses for the most commonly used single crystal diamonds.

OCT optimizes a set of controls based on the given input control parameters, initial conditions and control algorithm. Using these inputs, the algorithm optimizes the control parameters to find the desired output target. Practically, this may be realized through experiments such as optimizing the spacing time between applied π pulses to minimize the sensitivity to magnetic fields as a function of the total sensing time and the phase of the sensing field, [84]. In other instances, gradient and non-gradient based algorithms are used to create shaped pulses designed to find desired target unitaries or state-to-state transfers based on a set of input controls, cost functions and Hamiltonians, [89].

In this thesis, the gradient based gradient ascent pulse engineering (GRAPE) algorithm is used to design shaped pulses which realize state-to-state transfers of NV centers for all four orientations in a single crystal diamond. The inputs to the algorithm include the initial state, control Hamiltonians for each NV orientation, control parameters given by the microwave control field, time step resolution of the shaped pulse and total time of the pulse.

The control Hamiltonians are designed to include the four orientations of NV centers with a generalized microwave source. The OCT controls have also been designed to demonstrate selective control of each orientation in the absence of a static magnetic field and without the restriction of having a known geometric location of the NVs. There have been previous works showing selective transitions for single and ensembles of NVs in the absence of magnetic field, [6, 60, 77, 121, 122, 127, 128].

The quantization axis of the NV center lies along the principle axis system (P.A.S). This vector is defined by the bond between nitrogen and vacancy in the crystal lattice. Ensembles of NVs, require control of the four P.A.S in the crystal. An incoming control field would project differently onto each principle axis, making the control solutions non-trivial.

Outside of OCT control, some approaches to ensemble experiments focus on reducing the number of active orientations. One strategy is to select only one orientation by suppressing the fluorescence from the others with a chosen optical polarization, [5, 110]. Another solution involves changing the growth of the crystal structure, so the lattice grows preferentially along one axis, reducing the distribution of NV center orientations, [35, 82, 107].

Chapter one also described experiments using multiple microwave frequencies to address each orientation, [93, 119]. OCT controls are able to find a pulse to target all four NV orientations within a single crystal in the absence of a magnetic field, with two independently controlled microwave channels.

In this thesis, a general solution for the design of the control Hamiltonian is presented for OCT control of NV ensembles. In the first section of this chapter, the generalized control Hamiltonian will be described for any single NV orientation in any of the three chosen single crystal diamonds (100), (110), and (111). This will be followed by describing an ensemble of NVs within one single crystal for any incoming control field in the absence of a magnetic field. In the second part of the chapter, simulated OCT controls will be shown using a 2D magnetic field generated by two parallel microstrips, detailing key examples of NV ensemble control on the (100), (110) and (111) diamonds. Chapter five will use the insight from the simulations completed in this chapter to demonstrate experimental OCT control on the (100) diamond.

3.1 Describing the Control Hamiltonian

This section will describe the control Hamiltonian capable of performing OCT experiments. First, a description of the eigenstates and values of the NV center ground state are found. This is followed by expressing the control Hamiltonian and NV Hamiltonian in the same frame. As the control Hamiltonian is defined by microwave fields in the lab frame, and the NV frame is defined by its principle axis, these must be described in the same frame so that the effective Hamiltonian may be found. The effective Hamiltonian is described for both a single NV along any principle axis and then expanded to an ensemble of NVs. Once the effective Hamiltonian is found, for a general microwave control field, an experimental configuration is added to describe the control Hamiltonian reflective of the experimental setup. Following this, OCT pulses will be simulated using the effective Hamiltonian to demonstrate collective and selective control on NV ensembles in the (100), (110) and (111) diamonds.

3.1.1 The Eigenstates and Values of the NV Ground State Hamiltonian

To begin describing the control Hamiltonian for an NV center ensemble, eigenstates and values for the ground state Hamiltonian must be defined. As explored in chapter two (section 2.2), the crystal conditions allow for only the zero field splitting term of the ground state Hamiltonian to be included, so the eigenstates and values are quite simple.

As the NV^- center is an effective spin-1 particle, spin-1 (S_x, S_y, S_z) operators are used; outlined in their matrix form below:

$$S_x = \begin{pmatrix} 0 & \frac{1}{\sqrt{2}} & 0 \\ \frac{1}{\sqrt{2}} & 0 & \frac{1}{\sqrt{2}} \\ 0 & \frac{1}{\sqrt{2}} & 0 \end{pmatrix}; S_y = \begin{pmatrix} 0 & \frac{-i}{\sqrt{2}} & 0 \\ \frac{i}{\sqrt{2}} & 0 & \frac{-i}{\sqrt{2}} \\ 0 & \frac{i}{\sqrt{2}} & 0 \end{pmatrix}; S_z = \begin{pmatrix} 1 & 0 & 0 \\ 0 & 0 & 0 \\ 0 & 0 & -1 \end{pmatrix}; \tag{3.1}$$

As these experiments will be conducted in the absence of a magnetic field, only the zero field splitting (ZFS) term of the ground state Hamiltonian will be considered, $\mathcal{H} = \Delta S_z^2$.

The eigenstates are listed below:

$$|-1\rangle = \begin{pmatrix} 1 \\ 0 \\ 0 \end{pmatrix}; |0\rangle = \begin{pmatrix} 0 \\ 1 \\ 0 \end{pmatrix}; |+1\rangle = \begin{pmatrix} 0 \\ 0 \\ 1 \end{pmatrix} \tag{3.2}$$

With eigenvalues:

$$\lambda_{|-1\rangle} = \Delta;\ \lambda_{|0\rangle} = 0;\ \lambda_{|+1\rangle} = \Delta \tag{3.3}$$

Typically, to address selective transitions between the $|0\rangle \rightarrow |+1\rangle$ *or* $|-1\rangle$, a static field is added to split the degeneracy between the $|\pm 1\rangle$ states. The control field is then put on resonance with one of the two split states so the transition between the $|0\rangle$ and $|+1\rangle$ or $|-1\rangle$ state is favoured and the other state remains unpopulated, [80, 81]. While this does allow to treat the NV as an effective spin-$\frac{1}{2}$ particle, it does so while sacrificing the sensitivity to external magnetic fields that are aiming to be detected, [122].

While the $|\pm 1\rangle$ states are degenerate, the transitions between them are sensitive to the polarization of the incoming microwave control field. Selective single transitions from the $|0\rangle \rightarrow |+1\rangle$ or $|-1\rangle$ may be achieved through the use of circularly polarized control fields, [6, 60, 77, 121, 122, 127, 128]. Additionally, using circularly polarized microwaves grants access to the $|\pm 1\rangle$ state manifold, which enhances the sensitivity to external magnetic fields, [76]. Circularly polarized controls are created by combining the fields from two linearly polarized microwave sources. The details of creating circularly polarized microwave control fields will be discussed in chapter four (section 4.3).

3.1.2 Expressing the Control Hamiltonian and NV Principle Axis System in the Same Frame

The control Hamiltonian is defined by microwave fields in the lab frame, while the NV centers' frame is dictated by its principle axis. As there are four orientations of NV centers within a single crystal diamond, the control Hamiltonian will project differently onto each of the four orientations of NV centers. Recall the four P.A.S of the NV centers are oriented 109.471° relative to each other, consistent with a sp_3 hybridized structure, [26, 32]. For a visualization of how the NVs are oriented within the diamond lattice structure, refer back to figure 2.2.

To account for how the control Hamiltonian will project onto each of the four orientations, three frames are considered. These are labelled the NV frame, crystal frame and lab frame.

Before proceeding, the "z" axis of each frame can be defined. This is where most of the frame transformations will be centered about.

- **NV P.A.S:** The vector between the Nitrogen and the Vacancy within the diamond crystal forms the P.A.S. This marks the NVs "z" axis. It is also the quantization axis.
- **Diamond crystal:** (100), (110), (111) indicates the vectors perpendicular to the diamonds crystal face and the diamonds "z" axis.
- **Lab frame:** Gravity marks the negative "z" axis. This may also be chosen as the optical "z" axis. Gravity was chosen as it is easier to visualize.

Recalling back to chapter two, figure 2.3 shows each of the four NV centers P.A.S in the lab frame for each diamond crystal. The rotation from the NV to the lab frame may be broken into two stages. The first rotation stage is to find a rotation matrix which takes the "z" axis of the diamond crystal to the lab "z" vector. The second stage is to find a rotation matrix which takes the NV principle axis z vectors to the diamond crystal z vectors. The product of the two rotations will take the NV P.A.S to the lab frame and the inverse, the lab frame to the NV.

The bonds that form the diamonds' lattice all lie along the (1,1,1) axis. The crystal orientation is defined as the vector perpendicular to the face that the diamond was cut along. This is found in a (100), (110) or (111) orientation, shown in figure 3.1. Cutting the face of the diamond along the three different axes changes the relative orientation of the (1,1,1) bond, the NV bond, relative to the surface. This does not change the relative orientation of NVs relative to each other.

Figure 3.1 shows the diamond crystal "z" axis **(red)** and lab frame "z" axis **(blue, dashed)**. In the most trivial case, it is evident that the (100) diamond just requires a simple $\frac{\pi}{2}$ rotation about the lab "y" axis to align the two axes. The (110) and (111) crystals are not as trivial, but a general procedure to rotate can be found.

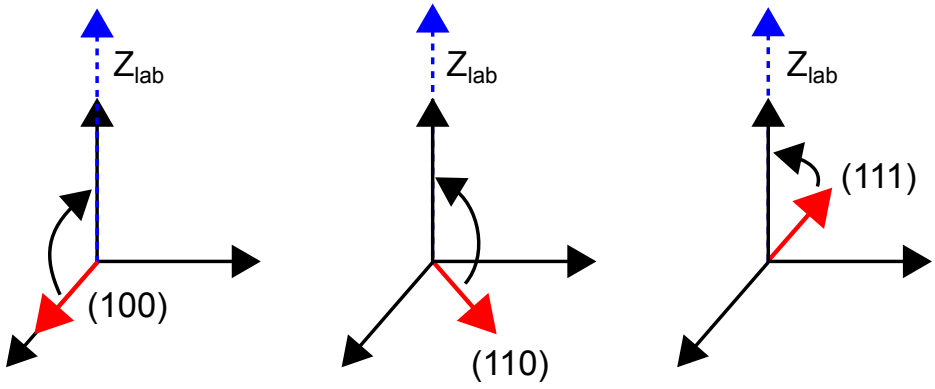

Figure 3.1: Rotating the diamond crystal "z" axis to the lab frame "z" axis. The lab frame "z" axis is marked in **(blue, dashed)**, while the diamond "z" vector is marked in **(red)**. The most trivial rotation is for the (100) diamond, which just requires a $\frac{\pi}{2}$ rotation about the "y" axis to align the diamond (100) axis with the lab frame axis. The (110) and (111) are less trivial, but a generalized solution can be found.

As the frame rotations are not trivial, a generalized procedure is established. This is listed below:

1. Normalize the starting vector being rotated (labelled $\vec{a}$)
2. Find the cross product between the starting vector ($\vec{a}$) and the desired vector ($\vec{b}$) to yield the rotation axis ($\vec{c}$)
3. Find the dot product between $\vec{a}$ and $\vec{b}$ to yield the rotation angle ($\theta_{(ab)}$)
4. Create a rotation matrix, which rotates $\vec{a}$ about $\vec{c}$ by $\theta_{(ab)}$ to arrive at $\vec{b}$

Formally, the general form of the rotation matrix is given by the Rodrigues' rotation formula, where k is the rotation axis and θ is the angle of rotation. In practice, the rotation matrices were found using the angles and rotation axis as inputs to the "RotationMatrix" function in Mathematica.

$$R = \mathbb{1}\cos(\theta) + [k]_x \sin(\theta) + (1 - \cos(\theta))kk^T \tag{3.4}$$

Applying this procedure finds, the resulting vectors $\vec{c}_{DL}$, and angles, θ_{DL} to rotate each diamond crystal "z" vector to the lab frame "z" vector, shown in figure 3.2. As was seen in the trivial case, rotating about the negative "y" axis by $\frac{\pi}{2}$ takes the (100) diamond to the lab frame "z" axis. The (110) and (111) rotate about an axis on the xy plane, but with different angles, to arrive at the lab frame "z".

$\vec{c}$DL for different Diamond Crystals

	$\vec{c}$DL	ΘDL
(100)	$0\ -1\ 0$	$\frac{\pi}{2}$
(110)	$\frac{1}{\sqrt{2}}\ -\frac{1}{\sqrt{2}}\ 0$	$\frac{\pi}{2}$
(111)	$\frac{1}{\sqrt{2}}\ -\frac{1}{\sqrt{2}}\ 0$	$\text{ArcCos}\left[\frac{1}{\sqrt{3}}\right]$

Figure 3.2: The vector $\vec{c}_{DL}$ and angle θ_{DL} to rotate each diamond crystal "z" axis to the lab frame "z" axis.

These vectors and rotations angles now yield the rotation matrix shown in figure 3.3. This rotation matrix can now be applied to any vector in each diamond crystal to rotate it to the lab frame.

Crystal	Rotation Matrix from Crystal to Lab Frame
(100)	$\begin{pmatrix} 0 & 0 & -1 \\ 0 & 1 & 0 \\ 1 & 0 & 0 \end{pmatrix}$
(110)	$\begin{pmatrix} \frac{1}{2} & -\frac{1}{2} & -\frac{1}{\sqrt{2}} \\ -\frac{1}{2} & \frac{1}{2} & -\frac{1}{\sqrt{2}} \\ \frac{1}{\sqrt{2}} & \frac{1}{\sqrt{2}} & 0 \end{pmatrix}$
(111)	$\begin{pmatrix} \frac{1}{6}\left(3+\sqrt{3}\right) & \frac{1}{6}\left(-3+\sqrt{3}\right) & -\frac{1}{\sqrt{3}} \\ \frac{1}{6}\left(-3+\sqrt{3}\right) & \frac{1}{6}\left(3+\sqrt{3}\right) & -\frac{1}{\sqrt{3}} \\ \frac{1}{\sqrt{3}} & \frac{1}{\sqrt{3}} & \frac{1}{\sqrt{3}} \end{pmatrix}$

Figure 3.3: These rotation matrices may be applied to any vector in the diamond frame, and have it rotated to the lab frame for each of the (100), (110) and (111) crystal lattices.

The rotation matrices are tested by applying them to the normalized crystal frame vectors. When the rotation matrix is applied to the crystal vector, it is rotated to the lab frame "z" axis. When the inverse of the rotation matrix is applied to the lab frame "z", each of the three crystal axes are found for the three rotation matrices.

Crystal Frame z	Lab Frame z
$1\ 0\ 0$	$0\ 0\ 1$
$\frac{1}{\sqrt{2}}\ \frac{1}{\sqrt{2}}\ 0$	$0\ 0\ 1$
$\frac{1}{\sqrt{3}}\ \frac{1}{\sqrt{3}}\ \frac{1}{\sqrt{3}}$	$0\ 0\ 1$

Lab Frame z	Crystal Frame z
$0\ 0\ 1$	$1\ 0\ 0$
$0\ 0\ 1$	$\frac{1}{\sqrt{2}}\ \frac{1}{\sqrt{2}}\ 0$
$0\ 0\ 1$	$\frac{1}{\sqrt{3}}\ \frac{1}{\sqrt{3}}\ \frac{1}{\sqrt{3}}$

Figure 3.4: The crystal frame "z" is multiplied by the rotation matrix for each crystal to arrive at the lab frame "z" **(left)**. Applying the inverse of the rotation matrix to the lab frame z produces the crystal frame "z" **(right)**.

The NVs may be labelled in their crystal axis description, which are permutations of the (1,1,1) bond. The NVs in the crystal axis are labelled as (1,1,1), (-1,-1,1), (-1,1,-1) and (1,-1,-1). Recall that the rotation matrix may be applied to any vector in the diamond crystal. As such, applying the rotation matrices for each crystal to the NVs expresses them in the lab frame. Figure 3.5 shows the NV vectors in the lab frame for each crystal. It is noted here that the (1,1,1) NV in the (111) crystal is aligned with the lab frame "z". These vectors shown were used to create 2.3, depicting each of the four NV orientations in the (100), (110) and (111) diamonds in the lab frame.

NVs Transformation from Crystal to Lab Frame

	NV in Lab Frame (100)	NV in Lab Frame (110)	NV in Lab Frame (111)
(1, 1, 1)	$-\frac{1}{\sqrt{3}}\ \ \frac{1}{\sqrt{3}}\ \ \frac{1}{\sqrt{3}}$	$-\frac{1}{\sqrt{6}}\ \ -\frac{1}{\sqrt{6}}\ \ \sqrt{\frac{2}{3}}$	0 0 1
(-1, -1, 1)	$-\frac{1}{\sqrt{3}}\ \ -\frac{1}{\sqrt{3}}\ \ -\frac{1}{\sqrt{3}}$	$-\frac{1}{\sqrt{6}}\ \ -\frac{1}{\sqrt{6}}\ \ -\sqrt{\frac{2}{3}}$	$-\frac{2}{3}\ \ -\frac{2}{3}\ \ -\frac{1}{3}$
(-1, 1, -1)	$\frac{1}{\sqrt{3}}\ \ \frac{1}{\sqrt{3}}\ \ -\frac{1}{\sqrt{3}}$	$-\frac{1}{\sqrt{3}}+\frac{1}{\sqrt{6}}\ \ \frac{1}{\sqrt{3}}+\frac{1}{\sqrt{6}}\ \ 0$	$\frac{1}{3}-\frac{1}{\sqrt{3}}\ \ \frac{1}{3}+\frac{1}{\sqrt{3}}\ \ -\frac{1}{3}$
(1, -1, -1)	$\frac{1}{\sqrt{3}}\ \ -\frac{1}{\sqrt{3}}\ \ \frac{1}{\sqrt{3}}$	$\frac{1}{\sqrt{3}}+\frac{1}{\sqrt{6}}\ \ -\frac{1}{\sqrt{3}}+\frac{1}{\sqrt{6}}\ \ 0$	$\frac{1}{3}+\frac{1}{\sqrt{3}}\ \ \frac{1}{3}-\frac{1}{\sqrt{3}}\ \ -\frac{1}{3}$

Figure 3.5: The NVs lie along the (1,1,1) axes of the crystal. These four orientations are (1,1,1), (-1,-1,1), (-1,1,-1) and (1,-1,-1). Applying the crystal to lab rotation matrix to the NVs with this description expresses the NVs as a lab frame vector.

Now that the NVs are expressed in the lab frame, the rotation matrix between expressing the NVs in the lab frame and in the frame of the P.A.S may be found. Note that for each individual NV, the P.A.S is defined as the "z" axis $\{0, 0, 1\}$, so the rotation matrix will rotate between each of the NV vectors in the lab frame, outlined in figure 3.5 and $\{0, 0, 1\}$. The same procedure outlined to find the rotation matrix between the diamond crystal "z", and lab frame "z" may be applied and arrive at the rotation matrix for the NV centers from their P.A.S to their lab frame vectors. Figure 3.6 shows the vectors $\vec{c}$ and angles θ to rotate about.

C vector to rotate about for NV to Lab Frame

	(100)	(110)	(111)
(1, 1, 1)	$\frac{1}{\sqrt{2}}$ $\frac{1}{\sqrt{2}}$ 0	$-\frac{1}{\sqrt{2}}$ $\frac{1}{\sqrt{2}}$ 0	0 0 1
(-1, -1, 1)	$-\frac{1}{\sqrt{2}}$ $\frac{1}{\sqrt{2}}$ 0	$-\frac{1}{\sqrt{2}}$ $\frac{1}{\sqrt{2}}$ 0	$-\frac{1}{\sqrt{2}}$ $\frac{1}{\sqrt{2}}$ 0
(-1, 1, -1)	$\frac{1}{\sqrt{2}}$ $-\frac{1}{\sqrt{2}}$ 0	$\frac{1}{\sqrt{3}}+\frac{1}{\sqrt{6}}$ $\frac{1}{\sqrt{3}}-\frac{1}{\sqrt{6}}$ 0	$\frac{1+\sqrt{3}}{2\sqrt{2}}$ $\frac{-1+\sqrt{3}}{2\sqrt{2}}$ 0
(1, -1, -1)	$-\frac{1}{\sqrt{2}}$ $-\frac{1}{\sqrt{2}}$ 0	$-\frac{1}{\sqrt{3}}+\frac{1}{\sqrt{6}}$ $-\frac{2+\sqrt{2}}{2\sqrt{3}}$ 0	$-\frac{-1+\sqrt{3}}{2\sqrt{2}}$ $-\frac{1+\sqrt{3}}{2\sqrt{2}}$ 0

Θ angle we rotate our C vec for NV to Lab Frame

	(100)	(110)	(111)
(1, 1, 1)	$\text{ArcSec}\left[\sqrt{3}\right]$	$\text{ArcCos}\left[\sqrt{\frac{2}{3}}\right]$	0
(-1, -1, 1)	$\text{ArcCos}\left[-\frac{1}{\sqrt{3}}\right]$	$\text{ArcCos}\left[-\sqrt{\frac{2}{3}}\right]$	$\text{ArcSec}[-3]$
(-1, 1, -1)	$\text{ArcCos}\left[-\frac{1}{\sqrt{3}}\right]$	$\frac{\pi}{2}$	$\text{ArcSec}[-3]$
(1, -1, -1)	$\text{ArcSec}\left[\sqrt{3}\right]$	$\frac{\pi}{2}$	$\text{ArcSec}[-3]$

Figure 3.6: The rotation vector and angle to rotate the NV P.A.S to the lab frame for all four orientations in each of the (100), (110) and (111) diamond.

Using these rotation axes and angles, the rotation matrices from the NV to the lab frame may be found. To avoid too much repetition, only the matrix rotating from the lab to the NV frame is shown.

Rotation Matrix from Lab Frame to NV Frame

	(100)	(110)	(111)
(1, 1, 1)	$\begin{pmatrix} \frac{1}{6}\left(3+\sqrt{3}\right) & \frac{1}{6}\left(3-\sqrt{3}\right) & \frac{1}{\sqrt{3}} \\ \frac{1}{6}\left(3-\sqrt{3}\right) & \frac{1}{6}\left(3+\sqrt{3}\right) & -\frac{1}{\sqrt{3}} \\ -\frac{1}{\sqrt{3}} & \frac{1}{\sqrt{3}} & \frac{1}{\sqrt{3}} \end{pmatrix}$	$\begin{pmatrix} \frac{1}{2}+\frac{1}{\sqrt{6}} & -\frac{1}{2}+\frac{1}{\sqrt{6}} & \frac{1}{\sqrt{6}} \\ -\frac{1}{2}+\frac{1}{\sqrt{6}} & \frac{1}{2}+\frac{1}{\sqrt{6}} & \frac{1}{\sqrt{6}} \\ -\frac{1}{\sqrt{6}} & -\frac{1}{\sqrt{6}} & \sqrt{\frac{2}{3}} \end{pmatrix}$	$\begin{pmatrix} 1 & 0 & 0 \\ 0 & 1 & 0 \\ 0 & 0 & 1 \end{pmatrix}$
(-1, -1, 1)	$\begin{pmatrix} \frac{1}{6}\left(3-\sqrt{3}\right) & \frac{1}{6}\left(-3-\sqrt{3}\right) & \frac{1}{\sqrt{3}} \\ \frac{1}{6}\left(-3-\sqrt{3}\right) & \frac{1}{6}\left(3-\sqrt{3}\right) & \frac{1}{\sqrt{3}} \\ -\frac{1}{\sqrt{3}} & -\frac{1}{\sqrt{3}} & -\frac{1}{\sqrt{3}} \end{pmatrix}$	$\begin{pmatrix} \frac{1}{2}-\frac{1}{\sqrt{6}} & -\frac{1}{2}-\frac{1}{\sqrt{6}} & \frac{1}{\sqrt{6}} \\ -\frac{1}{2}-\frac{1}{\sqrt{6}} & \frac{1}{2}-\frac{1}{\sqrt{6}} & \frac{1}{\sqrt{6}} \\ -\frac{1}{\sqrt{6}} & -\frac{1}{\sqrt{6}} & -\sqrt{\frac{2}{3}} \end{pmatrix}$	$\begin{pmatrix} \frac{1}{3} & -\frac{2}{3} & \frac{2}{3} \\ -\frac{2}{3} & \frac{1}{3} & \frac{2}{3} \\ -\frac{2}{3} & -\frac{2}{3} & -\frac{1}{3} \end{pmatrix}$
(-1, 1, -1)	$\begin{pmatrix} \frac{1}{6}\left(3-\sqrt{3}\right) & \frac{1}{6}\left(-3-\sqrt{3}\right) & -\frac{1}{\sqrt{3}} \\ \frac{1}{6}\left(-3-\sqrt{3}\right) & \frac{1}{6}\left(3-\sqrt{3}\right) & -\frac{1}{\sqrt{3}} \\ \frac{1}{\sqrt{3}} & \frac{1}{\sqrt{3}} & -\frac{1}{\sqrt{3}} \end{pmatrix}$	$\begin{pmatrix} \frac{1}{6}\left(3+2\sqrt{2}\right) & \frac{1}{6} & \frac{1}{\sqrt{3}}-\frac{1}{\sqrt{6}} \\ \frac{1}{6} & \frac{1}{6}\left(3-2\sqrt{2}\right) & -\frac{2+\sqrt{2}}{2\sqrt{3}} \\ -\frac{1}{\sqrt{3}}+\frac{1}{\sqrt{6}} & \frac{1}{\sqrt{3}}+\frac{1}{\sqrt{6}} & 0 \end{pmatrix}$	$\begin{pmatrix} \frac{1}{3}+\frac{1}{\sqrt{3}} & \frac{1}{3} & -\frac{1}{3}+\frac{1}{\sqrt{3}} \\ \frac{1}{3} & \frac{1}{3}-\frac{1}{\sqrt{3}} & -\frac{1}{3}-\frac{1}{\sqrt{3}} \\ \frac{1}{3}-\frac{1}{\sqrt{3}} & \frac{1}{3}+\frac{1}{\sqrt{3}} & -\frac{1}{3} \end{pmatrix}$
(1, -1, -1)	$\begin{pmatrix} \frac{1}{6}\left(3+\sqrt{3}\right) & \frac{1}{6}\left(3-\sqrt{3}\right) & -\frac{1}{\sqrt{3}} \\ \frac{1}{6}\left(3-\sqrt{3}\right) & \frac{1}{6}\left(3+\sqrt{3}\right) & \frac{1}{\sqrt{3}} \\ \frac{1}{\sqrt{3}} & -\frac{1}{\sqrt{3}} & \frac{1}{\sqrt{3}} \end{pmatrix}$	$\begin{pmatrix} \frac{1}{6}\left(3-2\sqrt{2}\right) & \frac{1}{6} & -\frac{2+\sqrt{2}}{2\sqrt{3}} \\ \frac{1}{6} & \frac{1}{6}\left(3+2\sqrt{2}\right) & \frac{1}{\sqrt{3}}-\frac{1}{\sqrt{6}} \\ \frac{1}{\sqrt{3}}+\frac{1}{\sqrt{6}} & -\frac{1}{\sqrt{3}}+\frac{1}{\sqrt{6}} & 0 \end{pmatrix}$	$\begin{pmatrix} \frac{1}{3}-\frac{1}{\sqrt{3}} & \frac{1}{3} & -\frac{1}{3}-\frac{1}{\sqrt{3}} \\ \frac{1}{3} & \frac{1}{3}+\frac{1}{\sqrt{3}} & -\frac{1}{3}+\frac{1}{\sqrt{3}} \\ \frac{1}{3}+\frac{1}{\sqrt{3}} & \frac{1}{3}-\frac{1}{\sqrt{3}} & -\frac{1}{3} \end{pmatrix}$

Figure 3.7: Rotation matrix from the lab frame to the NV frame for all NVs in three crystals. NVs are labelled (1,1,1), (-1,-1,1), (-1,1,-1) and (1,-1,-1). Diamonds are labelled (100), (110) and (111).

The general symbolic control Hamiltonian for any NV orientation

While the rotation matrices will rotate the control Hamiltonian to the NV frame for each orientation, it is more convenient to write the Hamiltonian in a symbolic form so the general relationships between the control field and the P.A.S may be found. Following this, the values from the numerical rotation matrices may be substituted in for each NV orientation.

For the following calculations, the control Hamiltonian for only a single NV will be considered, so the intuition for how to apply the same concept to an ensemble of NVs may be gained. In this case, the control field will be rotated to the quantization axis of the NV frame. The general rotation matrix is shown in equation 3.5. These generic values need only to be replaced by those listed in the rotation matrices above for each NV.

$$R = \begin{pmatrix} xx & xy & xz \\ yx & yy & yz \\ zx & zy & zz \end{pmatrix} \tag{3.5}$$

Equation 3.6, shows that the rotation matrix may be applied either after the control field has been described in the lab frame ($\vec{C}(t)$), **(left)**, or may be applied first to rotate the vector describing the base spin operators ($\vec{S}$) **(right)**. Both are equivalent. In this text, the rotation matrix is applied first to the spin operators, as shown on the right.

$$(R^T \cdot \vec{C}(t)) \cdot \vec{S} = \vec{C}(t)(R \cdot \vec{S}) \tag{3.6}$$

$\vec{C}(t)$ is the vector describing the direction of the microwave field applied. A field in the xz lab direction would be $\vec{C}(t) = \{C_x(t), 0, C_z(t)\}$ and $\vec{S}$ is the vector representing the spin-1 operators $\vec{S} = \{S_x, S_y, S_z\}$

Applying the rotation matrix to the spin operators in their original frame expressed them in the rotated frame ($\vec{\tilde{S}}$):

$$R\vec{\tilde{S}} = \begin{pmatrix} xx & xy & xz \\ yx & yy & yz \\ zx & zy & zz \end{pmatrix} \cdot (\tilde{S}_x, \tilde{S}_y, \tilde{S}_z)^T \tag{3.7}$$

Expressing the individual spin operators in the rotated frame as:

$$\begin{aligned} \tilde{S}_x &\rightarrow (xxS_x + xyS_y + xzS_z) \\ \tilde{S}_y &\rightarrow (yxS_x + yyS_y + yzS_z) \\ \tilde{S}_z &\rightarrow (zxS_x + zyS_y + zzS_z) \end{aligned} \tag{3.8}$$

Applying the rotation to the control field in the lab frame, a general control Hamiltonian with generic microwave field direction, in the NV frame is expressed as:

$$\begin{aligned} \mathcal{H}_{CTRL} &= \vec{C(t)} \cdot \vec{\tilde{S}} \\ \mathcal{H}_{CTRL} &= C_x(t)(xxS_x + xyS_y + xzS_z) \\ &\quad + C_y(t)(yxS_x + yyS_y + yzS_z) \\ &\quad + C_z(t)(zxS_x + zyS_y + zzS_z) \end{aligned} \tag{3.9}$$

At this point, the control Hamiltonian and NV ground state Hamiltonian are both expressed in the same NV frame. This general representation extends to any single NV. Now that they are both in the same frame, the effective Hamiltonian may be found for a single NV center.

3.1.3 Finding the Effective Control Hamiltonian for a Single NV along any Principle Axis

Now that the control Hamiltonian has been expressed in the frame of the NV P.A.S, the effective Hamiltonian may be found. The total Hamiltonian is the summation of the ZFS of the NV center and microwave control Hamiltonian. Recall that the rotation terms (xx,xy etc.) are unique for each NV orientation.

$$\begin{aligned}\mathcal{H}_{Tot} = \Delta S_z^2 + C_x(t)(xxS_x + xyS_y + xzS_z) \\ + C_y(t)(yxS_x + yyS_y + yzS_z) + C_z(t)(zxS_x + zyS_y + zzS_z)\end{aligned} \tag{3.10}$$

The following equation is used to find the effective Hamiltonian:

$$\mathcal{H}_{Eff} = U^\dagger(t)(\mathcal{H}_{Tot} - \mathcal{H}_{Rot})U(t) \tag{3.11}$$

Where the rotation Hamiltonian ($\mathcal{H}_{Rot}$) is the P.A.S of the NV center set at the transmitter frequency (ω_T):

$$\mathcal{H}_{Rot} = \omega_T S_z^2 \tag{3.12}$$

And the matrix exponential of which is:

$$U(t) = e^{-i\mathcal{H}_{Rot}t} = \mathbb{1} - \left(1 - e^{-i\omega_T t}\right) S_z^2 \tag{3.13}$$

The rotation Hamiltonian and its matrix exponential are substituted into equation 3.11:

$$\begin{aligned}\mathcal{H}_{Eff} = &\left(\mathbb{1} - \left(1 - e^{i\omega_T t}\right) S_z^2\right) \\ &\big((\Delta - \omega_T)S_z^2 \\ &+ C_x(t)(xxS_x + xyS_y + xzS_z) \\ &+ C_y(t)(yxS_x + yyS_y + yzS_z) \\ &+ C_z(t)(zxS_x + zyS_y + zzS_z)\big) \\ &\left(\mathbb{1} - \left(1 - e^{-i\omega_T t}\right) S_z^2\right)\end{aligned} \tag{3.14}$$

Equation 3.14 is expanded. To simplify, recall the following spin-1 operator relationships:

$$\begin{aligned}S_z^{2n} = S_z^2 \text{ and } S_z^{2n+1} = S_z \\ S_z^2 S_{x/y} S_z^2 = 0\end{aligned} \tag{3.15}$$

Some trigonometric identities and Euler's formula may also be used to simplify:

$$\begin{aligned}(1 - e^{i\omega_T t})(1 - e^{-i\omega_T t}) = 2 - 2\cos(\omega_T t) \\ e^{i\pm\omega_T t} = \cos(\omega_T t) \pm i\sin(\omega_T t)\end{aligned} \tag{3.16}$$

Finally, using the commutators and anti-commutator relationships of the spin operators:

$$\begin{aligned}
\{S_{x/y/z}, S_z^2\} &= S_{x/y} \\
\{(xxS_x + xyS_y + xzS_z), S_z^2\} &= (xxS_x + xyS_y + xzS_z) \\
\{(yxS_x + yyS_y + yzS_z), S_z^2\} &= (yxS_x + yyS_y + yzS_z) \\
\{(zxS_x + zyS_y + zzS_z), S_z^2\} &= (zxS_x + zyS_y + zzS_z) \\
[(xxS_x + xyS_y + xzS_z), S_z^2] &= xx[S_x, S_z^2] + xy[S_y, S_z^2] \\
[(yxS_x + yyS_y + yzS_z), S_z^2] &= yx[S_x, S_z^2] + yy[S_y, S_z^2] \\
[(zxS_x + zyS_y + zzS_z), S_z^2] &= zx[S_x, S_z^2] + zy[S_y, S_z^2]
\end{aligned} \tag{3.17}$$

Further expanding and simplifying using the above relationships, the effective Hamiltonian for a general transmitter frequency (ω_T), microwave field direction (C_x, C_y, C_z) and NV orientation (xx,xy, etc.) is found:

$$\begin{aligned}
\mathcal{H}_{Eff} &= (\Delta - \omega_T)S_z^2 \\
&\quad + (xzC_x + yxC_y + zzC_z)Sz \\
&\quad + (xxC_x + yxC_y + zxC_z)\left(\cos(\omega_T t)Sx - i\sin(\omega_T t)[S_x, S_z^2]\right) \\
&\quad + (xyC_x + yyC_y + zyC_z)\left(\cos(\omega_T t)Sy - i\sin(\omega_T t)[S_y, S_z^2]\right)
\end{aligned} \tag{3.18}$$

The microwave controls (C_x, C_y, C_z) can now be expanded to give more context for the experiments conducted and abilities with each set of controls.

Consider the case where the microwave field is controlled by two independent channels. Two independent channels were chosen as the combination of these will yield circularly polarized microwaves, allowing single selective transitions between the $|0\rangle \rightarrow |+1\rangle$ or $|-1\rangle$ states.

These two channels may both emit in the (x,y,z) directions. An example may be two microstrips which each have components in multiple directions. Under the assumption of two independent channels emitting along the (x,y,z) directions, (C_x, C_y, C_z) may be expanded as:

$$\begin{aligned}
C_x &= C_1(t)w_{x1} + C_2(t)w_{x2} \\
C_y &= C_1(t)w_{y1} + C_2(t)w_{y2} \\
C_z &= C_1(t)w_{z1} + C_2(t)w_{z2}
\end{aligned} \tag{3.19}$$

The quantities $w_{x1/2}$ describes the x-component of the field for channels 1 and 2, respectively. This is similar for $w_{y1/2}$ and $w_{z1/2}$. These fields are defined by the configuration of the control field, but may be expressed in the general case above.

$C_{1/2}(t)$ represent the time dependent controls shaped by the arbitrary waveform generator (AWG), IQ mixer and set at the transmitter frequency. This will be further expanded upon in chapter four (section 4.3.1). In an ideal case, $C_{1/2}(t)$ are:

$$C_{1/2}(t) = I_{1/2}(t)\cos(\omega_T t) + Q_{1/2}(t)\sin(\omega_T t) \tag{3.20}$$

To further simply, the squares of the cosine and sine functions may be expanded:

$$\begin{aligned} \cos^2(\omega_T t) &= \frac{1}{2}(1+\cos(2\omega_T t)) \\ \cos(\omega_T t)\sin(\omega_T t) &= \frac{1}{2}\sin(2\omega_T t) \\ \sin^2(\omega_T t) &= \frac{1}{2}(1-\cos(2\omega_T t)) \end{aligned} \tag{3.21}$$

Expanding the controls for each channel, (C_x, C_y, C_z), into the Hamiltonian in equation 3.18, and using the trigonometric identities listed above yields the generalized effective Hamiltonian. In this instance, the values for I and Q are being analyzed at each discrete time step, so the time-dependency has been dropped.

$$\begin{aligned} \mathcal{H}_{eff} &= (\Delta - \omega_T)S_z^2 \\ &+ \left(\cos(\omega_T t)(I_1 w_{A1} + I_2 w_{A2}) + \sin(\omega_T t)(Q_1 w_{A1} + Q_2 w_{A2})\right) S_z \\ &+ \left(\frac{1}{2}(1+\cos(2\omega_T t))(I_1 w_{B1} + I_2 w_{B2}) + \frac{1}{2}\sin(2\omega_T t)(Q_1 w_{B1} + Q_2 w_{B2})\right) S_x \\ &- \left(\frac{i}{2}\sin(2\omega_T t)(I_1 w_{B1} + I_2 w_{B2}) + \frac{i}{2}(1-\cos(2\omega_T t))(Q_1 w_{B1} + Q_2 w_{B2})\right) [S_x, S_z^2] \\ &+ \left(\frac{1}{2}(1+\cos(2\omega_T t))(I_1 w_{C1} + I_2 w_{C2}) + \frac{1}{2}\sin(2\omega_T t)(Q_1 w_{C1} + Q_2 w_{C2})\right) S_y \\ &- \left(\frac{i}{2}\sin(2\omega_T t)(I_1 w_{C1} + I_2 w_{C2}) + \frac{i}{2}(1-\cos(2\omega_T t))(Q_1 w_{C1} + Q_2 w_{C2})\right) [S_y, S_z^2] \end{aligned} \tag{3.22}$$

$w_{A1/2}$, $w_{B1/2}$ and $w_{C1/2}$ represent the microwave field components and NV rotational terms, gathered to reduce the complexity of the Hamiltonian.

$$\begin{aligned} w_{A1/2} &= xzw_{x1/2} + yzw_{y1/2} + zzw_{z1/2} \\ w_{B1/2} &= xxw_{x1/2} + yxw_{y1/2} + zxw_{z1/2} \\ w_{C1/2} &= xyw_{x1/2} + yyw_{y1/2} + zyw_{z1/2} \end{aligned} \tag{3.23}$$

As the experiments are all performed in the absence of a magnetic field, the center transmitter frequency (ω_T), is set to the ZFS (Δ). All resulting terms then proportional to (2Δ) may be dropped. The terms proportional to S_z also become negligible, as they would induce a Zeeman splitting, proportional to the strength of the microwave controls, but oscillating at 2.87 GHz, and so would be averaged out compared to the other more slowly varying terms.

This yields the time-independent effective Hamiltonian for two independently controlled channels for a generalized field in the (x, y, z) directions. The Hamiltonian is presented with letter terms (A, B, C, D) for simplicity.

$$\begin{aligned} \mathcal{H}_{eff} &= AS_x + iB[S_x, S_z^2] + CS_y + iD[S_y, S_z^2] \\ A &= \frac{1}{2}(I_1 w_{B1} + I_2 w_{B2}) \\ B &= -\frac{1}{2}(Q_1 w_{B1} + Q_2 w_{B2}) \\ C &= \frac{1}{2}(I_1 w_{C1} + I_2 w_{C2}) \\ D &= -\frac{1}{2}(Q_1 w_{C1} + Q_2 w_{C2}) \end{aligned} \tag{3.24}$$

Finally, expanding the values for the microwave components (w_{B1}) etc. yields the full Hamiltonian.

$$\begin{aligned} \mathcal{H}_{eff} &= AS_x + iB[S_x, S_z^2] + CS_y + iD[S_y, S_z^2] \\ A &= \frac{1}{2}(xx(I_1 w_{x1} + I_2 w_{x2}) + yx(I_1 w_{y1} + I_2 w_{y2}) + zx(I_1 w_{z1} + I_2 w_{z2})) \\ B &= -\frac{1}{2}(xx(Q_1 w_{x1} + Q_2 w_{x2}) + yx(Q_1 w_{y1} + Q_2 w_{y2}) + zx(Q_1 w_{z1} + Q_2 w_{z2})) \\ C &= \frac{1}{2}(xy(I_1 w_{x1} + I_2 w_{x2}) + yy(I_1 w_{y1} + I_2 w_{y2}) + zy(I_1 w_{z1} + I_2 w_{z2})) \\ D &= -\frac{1}{2}(xy(Q_1 w_{x1} + Q_2 w_{x2}) + yy(Q_1 w_{y1} + Q_2 w_{y2}) + zy(Q_1 w_{z1} + Q_2 w_{z2})) \end{aligned} \tag{3.25}$$

Equation 3.24 shows the basic structure with the letter format. Each pre-factor (A, B, C, D) is dependent on the AWG envelope of control $(I_{1/2}, Q_{1/2})$, direction and strength of the microwave field at the site of the NVs, $(w_{x1/2}, w_{y1/2}, w_{z1/2})$ for each independent channel, and last by the NV rotation term, (xx,xy,xz etc.).

Although this Hamiltonian describes a single NV, from here it is clear to see the difficulty in controlling ensembles of NV centers as the projection of the effective Hamiltonian is scaled by the orientation of the NV center, and if the volume of NVs is large, the microwave field strength and direction of each also scales over the volume.

In the following section, the Hamiltonian will be manipulated, without loss of generality to show how to account for the projection of the Hamiltonian into each NV orientation in a more mathematically convenient way for achieving single transitions.

3.1.4 Expressing the Control Hamiltonian with Pseudo Spin-$\frac{1}{2}$ Operators

To ease the calculations in solving for selective ground state transitions in the Hamiltonian, the spin-1 operators may be written as a sum of pseudo spin-$\frac{1}{2}$ operators. These are of course not true spin-$\frac{1}{2}$ operators, as the ground state $|\pm 1\rangle$ states share a space with the same $|0\rangle$ state. Expressing the spin-1 operators in this form, allows for the selective transitions between $|0\rangle \rightarrow |+1\rangle$ / $|-1\rangle$ in the absence of a magnetic field, to be found more easily.

The pseudo spin-$\frac{1}{2}$ operators are labelled as $S_x^{\pm}$ and $S_y^{\pm}$ for the $|+1\rangle$ and $|-1\rangle$ pseudo sub-spaces, respectively. The operators are shown below:

$$\begin{aligned} S_x^+ &= \frac{1}{\sqrt{2}}(S_x + i[S_y, S_z^2]) \\ S_y^+ &= \frac{1}{\sqrt{2}}(S_y - i[S_x, S_z^2]) \\ S_x^- &= \frac{1}{\sqrt{2}}(S_x - i[S_y, S_z^2]) \\ S_y^- &= \frac{1}{\sqrt{2}}(S_y + i[S_x, S_z^2]) \end{aligned} \tag{3.26}$$

In matrix form, the resemblance to the Pauli operators can be seen, as is the intention.

$$\begin{aligned} S_x^+ &= \begin{pmatrix} 0 & 0 & 0 \\ 0 & 0 & 1 \\ 0 & 1 & 0 \end{pmatrix}; S_y^+ = \begin{pmatrix} 0 & 0 & 0 \\ 0 & 0 & -i \\ 0 & i & 0 \end{pmatrix}; \\ S_x^- &= \begin{pmatrix} 0 & 1 & 0 \\ 1 & 0 & 0 \\ 0 & 0 & 0 \end{pmatrix}; S_y^- = \begin{pmatrix} 0 & -i & 0 \\ i & 0 & 0 \\ 0 & 0 & 0 \end{pmatrix}; \end{aligned} \tag{3.27}$$

The Hamiltonian in equation 3.25 has already been grouped in accordance to the pseudo spin-$\frac{1}{2}$ operators, so substituting the pseudo spin-$\frac{1}{2}$ operators, and collecting to isolate for these are trivial. Re-arranging the pseudo spin-$\frac{1}{2}$ operators in the original spin-1 form, the following is substituted into the Hamiltonian:

$$\begin{aligned} S_x &= \frac{1}{\sqrt{2}}(S_x^+ + S_x^-) \\ S_y &= \frac{1}{\sqrt{2}}(S_y^+ + S_y^-) \\ i[S_x, S_z^2] &= \frac{1}{\sqrt{2}}(S_y^- - S_y^+) \\ i[S_y, S_z^2] &= \frac{1}{\sqrt{2}}(S_x^+ - S_x^-) \end{aligned} \tag{3.28}$$

Now re-arranging for the pseudo spin-$\frac{1}{2}$ operators, without loss of generality, the Hamiltonian is written with the pseudo spin-$\frac{1}{2}$ operators. New pre-factors $(\tilde{A}, \tilde{B}, \tilde{C}, \tilde{D})$ are used to distinguish between the pre-factors for the Hamiltonian written in equation 3.25:

$$\begin{aligned} \mathcal{H} &= \tilde{A}S_x^+ + \tilde{B}S_y^+ + \tilde{C}S_x^- + \tilde{D}S_y^- \\ \tilde{A} &= \frac{1}{2\sqrt{2}}(I_1 w_{B1} + I_2 w_{B2} - Q_1 w_{C1} - Q_2 w_{C2}) \\ \tilde{B} &= \frac{1}{2\sqrt{2}}(I_1 w_{C1} + I_2 w_{C2} + Q_1 w_{B1} + Q_2 w_{B2}) \\ \tilde{C} &= \frac{1}{2\sqrt{2}}(I_1 w_{B1} + I_2 w_{B2} + Q_1 w_{C1} + Q_2 w_{C2}) \\ \tilde{D} &= \frac{1}{2\sqrt{2}}(I_1 w_{C1} + I_2 w_{C2} - Q_1 w_{B1} - Q_2 w_{B2}) \end{aligned} \tag{3.29}$$

The full Hamiltonian written by expanding the terms $w_{B1/2}$ and $w_{C1/2}$, is shown below:

$$\begin{aligned}
\mathcal{H} =& \tilde{A}S_x^+ + \tilde{B}S_y^+ + \tilde{C}S_x^- + \tilde{D}S_y^- \\
\tilde{A} =& \frac{1}{2\sqrt{2}}(xx(I_1w_{x1} + I_2w_{x2}) + yx(I_1w_{y1} + I_2w_{y2}) + zx(I_1w_{z1} + I_2w_{z2}) \dots \\
& - xy(Q_1w_{x1} + Q_2w_{x2}) - yy(Q_1w_{y1} + Q_2w_{y2}) - zy(Q_1w_{z1} + Q_2w_{z2})) \\
\tilde{B} =& \frac{1}{2\sqrt{2}}(xy(I_1w_{x1} + I_2w_{x2}) + yy(I_1w_{y1} + I_2w_{y2}) + zy(I_1w_{z1} + I_2w_{z2}) \dots \\
& + xx(Q_1w_{x1} + Q_2w_{x2}) + yx(Q_1w_{y1} + Q_2w_{y2}) + zx(Q_1w_{z1} + Q_2w_{z2})) \\
\tilde{C} =& \frac{1}{2\sqrt{2}}(xx(I_1w_{x1} + I_2w_{x2}) + yx(I_1w_{y1} + I_2w_{y2}) + zx(I_1w_{z1} + I_2w_{z2}) \dots \\
& + xy(Q_1w_{x1} + Q_2w_{x2}) + yy(Q_1w_{y1} + Q_2w_{y2}) + zy(Q_1w_{z1} + Q_2w_{z2})) \\
\tilde{D} =& \frac{1}{2\sqrt{2}}(xy(I_1w_{x1} + I_2w_{x2}) + yy(I_1w_{y1} + I_2w_{y2}) + zy(I_1w_{z1} + I_2w_{z2}) \dots \\
& - xx(Q_1w_{x1} + Q_2w_{x2}) - yx(Q_1w_{y1} + Q_2w_{y2}) - zx(Q_1w_{z1} + Q_2w_{z2}))
\end{aligned} \tag{3.30}$$

To isolate the transitions between the $|0\rangle \rightarrow |-1\rangle$ or $|+1\rangle$, trivial solutions may be found to yield the pre-factors equal to zero for each of the pseudo sub spaces. To isolate the positive transition, $(\tilde{C}, \tilde{D})$ substitutions for the four control parameters are made to equate these pre-factors to zero, and likewise for the negative transitions.

In addition to finding the conditions for single transitions in single NVs, expressing the Hamiltonian grouped by the pseudo spin-$\frac{1}{2}$ operators allows for OCT solutions for collective and selective NV control in an ensemble of NVs to be found more easily. To find the OCT solutions, the design of the microwave control field must be substituted in. The following section will outline an example of a configuration for the microwave control field.

3.1.5 Experimental Configuration - Expressing the Control Hamiltonian with Two Independently Controlled Microstrips

To find OCT solutions for single and ensembles of NV centers, it is now necessary to sub in the values for the microwave control field to reflect the experimental setup.

The source of the control field is emitted from two independently controlled infinite strip lines with fields only along the (x) and (z) plane. This would result in $(w_{y1} = w_{y2} = 0)$, resulting in the Hamiltonian being reduced to:

$$\begin{aligned}
\mathcal{H} =& \tilde{A}S_x^+ + \tilde{B}S_y^+ + \tilde{C}S_x^- + \tilde{D}S_y^- \\
\tilde{A} =& \frac{1}{2\sqrt{2}}(xx(I_1 w_{x1} + I_2 w_{x2}) + zx(I_1 w_{z1} + I_2 w_{z2}) \dots \\
& - xy(Q_1 w_{x1} + Q_2 w_{x2}) - zy(Q_1 w_{z1} + Q_2 w_{z2})) \\
\tilde{B} =& \frac{1}{2\sqrt{2}}(xy(I_1 w_{x1} + I_2 w_{x2}) + zy(I_1 w_{z1} + I_2 w_{z2}) \dots \\
& + xx(Q_1 w_{x1} + Q_2 w_{x2}) + zx(Q_1 w_{z1} + Q_2 w_{z2})) \\
\tilde{C} =& \frac{1}{2\sqrt{2}}(xx(I_1 w_{x1} + I_2 w_{x2}) + zx(I_1 w_{z1} + I_2 w_{z2}) \dots \\
& + xy(Q_1 w_{x1} + Q_2 w_{x2}) + zy(Q_1 w_{z1} + Q_2 w_{z2})) \\
\tilde{D} =& \frac{1}{2\sqrt{2}}(xy(I_1 w_{x1} + I_2 w_{x2}) + zy(I_1 w_{z1} + I_2 w_{z2}) \dots \\
& - xx(Q_1 w_{x1} + Q_2 w_{x2}) - zx(Q_1 w_{z1} + Q_2 w_{z2}))
\end{aligned} \tag{3.31}$$

The quantities $w_{x1/2}$ and $w_{z1/2}$ are the x and z components of the field emitted from the first and second microstrips at the site of the NV center. As both the magnitude and direction of the field is important, these components will be expressed in polar coordinates. The microstrips are placed 150 μm apart in x. If a 500 μm diamond were placed on top of the microstrips, and a typical oil immersion lens used with a working distance of 160 μm, it is reasonable to expect the NV would likely be positioned approximately 400 μm away from the microstrips in the "z" direction. For this simulation, the x position of the NV has been chosen at a random position between the two microstrips, 108 μm. Using the Cartesian coordinates of the position of the NV in "x" and "z", the radial distance from each stripline $(r_{1/2})$ and angle from each stripline $(\phi_{1/2})$ is found, the summary shown in figure 3.8:

x [μm]	z [μm]	r_1[μm]	r_2[μm]	ϕ_1[°]	ϕ_2[°]
108.	400.	414.324	402.199	74.8904	95.9941

Figure 3.8: Example field components for an NV found in a thick diamond placed on top of two infinite microstrips emitting a field along the x and z plane.

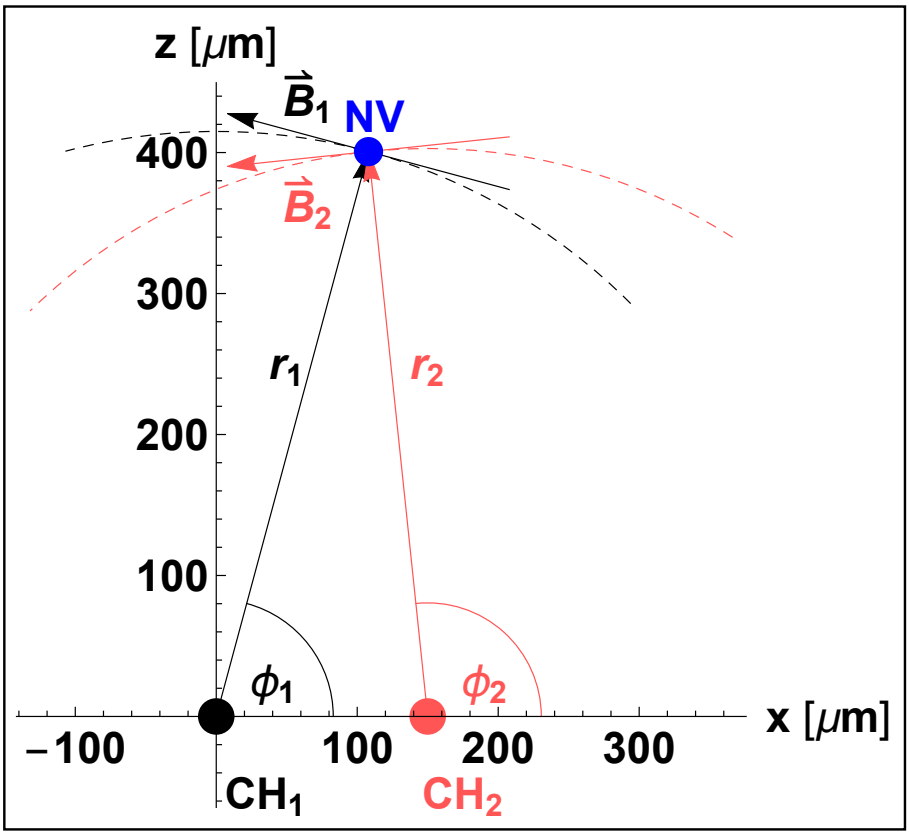

Figure 3.9: Field distribution from the microstrips. The NV **(blue)** was placed at a random distance between the microstrips, marked wire 1 **(black)** and 2 **(red)**, in "x", and at a distance away from the microstrips in "z" that would reflect having a low depth of field objective with a thick diamond. The radial distance from each wire $r_{1/2}$ is noted with the solid **(black, red)** lines, respectively. The field is marked with a dashed line, with the field direction at the site of the NV noted as $\vec{B}_{1/2}$.

Figure 3.9 shows this example of a field scenario. The NV is shown **(blue)**, with each of the microstrips shown **(black, red)**. The radial distance from each stripline to the NV is marked with a solid line. The dashed line indicates the field direction, and the fields $\vec{B}_{1/2}$ are marked at the site of the NV.

Using this field configuration, a couple definitions for the coordinates can be made:

- x-distance from stripline 1 to NV: $x_1 = x$
- x-distance from stripline 2 to NV: $x_2 = x_1 - l = x - l$ where l is the distance between the microstrips
- z-distance from stripline 1 and 2 to NV: $z_1 = z_2 = z$

The figure above properly illustrates the direction of the field, which is tangential to the angle (ϕ) from each stripline to the NV center. To capture the direction of the field and the distance from each stripline to the NV center, the field will be expressed in polar coordinates.

$$\begin{aligned} r_1 &= \sqrt{x^2 + z^2} \\ r_2 &= \sqrt{(x-l)^2 + z^2} \\ \phi_1 &= \tan^{-1}\left(\frac{z}{x}\right) \\ \phi_2 &= \tan^{-1}\left(\frac{z}{x-l}\right) \end{aligned} \tag{3.32}$$

The normalized vectors of the field $\gamma_{1/2}$ may be expressed as:

$$\gamma_{1/2}(\phi_{1/2}) = \{\cos(\phi_{1/2}), 0, \sin(\phi_{1/2})\} \tag{3.33}$$

The tangential field is the derivative of the field listed above:

$$\dot{\gamma}_{1/2}(\phi_{1/2}) = \{-\sin(\phi_{1/2}), 0, \cos(\phi_{1/2})\} \tag{3.34}$$

Assuming that the two microstrips are infinite compared to the NV center, the magnitude of the field may be expressed with Biot-Savart $||B|| = \frac{\mu_o I}{2\pi r}$, [23]. Substituting the magnitude and direction, the equation for the field is shown below. I is the current running through each stripline, and r is the distance from the stripline to the NV.

$$\vec{B}_{1/2} = \frac{\mu_o I}{2\pi r_{1/2}}\{-\sin(\phi_{1/2}), 0, \cos(\phi_{1/2})\} \tag{3.35}$$

Substituting the field into the generic controls $w_{x1/2}$ and $w_{z1/2}$ in the Hamiltonian expressed in equation 3.31, the expanded controls are shown. The current value, I has been substituted for $I_{1/2}$ and $Q_{1/2}$:

$$\begin{aligned}
I_1 w_{x1} + I_2 w_{x2} &= \frac{\mu_o}{2\pi}\left(-\frac{I_1}{r_1}\sin(\phi_1) - \frac{I_2}{r_2}\sin(\phi_2)\right) \\
Q_1 w_{x1} + Q_2 w_{x2} &= \frac{\mu_o}{2\pi}\left(-\frac{Q_1}{r_1}\sin(\phi_1) - \frac{Q_2}{r_2}\sin(\phi_2)\right) \\
I_1 w_{z1} + I_2 w_{z2} &= \frac{\mu_o}{2\pi}\left(\frac{I_1}{r_1}\cos(\phi_1) + \frac{I_2}{r_2}\cos(\phi_2)\right) \\
Q_1 w_{z1} + Q_2 w_{z2} &= \frac{\mu_o}{2\pi}\left(\frac{Q_1}{r_1}\cos(\phi_1) + \frac{Q_2}{r_2}\cos(\phi_2)\right)
\end{aligned} \tag{3.36}$$

This is just an example of a field design and how it connects to the Hamiltonian's controls. Another example could be a field emitted through a set of coils, along the "x" and "y" axes, or a three-dimensional field sourcing a field along the "x", "y" and "z" directions. The three-dimensional field would be optimal for solving any general solution for single NVs and NV ensembles, but a simple field that works well in two dimensions was investigated here to show the basic concepts and control available.

The control Hamiltonian has now been described for any single NV center in a single crystal diamond, with a microwave field generated by two independently controlled microstrips. To conclude this section, the Hamiltonian will be described for an ensemble of NV centers in a single crystal diamond.

3.1.6 The Effective Control Hamiltonian for an Ensemble of NVs

Thus far, the Hamiltonian has been described for any single NV. The Hamiltonian described in equation 3.25 describes a general solution for the effective Hamiltonian in the frame of the NV, with the quantization axis aligned along the NV P.A.S This Hamiltonian may be expanded to describe an ensemble of NVs under the condition that the NVs are independent, having no interaction between them, [115].

The ensemble Hamiltonian must be expanded to include the Hilbert space of each of the four NVs with tensor products. $\mathcal{H}_{NV_i}$ refers to the Hamiltonian for each NV orientation. $\mathbb{1}_3$ is the spin-1 identity operator.

$$\begin{aligned}\mathcal{H}_{Ensemble} =& \mathcal{H}_{NV_1} \otimes \mathbb{1}_3 \otimes \mathbb{1}_3 \otimes \mathbb{1}_3 \\ &+ \mathbb{1}_3 \otimes \mathcal{H}_{NV_2} \otimes \mathbb{1}_3 \otimes \mathbb{1}_3 \\ &+ \mathbb{1}_3 \otimes \mathbb{1}_3 \otimes \mathcal{H}_{NV_3} \otimes \mathbb{1}_3 \\ &+ \mathbb{1}_3 \otimes \mathbb{1}_3 \otimes \mathbb{1}_3 \otimes \mathcal{H}_{NV_4}\end{aligned} \tag{3.37}$$

The ensemble Hamiltonian above includes the case where there is no interaction between the NV centers, but still takes the full Hilbert space into account. In the case where the NVs do have some coupling present, they can no longer be treated independently and thus cannot be expressed in their individual quantization axis, but in the common lab frame. In this case, the ensemble Hamiltonian would include each of the four NV orientations expressed in the lab frame with the addition of the coupling terms between each NV orientation, as has been shown for some particular examples in [19, 80, 115, 129].

The control Hamiltonian described in this section accounts for the orientation of the NV center, the location of the NV center relative to the microwave source, the configuration of the microwave source as two infinite microstrips and is expressed in both a spin-1 and pseudo spin-$\frac{1}{2}$ operators. Using this control Hamiltonian, the next section will show the OCT controls for NV ensembles, under the condition where there is no interaction between the NVs.

3.2 Optimal Control Theory Pulses for Collective Control

3.2.1 Implementing Pulses with the GRAPE Algorithm

In this section, simulations for optimal control theory (OCT) pulses for NV ensembles are shown for a few key examples in the (100), (110) and (111) diamonds. The principles of these simulations will be applied in chapter five, demonstrating OCT control in the (100) diamond. OCT is a tool which optimizes the shape of a control pulses to achieve a target output restrained by a set of control parameters. OCT may utilize a variety of algorithms to optimize for the desired pulse shape, both gradient and non-gradient based. In this thesis, the gradient ascent pulse engineering (GRAPE) algorithm is used to find the desired sequences for the OCT pulses for NV ensembles, as a tool given in the *Quantum Utils* program in Mathematica, [114].

To create a pulse, an initial guess is made for the shape to achieve the desired target. After each proceeding time step, the output state is evaluated, which then serves as the updated input guess for the next time step. The control parameters are then adjusted, and the process repeats, the accuracy improving with each step. The range of amplitude for the control parameters, target unitary or state transfer, target fidelity, internal Hamiltonian, control Hamiltonian and parameter distributions are all inputs. The total length of the pulse is given by the number of time steps multiplied by the resolution of the length of each time step. This algorithm is described in great detail in the following works, but in this case was only used as an existing tool for finding the desired output pulses, [43, 52, 89].

The "FindPulse" function from the *QuantumUtils* package in Mathematica accepts the following inputs, [114]. This function is used to generate the pulses used in the following simulations and the experiments shown in chapter five (section 5.8.2).

- Number of time steps
- Resolution of the time steps
- Initial Guess for the pulse
- Description of the Internal and Control Hamiltonian
- Control Parameters and their Ranges

- Desired Target State-to-State Transfer or Unitary Operator
- Desired Target State Overlap or Unitary Fidelity

For the simulations shown in this chapter, the time step resolution was 2 ns with 500 time steps, for a total pulse time of 1 μs to accommodate a typical T_2^* value for a CVD grown diamond (1 μs), [99, 100]. The initial guess for the pulse is made by the "RandomSmoothPulse" function in the *QuantumUtils* package, [114].

The internal Hamiltonian used in the control pulses includes only the zero field splitting of the NV center. This internal Hamiltonian may be expanded to include the hyperfine interaction with the nitrogen nuclear spin, and other ground state features of the NV Hamiltonian in future optimizations.

There are four iterations of the control Hamiltonian being used, given by the four Hamiltonians that describe each NV orientation for a chosen diamond crystal. These control Hamiltonians also depend on the geometric location away from the microwave source as outlined in the previous section, shown in equation 3.31. The control Hamiltonian was written in the pseudo spin-$\frac{1}{2}$ operator form, as it makes it easier for the algorithm to find the correct target. Writing the control Hamiltonian in this manner also allows trivial solutions to be found for individual NVs for selective control of the $|0\rangle \rightarrow |-1\rangle$ or $|+1\rangle$ states.

There are four control parameters used, I_1, I_2, Q_1 and Q_2, which reflect the four control channels available in the AWG. An example of how the control parameters vary over the length of the pulse is shown in figure 3.10. Each of these four control parameters may be restricted to the desired range and in whatever unit is desired for that particular pulse, typically given in frequency, power, current, voltage or an arbitrary amplitude which may then be scaled by a global envelope. The control parameters shown in the figure, vary in amplitude of the Rabi frequency, with a maximum allowed amplitude of 50 MHz. Using a Rabi frequency at the site of the NV ensemble as the amplitude control is a convenient tool that allows pulses to be designed independent of the microwave source geometries. For the purposes of the simulations conducted here, a sample location for the NV was chosen so the angle and relative distance from each stripline was chosen to scale the frequency of the controls at the site of the NV. To design a pulse for the experimental setup, the geometry of the NV ensemble located away from the microwave source must be taken into account, so the control parameters will vary with a unitless amplitude, then scaled by experimental values. This will be elaborated upon in chapter five (section 5.8.2).

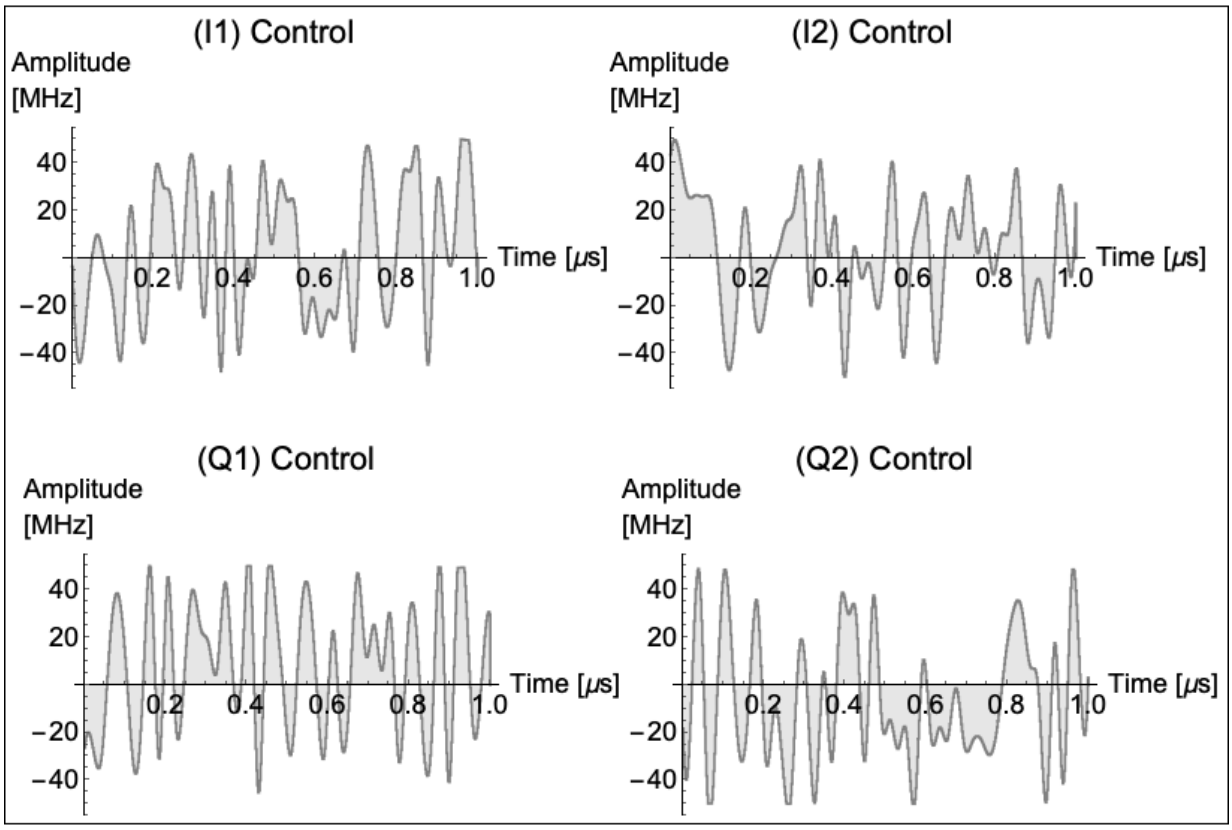

Figure 3.10: OCT Sample Controls. A sample plot for the four control parameters I_1 etc, with maximum allowed amplitude 50 MHz, 2 ns resolution and total pulse length 1 μs. The 2 ns resolution was chosen in line with the switching time capable of the AWG. This pulse is an example of what would be the instructions sent to the AWG to be implemented in an experiment. It is noted that this is just a sample of the controls and independent of the microwave source geometry.

For all of the following simulations, the desired target was given by a state-to-state transfer, given by an initial and desired density matrix. An example is shown below for a selective transition between the $|0\rangle$ and $|+1\rangle$ state, labelled as a π_+ pulse.

$$|0\rangle\langle 0| \rightarrow |+1\rangle\langle +1| \tag{3.38}$$

The success metric of the pulse is given by the state overlap between the target and realized output density matrix. In the case where the target is given by a unitary, this metric would be determined by the fidelity of the output unitary.

The targets are arranged so each control Hamiltonian referencing a specific NV orientation is given a specific target output. As the control Hamiltonians being used assume the NVs are independent, they may be treated as separate non-interacting Hamiltonians and the pulses may be optimized for each of their individually set targets. The targets may be set so the NV orientations are instructed to find the same output target density matrix, or individual matrices for each.

The following sections will exhibit a few sample state-to-state transfers for the same desired target for all NV orientations within the (100), (110), or (111) diamond. This will then be proceeded by demonstrating individual target state-to-state transfers for each NV orientation. All of these simulations were completed with a microwave field aligned along the "x" and "z" axis to understand the response of each diamond crystal under these field restrictions. Of course in an ideal experimental world, a microwave field along the "x","y" and "z" direction may be designed so universal control for each crystal may be achieved, but this analysis was done in a sense that is viable with a more simple experimental setup, more easily scalable for a portable device. In this instance, understanding the response to the direction of the field may be better understood than in an ideal case.

3.2.2 Collective π Pulse for Sub-Ensembles in the (100) Diamond

The first example of OCT pulse will be a selective transition between the $|0\rangle\langle 0| \rightarrow |+1\rangle\langle +1|$ state in the (100) diamond in the absence of a magnetic field. The starting state is the $|0\rangle\langle 0|$ state for all orientations, achieved through the initialization process. The control field is simulated as originated from two microstrips, generating a microwave field in the "x" and "z" lab frame, the same geometry as shown in figure 3.9.

Under a control field in the "x" and "z" lab frame, the (xx,xy,zx,zy) components of the rotation matrix for each NV orientation are used. These are listed in table 3.1 below for each NV orientation in the (100) Diamond. Recall that in chapter two, figure 2.3 illustrated NV orientations for the (100) diamond. Each NV is oriented at equal angles away from the "x" and "z" axes with opposite signs. The symmetry between these values result in the uniform behaviour between the (1,1,1) and (-1,1,-1) pair and (-1,-1,1) and (1,-1,-1) pair, resulting in the orientations acting as two pairs of orientations rather than four unique NVs. Recall that from the figure dictating the NV centers in the lab frame, the (1,1,1) and (-1,1,-1) NVs were rotated positively away from the "z" axis while the (1,-1,-1) and (-1,-1,1) were oriented negatively about the "z" axis. This shows there is selection about the "z" axis, but not about the "x" and "y" axis with this configuration of magnetic control field.

Table 3.1: Rotation matrix components in the control Hamiltonian for the (100) diamond with field aligned along the "x" and "z" axes.

NV	xx	xy	zx	zy
(1,1,1)	$\frac{1}{6}(3+\sqrt{3})$	$\frac{1}{6}(3-\sqrt{3})$	$-\frac{1}{\sqrt{3}}$	$\frac{1}{\sqrt{3}}$
(-1,-1,1)	$\frac{1}{6}(3-\sqrt{3})$	$\frac{1}{6}(-3-\sqrt{3})$	$-\frac{1}{\sqrt{3}}$	$-\frac{1}{\sqrt{3}}$
(-1,1,-1)	$\frac{1}{6}(3-\sqrt{3})$	$\frac{1}{6}(-3-\sqrt{3})$	$\frac{1}{\sqrt{3}}$	$\frac{1}{\sqrt{3}}$
(1,-1,-1)	$\frac{1}{6}(3+\sqrt{3})$	$\frac{1}{6}(3-\sqrt{3})$	$\frac{1}{\sqrt{3}}$	$-\frac{1}{\sqrt{3}}$

This symmetry will be important when designing pulses for the (100) diamond. Treating the (100) diamond as having two pairs rather than four orientations allows for target state-to-state transfers to be achieved with only designing pulses for two orientations rather than four.

Evaluating the evolution of the designed pulse using the eigenstates of the NV center

Here the trajectory of the state will be shown using two methods. The first is observing the state overlap with the $|0\rangle, |+1\rangle$ and $|-1\rangle$ states through the evolution of the pulse. This is followed by the introduction of using two adapted Bloch spheres, used to describe the evolution of the states for each the $|+1\rangle$ and $|-1\rangle$ evolution. As the NV is a spin-1, one Bloch sphere may not give the full state description, but two modified Bloch spheres can.

The first method to discern the success of the pulse is to observe the overlap of the target state with the eigenvalues of the NV center through their evolution in time. Figure 3.11 shows the time evolution of the eigenstates for each NV orientation under the designed pulse for a state-to-state transfer of $|0\rangle\langle 0| \rightarrow |+1\rangle\langle +1|$. The left most column depicts the evolution of the $|0\rangle\langle 0|$ state, the middle, the $|+1\rangle\langle +1|$ and the right column, the $|-1\rangle\langle -1|$. The rows show the evolution of each of these three states for all four NV centers, from top to bottom, the (1,1,1),(-1,-1,1),(-1,1,-1) and (1,-1,-1).

To produce the figure below, the trace of the density state generated by the pulse is evaluated at each time step (ρ_t) for the observables associated with each eigenstate of the NV center:

$$\begin{aligned} \langle 0\rangle &= Tr[|0\rangle\langle 0| . \rho_t] \\ \langle +1\rangle &= Tr[|+1\rangle\langle +1| . \rho_t] \\ \langle -1\rangle &= Tr[|-1\rangle\langle -1| . \rho_t] \end{aligned} \tag{3.39}$$

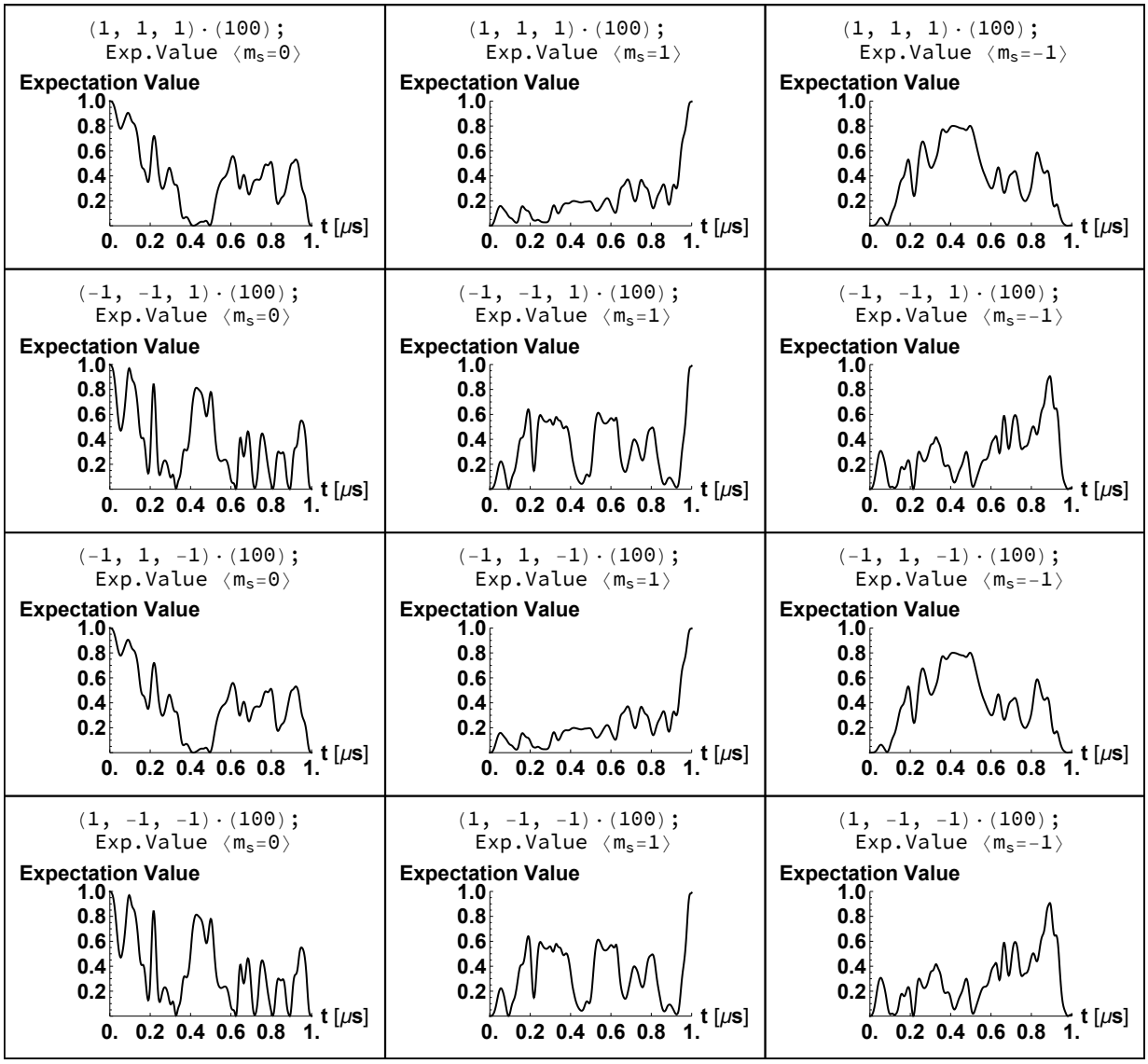

Figure 3.11: Evolution of the Spin-1 Observables in time for all NV orientations - target state-to-state transfer $|0\rangle\langle 0| \rightarrow |+1\rangle\langle +1|$. The evolution of the spin-1 observables for each NV orientation in the (100) diamond. Recall that under an "x" and "z" microwave field, the NV orientations in this diamond are split into two pairs, which is reflected in their responses, where the same evolution is observed for the (1,1,1) and (-1,1,-1) pair and the (-1,-1,1) and (1,-1,-1) pair. Under the evolution of the designed pulse, the evolution does not appear to follow any regular pattern, but the desired population is reached.

As the pulse progresses, the evolution of all four NVs proceeds from the starting state of $|0\rangle\langle 0|$ with a value of 1, and finishes with the $|+1\rangle\langle +1|$ state fully populated for each NV with a value of 0.99, while the $|-1\rangle\langle -1|$ state remains unpopulated, as was the design of the pulse. What should also be observed is the symmetry between the (1,1,1) and (-1,1,-1) NV pair, and the (-1,-1,1) and (1,-1,-1) pair. Both pairs follow identical trajectories with this pulse. This relationship confirms the symmetry relationship with the (100) diamond using a magnetic field configuration aligned along the "x" and "z" axis. This symmetry under these field conditions can be used as a convenient tool to design pulses meant for two orientations and have them enact on four orientations.

The final population of the NVs are shown in table 3.2. This is a convenient metric to use to judge the success of the target state overlap. In this case, the target state overlap was 0.99 into the $|+1\rangle\langle +1|$ state, beginning from the $|0\rangle\langle 0|$ state. It is clear that the target has been met looking at the populations of the states below.

Table 3.2: Final state for $|0\rangle\langle 0| \rightarrow |+1\rangle\langle +1|$ pulse for all NVs in (100) diamond. Evaluating the final state shows the pulsing sequence was successful, rotating each NV to the $|+1\rangle\langle +1|$ state, from the starting state of $|0\rangle\langle 0|$.

Final Expectation Values

	(1, 1, 1)	(-1, -1, 1)	(-1, 1, -1)	(1, -1, -1)
⟨0⟩	0.00048	0.00051	0.00048	0.00051
⟨+1⟩	0.99526	0.99767	0.99526	0.99767
⟨-1⟩	0.00426	0.00181	0.00426	0.00181

Plotting the Trajectory of the State on two Bloch Spheres

While evaluating the state overlap of the final state shows the success of the OCT pulse, it does not provide a good visual for observing the trajectory of the state. A more convenient tool for visualizing the trajectory of the state may be viewed on a Bloch sphere. As the NV is a spin-1 particle, a simple Bloch sphere can not be used to represent the full state description. However, two Bloch spheres may be used to describe the $|0\rangle\langle 0| \rightarrow |+1\rangle\langle +1|$ and $|0\rangle\langle 0| \rightarrow |-1\rangle\langle -1|$ domains.

Evaluating the trajectory of the state on the positive and negative Bloch sphere makes use of the positive and negative operators used to describe the Hamiltonian. Recall the spin-1 operators, (S_x, S_y, S_z) may be written in the form of (S_x^+, S_y^+) and (S_x^-, S_y^-) operators to distinguish the actions of the positive and negative transitions in the ground state. Their matrix form shown is in equation 3.27.

To plot the trajectory onto two Bloch spheres, the trace of the positive and negative operators on the full state (ρ_t) is evaluated at each time step as shown in the equation below:

$$\begin{aligned} \left\langle X^{+/-} \right\rangle &= Tr[S_x^{+/-}.\rho_t] \\ \left\langle Y^{+/-} \right\rangle &= Tr[S_y^{+/-}.\rho_t] \\ \left\langle Z^{+/-} \right\rangle &= Tr[S_z^{+/-}.\rho_t] \end{aligned} \tag{3.40}$$

The positive and negative pseudo spin-$\frac{1}{2}$ operator for S_z has also been introduced here, analogous to the $S_x^{+/-}$ and $S_y^{+/-}$ operators.

$$\begin{aligned} S_z^+ &= \frac{1}{2}S_z + \mathbb{1}_3 - \frac{3}{2}S_z^2 \\ &= \begin{pmatrix} 0 & 0 & 0 \\ 0 & 1 & 0 \\ 0 & 0 & -1 \end{pmatrix}; \\ S_z^- &= \frac{1}{2}S_z - \mathbb{1}_3 + \frac{3}{2}S_z^2 \\ &= \begin{pmatrix} 1 & 0 & 0 \\ 0 & -1 & 0 \\ 0 & 0 & 0 \end{pmatrix}; \end{aligned} \tag{3.41}$$

At each time step, the $\{X^{+/-}, Y^{+/-}, Z^{+/-}\}$ components of the state are gathered, and expressed as a vector in each of the positive and negative Bloch spheres to show the trajectory, the same as it would be plotted on a traditional Bloch sphere for a spin-$\frac{1}{2}$ particle. Visualizing the Bloch sphere as two representing the positive and negative domains is just a convenient tool for visualizing the state trajectory and showing the selectivity between the positive and negative ground states of the NV.

Figure 3.12 shows the positive (left column) and negative (right column) Bloch spheres. For each column, the state trajectory for each NV orientation is shown in the rows, from top to bottom (1,1,1),(-1,-1,1),(-1,1,-1) and (1,-1,-1). The starting state $|0\rangle\langle 0|$ is marked by a red sphere, and the final state $|+1\rangle\langle +1|$ marked by a black sphere. The blue line plots the trajectory of the state under the OCT pulse. The "z"-axes of each Bloch sphere mark the $|0\rangle$ and $|+1\rangle$ or $|-1\rangle$ states, respectively. It is noted that the $|0\rangle$ state is along the positive "z" axis in the positive domain and the negative "z" axis in the negative domain, consistent with the sign of the $|0\rangle$ state in the $S_z^{+/-}$ operator. The xy axes emulate the states analogous to a spin-$\frac{1}{2}$ Bloch sphere, for each of the positive and negative domains. The specifics of the xy axes will be elaborated upon when discussing $\frac{\pi}{2}$ like pulses.

Though the trajectory is not trivial, the Bloch sphere describing the positive domain shows the successful transition of the starting $|0\rangle\langle 0|$ state to the final $|+1\rangle\langle +1|$ state. It is interesting to compare this to the evolution of the state in the negative sphere. The beginning $|0\rangle\langle 0|$ state is again marked by a red sphere, but the final state is at the origin. This would indicate that there are no components of the final state left in the negative domain, showing a complete state transfer to the $|+1\rangle\langle +1|$ state.

As with observing the trace of the $|0\rangle\langle 0|, |+1\rangle\langle +1|, |-1\rangle\langle -1|$ states of the NV center shown in the figure 3.11, the Bloch sphere shows that there is not exclusively evolution in each of the positive or the negative domains. As the NV ground state is a spin-1 particle, exclusive evolution in the positive or negative spheres would not be expected.

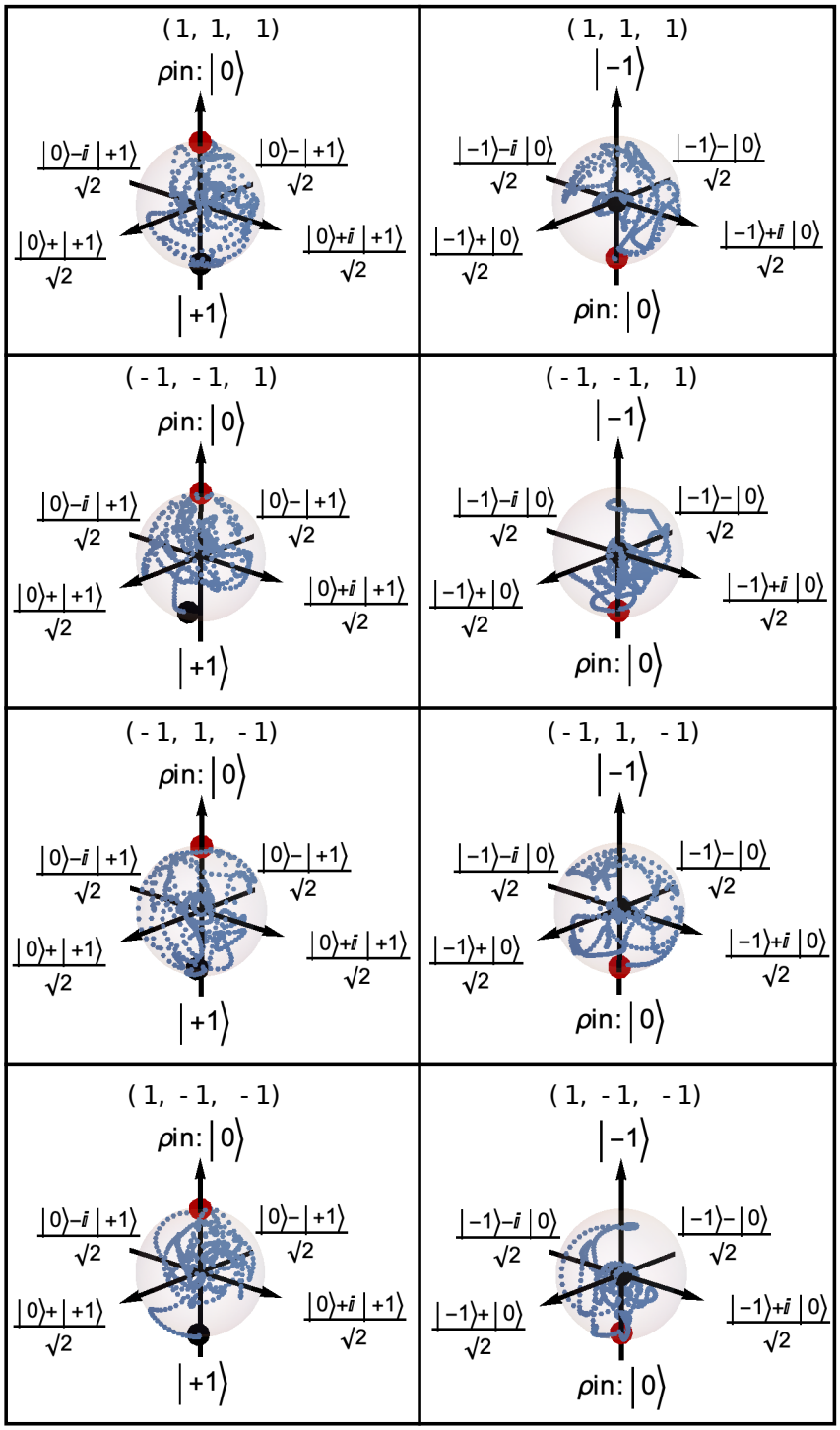
(1, 1, 1)
ρin: |0⟩
|0⟩−i |+1⟩ / √2
|0⟩− |+1⟩ / √2
|0⟩+ |+1⟩ / √2
|0⟩+i |+1⟩ / √2
|+1⟩
(1, 1, 1)
|−1⟩
|−1⟩−i |0⟩ / √2
|−1⟩− |0⟩ / √2
|−1⟩+ |0⟩ / √2
|−1⟩+i |0⟩ / √2
ρin: |0⟩
(- 1, - 1, 1)
ρin: |0⟩
|0⟩−i |+1⟩ / √2
|0⟩− |+1⟩ / √2
|0⟩+ |+1⟩ / √2
|0⟩+i |+1⟩ / √2
|+1⟩
(- 1, - 1, 1)
|−1⟩
|−1⟩−i |0⟩ / √2
|−1⟩− |0⟩ / √2
|−1⟩+ |0⟩ / √2
|−1⟩+i |0⟩ / √2
ρin: |0⟩
(- 1, 1, - 1)
ρin: |0⟩
|0⟩−i |+1⟩ / √2
|0⟩− |+1⟩ / √2
|0⟩+ |+1⟩ / √2
|0⟩+i |+1⟩ / √2
|+1⟩
(- 1, 1, - 1)
|−1⟩
|−1⟩−i |0⟩ / √2
|−1⟩− |0⟩ / √2
|−1⟩+ |0⟩ / √2
|−1⟩+i |0⟩ / √2
ρin: |0⟩
(1, - 1, - 1)
ρin: |0⟩
|0⟩−i |+1⟩ / √2
|0⟩− |+1⟩ / √2
|0⟩+ |+1⟩ / √2
|0⟩+i |+1⟩ / √2
|+1⟩
(1, - 1, - 1)
|−1⟩
|−1⟩−i |0⟩ / √2
|−1⟩− |0⟩ / √2
|−1⟩+ |0⟩ / √2
|−1⟩+i |0⟩ / √2
ρin: |0⟩

Figure 3.12: OCT Pulse - π_+ pulse, $|0\rangle\langle 0| \rightarrow |+1\rangle\langle +1|$ for all NVs in the (100) diamond. The microwave source used to simulate this pulse was from two wires emitting a field in the "x" and "z" lab frame, the geometry shown in figure 3.9. This pulse shows the state transfer from the $|0\rangle\langle 0| \rightarrow |+1\rangle\langle +1|$ state for all NVs in the (100) diamond. Both images show the starting state **(red)** and final state **(black)**, with the trajectory of the state **(blue)** plotted as a function of each increment of the pulse. Recalling that the NV is an effective spin-1 particle, a Bloch sphere cannot be used to describe the full state description, so two Bloch spheres, showing the $|0\rangle\langle 0| \rightarrow |+1\rangle\langle +1|$ and $|0\rangle\langle 0| \rightarrow |-1\rangle\langle -1|$ domains can be used in its place. The positive domain is quite clear in indicating the final desired state of $|+1\rangle\langle +1|$ was reached for all NV orientations. Another interesting point to see is that in the negative domain, the starting state is the same as the positive $|0\rangle\langle 0|$, but the final state is at the origin, indicating that there is no remaining piece of the state in the negative domain. Observing the evolution in this manner also shows the evolution occurs in both domains, as expected as the NV is a spin-1 particle and does not have exclusive subspaces.

This section demonstrated a selective pulse from the $|0\rangle\langle 0| \rightarrow |+1\rangle\langle +1|$ for all NV orientations in the (100) diamond. The trajectory of the state was shown, evaluated for both the expectation value of the $|0\rangle, |+1\rangle, |-1\rangle$ states and the positive and negative domains of an adapted Bloch sphere. Thus far, all the state-to-state descriptions have detailed a density matrix form of $|initial\rangle\langle initial| \rightarrow |final\rangle\langle final|$. From this point on, the state-to-state transfer will be only described using the notation of $|initial\rangle \rightarrow |final\rangle$ for simplicity, but it is noted, the pulses themselves have all been designed as a transfer of an initial and final density matrix.

The following section will show the capabilities of a (100) diamond when designing a $\frac{\pi}{2}$ like pulse for all NV orientations.

3.2.3 Collective $\frac{\pi}{2}$ Pulse for All Orientations in the (100) Diamond

A second example of a state-to-state transfer is now considered. Recall that the symmetry of the (100) diamond makes only two distinguishable pairs of NVs with a field along the "x" and "z" axes. In this section, a $\frac{\pi}{2}$ like pulse will be implemented in a (100) diamond optimizing on the pairs of NVs. In this example, the state-to-state transfer of $|0\rangle \rightarrow \frac{|0\rangle+|+1\rangle}{\sqrt{2}}$ will be designed for the (1,1,1) and (-1,-1,1) NV orientations. Table 3.3 shows the final populations for the output states given this design. The final output states do show that the populations for all the NV orientations do reach the desired output, with an even divide between the $|0\rangle$ and $|+1\rangle$ states.

Table 3.3: Final state for a $|0\rangle \rightarrow \frac{|0\rangle+|+1\rangle}{\sqrt{2}}$ state transfer in the (100) diamond. Due to the symmetry of the diamond, the controls were only given to the (1,1,1) and (-1,-1,1) NVs, while the other two evolved freely under the pulse. The populations indicate that for all NVs, the desired population levels were reached, having the populations equally divided between the $|0\rangle$ and $|+1\rangle$ states.

Final Expectation Values

	(1, 1, 1)	(-1, -1, 1)	(-1, 1, -1)	(1, -1, -1)
⟨0⟩	0.4889	0.5054	0.4889	0.5054
⟨+1⟩	0.51109	0.4939	0.51109	0.4939
⟨-1⟩	0.00001	0.0007	0.00001	0.0007

While the populations of the eigenstates of NVs do show that the desired distribution of the $|0\rangle$ and $|+1\rangle$ population for all orientations, it does not indicate the success of the phase of the achieved pulse. The Bloch trajectories outlined in the previous section may be used to show if the designed pulse has reached the correct output state. The $\frac{|0\rangle+|+1\rangle}{\sqrt{2}}$ state lies on the positive "x" axis of the positive Bloch sphere.

Table 3.4 shows the final state overlap with the XYZ expectation values $\langle X^{\pm}\rangle, \langle Y^{\pm}\rangle, \langle Z^{\pm}\rangle$. As by the pulse design, the (1,1,1) and (-1,-1,1) NVs do populate X^{+}, corresponding to the $\frac{|0\rangle+|+1\rangle}{\sqrt{2}}$ state. The (-1,1,-1) and (1,-1,-1) NVs freely evolve under the pulse and result in a final state aligned along the negative and positive Y^{+} axes, respectively. The negative and positive Y^{+} axis represent the $\frac{|0\rangle-i|+1\rangle}{\sqrt{2}}$ and $\frac{|0\rangle+i|+1\rangle}{\sqrt{2}}$ states.

Table 3.4: Final positive domain expectation values for a $|0\rangle \rightarrow \frac{|0\rangle+|+1\rangle}{\sqrt{2}}$ state transfer in the (100) diamond. The (1,1,1) and (-1,-1,1) indicate the correct final state of X^+, corresponding to the $\frac{|0\rangle+|+1\rangle}{\sqrt{2}}$ state, while the (-1,1-1) and (1,-1,-1) NVs evolve freely under the pulse, resulting in the negative and positive Y^+ to be occupied, corresponding to the $\frac{|0\rangle-i|+1\rangle}{\sqrt{2}}$ and $\frac{|0\rangle+i|+1\rangle}{\sqrt{2}}$ states.

Final Expectation Values

	(1, 1, 1)	(-1, -1, 1)	(-1, 1, -1)	(1, -1, -1)
$\langle X^+ \rangle$	0.99944	0.99802	0.02463	0.04916
$\langle Y^+ \rangle$	0.02463	-0.04916	-0.99944	0.99802
$\langle Z^+ \rangle$	-0.0222	0.0115	-0.0222	0.0115

The Bloch plots reflect the same final state as table 3.4 indicated. As with the section above, the initial state is indicated by the red sphere, the final state by the black sphere and the trajectory of the state with the blue line. The positive Bloch plot is shown in the left column, while the negative Bloch plot is shown in the right column each divided into four rows representing the four NV orientations. The (1,1,1) and (-1,-1,1) orientations rest in the positive domain on the positive "x" axis, the $\frac{|0\rangle+|+1\rangle}{\sqrt{2}}$ state, which was the designed target state. The (-1,1,-1) and (1,-1,-1) orientations also result in a final state in the positive domain, but have a 90° phase shift from the target state.

Another interesting piece to observe here is by looking at the final state of the negative Bloch spheres. In these spheres, the final state does not rest at the origin as was seen with the π like pulses. This is because the positive and negative Bloch spheres share the common $|0\rangle$ state. The final state lying on the "z" axis, halfway between the starting $|0\rangle$ state and origin is expected, as the final state has half of the population in the $|0\rangle$ state and does not have any final components in the X or Y axes of the negative Bloch sphere for any of the orientations.

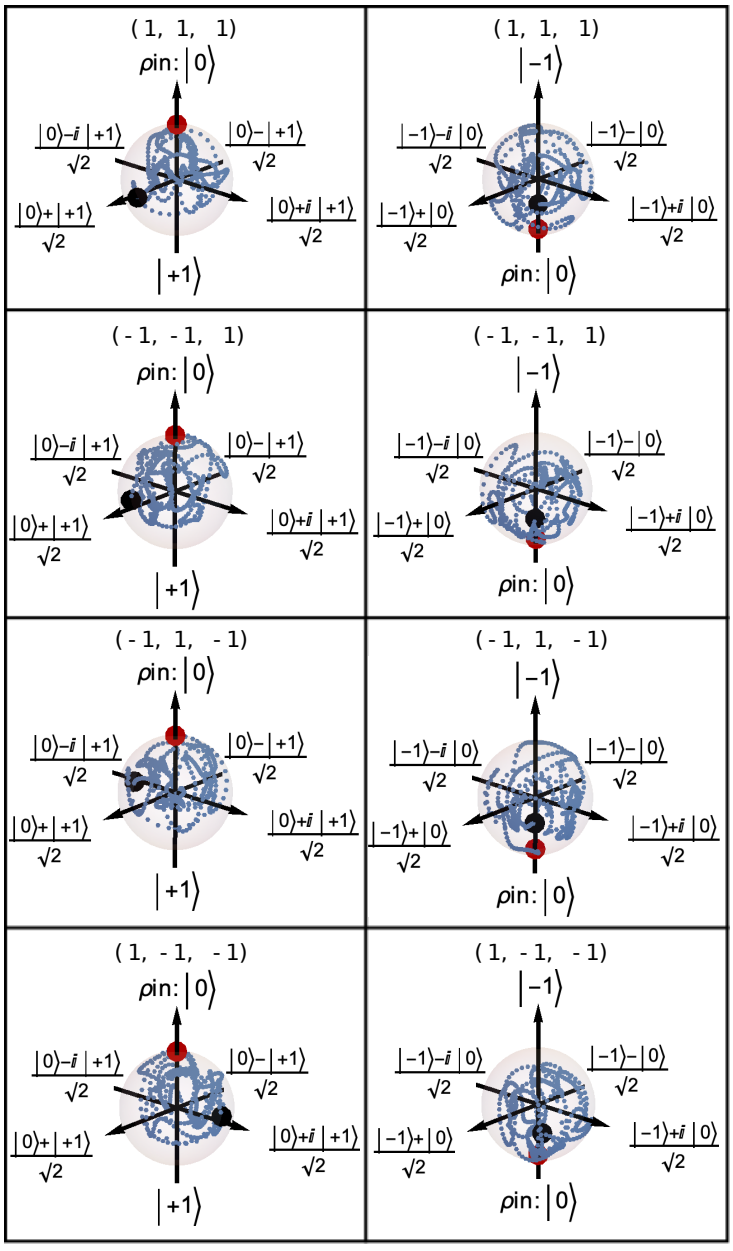

Figure 3.13: OCT Pulse - $|0\rangle \rightarrow \frac{|0\rangle+|+1\rangle}{\sqrt{2}}$ pulse, given to NVs (1,1,1) and (-1,-1,1). The pulse was successful for the two desired orientations. Due to the symmetry of the diamond, the other two orientations also show a $\frac{\pi}{2}$ rotation, but result in a rotated phase from the (1,1,1) and (-1,-1,1). This could be used as an advantage for observing different phases in a sensing experiment if this were the starting state.

This configuration of magnetic field control allows for only control over two of the four orientations, so free evolution of two orientations is a necessary piece of this pulse design. This phase difference between the freely evolving orientations may be used as an advantage when designing a pulse which desires a different final state for all four orientations of the (100) diamond. This will be explored later in this chapter (section 3.3.1), this section is only demonstrating pulses designed for the same final state of all orientations of NV centers.

Optimizing for only two of the four orientations in the (100) diamond is still advantageous because it first allows for easier analysis of the NV response to the magnetic field configuration and second, for more simple pulses to be tested. The following section will explore the (110) diamond, which does allow for control over all four NV orientations. In this case, a pulse designed for the correct population distribution and final phase distribution is possible.

3.2.4 Collective $\frac{\pi}{2}$ Pulse for All Orientations in the (110) Diamond

Unlike the (100) diamond, the (110) possess four unique orientation responses under the x and z control fields. Again, the microwave configuration being considered is outlined in figure 3.9. The components included in the Hamiltonian are listed in table 3.5. Comparing these rotation values to that of the (100) it can be seen immediately there is much less symmetry. The combination of these rotation values yield four unique control Hamiltonians.

Table 3.5: Rotation matrix components in the control Hamiltonian for the (110) diamond, with field aligned along the x and z axes.

NV	xx	xy	zx	zy
(1,1,1)	$\frac{1}{2}+\frac{1}{\sqrt{6}}$	$-\frac{1}{2}+\frac{1}{\sqrt{6}}$	$-\frac{1}{\sqrt{6}}$	$-\frac{1}{\sqrt{6}}$
(-1,-1,1)	$\frac{1}{2}-\frac{1}{\sqrt{6}}$	$-\frac{1}{2}-\frac{1}{\sqrt{6}}$	$-\frac{1}{\sqrt{6}}$	$-\frac{1}{\sqrt{6}}$
(-1,1,-1)	$\frac{1}{6}(3+2\sqrt{2})$	$\frac{1}{6}$	$-\frac{1}{\sqrt{3}}+\frac{1}{\sqrt{6}}$	$\frac{1}{\sqrt{3}}+\frac{1}{\sqrt{6}}$
(1,-1,-1)	$\frac{1}{6}(3-2\sqrt{2})$	$\frac{1}{6}$	$\frac{1}{\sqrt{3}}+\frac{1}{\sqrt{6}}$	$-\frac{1}{\sqrt{3}}+\frac{1}{\sqrt{6}}$

To demonstrate the success of the unique response, the desired state-to-state transfer of $|0\rangle \rightarrow \frac{|0\rangle+|+1\rangle}{\sqrt{2}}$, that is a $\frac{\pi}{2}$ rotation about the Y axis in the positive domain, was given to each NV orientation in the (110) diamond. As with the (100) diamond, the final eigenstates indicated the correct distribution of even population between the $|0\rangle$ and $|+1\rangle$ states for all orientations. For more clarity on the success of the pulse, the final distribution of the $\langle X^{\pm}\rangle, \langle Y^{\pm}\rangle, \langle Z^{\pm}\rangle$ values is found. Recall the $\langle X^{+}\rangle$ represents $\frac{|0\rangle+|+1\rangle}{\sqrt{2}}$, which is the desired final state. Table 3.6 shows the final state of each NV orientation after the pulse was simulated. Each orientation correctly results in the desired final state of $\frac{|0\rangle+|+1\rangle}{\sqrt{2}}$, aligning along the positive "x" axis of the positive Bloch sphere.

Table 3.6: Final state for a $|0\rangle \rightarrow \frac{|0\rangle+|+1\rangle}{\sqrt{2}}$ state transfer in the (110) diamond. Each NV orientation arrived at the correct final state of $\langle X^{+}\rangle$, representing the $\frac{|0\rangle+|+1\rangle}{\sqrt{2}}$ state.

Final Expectation Values

	(1, 1, 1)	(-1, -1, 1)	(-1, 1, -1)	(1, -1, -1)
$\langle X^{+}\rangle$	0.99523	0.99403	0.99393	0.97379
$\langle Y^{+}\rangle$	-0.00139	0.06706	-0.08872	-0.03619
$\langle Z^{+}\rangle$	-0.0884	-0.0064	0.01624	0.12081

The Bloch plots clearly show the successful $|0\rangle \rightarrow \frac{|0\rangle+|+1\rangle}{\sqrt{2}}$ state transfer for the (110) diamond, achieving not only the correct population distribution between the $|0\rangle$ and $|+1\rangle$ states, but the correct phase as well. This is most evident by looking at the positive Bloch sphere with all the final states aligning along the positive "x" axis. As with the (100) diamond, the final state in the negative Bloch sphere is aligned along the "z" axis, halfway between the $|0\rangle$ state and the origin, indicating there is population left in the $|0\rangle$ state, but no coherence on the X or Y axis of the negative Bloch sphere.

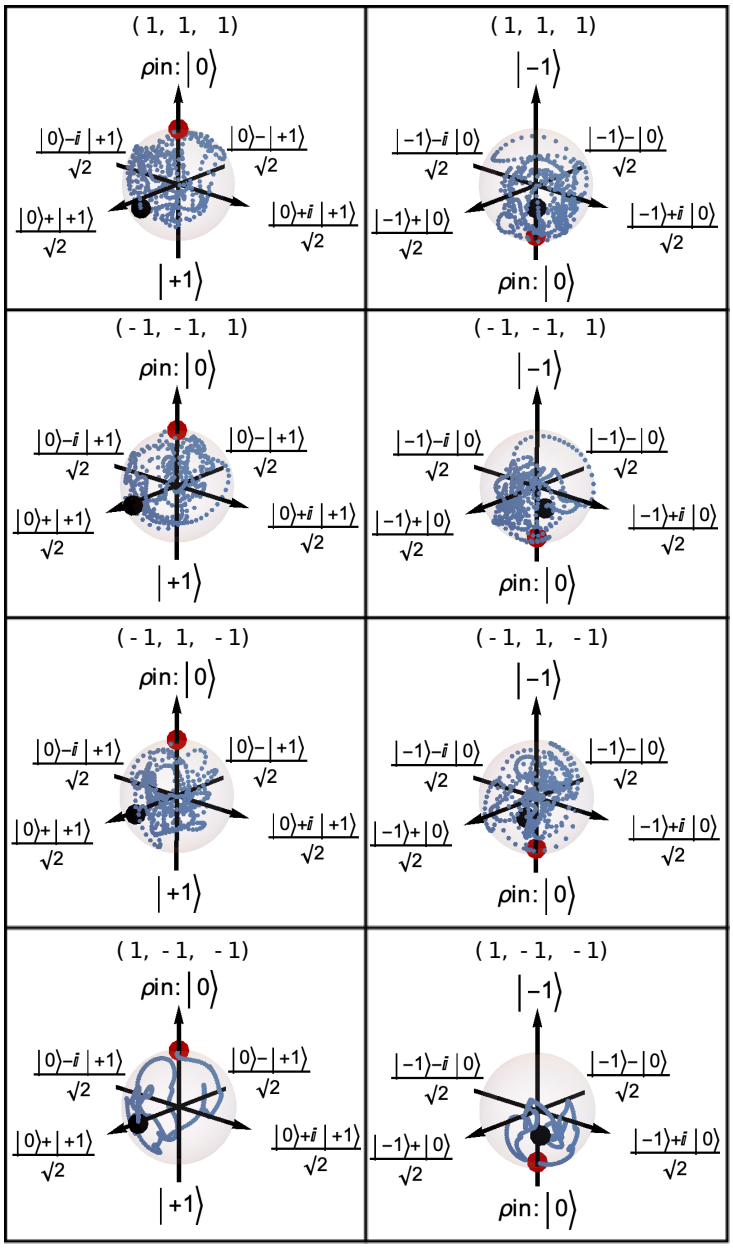

Figure 3.14: OCT Pulse - $|0\rangle \rightarrow \frac{|0\rangle+|+1\rangle}{\sqrt{2}}$ state transfer for all NV orientations in the (110) diamond. The plot indicates not only the correct population distribution for the $|0\rangle$ and $|+1\rangle$ states, as was achieved with the (100) diamond, but also the correct phase. This is due to the unique response of each Hamiltonian with the fields aligned along the "x" and "z" direction.

The success of this simulation indicates that this crystal orientation is the most optimal to be used for control fields lying along the x and z axis as each NV may be controlled uniquely, allowing any desired state to be reached. This analysis was conducted this way to compare the many useful experiments that may be achieved with the (100) diamond, analyzing at first a more simple response with only two orientations to consider. While there are many applications available to the (100) diamond with this microwave field geometry, for universal control of all the orientations of NV centers, the (110) diamond should be used.

In the following section, the (111) diamond will show as an example of an interesting case where linear and circular polarization control are mixed within the same diamond crystal. It indicates the success of control for the applications of when the (111) diamond is desired for experimental purposes.

3.2.5 Collective Control on Three Orientations in the (111) Diamond

The previous section showed the possibilities of control when there are four unique projections of the NV orientations with magnetic field control in the "x" and "z" direction. This section will show the applications of control when there are four unique projections, but for one orientation, only linear microwave polarization is used to control the NV.

The (111) diamond has one of the NV orientations which aligns perfectly along the lab and crystal frame ("z" axis). When an x and z microwave control source is used, this source is unable to access selective single transitions for the (1,1,1) orientation as one of the sources lies parallel to the axes and is therefore treated as a single linear source. Circular polarization is required to access the single transitions. This is shown in table 3.7 which shows the rotation matrix values incorporated into the control Hamiltonian with a field along the x and z axes. The limitations for the (1,1,1) orientation are obvious here, as the only component that is non-zero is the xx value. As the other three orientations have unique values for both the x and z rotation values, select control of these orientations is possible. The optimal field value for this diamond crystal would be along the x and y field direction as that field uses the rotation matrix values of xx=1 and yy=1 for the (1,1,1) orientation, but here, the results are being compared directly with the other crystals under the designed field along the x and z axes.

This section is analyzing the opportunity to use the (111) diamond with this magnetic field configuration. If the experimental applications require the use of the (111) diamond specifically, analysis with this magnetic field configuration is required.

Table 3.7: Rotation matrix components in the control Hamiltonian for the (111) diamond with field aligned along the x and z axes.

NV	xx	xy	zx	zy
(1,1,1)	1	0	0	0
(-1,-1,1)	$\frac{1}{3}$	$-\frac{2}{3}$	$-\frac{2}{3}$	$-\frac{2}{3}$
(-1,1,-1)	$\frac{1}{3}+\frac{1}{\sqrt{3}}$	$\frac{1}{3}$	$\frac{1}{3}-\frac{1}{\sqrt{3}}$	$\frac{1}{3}+\frac{1}{\sqrt{3}}$
(1,-1,-1)	$\frac{1}{3}-\frac{1}{\sqrt{3}}$	$\frac{1}{3}$	$\frac{1}{3}+\frac{1}{\sqrt{3}}$	$\frac{1}{3}-\frac{1}{\sqrt{3}}$

As an example to show the control over the (111), if a state transfer of the $|0\rangle \rightarrow |+1\rangle$ is desired, all orientations are able to reach the desired output population, except for the (1,1,1) NV. It performs as a linear microwave π pulse would, evenly distributing the population between the $|\pm 1\rangle$ states.

Table 3.8: Final state for $|0\rangle \rightarrow |+1\rangle$ pulse for all NVs in (111) diamond. As the (1,1,1) orientation lies along the "z" axis, the source is seen as one linear source instead of two sources combining to form a circular polarization which is required to access the single transitions. The population is therefore shown to be evenly distributed in the $|\pm 1\rangle$ states, as it would be for a linear source. The other orientations, which lie off the "z" axis, show a successful selective π pulse to the $|0\rangle \rightarrow |+1\rangle$.

Final Expectation Values

	(1, 1, 1)	(-1, -1, 1)	(-1, 1, -1)	(1, -1, -1)
⟨0⟩	0.00007	0.00016	0.00017	0.00002
⟨+1⟩	0.49997	0.99814	0.99863	0.99997
⟨-1⟩	0.49997	0.0017	0.0012	0.00001

Control of the (111) diamond for three orientations is possible given the current microwave field configuration. It is possible to keep the (1,1,1) in the $|0\rangle$ state, with linear control only, while controlling the other three orientations as desired. As a toy example, a $|0\rangle \rightarrow \frac{|0\rangle+i|+1\rangle}{\sqrt{2}}$ pulse has been designed for all NVs except the (1,1,1) orientation, while the (1,1,1) orientation is set to remain in the $|0\rangle$ state. Table 3.9 shows the results of the $\langle X^+\rangle, \langle Y^+\rangle, \langle Z^+\rangle$ values for the final state of each NV orientation. The pulse designed for the $\frac{|0\rangle+i|+1\rangle}{\sqrt{2}}$ final state aligns with the positive "y" axis in the positive Bloch sphere, so a complete overlap with the $\langle Y^+\rangle$ state is expected for this state-to-state transfer. As designed, all orientations, except the (1,1,1) NV show the target overlap of 0.99 with this state. The (1,1,1) state shows a final overlap of 0.99 with $\langle Z^+\rangle$, as expected. The positive "z" axis in the positive Bloch sphere represented the $|0\rangle$ state.

Table 3.9: Final state for a $|0\rangle \rightarrow \frac{|0\rangle+i|+1\rangle}{\sqrt{2}}$ state in the (111) diamond for all NV orientations except the (1,1,1). The (1,1,1) had a target pulse to remain in the $|0\rangle$ state. This pulse was successful, achieving the desired population transfer for each orientation.

Final Expectation Values

	(1, 1, 1)	(-1, -1, 1)	(-1, 1, -1)	(1, -1, -1)
$\langle X^+ \rangle$	0.00703	-0.05904	0.13821	-0.0199
$\langle Y^+ \rangle$	-0.05886	0.98648	0.98891	0.98726
$\langle Z^+ \rangle$	0.99736	0.13582	0.01223	0.125

The Bloch plot evolution of the desired target is shown in figure 3.15. All NV orientations with the exception of the (1,1,1) NV was given the target state to state transfer of $|0\rangle \rightarrow \frac{|0\rangle+i|+1\rangle}{\sqrt{2}}$, which is successful. The (111) diamond may be compared to the (100) diamond with this magnetic field configuration. While the (100) diamond did have the correct population distribution between the $|0\rangle$ and $|+1\rangle$ state, it could only optimize the same phase for two of the four orientations. In the case of the (111) diamond, the same final state may be achieved for three of the four orientations.

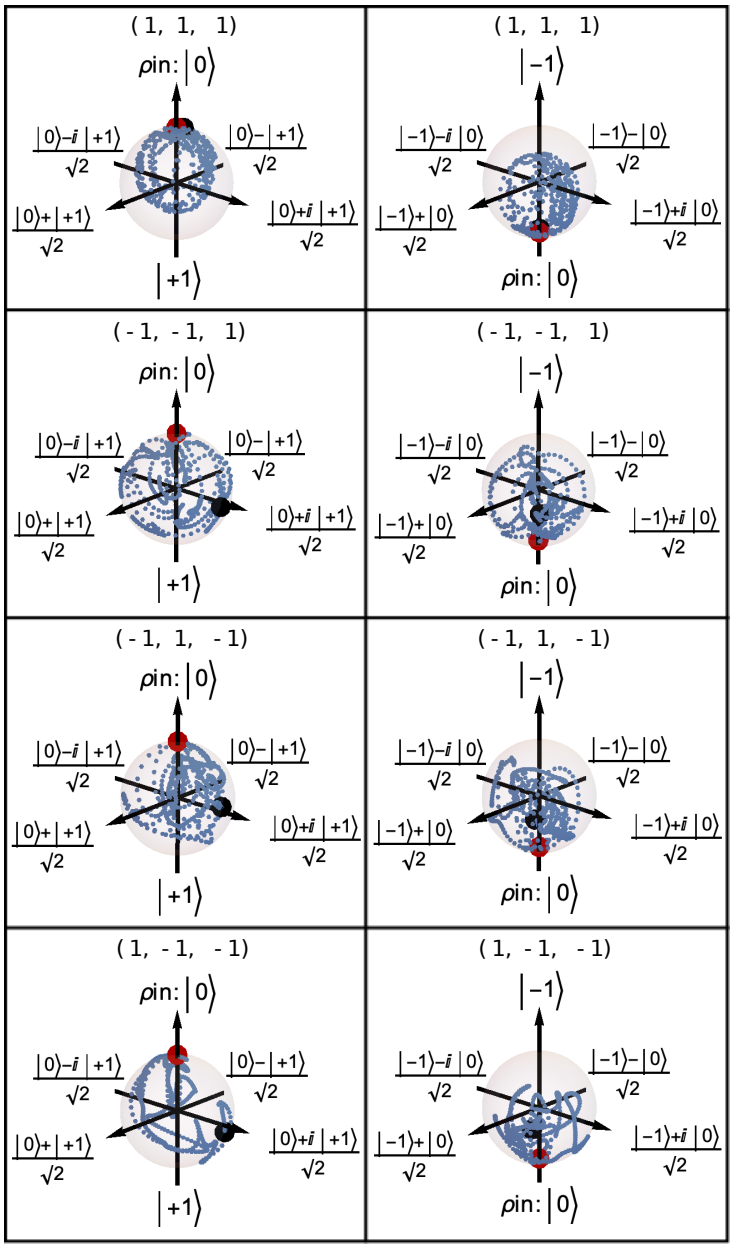

Figure 3.15: OCT Pulse - $|0\rangle \rightarrow \frac{|0\rangle+i|+1\rangle}{\sqrt{2}}$ pulse for three NV orientations in the (111) diamond, $|0\rangle \rightarrow |0\rangle$ for NV (1,1,1). Rather than letting the (1,1,1) NV evolve freely, it was given a target pulse to remain in the $|0\rangle$ state so it does not add noise to the results. The other three orientations evolve as desired.

3.2.6 Target State Overlap Summary for Collective Control

The first examples of OCT pulses have been shown in this section, for collective control on each of the (100), (110) and (111) diamond. Collective control has been defined here as having the same target state-to-state transfer given to each NV orientation for each of the three diamonds. In each case, a π like pulse and $\frac{\pi}{2}$ like pulses were given, though these are not an extensive list of the achievable pulses. As these are state-to-state transfers rather than unitaries, they cannot be exactly addressed as π and $\frac{\pi}{2}$, but the exact density state transfers defined. The following tables show a summary of results for the target state overlap of the target pulses, for a field along the "x" and "z" axis in the lab frame. Of course the field may be adjusted such that it is suited for each diamond crystal orientation, and in the best scenario, a field that is designed to be along the "x","y" and "z" directions would be the most ideal for achieving any target state-to-state transfer within each diamond crystal.

Analyzing the advantages of each crystal with respect to a set 2D field yielded interesting results. The symmetry of the (100) diamond reduces the orientations from four unique to two sets of sub-ensembles. This reduces the computational demands on the pulse. The (110) diamond possess four unique responses to the field, and thus may be used to achieve any target state-to-state transfer. The (111) diamond is able to use three of the four orientations, while keeping the (1,1,1) orientation in the $|0\rangle$ state. Each of these three crystals may be used for unique applications, without the need to change the setup if an xz field is used.

Table 3.10 shows the summary of results for all diamond crystals targeting a $|0\rangle \rightarrow |+1\rangle$ or $|-1\rangle$ state transfer. The (100) and (110) diamonds are able to achieve these desired state transfers for all orientations of NVs, while the (111) diamond may do this if the (1,1,1) NV orientation is kept at the $|0\rangle$ state.

Table 3.10: Pulse target state overlap for the collective π pulses on all NV orientations in each of the diamond crystals. With the field sourced from two microstrips, aligned along the "x" and "z" direction in the lab frame, the target state overlap of 0.99 for the (100) and (110) diamond has been reached for all orientations of NVs. The (111) diamond may reach the desired target state overlap if the (1,1,1) NV remains in the $|0\rangle$ state.

	(100)	(110)	(111)
	$\|+1\rangle \rightarrow$ 0.997113	$\|+1\rangle \rightarrow$ 0.990949	$\|+1\rangle \rightarrow$ 0.875 Except(1,1,1)$\rightarrow$ 0.995881
	$\|-1\rangle \rightarrow$ 0.993346	$\|-1\rangle \rightarrow$ 0.990017	$\|-1\rangle \rightarrow$ 0.864512 Except(1,1,1)$\rightarrow$ 0.991689

Table 3.11 shows the summary of target state overlap for achieving a $|0\rangle \rightarrow \frac{|0\rangle+i|+1\rangle}{\sqrt{2}}(\overline{x})$ or $|0\rangle \rightarrow \frac{|0\rangle+|+1\rangle}{\sqrt{2}}(y)$, for all orientations. The (110) diamond is successful in achieving these exact state transfers. The (100) diamond is able to achieve the desired population for a $\frac{\pi}{2}$ pulse, but the phase differs for each of the orientations.The target state overlap shown below is for a pulse designed for only the (1,1,1) and (-1,-1,1) NV while the other two orientations evolve freely. The target overlap shown indicated the success of the target state overlap for only the two orientations that the pulse was designed for. Last, again the (111) diamond shows the desired target state overlap if the (1,1,1) NV orientation is kept in the $|0\rangle$ state.

Table 3.11: Pulse target state overlap for the collective $\frac{\pi}{2}$ pulses on all NV orientations in each of the diamond crystals. The (110) diamond is best suited for having a control field along the xz field, with a target state overlap of 0.99 and as was seen in those specific results, can achieve the correct phases as well for the outlined state-to-state transfers. The (100) diamond is interesting as it is able to achieve a $\frac{\pi}{2}$ pulse, but the phases between pairs of ensembles of NVs are not the same, so while the population distribution is correct between the desired states of $|0\rangle$ and $|+1\rangle$ or $|-1\rangle$, the phase value will different between orientations. This may be used to an advantage if the experiment is looking to pick up different phases between each NV orientation. The (111) diamond is able to achieve the target state overlap if the (1,1,1) NV is given the target pulse of $|0\rangle \rightarrow |0\rangle$.

(100)	(110)	(111)
$\overline{x} \rightarrow$ 0.994729	$\overline{x} \rightarrow$ 0.99418	$\overline{x} \rightarrow$ 0.9375 Except(1,1,1)$\rightarrow$ 0.990378
y $\rightarrow$ 0.993584	y $\rightarrow$ 0.990026	y $\rightarrow$ 0.9375 Except(1,1,1)$\rightarrow$ 0.993041

This section detailed the abilities of a control field aligned along the "x" and "z" field for each of the (100), (110) and (111) diamond for the same state-to-state transfer. The next section will show the abilities of this field configuration if unique output states are desired for the NV orientations.

3.3 Optimal Control Theory Pulses for Selective Control

The previous section established how this magnetic field configuration may control an ensemble of NVs within the (100), (110) and (111) diamonds with the same target state-to-state transfer. In some experimental cases, it is desired to have only one NV orientation active while the other orientations remain in the $|0\rangle$ state. The NVs may also be controlled with unique operators for each, with each having a different target. Being able to control the NVs individually, and actively move each orientation from the $|0\rangle$ state to some other state, allows each of them to be turned on sequentially without the need of changing hardware. Recall there are existing schemes which already accomplish this using multiple microwave frequencies to target each orientation, [93, 119]. This method achieves a similar result without having to alter the setup from the magnetic field configuration shown in figure 3.9.

The following section will demonstrate examples for each of the (100), (110) and (111) diamonds and their ability to have individual targets on each orientation.

3.3.1 Selective Control for NV Sub-Ensembles in the (100) Diamond

Demonstrating selective single transitions for sub-ensembles

The previous section demonstrated single transitions from the $|0\rangle \rightarrow |+1\rangle$ or $|-1\rangle$ state for each of the pairs of orientations in the (100) diamond. Keeping with treating the orientations as two pairs, rather than four orientations, each of the pairs may be selectively controlled while the other pair is kept in the $|0\rangle$ state. Figure 3.16 shows a selective state-to-state transfer which rotates the (1,1,1) and (-1,1,-1) NVs from the $|0\rangle$ to the $|+1\rangle$ state, while the (-1,-1,1) and (1,-1,-1) are instructed to transfer from the $|0\rangle \rightarrow |0\rangle$ state.

While this shows the success of selective control on the sub-ensembles of NV orientations within the (100) diamond, it does not show the full potential of designing a control pulse for only two of the four orientations and achieving four unique state-to-state transfers.

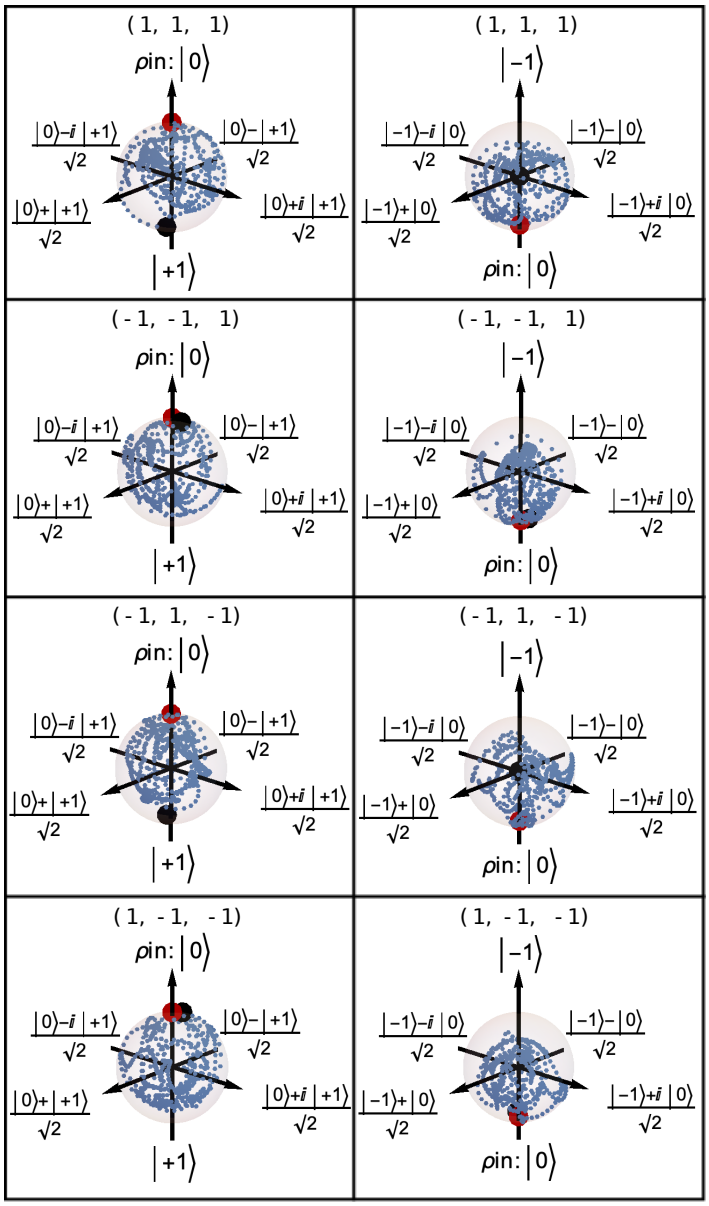

Figure 3.16: OCT Pulse - selective $|0\rangle \rightarrow |+1\rangle$ pulse for one pair, and $\mathbb{1}$ on the other pair of NVs. The symmetry of this diamond allows for selective pulses on two sub-ensembles rather than four orientations. The beginning state of all orientations **(red)** is $|0\rangle$ while the final state **(black)** of the (1,1,1) and (-1,1,-1) has been set to $|+1\rangle$ and the final state of (-1,-1,1) and (1,-1,-1) is $|0\rangle$. The trajectory of the pulse is shown in **(blue)**. The positive Bloch sphere indicates these beginning and final states quite clearly. The final state of the negative sphere is at the origin for the $|+1\rangle$ final states and $|0\rangle$ for the intended $|0\rangle$ states.

Using crystal symmetry to achieve unique final states

In this pulse, the control was intentionally only placed on the (1,1,1) and (-1,-1,1) NVs. As was seen when the collective control was attempted to transfer all NV pairs from $|0\rangle \rightarrow \frac{|0\rangle+|+1\rangle}{\sqrt{2}}$, if control was placed only on the (1,1,1) and (-1,-1,1) NV, and the other orientations were allowed to evolve freely, all achieved the correct distribution of population between the $|0\rangle$ and $|+1\rangle$ states, but the phases were only correct for the target orientations. The (-1,1,-1) evolved to the $\frac{|0\rangle-i|+1\rangle}{\sqrt{2}}$ state, while the (1,-1,-1) evolved to the $\frac{|0\rangle+i|+1\rangle}{\sqrt{2}}$ state, $\mp 90°$ from the intended final state.

In this case, this phase evolution was intentionally used so that four unique final states could be achieved by only targeting two orientations. The (1,1,1) NV was given the target state-to-state transfer of $|0\rangle \rightarrow \frac{|-1\rangle+|0\rangle}{\sqrt{2}}$. The (-1,-1,1) NV was given the target of $|0\rangle \rightarrow \frac{|-1\rangle+i|0\rangle}{\sqrt{2}}$. The (-1,1,-1) and (1,-1,-1) were left to evolve freely under these target pulses.

Table 3.12: Final states for the selective pulse on NVs (1,1,1) and (-1,-1,1) to a superposition of the $|0\rangle$ and $|-1\rangle$ states. The (1,1,1) and (-1,-1,1) evolve as designed to the positive X and "y" axis in the negative Bloch sphere, while the (-1,-1,1) and (-1,1,-1) evolve freely to the negative Y and "x" axis in the negative space. By optimizing only two orientations, four unique states may be reached.

Final Expectation Values

	(1, 1, 1)	(-1, -1, 1)	(-1, 1, -1)	(1, -1, -1)
$\langle X^- \rangle$	0.99911	0.00002	0.00764	-0.98173
$\langle Y^- \rangle$	0.00764	0.98173	-0.99911	0.00002
$\langle Z^- \rangle$	0.02493	-0.09917	0.02493	-0.09917

The Bloch plots in figure 3.17 show how the pulse was successful in achieving a unique final state for each NV orientation. The 90° phase difference accumulated when the pairs of NVs evolve freely under the target pulse was used as an advantage here to set all four orientations in a superposition of the $|0\rangle$ and $|-1\rangle$ plane with a different phase. The positive Bloch sphere shows the final state aligned along the "z" axis, with no phase in the "x" or "y" plane, halfway between the $|0\rangle$ and origin, indicating there is a shared population with the $|0\rangle$ state, but no phase in the positive Bloch sphere as intended.

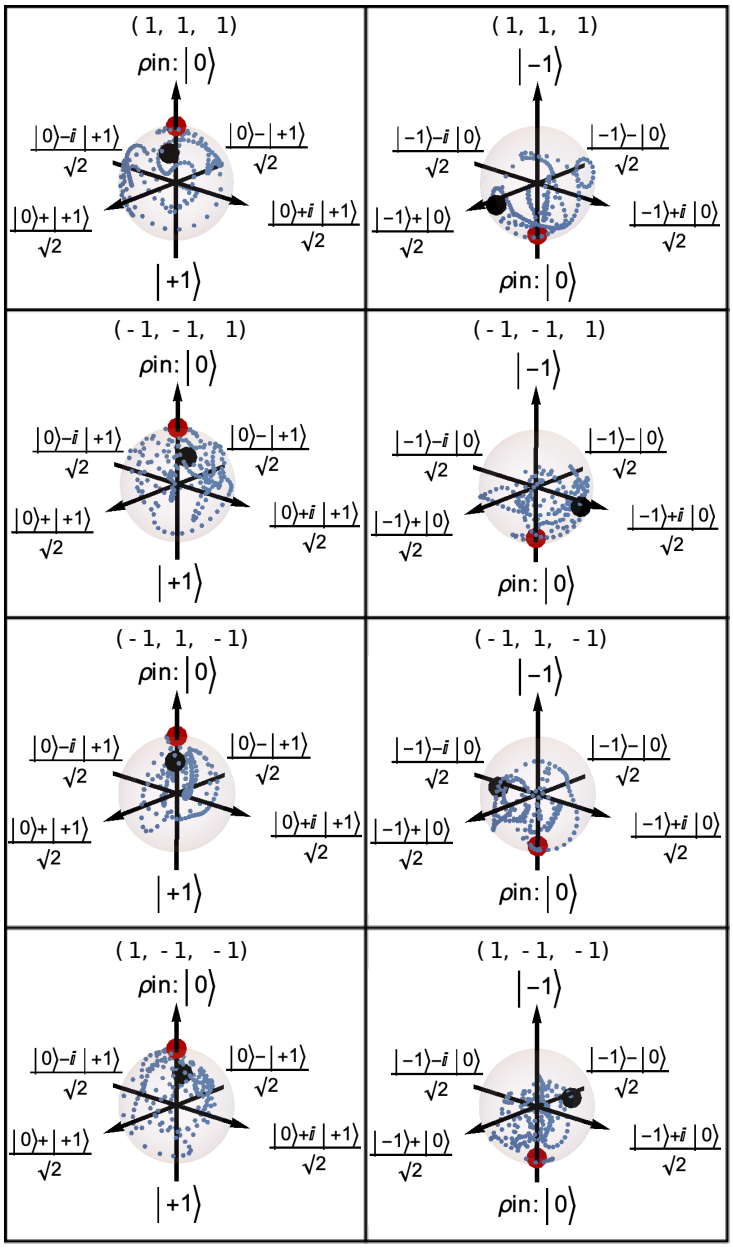

Figure 3.17: OCT Pulse - selective pulses for NVs (1,1,1) and (-1,-1,1) while NVs (-1,1,-1) and (1,-1,-1) evolve freely. Intentionally setting the (1,1,1) NV to evolve to $\frac{|-1\rangle+|0\rangle}{\sqrt{2}}$ and (-1,-1,1) to $\frac{|-1\rangle+i|0\rangle}{\sqrt{2}}$ and allowing the other two orientations to evolve freely results in four unique outputs. The symmetry within the (100) crystal may be used to create intentional useful final states given these limits.

The negative Bloch sphere indicates the four final unique state, corresponding to table 3.12. Recall the axes in the Bloch sphere aligning with the following states:

$$\begin{aligned}
(1,1,1) &\rightarrow \tfrac{|-1\rangle+|0\rangle}{\sqrt{2}} &&; +|X^-\rangle \\
(-1,-1,1) &\rightarrow \tfrac{|-1\rangle+i|0\rangle}{\sqrt{2}} &&; +|Y^-\rangle \\
(-1,1,-1) &\rightarrow \tfrac{|-1\rangle-i|0\rangle}{\sqrt{2}} &&; -|Y^-\rangle \\
(1,-1,-1) &\rightarrow \tfrac{|-1\rangle-|0\rangle}{\sqrt{2}} &&; -|X^-\rangle
\end{aligned} \tag{3.42}$$

Complete selective control is possible for the sub-ensembles of the (100) diamond, each containing a pair of NVs. In addition, the symmetry of the crystal may be used as an advantage so that pulses designed to be optimized over only two orientations allows for four unique final states. Arriving at a unique final state after using the pulse allows for each NV to then evolve with a different starting phase, useful for sensing applications.

The next section will show how each of the four NVs may be actively controlled with a unique state-to-state transfer while the other three NVs remain in the $|0\rangle$ state in the (110) diamond. Unlike the (100) diamond which allows control over two sub-ensembles, the (110) allows for any combination of state-to-state transfer for all four orientations.

3.3.2 Selective Control for Four NV Orientations in the (110) Diamond

The (110) oriented diamond has already shown to be well suited for this configuration of microwave geometry, achieving the same target state-to-state transfer for all four orientations of NVs in the ensemble. This section will show how a selective state-to-state transfer may be achieved for one orientation of NV while the the three remaining remain in the $|0\rangle$ state. This was demonstrated for the two sub-ensembles in the (100) diamond, but extending this to all four orientations in the (110) enhances magnetic field sensing capabilities.

As an example to show the achievable selectively in this crystal orientation is to demonstrate a $|0\rangle \rightarrow \frac{|0\rangle+i|+1\rangle}{\sqrt{2}}$ pulse on NV (1,1,1), while all the other orientations are kept in the $|0\rangle$ state. Four experiments could be run sequentially, moving each NV orientation into the transverse plane for sensing, while the other three are kept in the $|0\rangle$ state, as has been conducted in previous sensing experiments, [120, 123]. This achieves the same results, with a more compact experimental design.

The final states achieved after implementing the pulse are shown in table 3.13. A final state overlap with the positive "y" axis $\langle Y^+\rangle = 0.99$ for the (1,1,1) NV corresponds to the state transfer of $|0\rangle \rightarrow \frac{|0\rangle+i|+1\rangle}{\sqrt{2}}$ while the other three final states overlap with the positive "z" axis $\langle Z^+\rangle = 0.99$ in the positive Bloch sphere, corresponding to the $|0\rangle \rightarrow |0\rangle$ state-to-state transfer.

Table 3.13: The final states for a selective state-to-state transfer on the (1,1,1) NV to the positive "y" axis, $|0\rangle \rightarrow \frac{|0\rangle+i|+1\rangle}{\sqrt{2}}$, while all others remain in $|0\rangle$. The pulse on (1,1,1) NV corresponds to a state overlap of $\langle Y^+\rangle = 0.99$ and $\langle Z^+\rangle = 0.99$ for all other orientations.

Final Expectation Values

	(1, 1, 1)	(-1, -1, 1)	(-1, 1, -1)	(1, -1, -1)
⟨X⁺⟩	0.0212	-0.02027	0.03801	0.00371
⟨Y⁺⟩	0.98789	0.03722	-0.02257	-0.02443
⟨Z⁺⟩	0.09197	0.99779	0.99762	0.99893

The Bloch plots show the trajectory for each NV orientation under this pulse design, and indicate the correct final state as table 3.13. The positive Bloch sphere shows the desired state-to-state transfer for the (1,1,1) NV orientation. The remaining three orientations show an identity like pulse, with the starting and stopping state overlapping with $|0\rangle = 0.99$.

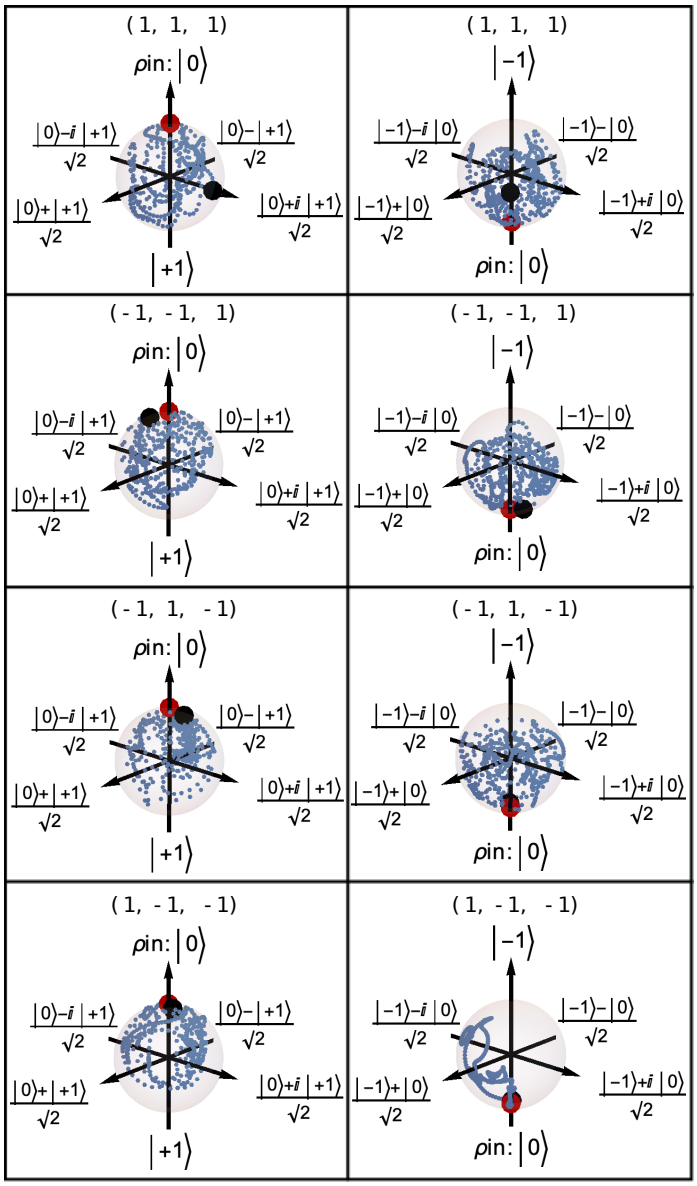

Figure 3.18: OCT Pulse - $|0\rangle \rightarrow \frac{|0\rangle+i|+1\rangle}{\sqrt{2}}$ pulse for the (1,1,1) NV and $|0\rangle \rightarrow |0\rangle$ on all others in the (110) diamond. The positive Bloch plot indicates the success of this pulse. This serves as an example for the selective abilities of the (110) diamond with a field aligned along the x and z axes. Any target unitary for each of the four NVs is possible with this field orientation and crystal. The ability to selectively rotate one orientation of NVs and keep the others in a $|0\rangle$ state in four successive pulses, each designed for one of the four orientations, allows for selective sensing of each of the four orientations, advantageous for sensing applications.

While this is only one example to demonstrate state-to-state transfer for selective NV orientations, the (110) diamond is able to perform any selective target unitary for each individual NV orientation. This makes it the most adaptable for experimental applications with the given control field lying along the "x" and "z" axis. The (100) and (111) diamond may also be controlled as the (110) diamond has been shown in this case, but with a field aligned along the "x" and "y" direction. However, the purpose of this thesis is to dictate the capabilities of a microwave field configuration that is realized in a planar structure, using two microstrips. This configuration is easily adaptable for a portable sensing device, as the envelope for a PCB board with two printed microstrips already has a low profile.

The following section will show the capabilities of the (111) diamond for selective control on individual NV orientations.

3.3.3 Selective Control for Three NV Orientations in the (111) Diamond

As was the case with the collective pulse on each of the four orientations within the (111) diamond, the (1,1,1) cannot have selective control beyond those allowable for a linear microwave source while the field is aligned along the "x" and "z" axes. This restricts the control within this crystal to the other three NV orientations, but within these three orientations unique selective control of each is possible. Like as was seen with the (110) diamond, three of the orientations may be selectively rotated while the others are kept idle at $|0\rangle$. In doing so, again, some sensing experiments may be performed, which utilizes three of these four orientations. This crystal may be chosen over the (110) diamond because the relative orientations of each of the three active NV orientations would have a different relation to the surface compared to the (110) diamond. If this relationship between the NV orientation and the diamond surface can change how the NVs are interacting with surface moieties it may be advantageous to use three active NV orientations in the (111) diamond compared with four active NV orientations in the (110) diamond.

In this toy example, four different target final states were given to the NVs in the (111) diamond. The starting state for all orientations is $|0\rangle$. Within the limitations of the field relative to the crystal orientation, the (1,1,1) orientation is kept at $|0\rangle$, achievable with linear microwave control. The other three orientations were given final states resulting in a selective superposition between the $|0\rangle$ and $|+1\rangle$ or $|-1\rangle$ and with differing phase. This is different from achieving four different final states in the (100) diamond case.

In the case of the (100) diamond, the symmetry of the diamond was used as a convenient tool to result in NVs having a superposition of the $|0\rangle$ and $|+1\rangle$ state with different phases while only designing a pulse for two of the four orientations. For the pulses designed in the (111) diamond, each control Hamiltonian was given a different target control to demonstrate OCTs range of abilities.

The target states for each of the four NVs are as such:

$$\begin{array}{lll} (1,1,1) & \rightarrow |0\rangle & ;+|Z^+\rangle = -|Z^-\rangle \\ (-1,-1,1) & \rightarrow \frac{|-1\rangle+i|0\rangle}{\sqrt{2}} & ;+|Y^-\rangle \\ (-1,1,-1) & \rightarrow \frac{|0\rangle+|+1\rangle}{\sqrt{2}} & ;+|X^+\rangle \\ (1,-1,-1) & \rightarrow \frac{|0\rangle+i|+1\rangle}{\sqrt{2}} & ;+|Y^+\rangle \end{array} \tag{3.43}$$

Table 3.14 yields the corresponding final state overlap values in the positive and negative domains. All state overlaps yield a target state overlap of ≥ 0.98.

Table 3.14: Final state overlap for unique selective pulses on the (111) diamond. (1,1,1) NV $|0\rangle \rightarrow |0\rangle$; (-1,-1,1) NV $|0\rangle \rightarrow \frac{|-1\rangle+i|0\rangle}{\sqrt{2}}$; (-1,1,-1) NV $|0\rangle \rightarrow \frac{|0\rangle+|+1\rangle}{\sqrt{2}}$; (1,-1,-1) NV $|0\rangle \rightarrow \frac{|0\rangle+i|+1\rangle}{\sqrt{2}}$

Final Expectation Values

	(1, 1, 1)	(-1, -1, 1)	(-1, 1, -1)	(1, -1, -1)
$\langle X^+ \rangle$	0.00836	0.0977	0.9781	0.0427
$\langle Y^+ \rangle$	-0.08385	-0.02504	-0.18467	0.9981
$\langle Z^+ \rangle$	0.99466	0.49069	-0.09553	-0.0227

Final Expectation Values

	(1, 1, 1)	(-1, -1, 1)	(-1, 1, -1)	(1, -1, -1)
$\langle X^- \rangle$	0.00836	0.15115	0.00027	-0.02504
$\langle Y^- \rangle$	0.08385	0.98332	-0.00884	-0.02823
$\langle Z^- \rangle$	-0.99466	0.00323	-0.45217	-0.48755

The positive and negative Bloch plots in figure 3.19 show the success of the designed pulse. The positive spheres show the successful pulse of the (-1,1,-1) and (1,-1,-1) orientations, while the negative sphere shows the successful final state of the (-1,-1,1) NV orientation. As the $|0\rangle$ state is indicated in both the positive and negative spheres, the (1,1,1) final state is evident in both.

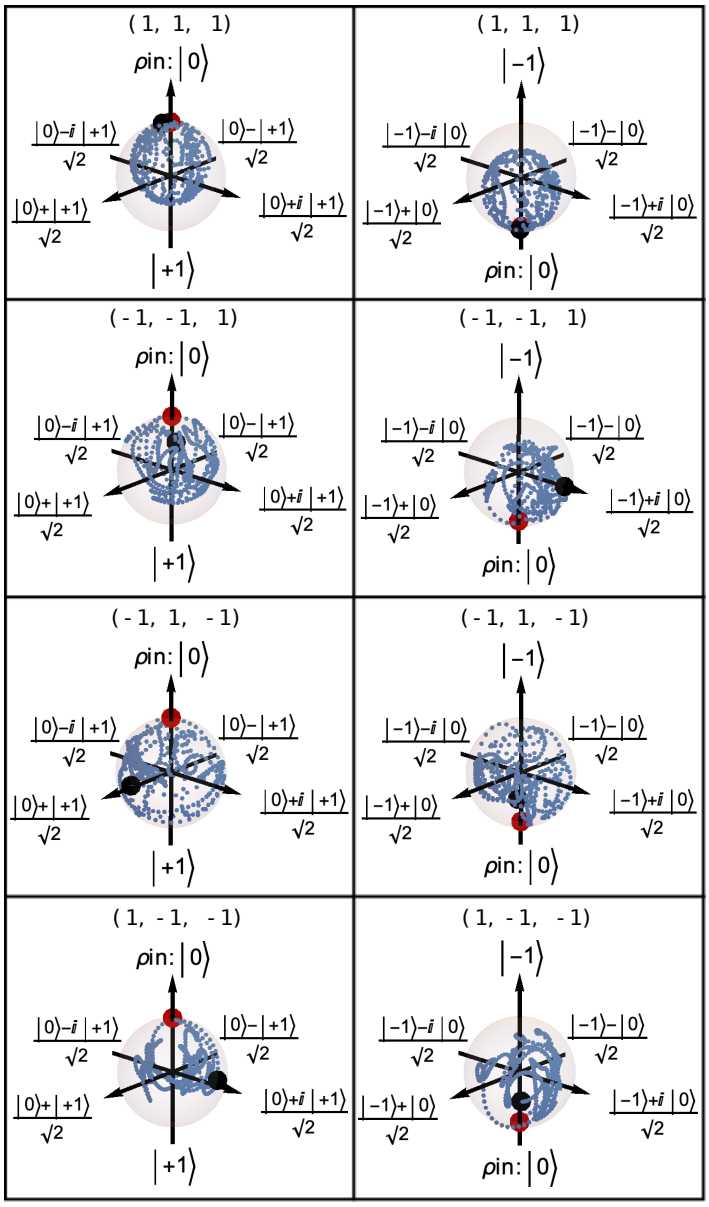

Figure 3.19: OCT Pulse - Selective pulses for all orientations in the (111) diamond. All orientations are shown to begin in the $|0\rangle$ state **(red)**. The (1,1,1) NV orientation was given a target final state of $|0\rangle$, evident in both the positive and negative Bloch spheres. The final state of the (-1,-1,1) NV is evident in the negative Bloch sphere, arriving at the intended $\frac{|-1\rangle+i|0\rangle}{\sqrt{2}}$ state. The positive Bloch sphere shows the final states of the (-1,1,-1) and (1,-1,-1) NVs, $\frac{|0\rangle+|+1\rangle}{\sqrt{2}}$ and $\frac{|0\rangle+i|+1\rangle}{\sqrt{2}}$, respectively. The (1,1,1) NV does have limited control with this control field, but the other three remaining NVs may reach any point on either Bloch sphere. This toy model was shown to demonstrate four unique final states.

This is a key demonstration to show the selectivity capabilities for each NV orientation, even given the restraints on the crystal orientation with respect to the control field. While the (1,1,1) state is effectively removed from the output of the experiment, the other three NV orientations may reach anywhere on either the positive or negative Bloch sphere, independently. Thus far, a view of each of the three diamonds has been analyzed for selective control of the NV orientations. The chapter will conclude to summarize the abilities of selective control on each of the three diamond orientations with the same microwave field configuration.

3.3.4 Target State Overlap Summary for Selective Control

As with the collective control on each of the (100), (110) and (111) diamonds, the selective control for each of these diamonds may be summarized. A table containing the summary of target state-to-state overlap achieved for selective single transition control pulses is shown in table 3.15. The selective transitions were tested with $|0\rangle \rightarrow |+1\rangle$ or $|-1\rangle$ while the other orientations were kept at the $|0\rangle$ state. The (100) diamond is treated as two sub-ensembles as opposed to having four orientations of NVs, which allows the target state overlap of 0.99 to be reached. The (110) diamond demonstrated individual control of each NV orientation allowing select NVs to be rotated to the single transition while the other three orientations remained in the $|0\rangle$ state. The (111) diamond is unable to achieve the target state overlap while including the (1,1,1) NV orientation as it only sees a linear field, so single selective transition is not possible. If this orientation is removed by being kept at the $|0\rangle$ state, the other three orientations may be individually rotated.

Table 3.15: Pulse target state overlap for selective single transitions to the $|+1\rangle$ or $|-1\rangle$ states for all diamond single crystals. The (100) and (110) diamond are able to achieve selective pulses for the two pairs of NVs in the (100) diamond and all orientations in the (110) diamond. The (111) diamond is able to achieve selective pulses for all orientations with the exception of the (1,1,1) orientation.

	(100)	(110)	(111)
	$\|+1\rangle \rightarrow$ 0.990073	$\|+1\rangle \rightarrow$ 0.992715	$\|+1\rangle \rightarrow$ 0.875 Except(1,1,1)$\rightarrow$ 0.990668
	$\|-1\rangle \rightarrow$ 0.991981	$\|-1\rangle \rightarrow$ 0.993158	$\|-1\rangle \rightarrow$ 0.875 Except(1,1,1)$\rightarrow$ 0.990461

The summary of target state overlap achieved for selective $\frac{\pi}{2}$ like pulses is shown in table 3.16. In this example, a transition to either the $\frac{|0\rangle+|+1\rangle}{\sqrt{2}}$ or $\frac{|0\rangle+i|+1\rangle}{\sqrt{2}}$ was attempted for one of the NV orientations while the others were given a final state of $|0\rangle$. The same trends were seen as previously, the (100) diamond being able to rotate single orientations selectively. The target state overlap of 0.99 is achieved when control is given only to each pair of ensembles, not all four orientations, while the other two are allowed to evolve freely under the designed pulse. If all four are targeted, a state overlap of 0.92 was reached.

It is clear that for a field aligned along the "x"-"z" axes in the lab frame, the (110) diamond is the most optimal to use for selective control. The (111) diamond is able to optimize over three of the four orientations, again useful for many applications. Also recall that while the phase of the $\frac{\pi}{2}$ pulses in the (100) diamond are not the desired phase, the populations are still the desired populations, so there are applications in which this pulse would be useful for experiments that can differentiate the phase picked up from each orientation, while keeping the other sub-ensembles in the identity state.

Table 3.16: Pulse target state overlap for the selective $\frac{\pi}{2}$ pulses, and $\mathbb{1}$ on others for each of the diamond crystals. Recall the (100) diamond achieves the correct population distribution, but incorrect phase. The (110) diamond is able to achieve $\frac{\pi}{2}$ for all select orientations, and the (111) diamond is able to achieve for all orientations except the (111) orientation.

(100)	(110)	(111)
$\overline{x} \rightarrow 0.992039$	$\overline{x} \rightarrow 0.99083$	$\overline{x} \rightarrow 0.9375$ Except(1,1,1)$\rightarrow 0.990013$
$y \rightarrow 0.99452$	$y \rightarrow 0.990143$	$y \rightarrow 0.9375$ Except(1,1,1)$\rightarrow 0.992558$

In the examples, $\frac{\pi}{2}$ like pulses were shown as it is an easy way to visually gauge the success of the pulse in addition to using the state overlap as a metric of success. For the (110) and three of the four orientations of the (111) diamond, complete access to anywhere on the positive and negative Bloch sphere is possible, but more difficult to visually indicate, so they were not shown in these toy examples.

These two tables are not an exhaustive list of the capabilities of the OCT pulses, but do provide a summary demonstrating the reach of the controls. Combined with the collective control summary, the intuition for the OCT pulses with this microwave configuration and three diamond crystals may be gained.

Simulations to the experimental setup

This chapter described how a control Hamiltonian may be written for any general NV orientation in a single crystal diamond, expanding to an ensemble of NVs within one diamond. Two independently controlled channels may be used to implement the control Hamiltonian. An example configuration was shown, featuring two parallel microstrips, to achieve OCT pulses. The features of the OCT controls simulated for the (100), (110) and (111) diamonds were shown with key examples, comparing cases were the same target state-to-state transfer is desired for all NV orientations, or selective control of each orientation. Compared to previous results, it was also shown that a random position of the NV ensemble does not impede the performance of the pulses, being able to find the target pulse for any position relative to the microstrips.

The (110) diamond was shown to be the most suitable crystal for this configuration of control field, capable of achieving any unique target state-to-state transfer for collective or selective NVs. If it is desired to have control over all four orientations uniquely, the (110) is most desired. The (111) diamond was shown as an interesting case to compare how OCT pulses may be implemented with only linear control on the (1,1,1) NV, and circular polarization on the other orientations. The (111) diamond may also be chosen because of its differing angle of orientation relative to the surface, compared to the other crystals. The (100) diamond possesses helpful symmetries, with this microwave field configuration, which reduces the orientations from four to two effective pairs, a very useful testbed to implement the pulses. The (100) diamond will be used for the experimental setup to implement the pulses in chapter five.

The following chapter will present the experimental setup required to implement the OCT pulses. A detailed account of the design and characterization of the optical and microwave configurations for NV ensemble experiments will be given.

Chapter 4

Experimental Setup

This chapter presents the experimental setup, capable of studying nitrogen vacancy (NV) ensembles. This chapter is divided into three main sections. First the optical layout of the experimental setup is explained. Following the description of the optical layout, the next section will describe the requirements of the beam power, collimation, profile, diameter and polarization for NV ensemble work. The final section describes both the layout and characterization of the microwave portion of the apparatus.

Two separate control systems are required to manipulate the optical and microwave transitions of the NV centers. This is realized through having an optical table controlling all incoming and detected photons from the NVs, while the top layer of the system houses all the microwave components. Figure 4.1 shows a picture of the complete setup. While this system is currently in use for NV ensemble measurements, it was designed to be easily adaptable to study single NV centers.

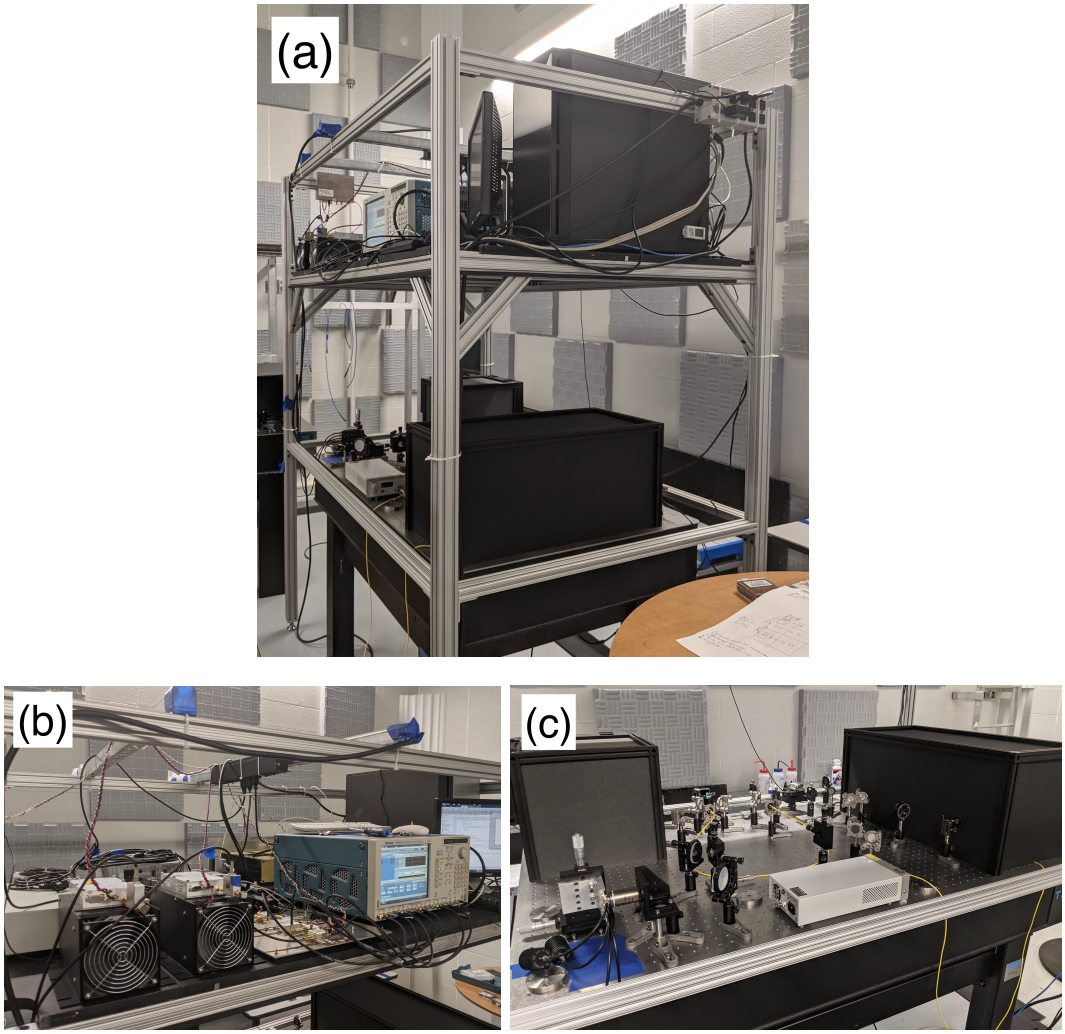

Figure 4.1: A picture of the complete system, with a more detailed photo of the optical and electronics layout. **(a)** The whole system, split into two levels, with the optics on the bottom floating table, while the electronics controlling all the active optical components and microwave components are placed on top. **(b)** Shows a view of the components required for microwave control while **(c)** shows a view of the optical table.

4.1 Experimental Setup Optical Requirements

The optical modules featured in this setup are the laser box, switch arm, mode shaping arm, scanning optics and detection box. Figure 4.2 shows the block layout containing each of these sections. The laser box generates the beam. A double pass switch arm follows, containing an optical switch for fast switching times and provides a high contrast between the ON and OFF intensity. Control of the polarization is used as a technique to re-direct the beam with a polarizing beam splitter (PBS) within the switch arm to save space on the optical table. From the switching arm, the mode shaping arm re-shapes the Gaussian beam and selects the desired polarization required for the NV ensembles. A dichroic mirror at the end of the mode shaping arm reflects green light into the scanning optics. Upon passing through the scanning optics, the green light excites the NVs, which then fluoresce with red light. This red light passes back through the same beam path as the incoming light, and then transmits through the dichroic mirror into the detection box. The detection box uses a pinhole as a spatial filter for unwanted emitters, and is then focused onto an avalanche photo diode (APD).

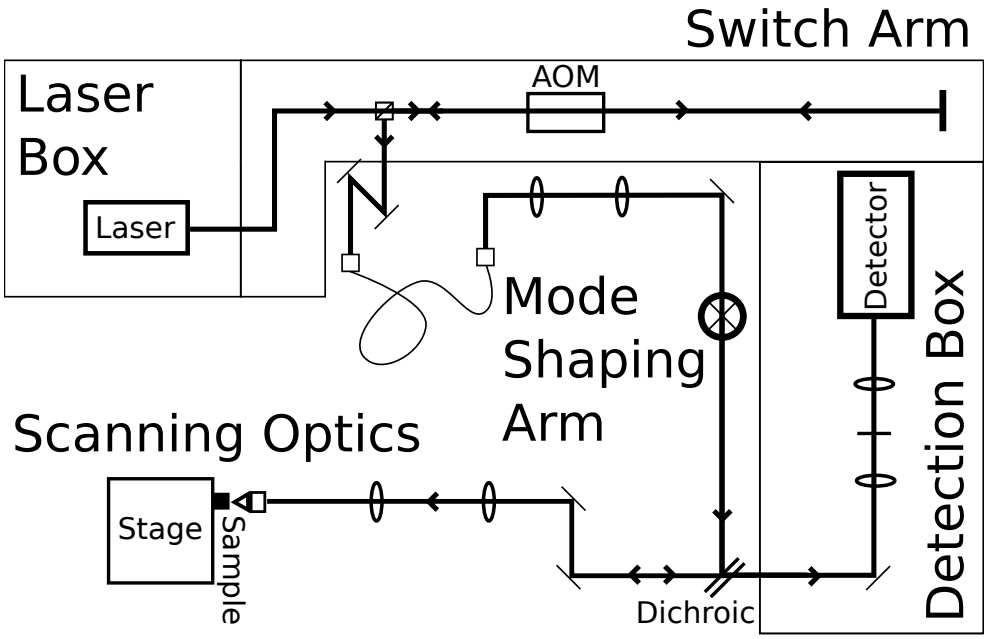

Figure 4.2: The block layout of the optical setup. The laser box generates a continuous beam at 532nm. A double pass switch arm contains the optical switch, used for its fast switching times and large contrast ratio between the ON and OFF intensity. The mode shaping arm corrects for beam shape aberrations as well as sets the desired optical polarization of the beam. The scanning optics focus the beam into the diamond sample, exciting the NVs with green light. The detector box collects the emitted red photons from the sample.

The figure above only shows the main components of each of the modules. Its purpose is to show how the main modules fit together and gather a sense for the general flow of the beam in the optical setup.

4.1.1 Laser Box

The laser box generates the beam, establishing its initial power, shape, collimation, diameter and polarization conditions. The layout of the laser box is shown in figure 4.3, followed by the table of associated parts in table 4.1. The laser model is a Coherent, Ti-sapphire laser, emitting up to 100 mW of light at 532 ± 2 nm. An attenuation wheel is used to attenuate the initial power of the beam, most often for alignment. It may also be attenuated for some experiments which desire a lower laser power to not overwhelm the photon count of the detector, or have an unwanted high level of reflected green light, lowering the output photon contrast. The telescope in the laser box expands the beam by two times its original diameter. This is done to satisfy the beam diameter requirements in the switch and mode shaping arm.

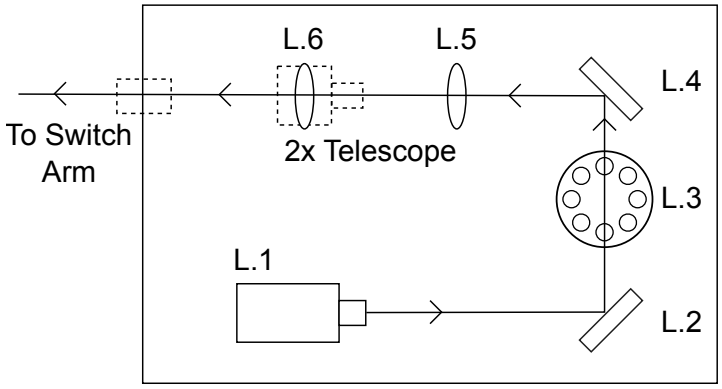

Figure 4.3: The layout of the laser box. The laser (L.1) supplies a Gaussian beam at 532 nm, up to 100 mW. The beam may be attenuated for alignment or some experimental purposes that desire a lower laser power by an attention wheel (L.3). A telescope (L.5/6) expands the diameter of the beam by two times.

Table 4.1: Laser Box components corresponding to figure 4.3.

List of Components By Block			
Label	**Component Name**	**Make**	**Part No.**
L.1	Laser	Coherent.	532-100 CW S/N 1176686
L.2	Mirror	Thorlabs Inc.	BB1-E02
L.3	ND Filter wheel	Thorlabs Inc.	FW1A
L.3A	ND Filters	Thorlabs Inc.	$50\% : NE03A$, $31\% : NE05A$, $25\% : NE06A$, $5\% : NE13A$, $1E-4\% : NE60A$
L.4	Mirror	Thorlabs Inc.	BB1-E02
L.5	Lens (f=50 mm)	Thorlabs Inc.	LA1131-A
L.6	Lens (f=100 mm)	Thorlabs Inc.	LA1509-A

4.1.2 Switch Arm

The beam exits the laser box and enters the switch arm, beginning with two mirrors redirecting the beam towards the optical switch. The switch arm contains the optical switch for the setup, in a double pass design, with a forward and backward pass. The double pass design improves both the contrast between the ON and OFF ratio of incoming power to the NV centers and is also used to save space. The layout and associated parts for the switch arm are shown in figure 4.5 and table 4.2, respectively.

On the forward pass, the beam is accepted from the laser box, and passes through a half wave plate (HWP) followed by a PBS. The PBS passes p-polarized light, and reflects s-polarized light. After passing through the PBS on the forward pass, the light is focused into the optical switch, an acousto-optic modulator (AOM), via a telescope, and re-collected on the opposite side of the AOM. Modulating the AOM changes the refractive index in the crystal, controlling its ON and OFF conditions. When OFF, the AOM simply passes the incoming 0^{th} order beam. When ON, it diffracts into multiple orders. Figure 4.4 shows the diffracted beams through the AOM. The switch arm is designed to select the 1^{st} order beam path, and block all others, when the AOM is ON.

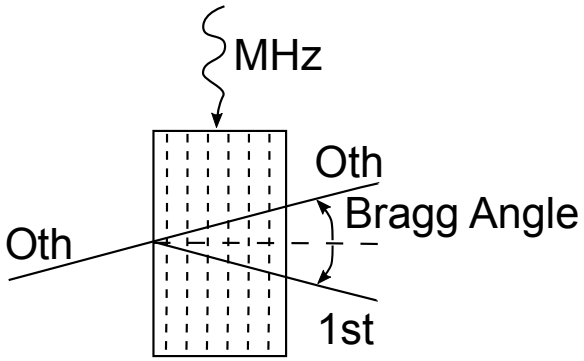

Figure 4.4: The concept of an acousto-optic modulator (AOM). The AOM contains a piezo crystal in the inner medium. The refractive index of the crystal changes when an acoustic wave is applied. When a beam enters the medium, while it is being modulated, the beam diffracts into multiple orders, with each order diverging at the Bragg Angle from the normal. The beam which follows along the original path is called the 0^{th} order beam. The distance between the 0^{th} and 1^{st} order is two times the Bragg Angle ($2\Theta_B$). The 1^{st} order beam is selected in the setup by placing an iris to block the 0^{th} order beam and pass the 1^{st} order.

After passing through the AOM, the beam travels through a quarter wave plate (QWP), reflecting off a mirror and passes through the same QWP again, resulting in a rotation of the polarization from p to s-polarized light. On the back pass of the switch arm, the beam passes back through the AOM, and toward the PBS. With the rotated polarization, the PBS now reflects the s-polarized light into the mode shaping arm. An iris in the mode shaping arm acts with the same purpose as the one in the switch arm, blocking the 0^{th} order beam, and selecting the 1^{st} order beam from the back-pass of the AOM.

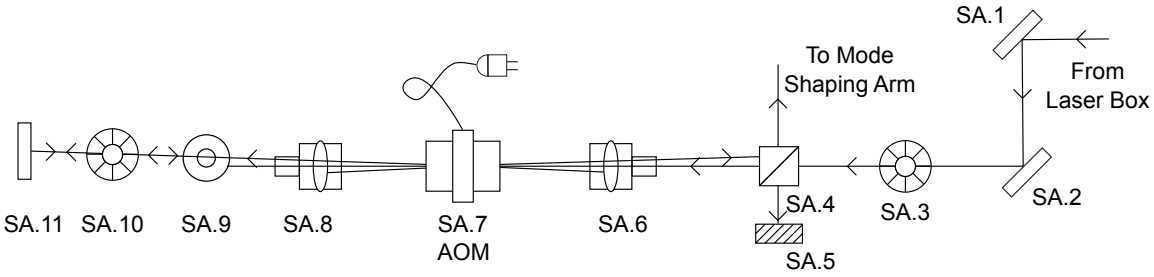

Figure 4.5: The layout of the switch arm. The beam enters from the laser box, travels through a HWP (SA.3) and then PBS (SA.4), which transmits p-polarized light and reflects s-polarized light. The AOM (SA.7), is the optical switch. A lens (SA.6) focuses the light into the AOM, while another lens (SA.8) on the back side re-collimates the light. When turned on, the AOM diffracts the beam into multiple orders. The zeroth order is blocked while the first beam is passed by an iris (SA.9). The first order diffracted beam passes through a QWP (SA.10), rotating the polarization of the beam by 45°. Hitting a mirror (SA.11) and passing back through the QWP rotates it a further 45° so the beam is now s-polarized on the back pass. When the beam hits the PBS once more, it now reflects into the mode shaping arm. The act of passing through the AOM twice is known as a double pass switch arm, and is used to improve the ON:OFF ratio of the beam intensity.

Table 4.2: Switch Arm components corresponding to figure 4.5.

List of Components By Block			
Label	**Component Name**	**Make**	**Part No.**
SA.1	Mirror	Thorlabs Inc.	BB1-E02
SA.2	Mirror	Thorlabs Inc.	BB1-E02
SA.3	Half Wave Plate @ 532 nm	Thorlabs Inc.	WPH05M-532
SA.4	Polarizing Beam Splitter	Newport	05BC16PC.3
SA.5	Beam Blocker	Thorlabs Inc.	LB1
SA.6	Lens (f=175 mm)	Thorlabs Inc.	LA1229-A
SA.7	AOM	Isomet	1250C-848
SA.8	Lens (f=150 mm)	Thorlabs Inc.	LA1433-A
SA.9	2” Iris	Thorlabs Inc.	ID25
SA.10	Quarter Wave Plate @ 532 nm	Thorlabs Inc.	WPHQ05M-532
SA.11	Mirror	Thorlabs	BB1-E02

4.1.3 Mode Shaping Arm

The mode shaping arm cleans up any spatial aberrations from the laser and switch arm, and selects the incoming polarization for the NV ensembles. The layout and corresponding parts for the mode shaping arm are shown in figure 4.6 and table 4.3, respectively. The iris at the beginning of the mode shaping arm is used to select the 1^{st} order diffracted beam from the AOM, an overhang from the switch arm. Of course this may be done in the switch arm, but for spatial reasons, the iris was placed in this position. Two alignment mirrors direct the beam into the single mode fiber (SMF) with associated fiber couplers on either side. The SMF allows only one spatial mode of light to pass through the core, acting as a filter and correcting any spatial aberrations accumulated from the laser and switch arm. It is important the beam has a circular profile heading into the objective because it evenly distributes the power of the beam along the radius of the beam, close to an ideal Gaussian beam.

Following the SMF, a telescope is used to expand the size of the beam by two times. Expanding the beam satisfies both the diameter requirements of the scanning optics and detection box. Two alignment mirrors direct the beam into a HWP, used to correct for a random polarization error induced by the SMF and to select the desired polarization for the NV ensembles.

The final component of the mode shaping arm is the dichroic mirror, which reflects one colour and transmits another. In this case, the dichroic mirror reflects green and transmits red. The incoming beam of green light is reflected off the dichroic mirror and into the scanning optics along the excitation path to excite the NVs. The emitted red light from the NVs will travel back along the same path in the scanning optics, but upon intersecting with the dichroic mirror, will transmit through and into the detection box.

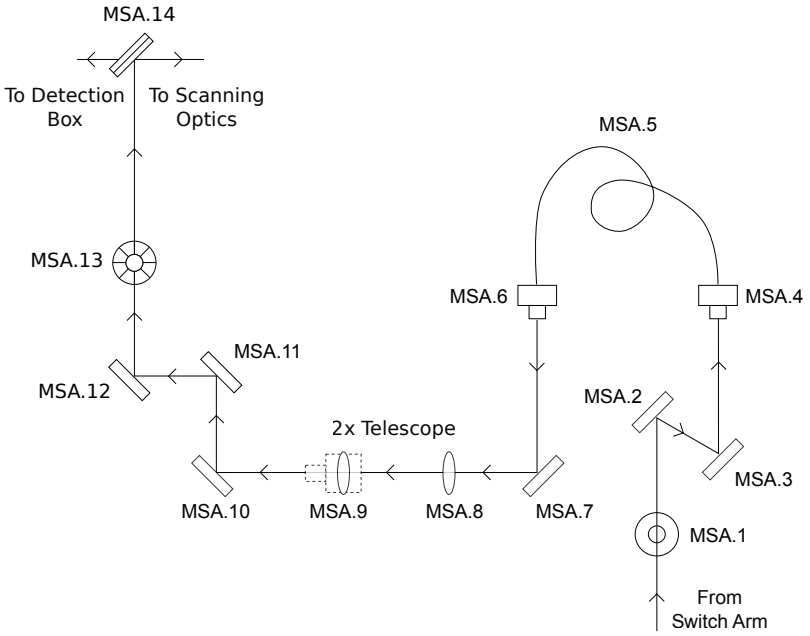

Figure 4.6: The layout of the Mode Shaping Arm. The Mode Shaping Arm corrects for aberrations in the beam shape, sets the desired polarization for the experiments, and uses a dichroic mirror to re-direct the green light into the scanning optics, later used to transmit red light into the detection box. Aberrations in beam shape are corrected using a SMF (MSA.4), which allows only one spatial mode of the light to pass. The beam is then expanded by a telescope (MSA.8/9) beyond the fiber, important to satisfy the size requirements of the scanning optics and detection box. A HWP (MSA.13) is placed after the telescope to both correct for the polarization errors induced from the fiber and select a polarization that is optimal for the NV ensemble. Once the beam has the correct shape and polarization, it then hits the dichroic mirror (MSA.14), which is reflected into the scanning optics.

Table 4.3: Mode Shaping Arm components corresponding to figure 4.6.

List of Components By Block			
Label	**Component Name**	**Make**	**Part No.**
MSA.1	1" Iris	Thorlabs Inc.	ID12
MSA.2	Mirror	Thorlabs Inc.	BB1-E02
MSA.3	Mirror	Thorlabs Inc.	BB1-E02
MSA.4	Fiber Coupler	Thorlabs Inc.	F240FC-A 543 nm
MSA.5	Single Mode Fiber	Thorlabs Inc.	P1-460B-FC-1
MSA.6	Fiber Coupler	Thorlabs Inc.	F240FC-A 543 nm
MSA.7	Mirror	Thorlabs Inc.	BB1-E02
MSA.8	Lens (f=50 mm)	Thorlabs Inc.	LA1131-A
MSA.9	Lens (f=100 mm)	Thorlabs Inc.	AC-254-100-A
MSA.10	Mirror	Thorlabs Inc.	BB1-E02
MSA.11	Mirror	Thorlabs Inc.	BB1-E02
MSA.12	Mirror	Thorlabs Inc.	BB1-E02
MSA.13	Half Wave Plate @ 532 nm	Thorlabs Inc.	WPH05M-532
MSA.14	Dichroic Mirror	Semrock	LPD01-532RS-25

4.1.4 Scanning Optics

The dichroic mirror reflects the incoming green light from the mode shaping arm into the scanning optics. At this point, the beam has now been corrected for spatial aberrations, is able to be switched on and off, the majority of the power loss through the system has been accounted for, and the polarization may be changed to suit the selected NVs. The scanning optics is now used to re-size the beam to the requirements for the chosen objective and focus it onto the NV sample. It contains the stage and NV sample, mounted atop the PCB board which delivers the microwave control field. It is the point at which the optical and microwave control setups meet.

The layout and corresponding table of parts for the scanning optics are shown in figure 4.7 and table 4.4. The dichroic mirror is shown in the layout for context in the scanning optics. Similar to the switch arm, the scanning optics have both a forward and backward pass, in this case referred to as the excitation and emission paths. The NVs are excited from the green light reflected off the dichroic mirror, passing through the scanning optics telescope and objective toward the sample. The telescope used in this module expands the beam by approximately three times, to overfill the back of the objective. When the objective is overfilled, the intensity of the power transmitting through the objective is more uniform, approaching a planar profile, essential for the initialization and readout of the NVs. It also ensures that the beam exiting the objective is collimated. To overfill, the beam is sized such that the diameter of the beam exceeds the diameter of the back of the objective. If the beam is set to be larger than this size, there is just more power loss, but the power would be more uniform through the objective. This setup was built to be a hybrid system, capable of being used for high and low density diamonds and for both ensemble and individual NVs, which requires two objectives to be used interchangeably. Therefore, the beam was expanded to be compliant with overfilling a 10x Nikon air-objective, with the diameter at the back of the objective being 12 mm. A 100x Nikon oil-immersion objective may be swapped (back diameter of 5.2 mm), with a minor loss in overall power to the NVs, without having to change the telescope of the scanning optics. A 10x objective would of course capture more NV centers, but the inhomogeneity due to the increased spot size (52 μm) depth and (2.71 μm) diameter for the 10x compared to (2.51 μm) depth and (0.59 μm) diameter for the 100x is an added experimental challenge, so the majority of the experiments were performed with a 100x objective.

As the excitation and emission paths of the scanning optics must support two different wavelengths of light, it is important the scanning optics are built so that the green and red paths are both collimated and overlap for the entire the beam path. If this does not happen, the microscope will lose its confocal ability, focusing the green and red at two different focal points. To accomplish this in practice, a red diode alignment laser is directed backwards through the detection box and scanning optics, while the green light is simultaneously directed from the green laser through the rest of the setup. Removing the objective from the scanning optics, the spatial overlap and collimation of the two paths are checked over many meters by deflecting the beam path with multiple mirrors.

The sample is mounted atop a PCB board, fixed to a three axis stage with manual actuators. For more precise measurements, piezo controlled stages may be added with no interference to the setup, however for the experiments performed, these were not required.

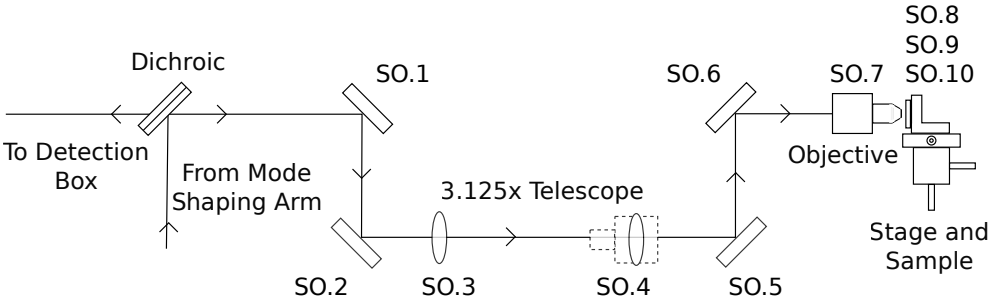

Figure 4.7: The layout of the scanning optics. The scanning optics contain the objective, diamond sample and stage. The green light comes in from the mode shaping arm, passing through the alignment mirrors (SO.1/2), telescope (SO.3/4) and into the objective (SO.7) to excite the NVs. The sample (SO.8) sits on atop a PCB board with two microstrips and mounted to a stage controlled by manual actuators. Once excited with green light, the NVs emit in the red spectra, which pass back through the same beam path and now transmits through the dichroic mirror into the detection box. It is important the scanning optics are built so that the green and red paths are both collimated and overlap for the entire length of the beam path. The telescope is used to expand the beam to overfill the objective. This system was built such that a 100x and 10x objective may be exchanged. With an objective with lower magnification, the volume of NVs increases greatly. For the chosen sample, the number of NVs was sufficient such that a 100x objective was used, so a smaller volume could be accommodated.

Table 4.4: Scanning Optics components corresponding to figure 4.7.

List of Components By Block			
Label	**Component Name**	**Make**	**Part No.**
SO.1	Mirror	Thorlabs Inc.	BB1-E02
SO.2	Mirror	Thorlabs Inc.	BB1-E02
SO.3	Lens (f=80 mm)	Thorlabs Inc.	AC254-080-A
SO.4	Lens (f=25 mm)	Thorlabs Inc.	AC254-250-A
SO.5	Mirror	Thorlabs Inc.	BB1-E02
SO.6	Mirror	Thorlabs Inc.	BB1-E02
SO.7	100x oil immersion objective	Nikon	Plan Fluor 100x/1.30 N.A (D.O.F 2.51 μm and min beam diameter 0.59 μm)
SO.8	Diamond Sample	Element Six Technologies	DNV-B1 (3×3×0.5 mm)
SO.9	PCB Sample Board	Home Built printed on Laminate (Rogers Corporation)	Laminate: TMM10i (0.76 mm thick)
SO.10	3 axis manual stage	Thorlabs Inc.	3x PT1

A picture of the diamond, PCB board and objective while the laser is on is shown in figure 4.8. The microstrips, two input and two output ports from the PCB board are visible. The sample beneath the objective appears to be entirely bathed with green light, however, only a small spot size of depth 2.51 μm and diameter 0.59 μm is actually in the focal point of the objective. Outside this focal volume, the intensity of the beam is very small, so only NVs within the focal volume are considered as part of the ensemble. Visible in person, stray red light emitted from the NV centers is seen on the edges of the diamond.

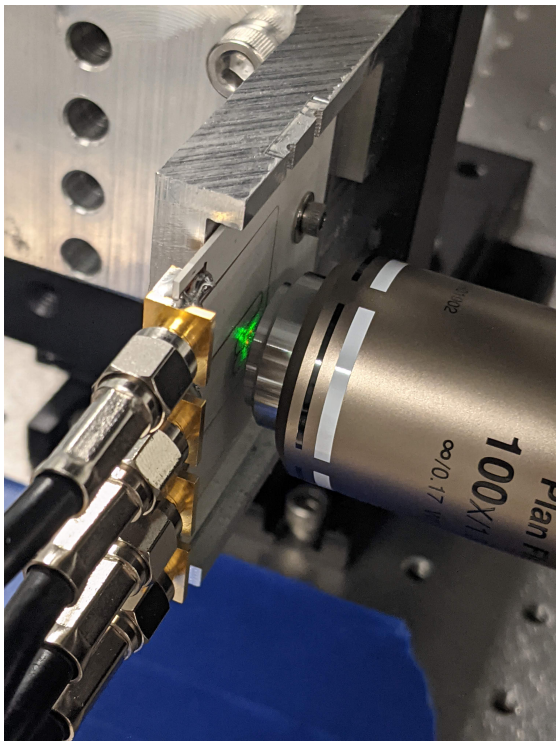

Figure 4.8: A picture of the mounted sample, objective and PCB board. The picture shows a large swelling of green light on the sample, but only those NVs that lie within the focal volume with depth of field 2.51 μm and diameter 0.59 μm are considered part of the ensemble. Most of the excess green light cannot be collected by the objective. The intensity of the green light that is re-collected by the objective is reduced by a knotch and long pass filter. The pinhole also blocks light from outside the focal point.

Mapping the intensity of the Gaussian Beam within the sample

The intensity of the Gaussian Beam may be mapped to gain an estimate for the number of NVs in the focal volume of the objective. The intensity of a Gaussian beam $I(r, z)$, is a function of the radial, (r) and axial, (z) distance away from the focal point (r=0,z=0), [98]:

$$I(r, z) = \frac{\omega_o^2}{w(z)} e^{\left(\frac{-2r^2}{w(z)^2}\right)} \tag{4.1}$$

ω_o is the minimum beam waist at the focal point (z=0), shown below.

$$\omega_o = \frac{\lambda}{\pi\theta_o} = 0.297 \pm 0.001 \ \mu\text{m} \tag{4.2}$$

$\lambda = 532 \pm 2$ nm is the incoming wavelength and $\theta_o = \arcsin\left(\frac{NA}{n_d}\right)$ is the minimum beam diameter half angle, NA= 1.3 is the numerical aperture of the objective and $n_d = 2.41$ is the refractive index of the diamond.

$w(z)$ describes how the beam waist expands as a function of z, the axial distance away from the focal point.

$$w(z) = \omega_o \sqrt{1 + \left(\frac{z}{Z_R}\right)} \tag{4.3}$$

The Rayleigh length, Z_R, is the point the beam waist has increased to $\sqrt{2}\omega_o$ and the peak intensity along the optical axis (r=0) is half the maximum value. Z_R is a function of the minimum beam waist (ω_o), the refractive index of the medium ($n_d = 2.41$) and the wavelength ($\lambda = 532 \pm 2$ nm) of light:

$$Z_R = \frac{\pi\omega_o^2 n_d}{\lambda} = 1.257 \pm 0.005 \ \mu\text{m} \tag{4.4}$$

Within the Rayleigh length, the beams' waist reduces to the minimum beam waist in accordance with $w(z)$. Outside the Rayleigh length, the beam expands linearly. The degree of the divergence is given by the beam divergence angle (θ_z):

$$\theta_z = \frac{\lambda}{\pi n_d \omega_o} = 13.5^\circ \tag{4.5}$$

Figure 4.9 shows the Gaussian Beam intensity at the focal point of the objective. The minimum beam waist (ω_o) and Rayleigh length (Z_R) are illustrated. The depth of the field is defined as twice the Rayleigh length, $\pm Z_R$ away from the center of the beam, (z=0). The minimum beam diameter is twice the beam waist, $\pm\omega_o$ away from the center (r=0). For the 100x oil immersion objective being used, the beam diameter is 0.594±0.002 μm and the depth of field is 2.514±0.009 μm.

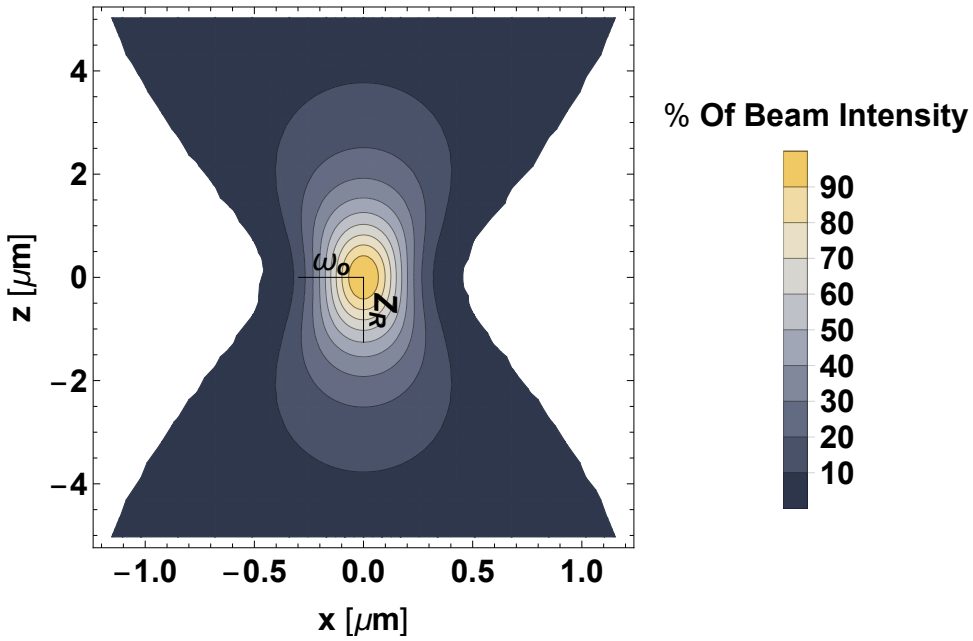

Figure 4.9: The intensity of a Gaussian Beam at the focal volume of the objective. The beam diameter is twice the minimum beam waist, ω_o. The depth of the field is twice the Rayleigh length Z_R. For the 100x objective being used, the beam diameter is 0.594±0.002 μm and the depth of field is 2.514±0.009 μm. At the Rayleigh length, along the optical axis, the intensity of the beam is 50% of the intensity at the maximum. At the edge of beam waist, the intensity is $\frac{1}{e^2}$ of the maximum at the center.

The intensity of the beam is maximized at the center of the beam (z=0,r=0). Away from this center, the intensity follows a Gaussian pattern along the radial and axial directions. Along the axial direction (r=0), at the Rayleigh length, Z_R, the intensity is reduced to half compared to the center. Along the radial direction (z=0), at the beam waist, (ω_o) away from the center, the intensity is $\frac{1}{e^2}$ of the maximum.

Figure 4.8 showed a large swelling of green light surrounding the diamond. It is important for only the NVs inside the focal volume to be excited. Figure 4.9 showed how quickly the intensity decayed away from the focal volume. Just 4 μm away from the focal point in the axial direction, and 0.5 μm away from the focal point in the radial direction, the intensity of the beam is only $\approx 1\%$ of the maximum.

Figure 4.10 puts the intensity beyond the focal volume into context, showing the relative sizes between the objective (grey trapezoid), microstrips (black lines) and diamond.

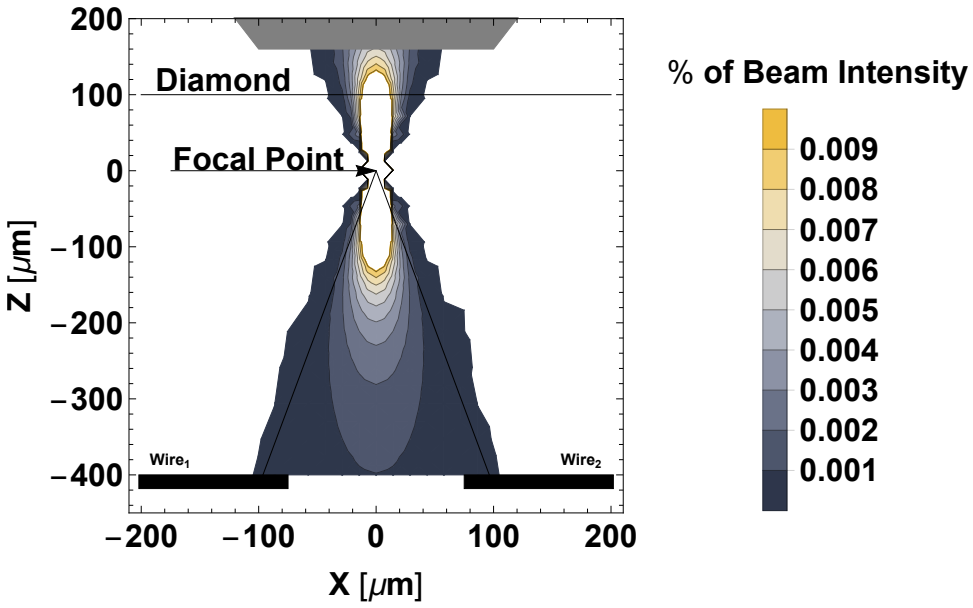

Figure 4.10: The simulated image shows the beam being focused into the diamond sample, indicating relative sizes of the diamond, PCB microstrips and NVs within the spot size of the objective. While there is swelling of the green light observed, the intensity of this quickly decays outside the focal volume. At $z = 120$ μm and $r = 15$ μm away from the focal point, this intensity is only $\approx 0.01\%$ of the maximum intensity.

The thickness of the (100) diamond used for the experiments is 500 μm, far exceeding the working distance of the objective (160 μm). Assuming there is a small droplet of oil with thickness $\approx$ 60 μm between the objective and the surface of the diamond, the objective would focus about 100 μm into the diamond. In the x direction, the focal point has been placed halfway in between the microstrips, spaced 150 μm apart. For this model, the change in beam divergence from the objective to the diamond is not shown, and the travel of the beam has been calculated as if existing in only the diamond.

The figure shows the swelling of the beam outside the focal point. The triangle indicates the linear divergence at θ_z away from the focal point. Although the swell of the beam looks large, the intensity of the beam is only up to $\approx$ 0.01% of the maximum beam intensity, within 120 μm axially, and 15 μm radially of the focal point. Within 40 μm axially and 10 μm radially, this only increases to $\approx$ 0.1% of the intensity. Only the NVs within the focal volume, have a beam intensity great enough to be excited and initialized for the experiment.

Collecting the NV emission

It is also important to consider the capture of red light emitted from the NVs. As the NVs emit in a sphere, half of the photons will be lost due to being pointed away from the objective. In addition, not all the photons emitted toward the objective will be captured. Diamond is a material with a high refractive index, (n $= 2.41$). When light travels from a high to a lower index material, only a portion of the photons will pass through from one medium to another. Any photons outside the critical angle will be reflected back into the diamond, due to total internal reflection. The critical angle is $\theta_c = \arcsin\left(\frac{n_2}{n_1}\right)$, where n_1 is the refractive index of the materials the photons start in, and n_2 is the medium the photons are travelling into.

An oil-immersion lens is used to help increase the critical angle between the diamond and the objective. Not shown in the figure 4.10 is the oil added in between the objective (grey trapezoid) and diamond surface. Oil is added to reduce the contrast between the refractive index of the diamond and the objective, and therefore increase the amount of photons collected by the NVs. In the absence of the oil, travelling from diamond (n= 2.41) to air (n= 1), a critical angle of 24° passes photons from the diamond to air. With an oil-immersion lens (n= 1.3), this angle is increased to 32°. This roughly increases the amount of photons accepted into the objective by 1.75x.

Estimating the Number of NVs within the focal volume

The intensity of the Gaussian beam is clear in determining that only the NVs within the focal volume may be initialized and used in experiments. Outside this volume, the intensity is so low, the centers are not useful for experiments.

The focal volume can be approximated by a cylinder of length equal to the depth of field (DOF) (DOF $= 2.514 \pm 0.009$ μm) and diameter equal to the beam diameter ($2 \times \omega_o = 0.594 \pm 0.002$ μm), giving a total volume of $V_f = 0.6978 \pm 0.007$ μm^3.

To find the number of NVs within this ensemble, the concentration of NVs within the sample being used must be accounted for.

The lattice constant of a diamond is $a_o = 3.57$ $\mathring{A}$ at 300K, [96]. As the lattice is a cubic structure, the total volume of the unit cell is $a_o^3 = 4.54 \times 10^{-11}$ μm^3.

To find the mass of Carbon within the unit cell, recall there are 8 atoms within the unit cell. Assuming they are all Carbon atoms, the total mass of Carbon (mC) in kg, within the unit cell is:

$$\begin{aligned} \text{mC} &= \frac{\text{MC} \times \text{NC}}{\text{NA}}/1000 \\ \text{mC} &= 1.59 \times 10^{-25} \text{ kg} \end{aligned} \tag{4.6}$$

MC is the molecular mass of Carbon, (12.011 g/mol), [22]. NA is Avogadro's number (6.022×10^{23} $\#/mol$), and NC is the number of Carbons within the unit cell (8), [54, 95].

The mass of Nitrogen within the unit cell is given by the concentration relationship between Carbon and Nitrogen. The sample being used is a (100) orientation, DNV-B1 from Element six, [99, 100]. The concentration of Nitrogen [N] reported is 800 PPB. The mass of Nitrogen (mN) in kg, is given by:

$$\text{mN} = [N] \text{ (PPB)} \times \text{mC (kg)} = 1.28 \times 10^{-28} \text{ kg} \tag{4.7}$$

The number of Nitrogen (NN) atoms within a unit cell is shown below, where MN is the molecular mass of Nitrogen (MN $= 28.014$ g/mol), [22].

$$\mathrm{NN} = \frac{\mathrm{mN} \times \mathrm{NA}}{\mathrm{MN}} = 2.74 \times 10^{-6} \tag{4.8}$$

The conversion rate from Nitrogen to NV centers is typically at a rate of 1%. However, this sample has undergone treatment by the manufacturer, Element Six, to have a higher conversion ratio of 37.5%, reporting NV concentrations of 300 PPB, [99, 100]. This gives the number of NVs per unit cell (nNV) to be 1.029×10^{-6}.

To find the volumetric density of NVs (ρ_{NV}), the number of NVs per unit cell must be divided by the volume of the unit cell

$$\begin{aligned} \rho_{NV} &= \frac{\mathrm{nNV}}{a_o^3} \\ \rho_{NV} &= 22\ 615 \left(\frac{1}{\mu\mathrm{m}^3}\right) \end{aligned} \tag{4.9}$$

The total number of NVs within the focal volume is given by the volumetric density of NVs (ρ_{NV}) multiplied by the focal volume:

$$\#NVs_f = \rho_{NV} \times V_f = 15\ 782 \pm 200 \tag{4.10}$$

In reality, this level of precision for determining the number of NVs is unrealistic for an ensemble of such size. Rather, the calculations are shown as a step by step guide to give an order of magnitude for the number of NV centers. These calculations indicate that the experiments are being conducted with tens of thousands of NV centers, around 15 000 centers.

If it required for experimental purposes to have a more accurate number of centers, the focal volume should be defined as the proper Gaussian shape which has an evolving beam diameter as a function of the depth of field, rather than approximating the volume as a cylinder of height and constant width equal to the DOF and beam diameter, respectively. In addition, measurements on the NV concentration to determine the uncertainties on this number should be conducted.

An estimate of the NVs outside the focal volume, but still within the swell of the beams' path, can also be estimated. Recall that outside the Rayleigh Range, the beam waist expands linearly, at the divergence angle ($\theta_z = 13.5°$). The volume of NVs outside the focal volume can be estimated as a cone with height equal to the difference of between the diamond thickness and the focal depth $hC = \approx 400$ μm and radius $rC = Tan(\theta_z) \times hC = 96$ μm. The cone is outlined in figure 4.10 as a triangle. The total volume of the cone of NVs under these conditions is $\approx 3.89 \times 10^6$ μm^3. The volumetric density of NVs throughout the sample is invariant, so the total number of NVs within this cone is on the order of 1×10^{10}.

While this number seems large, recall that the intensity of the beam here is less than 1% of the intensity at the maximum, and for most of the total volume is much less than 0.01% of the total intensity. So while there are many NVs present within the beam path, these should not contribute to the detected signal as the beam power is so low, they cannot be initialized and read-out within the experimental sequence. The initialization and readout time will be discussed in the chapter five (section 5.3).

The purpose of the scanning optics module is largely focused on exciting the NV ensemble with the incoming green light. However, it is also designed such that it may collect the red light emitted from the NVs and have it travel along the same beam path, without loss of the confocal conditions, and direct it towards the detection box.

4.1.5 Detection Box

The detection box collects the red light emitted from the NV ensemble, and focuses it through the pinhole and into the detector. In many ways, the combination of the scanning optics and detection box do not differ greatly from the original confocal microscope design.

According to the original design by Marvin Minsky in its basic form, a confocal microscope requires a mirror to re-direct the incoming light and a lens to focus onto the desired sample, [72]. The reflected light is sent back through the lens and mirror and focused into a detector. This basic design is adapted, allowing for fluorescent rather than reflective centers, shown in figure 4.11. In place of the pellicle mirror, a dichroic mirror is used to reflect the green light and transmits the red light on the excitation and emission paths. An objective is used in place of a lens to focus into a smaller spot size, and a pinhole is used as the second focal point to act as a spatial filter for unwanted emitters.

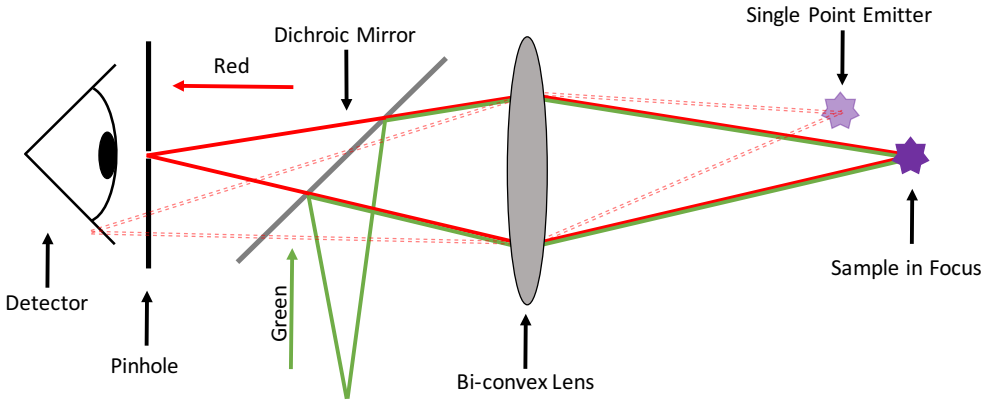

Figure 4.11: The conceptual drawing of a confocal microscope. The scanning optics and detection box form a confocal microscope. A confocal microscope gathers its name from a microscope with two conjugate focal points. The first point occurs at the focal point of the objective and the second at the pinhole. The solid line depicts the ideal beam path, with the sample in focus travelling through the objective (lens) and focused through the pinhole to be collected by the detector. If an unwanted emitter is either outside the focal plane, along the optical axis, or on the focal plane, but outside the optical axis, it will be blocked or out of focus on the conjugate point at the pinhole. The role of the dichroic mirror is also depicted here, reflecting the incoming beam of green light to the excitation pathway and passing the emitted red light through to the pinhole.

The conjugate focal (confocal) points are seen between the sample in focus and the pinhole. If an emitter is off axis in the xy plane, its confocal spot will be focused on the body of the pinhole and will be blocked, while emitters lying along the optical axis, but ahead or behind the focal plane will be focused behind or in front of the pinhole. This results in either being out of focus or having portions of the beam blocked entirely, depending on the size of the pinhole. If the green and red paths differ, this skews the desired focal points, focusing the desired emitters in front or behind the pinhole, which is why great lengths are taken to ensure the green and red paths overlap and focused at the same points.

Expanding beyond the basic components of the confocal microscope, the layout of the detection box is shown in figure 4.12.

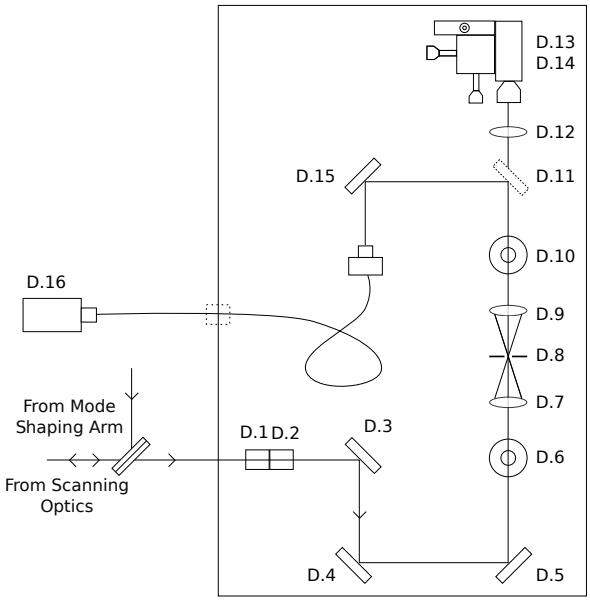

Figure 4.12: The layout of the detector box. To reduce the intensity of stray green light from the scanning optics, a long pass (D.1) and knotch filter (D.2) are added first. A lens (D.7) focuses the beam into the pinhole (D.8), which acts as a spatial filter, blocking unwanted fluorescence from outside the objective's focal point. After the pinhole, the beam is re-collimated by a second lens (D.9) and then focused into the single photon detector (D.13) . To aid with alignment, ensuring the green and red paths of light are overlapping, a red diode laser (D.16) is added to send light backwards through the detection box and into the scanning optics.

First, the emitted red light from the scanning optics passes back through the dichroic mirror and into the detection box. Knotch and long pass filters remove stray green light from the incoming beam, before hitting three alignment mirrors and a lens which focuses the beam into the pinhole. The pinhole acts a spatial filter, blocking any light from unwanted emitters collected by the objective. Following the pinhole, the light is captured by a second lens, re-collimating the beam, before being focused onto the APD. A second beam path is added with a mirror mounted on a flip mount. This beam path is for a red diode laser, used to send red light back through the detection path. This may be used for initial alignment of the lenses and pinhole, and to align the optics in the detector and scanning optics so that the paths for green and red light are overlapped.

Table 4.5: Detection Box components corresponding to figure 4.12.

List of Components By Block			
Label	**Component Name**	**Make**	**Part No.**
D.1	Long Pass Filter	Thorlabs Inc.	LP02-568RU-25
D.2	Knotch Filter	Thorlabs Inc.	NF03-532E-25
D.3	Mirror	Thorlabs Inc.	BB1-E02
D.4	Mirror	Thorlabs Inc.	BB1-E02
D.5	Mirror	Thorlabs Inc.	BB1-E02
D.6	1” Iris	Thorlabs Inc.	ID12
D.7	Lens (f=100 mm)	Thorlabs Inc.	AC254-100-A
D.8	50 μm Pinhole	Thorlabs Inc.	P50D
D.9	Lens (f=100 mm)	Thorlabs Inc.	AC254-100-A
D.10	1” Iris	Thorlabs Inc.	ID12
D.11	Mirror (on flip mount)	Thorlabs Inc.	BB1-E02
D.12	Lens (f=75 mm)	Thorlabs Inc.	AC254-075-A
D.13	Avalanche Photo Diode (APD)	Excelitas	SPCM-AQRH-13
D.14	3-axis stage	Thorlabs	PT3
D.15	Mirror	Thorlabs Inc.	BB1-E02
D.16	Red Diode Laser with fiber and coupler	Thorlabs Inc.	S1FC600

4.2 Characterization of Optical Setup

The optical layout was explained to understand the general function and interconnectedness of each module. This section will not be divided by module, but rather by each aspect of the beam that is critical for the function of the setup. The main beam aspects that will be addressed in this section are the beam power, collimation, profile, diameter, and polarization. Each aspect is explained, its ideal behaviour mapped through the setup, how to measure each and how to tune the setup so it may behave optimally. It is important to understand the health of the optical setup before the sample is mounted, and have tests to measure its function independent of measuring the NVs.

4.2.1 Beam Power

The beam power is a great first litmus test that the microscope is functioning correctly. If unexpected major power losses in the beam are encountered, it could mean a major misalignment, or faulty component, to name a few examples. At the site of the NV, the beam power needs to be at a minimum in order to excite the NVs, and the power across the profile needs to be as uniform as possible. The power across the profile will be explained in more detail in the beam profile section. This piece will focus on the major components affecting the beam power and what minimum is required at the site of the NV centers.

A power meter is placed in the beam path to measure the beam power. The measurement points are outlined in table 4.7. Note that all measurements were conducted with the S120C photodiode power sensor from Thorlabs, which has an uncertainty of $\pm 5\%$ on the measured power in [mW]. This uncertainty applies to all reported measured power values. Beam power measurements may be used to indicate general alignment through passive components, as well as determine if the active components are functioning correctly. If not aligned well, large power losses will be observed as the beam is likely cut on the component. All measurements were done with a power meter and the laser lowered to an eye safe level. All power measurements did have an absolute value associated with them, but a percentage value of power loss is more useful for gauging if the beam power is correct. For example, if the SMF is only translating 5% relative power, it may be better aligned to yield a higher percentage of relative power transmitted through the fiber.

The main aspects that affect the beam power are within the switch arm, single mode fiber and scanning optics into the objective, shown as a summary in table 4.6. Within the switch arm, the AOM diffracts the beam into multiple orders, diverting power from the 0^{th} to the 1^{st} order beam. As the beam passes through the AOM twice, there is significant power loss through the switch arm. For example, if 50% of the power diverts to the 1^{st} order beam on each pass through the AOM, there is a 50% power loss that occurs twice by design. Following the switch arm, the next largest change in power occurs when the beam passes through the single mode fiber, which typically allows transmission ranging up to 50%. Lastly, recall that the telescope in the scanning optics expands the beam to overfill the objective to ensure the beam entering is as close to planar as possible. Overfilling the objective physically cuts the beam, so there is again power loss by design, and additional loss through the transmission of the objective.

Table 4.6: A summary of the theoretical and measured beam power through each section of the microscope. Note that these are relative powers within each section of the setup. The total power loss is defined as the power exiting the laser compared with the intensity emerging from the objective.

Beam Power Measurements				
Label	**Component**	**Purpose of Component**	**Theoretical Power** (%)	**Measured Power** (%)
L.1	Laser	Starting Power	100%	100%
SA.4	Out of Switch Arm	AOM 50% + lens losses	Max: 22%	19%
MSA.7	Out of Fiber	N/A	Max 50%	29%
SO.7	Out of Objective	Account for transmission through the objective and beam loss due to overfilling	Max: 68% ($\frac{1}{e^2}$%) (beam diameter) of 80% transmission	63%
N/A	**Total Power** (%)	Good gauge to measure health of microscope by measuring pre-objective	Max: 7.7%	3.5%

The table shown above details the main aspects of power loss by design through the setup. It is at these points, the setup should be checked if the power appears to be lower than anticipated. Table 4.7 provides a closer look at how the beam power changes through the optical setup in each module. Recall there is a ±5% uncertainty on the measured power value in [mW] given by the S120C (Thorlabs) power sensor used. The labels given to the components are consistent with those described in the the optical layout for each module.

Table 4.7: The theoretical and measured beam power values for each module.

Beam Power Measurements				
Label	**Component**	**Purpose of Component**	**Theoretical Power [mW(%)]**	**Measured Power [mW(%)]**
L.1	Laser	Sets beam power up to 100 mW	10 mW	No measurement
L.3	Attenuation Wheel	Optional Attenuation for the laser. This value was set to the be starting power for alignment (relative 100%).	50%, 31%, 25%, 5%, $1E-4$%	Used 31%, 3.12 mW (Set this as 100%.)
SA.4	Polarizing Beam Splitter	Measure Post PBS on the first pass. Max transmission with p-polarized light.	100%	3.0 mW (96%)
SA.7	AOM (first pass)	Measure through AOM (OFF)	100%	2.82 mW (94%)
–	–	Measure $0^{th}$and 1^{st} order when AOM ON	100%	2.77 mW (92%)
–	–	Power diverted to 1^{st} order	Larger beam → more power to 1^{st}	% Diverted to 1^{st}; 1.11 mW (40%)
–	–	ON:OFF Ratio on 1^{st} order beam	1:0	1.11 mW:2 μW (555:1)
SA.7	AOM (back pass)	Measuring the back pass AOM diversion	–	% Diverted to 1^{st}; 1.11 mW (60%)

Continuation of Table 4.7

Label	**Component**	**Purpose of Component**	**Theoretical Power [mW(%)]**	**Measured Power [mW(%)]**
–	–	Total ON:OFF Ratio on 1^{st} order beam for double pass switch	1:0	0.590 mW: 0.050 μW (11806:1).
SA.4	Total Power through Switch Arm with AOM OFF	Measure when AOM is OFF	100%	0.970 mW(87%)
SA.4	Total Power through Switch Arm with AOM ON	Measure when AOM is ON	22%	19%
MSA.6	Single Mode Fiber	Transmission through the SMF	50% maximum transmission	29% transmission (590 μW:170 μW)
–	–	Take new relative 100% value past the fiber	N/A	155 μW
–	–	ON:OFF Ratio through fiber	1:0	5.10 mW: 0.006 μW (850 340:1)
MSA.9	Transmission through MSA telescope	Poor transmission indicates beam blockage	100% (155 μW)	97% (150 μW)
SO.2	Pre-Scanning Optics Telescope	No large expected changes	100% (150 μW)	97% (145 μW)
SO.7	Objective	10x Objective used for alignment purposes	80% Transmission through objective	63% (90 μW)

Within the laser box, there are only two key components that control the laser beam power. The beam has the relative maximum power at the laser, followed by an attenuation wheel. This wheel is convenient for use for alignment or experiments which require less laser power. The table indicates 100% relative power as the power following the attenuation wheel, as this power loss is set on purpose.

The first component in the switch arm that may affect the power of the beam is the PBS. The PBS passes the portion of the beam which is p-polarized, and reflects s-polarized light. The laser emits s-polarized light, so a half-wave plate placed right before the PBS rotates the polarization to p-polarization to transmit through the PBS. To maximize the power being transmitted through the PBS, a power meter is placed on the other side of the PBS while the half-wave plate is rotated until the maximum is found. Experimentally, this was maximized at 96% of the power emitted from the laser box. Recalling that the polarization rotates from the forward to the backward pass of the switch arm, the PBS is used again as a measure for the quality of the polarization. On the second exit from the AOM, the beam has now been rotated to s-polarized by passing through a QWP twice. When coming back into contact with the polarizing beam splitter, it now reflects the s-polarized beam, into the mode shaping arm. On the forward pass, the half-wave plate is rotated until the beam power passing through the PBS is maximized from the laser. On the backward pass, the quarter wave plate is rotated until the power is maximized reflecting off the PBS into the mode shaping arm. The total power measured through the switch arm was 87% when the AOM was off.

The AOM optical switch diffracts the main incoming beam into multiple orders when ON. Whether the switch is on or off, it always passes a 0^{th} order beam. When on, the optical switch diffracts the beam into multiple orders, separated by twice the Bragg angle of the piezo crystal inside the AOM. In this setup, the 1st order diffracted beam is selected when the switch is "ON" on both the forward and back pass, by placing an iris to block the 0^{th} order and pass the 1^{st} order beam on the front and back pass. The size of the beam heading into the AOM will determine both the switching time of the AOM and how much power diffracts from the 0^{th} to the 1^{st} order when the switch turns on. The smaller the beam heading into the AOM, the less power diverts to the 1^{st} order beam, but the faster the switching time. When aligning the AOM, first the power of the 0^{th} order beam is measured when the AOM is off. When off, the AOM passes 94% of the power. Then the total power of the 0^{th} and 1^{st} order beams are measured when the AOM is on. When on and measuring both the 0^{th} and 1^{st} order beam, 92% of the power is passes through the AOM, indicating there was very little total power loss when the AOM is turned on.

The iris following the AOM was then closed to select only the power diverted to the 1^{st} order beam, finding 40% of the power was diverted from the 0^{th} order to the 1^{st} order. Although the exact size of the beam cannot be determined through measurement because it is too small at the focal point, the amount of power may be used to determine is the beam is on the larger or smaller size heading into the AOM. For example, 55% diffraction to 1^{st} order indicates an 80 μm beam, compared to 90% with a 130 μm beam size. This measurement is repeated on the second pass of the AOM, which diverted 60% from the 0^{th} order to the 1^{st} order beam. Although the beam size may not be measured, the power diffracted to the 1^{st} order beam on the front and back pass were well within the acceptable limits of this microscope, so further adjustments were not pursued.

A double pass switch arm increases the contrast between the "ON" and "OFF" power of the beam because the beam passes through the AOM twice and therefore is diffracted twice. After the first pass, the contrast ratio between the on and off intensity is (555:1), while on the second pass the contrast ratio is (11806:1). It is important to have a large ratio between the ON and OFF intensity so the NVs are not excited when the switch is off. The ON:OFF ratio was also measured following the single mode fiber, which further increased to (850 340:1). To ensure the accuracy of that measurement, the laser had to be increased to full power.

The design of the switch arm does result in the most amount of relative power loss, due to diffracting the beam twice. When heading into the mode shaping arm, the beam is at 19% of the relative beginning power when the AOM is ON. In the mode shaping arm, the largest change in beam power will occur when the beam travels through the single mode fiber. 50% transmission through the single mode fiber is the theoretical maximum transition. 29% was the measured transmission through the fiber. A higher transmission is possible, but the absolute value of optical power was not an issue for this setup, so the alignment was stopped after 29% was reached. The beam power was checked for the remainder of the mode shaping arm telescopes and the scanning optics telescope, and no major losses were observed, with the beam power remaining above 90% the relative value after exiting the single mode fiber. The last instance the beam power was measured was through the objective. The objective has a theoretical maximum of 80% transmission. To have more uniform power intensity through the objective, the beam overfills the back of the objective, so there will be more natural power loss through the objective. 63% of the relative intensity was measured passing through the objective, which includes the effects from overfilling the objective and the transmission losses.

Overall, the final relative power from the laser to the sample was observed to be 3.5%, while the theoretical maximum is 7.7%. The theoretical measurement did not take into account the loss from lenses in theory, which would be about 1% each. Therefore, the theoretical power loss and measured power loss was determined to be sufficient.

It is important to ensure a minimum beam power is met and that power is uniform over the profile of the beam so the NVs may be excited uniformly. However, the ON:OFF ratio of the beam, shape, polarization and collimation are far more important aspects to be considered for the optical setup.

4.2.2 Beam Collimation

The collimation of the beam indicates the degree to which the beam is converging or diverging. In an ideal case, the degree is zero, but in practice, this is not achievable. To mimic a beam that is perfectly collimated, the beam path is extended far beyond the real path and collimated as much as possible. If the divergence or convergence of the beam is very small over the extended distance, it will be effectively collimated over the real beam path.

With the exception of when the beam is being focused through lenses, fiber coupler and the objective, the beam should be collimated at all times. When the beam is not collimated heading into these focusing components, the beam will not focus at the right point along the optical axis. In addition, if the beam is not collimated heading into the objective, the microscope will not satisfy the confocal conditions.

Table 4.8 outlines the key points to check the collimation of the beam, each is either before or after a telescope, or before or after the single mode fiber. To check collimation, multiple mirrors are placed in the beam path to divert and extend the beam path to tens of meters away. The size of the beam is checked before the first mirror and at the end of the path. If the size of the beam does not change over the course of this whole distance, it is collimated. The collimation is set over tens of meters to have minimal errors so that when the beam travels through its set beam path over centimeters, its collimation is as close to ideal as possible. The size of the beam is adjusted by changing the distance between the two lenses of a telescope. In the ideal case, when a collimated beam enters a telescope; if the lenses are distanced at the sum of the focal lengths away from each other, the beam will exit collimated.

Table 4.8: The table corresponds to the key places where it is necessary the beam is collimated. In essence, the beam should be collimated before and after each telescope. A brief description of the purpose of the key collimation pieces are included and will be further expanded upon when the beam diameter is described.

Beam Collimation Measurements		
Label	**Component**	**Purpose of Component**
L.1	Laser	Should be collimated leaving laser head
L.6	Laser Box Telescope	Telescope expands beam before the switch arm
SA.8	Switch Arm Telescope through AOM	Two lenses on either side focus through the AOM
MSA.6	Out of Fiber	If the fiber coupler is functioning properly, the beam should be collimated exciting the fiber coupler
MSA.9	Mode Shaping Arm Telescope	Expands the beam to satisfy requirements for both the detector and scanning optics module
SO.4	Scanning Optics Telescope	Expands the beam to overfill the objective
D.9	Detector Telescope through Pinhole	Telescope to focus the beam through the pinhole. Collimation is confirmed with the red diode alignment laser sent backwards through the beam path. In addition, the red and green paths are overlapped to ensure they follow the same path in the scanning optics and detector.

The red diode laser is used to check the collimation of the red path and its overlap with the green path over this collimation distance. To satisfy the confocal conditions, it is important the green and red paths are both collimated and overlap for the total beam path.

Figure 4.13 outlines an example of what happens when the beam is not collimated heading into key components. In the case of the scanning optics, if the beam is not collimated, the focal point on the NV side will not correspond to the focused point on the pinhole, violating the confocal conditions.

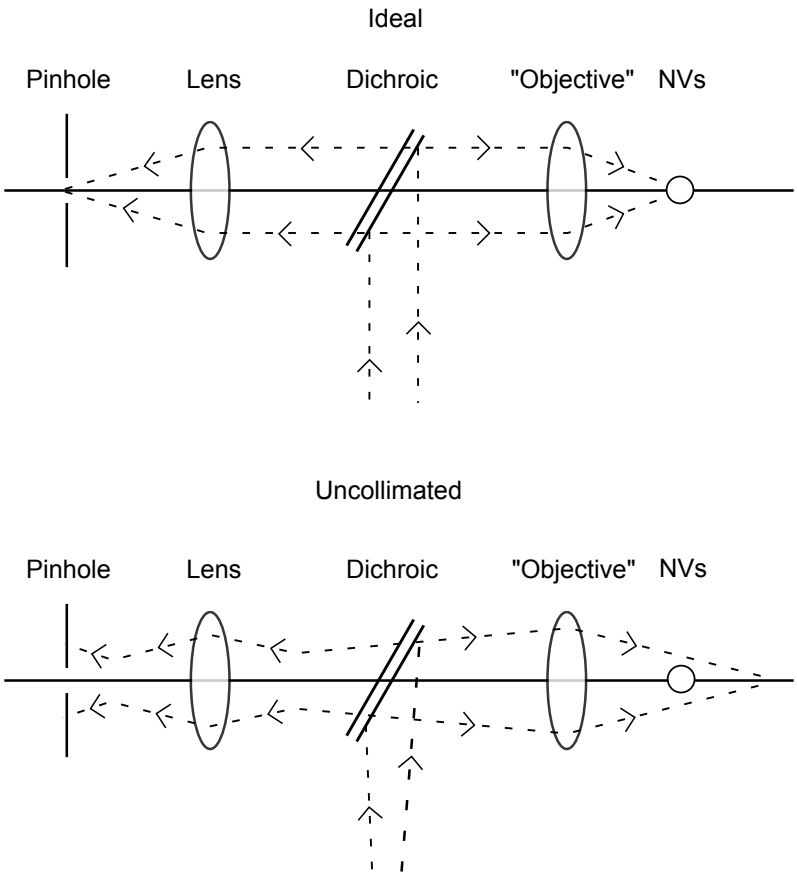

Figure 4.13: This figure dictates what happens when the beam is and is not collimated heading into the scanning optics and then into the detector box. When the beam is collimated, we see that the objective properly focuses on the desired NVs, which fluoresce, and travel back through the scanning optics into the detector box and are focused through the pinhole. When not collimated, in this case shown as being divergent, the beam is focused on another set of emitters, and then converges before the pinhole. When the beam converges before the pinhole, it becomes out of focus and a portion of the beam is blocked. So the two confocal points are not converging to the desired spots.

4.2.3 Beam Profile

In the ideal case, the shape of the beam should be Gaussian, named because the Gaussian profile of the intensity across the major and minor axes, [98]. The diameter of the major and minor axes should also be as close to equal as possible, making the 2D profile a circle. This is done to make the power intensity across the spot size of the objective as uniform as possible. If not, the initialization for NVs across the ensemble spot size will differ. The BC106-VIS (Thorlabs) profilometer was used to measure the profile and size of the beam, at key points in the setup, with the results shown in figure 4.14. The key points outlined in the figure below are, **(1)** The beam emitted from the laser, **(2)** Before the single mode fiber, **(3)** Exiting the single mode fiber and **(4)** Before the scanning optics telescope.

As expected, the beam emitted from the laser is Gaussian. The largest change observed here is the action through the single mode fiber from points **(2)** to **(3)**, where the beam is quite elliptical heading into the SMF, but circular exiting, as is its intended function. Finally, the beam heading into the scanning optics is checked. Recalling that the objective is meant to be overfilled, this beam is expanded with the scanning optics telescope so that only the first one or first two rings will be transmitted through the objective, to make the beam as close to planar as possible. As the beam diameter was expanded to be 12 mm, it was too large to be measured by the profilometer to be measured before the objective.

In addition to the profile and power distribution of the beam, other aberrations may be revealed by the profilometer. Poorly aligned lenses will show the beam blocked in portions. Additionally, if lenses are not perpendicular to the optical axis, interference between the lenses will result in rings present on the profile. The dark spots seen on the images on the figure below are from dirt on the profilometer not on the actual beam, confirmed through multiple measurements and shifting the beam around.

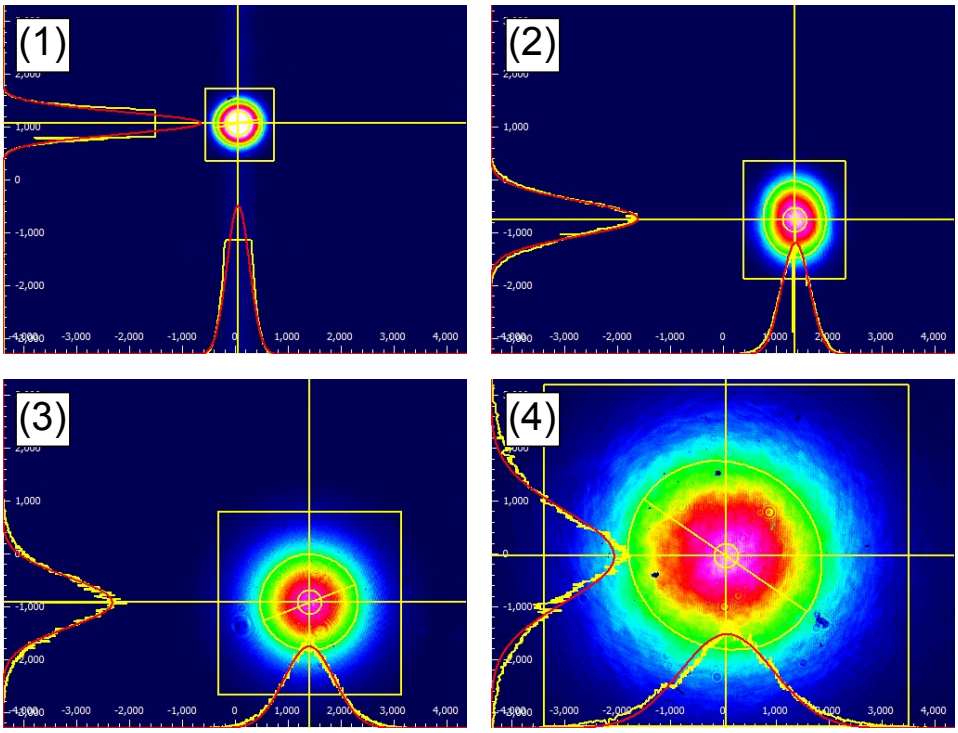

Figure 4.14: A profilometer measures the shape, intensity distribution and diameter of the beam. Ideally, the beam should have a 2D circular profile and have a Gaussian power distribution in both the x and y direction. There are four key points to measure the beam profile. **(1)** The beam as it exits the laser, which does look quite round and distribution in x and y is even. **(2)**, entering the single mode fiber. The beam became elliptical from travelling through the switch arm. The purpose of the SMF is to act as a spatial filter, cleaning up the shape of the beam. This is evident in **(3)**, as the beam is circular exiting out of the fiber. Last **(4)**, before the scanning optics telescope, showing a circular profile. Recall, the objective is overfilled, and emerging from the objective, only the inner ring of the beam will be passed, which is where the power of the beam is most intense and uniform. There are a few dark spots that may be seen on these figures, this is dirt present on the lens of the profilometer, not on the beam itself.

4.2.4 Beam Diameter

Much inline with the profile of the beam is the beam diameter. The BC106-VIS (Thorlabs) profilometer was also used to measure the diameter. Note for all of these measurements, there is an uncertainty on the diameter of ±5%, given by the specs of the profilometer used. The first measurement is at the laser, which outputs the beam at 0.9 mm, followed by a telescope, which expands the beam 2x to a measured value of 1.5 mm. The beam is expanded at this point in order to satisfy both the requirements of the beam entering the AOM and the size requirements of the beam heading into the single mode fiber coupler in the mode shaping arm.

As mentioned previously, the size of the beam entering the AOM will affect both the power diverted from the 0^{th} order to the 1^{st} order beam and the switching time of the AOM. The aperture size of the AOM is 1 mm, so the beam must be less than this size. Although the beam cannot be measured at the entrance of the AOM, an estimate of the size can be made with the measured power divergence to the 1^{st} order and by calculating the diffraction limited beam size (D) focusing from a lens, shown in the equation below. λ is the wavelength of the light [m], f is the focal length of the lens [m] and r is the beam waist $\left(\frac{1}{e^2}\right)$ of the incoming beam to the lens [m], [49].

$$D = \frac{\lambda f}{r} \tag{4.11}$$

On the first lens (f = 175 mm) heading into the AOM, the estimated beam size is 124 μm, which would yield a power diffraction close to 90% and switching time of 15 ns. The measured power diffraction efficiency to the 1^{st} order beam was 40%, which would indicate a much smaller beam entered the AOM, or that there were some alignment errors made. The measured values were well within the working parameters for this setup.

The second lens following the AOM has a shorter focal length (150 mm), resulting in the beam exiting the first pass of the telescope to be smaller (1.3 mm). On the back pass, this smaller beam size combined with the shorter focal length results in a similar beam size entering the AOM as on the front pass (122 μm). The measured power divergence to the 1^{st} order beam on the back pass was 60%, again, well within the accepted values for the operation of the microscope.

As the beam passes through the switch arm telescope twice, the beam is reduced on the front pass and then expanded on the back pass, so it enters the mode shaping arm the same size it entered the switch arm. The beam is then re-directed into the fiber coupler heading into the SMF, at the beam size of 1.3 mm to satisfy the size requirements of the fiber coupler.

Exiting the single mode fiber, the beam was measured to be 1.9 mm. Following the single mode fiber, another telescope expands the beam by two times to 3.9 mm to satisfy two requirements. The first being to satisfy the beam size when focused into the pinhole. The second being to satisfy the scanning optics telescope, which further expands the size of the beam to overfill the objective. The system was also designed so that scanning optics mirrors may be placed in between the dichroic mirror and the scanning optics telescope for future experiments. These mirrors need to be underfilled, so the beam can only be a maximum of 5 mm entering the optical scanning mirrors.

Once expanded from the mode shaping arm telescope, the beam reflects into the scanning optics, and expanded with the scanning optics telescope to a size of 11.7 mm, overfilling the objective. The diameter (D) of the back of an objective is defined in equation 4.12, where (Mag) is the magnification of the objective and (NA) is the numerical aperture. The incoming beam diameter must be larger than (D) to have the most uniform power intensity through the objective.

$$D = 2 \times NA \times (200/Mag) \tag{4.12}$$

This beam size was chosen to reflect the size requirements for a 10x objective, which would require a larger beam size. A 100x objective may be exchanged with the 10x objective. This results in an even larger overfill of the diameter of the objective (5.2 mm), which does result in more power loss, but a more uniform power intensity. Since the power intensity focused on the NVs through the objective is much greater in the 100x than the 10x, the extra power loss does not pose as a problem for the ensembles.

Once the beam reaches the detection box, a (100 mm) lens focuses it into the pinhole. If the pinhole is too small relative to the size of the incoming beam, it will act as a slit, and the beam will diverge greatly, depicted in figure 4.15. Making the pinhole 30% larger than the diffracted limited beam diameter (35 μm) allows it to still act with its intended operations, but not cut the beam such that it acts as a slit, diverging the beam. A pinhole of 45 μm is required for the measured incoming beam size and lens focal length, therefore a 50 μm pinhole was used. Following the pinhole, the beam is re-collimated by a second lens of focal length, (100 mm), and then again focused onto the detector. The detector requires the beam to be less than 180 μm to accommodate the size of its active are. The calculated diffracted limited beam diameter focusing into the detector was 26 μm, satisfying this condition.

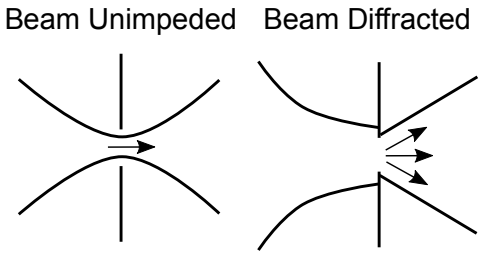

Figure 4.15: The pinhole is required to be 30% larger than the diffraction limited beam size. This is shown in the **(left)** half of the image as the focal point of the Gaussian beam travels through the pinhole unperturbed. When the pinhole is too small, it acts as a slit, diffracting the beam, **(right)**, which would lose a large amount of the beam to be focused into the detector.

The requirements for the beam diameter in the whole setup are outlined in table 4.9 below. There were a few points that measuring the beam diameter was not practically possible, these are labelled as "N/A" in the table.

Table 4.9: The table corresponds to the key places where it is necessary to measure the beam diameter. In correspondence with the collimation, the beam diameter is measured in many of the same places as when the beam is collimated. There is a ±5% uncertainty on the measured diameter given by the specs of the profilometer.

Beam Diameter Measurements				
Label	**Component**	**Purpose of Component**	**Theoretical Beam Diameter [mm]**	**Measured Beam Diameter [mm]**
L.1	Laser	Initial Beam Condition	0.7	0.9
L.6	Laser Box Telescope	Expands Beam 2x	1.4	1.5
SA.6	Lens into AOM (first pass)	Focuses the beam into the AOM (f=175 mm)	124 μm	N/A
SA.7	AOM	1 mm diameter aperture size		N/A
SA.8	Second lens of switch arm telescope (front pass)	Telescope reduces beam size to 85% of size into telescope (focuses to 122 μm spot size)	1.2	1.3
SA.8	Second lens of switch arm telescope (back pass)	Focuses beam back into AOM (f=150 mm) on back pass diameter	122 μm	N/A
SA.6	First lens of switch arm telescope (back pass)	Re-collimates beam back to original size to head into fiber coupler	1.4	1.3
MSA.6	Out of Fiber	Emerge according to fiber coupler specs	1.5	1.9
MSA.9	Mode Shaping Arm Telescope	Expands beam by 2x to underfill optional scanning mirrors and satisfy pinhole requirements	3.75	3.9
SO.4	Scanning Optics Telescope	Expands the beam by 3.125x to overfill the objective (designed for 10x objective)	11.7	Beam too large to measure

Continuation of Table 4.9

Label	Component	Purpose of Component	Theoretical Beam Diameter [mm]	Measured Beam Diameter [mm]
SO.7	100x oil-immersion Objective (With Optional 10x Air Objective)	Requires overfill for best power intensity and objective functionality. 100x may be swapped for minimal power loss.	10x(12 mm) 100x(5.2 mm)	Beam too large to measure
D.7	Lens into Pinhole	Focus into pinhole by diffraction limited diameter	35 μm	N/A
D.8	Pinhole	Pinhole must be 30% larger than the diffraction limited beam diameter	Requires 45 μm, 50 μm chosen	N/A
D.9	Lens out of Pinhole	Re-collimated beam to be sent to detector & receive from red diode alignment laser	3.75	N/A
D.12	Lens into detector	Focal spot size must be less than the active area of the detector	26 μm	N/A
D.13	Detector	Has 180 μm active area	26 μm satisfies the condition	N/A

4.2.5 Beam Polarization

Polarization is a key tool for several functions throughout the optical setup of the microscope. Light may be polarized linearly, circularly or elliptically. Linearly polarized light has only one vector describing the electric field as it travels along down the propagation (optical) axis, [49, 63]. Circularly and elliptically polarized light have two vectors describing the electric field, resulting in an evolving plane as the light propagates down the propagation axis. Elliptically polarized light and circularly polarized light differ in that circularly polarized light has the two components forming its electric field plane to be 90° from each other, while elliptically polarized light does not. Figure 4.16 provides a basic visual for linear, circularly and elliptically polarized light.

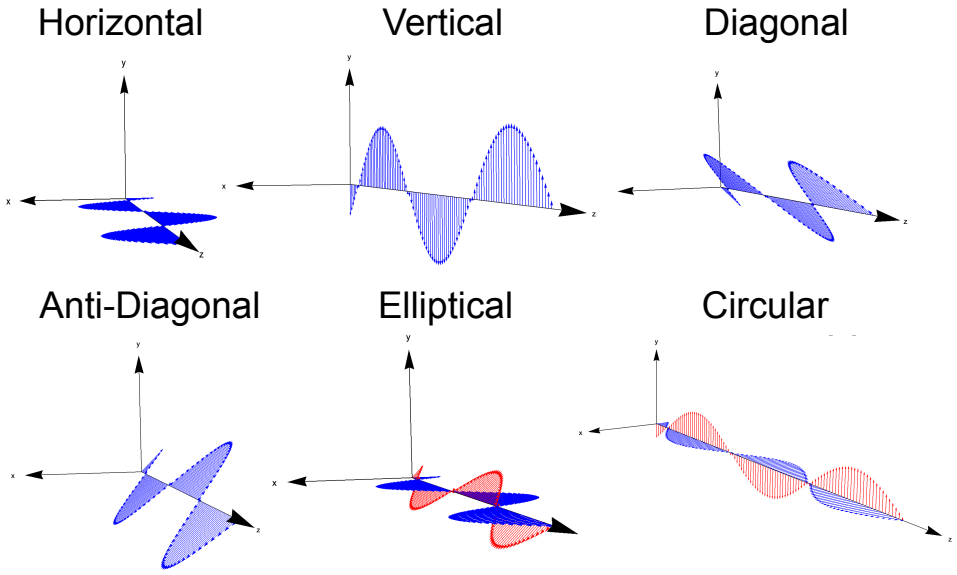

Figure 4.16: Linear polarization has the electric field described with one vector, which does not vary as it propagates down the optical axis. Linear polarization may be described as (s and p), or vertical and horizontal, diagonal and anti-diagonal as shown in the image above. Circular polarization has two components to the electric field, which are spaced a relative 90° from each other, while elliptical polarization also contains two components in the electric field, but these are not separated by 90°. For both circular and elliptical polarization, as the electric field propagates down the optical axis, the electric field plane varies, creating a helical motion. Depending on the handiness of the propagation, the light is either right or left circularly (elliptically) polarized.

Linearly polarized light is commonly described as s vs p-polarization and vertical (V) and horizontal (H) polarization. S and p-polarization refer to the direction of the electric field relative to the propagation axis, while vertical and horizontally polarized light base the electric field relative to gravity. S-polarization has the electric field portion of the light wave travelling perpendicular to the plane of incidence, while p-polarized has the electric field travelling in plane with the plane of incidence. Vertically polarized light has the electric field travelling parallel to the axis of gravity, while horizontal travels perpendicular to gravity, [49].

There are a few components which affect the polarization in the system. These are the HWP, QWP, mirrors, PBS, and SMF. As the function of each is important, they will be investigated.

Figure 4.17 shows how a wave plate rotates the polarization of light. Any linear polarization may be described as a vector using a sum of Vertical and Horizontal (or s and p) polarization components. A wave plate rotates the polarization about its rotation axis, changing the portion of Vertical and Horizontal components that make up the total polarization. Depending on what type of wave plate (half vs. quarter), the polarization will be rotated about the rotation axis by π vs. $\frac{\pi}{2}$. The rotation axis may be changed within the wave plates, altering what axis the polarization is rotated about, allowing any output linear polarization to be accessed from any incoming linear polarization, [49].

The Poincaré sphere depicts polarization as vectors on a sphere, analogous to using the Bloch sphere to depict spins, where Horizontal and Vertical polarization represent the positive and negative "z" axis. Diagonal and Anti-Diagonal are represented as the positive and negative "x" axis, while Left and Right Circular polarization are the positive and negative "y" axis. Changing the rotation axis allows a wave plate to accept an incoming polarization, rotate it about the rotation axis and arrive at the final state. The example in figure 4.17 shows a half-wave plate, which is accepting any incoming linear polarization, and rotating about a rotation axis to arrive at horizontal polarization, the desired outcome.

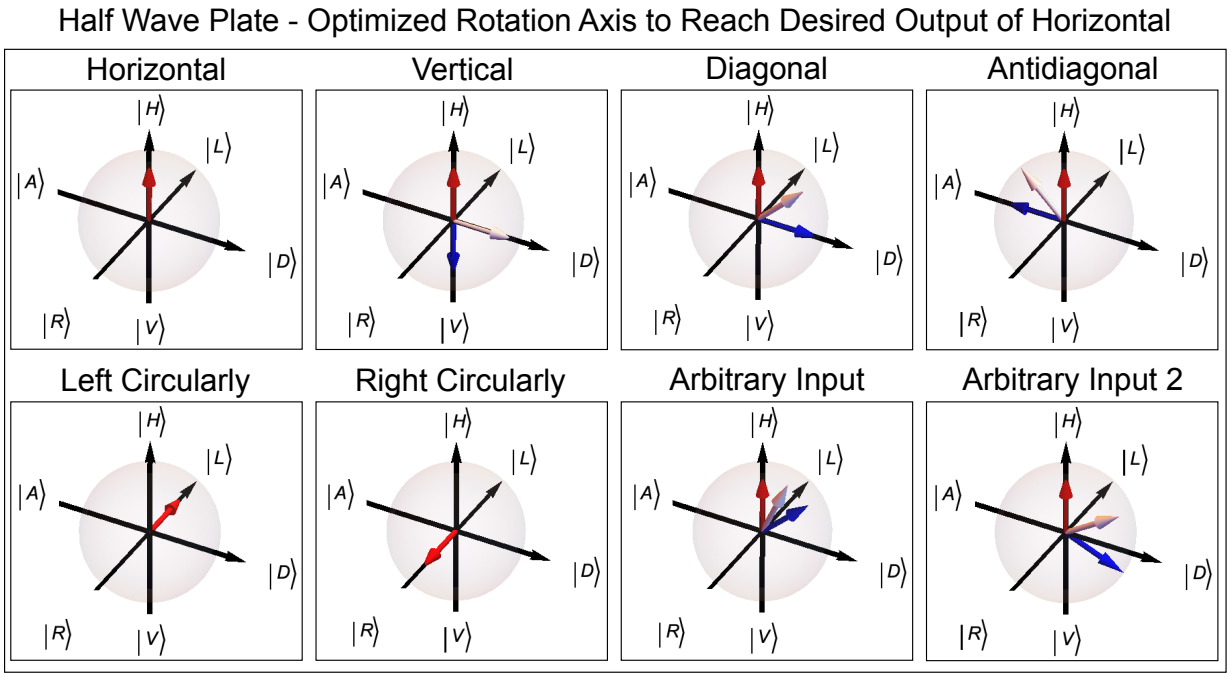

Figure 4.17: Demonstrating how a wave plate affects optical polarization. Wave plates rotate the polarization about their rotation axis. The Poincaré sphere may be used to depict polarization as a vector on a sphere, analogous to a Bloch sphere describing spin. The figure shows how the rotation axis of a half-wave plate may be adjusted to take any incoming polarization **(blue)**, rotate about the rotation axis **(grey)** by π and arrive at the final desired polarization **(red)**. The final desired polarization was horizontal for this example.

In addition to the wave plates found within the setup, the other major components affecting the polarization are mirrors, and the PBS. Mirrors do not have any effect on vertical or horizontally polarized light. They will swap anti-diagonal to diagonal polarization and vice versa, and additionally will swap the handiness of circularly polarization light from left to right and right to left circular polarization.

A PBS has two actions on the polarization, acting as a combination of a linear polarizer and a mirror. A linear polarizer allows passage of one type of linear polarization and absorb the rest. Instead of absorbing the unwanted polarization, a PBS will reflect the other polarization, acting as a mirror. For, example, a PBS may transmit vertical polarization, while it reflects horizontal polarization. Malus' Law will dictate the output intensity of a beam passing through a PBS with some input intensity and incoming polarization, [49, 63]. $I_{i/o}$ are the input and output light intensity, $\theta_{i/o}$ is the angle of the polarizer and incoming beam polarization off the horizontal axis of the Poincaré sphere.

$$I_o = I_i \cos(\theta_i - \theta_o) \tag{4.13}$$

Putting all these theoretical pieces together, a complete picture of how the polarization maps through the microscope is set. This is summarized in table 4.10.

Table 4.10: The table corresponds to the key places where it is necessary to measure the beam polarization. Polarization is a convenient tool to redirect the beam in the switch arm. Past the switch arm, the polarization is a tool used to acquire equivalent fluorescence from the NV ensemble.

Beam Polarization Measurements		
Label	**Component**	**Effect on Polarization**
L.1	Laser	Sets initial polarization to s-polarization (vertical)
SA.3	Half Wave Plate	Rotates (V) s to (H) p-polarization
SA.4	PBS (forward pass)	Transmits (H) p-polarization towards AOM
SA.10	Quarter Wave Plate (forward pass)	Rotates to right circular polarization
SA.11	Mirror	Swaps handiness from right to left circular polarization
SA.10	Quarter Wave Plate (backward pass)	Rotates left circular to (V) s-polarization
SA.4	PBS (backward pass)	Reflects (V) s-polarization toward Mode Shaping Arm
MSA.5	Single Mode Fiber	Induces an unknown polarization error
MSA.13	Half Wave Plate	Used to select polarization for NV ensemble

The light first emitted by the laser is s-polarized. A HWP following the laser rotates the polarization from s to p (V) to (H). The PBS then transmits the p-polarized (H) component of the beam. After passing through the AOM, a QWP rotates to right circularly polarized light. When the light hits the mirror, the mirror changes the handiness of the polarization to left circularly polarized light. When passing back through the quarter wave plate, the beam rotates from left circularly polarized light to s-polarized (vertical). After passing back through the AOM on the back pass, when the beam hits the PBS, it now reflects the beam, as it is s-polarized and re-directs the beam into the mode shaping arm.

Within the mode shaping arm, the beam enters the fiber, which induces a random polarization error on the beam. NVs are sensitive to the polarization of the beam, as they will emit a percentage of fluorescence depending on how the electric field of the light aligns with the electric dipole portion of the NVs principle axis. A half-wave plate corrects the error induced by the fiber, which rotates to any linear polarization best suited for the ensemble of NV centers. As the outgoing polarization from the fiber is unknown, the rotation of the half-wave plate was determined experimentally with an optically detected continuous wave (CW) experiment.

The polarization may be set such that the NVs will emit with either an equal level of fluorescence for each orientation, or to suppress the output from certain orientations. For the experiments preformed in this setup, the polarization was set such that the NVs emitted the same level of fluorescence.

4.3 Experimental Microwave Configuration

The microwave system controls the ground spin state of the NV. This section will outline the microwave layout used for this system, featuring two independently controlled microwave sources, capable of implementing the OCT experiments outlined in chapter three. Following this, the power throughout the microwave system will be characterized. The goal of this section is to understand how the amplitude traces from the arbitrary waveform generator (AWG) to the sample. The section will end by describing the chosen configuration for microwave sources, a PCB board with two parallel microstrips.

4.3.1 Layout for a Dual-Channel Microwave System

This system was designed to have two independently controlled microwave sources. This enables the implementation of circularly polarized microwaves for single transitions in the NV ground state without the need for a static magnetic field.

The equation below outlines the signal properties required for each channel. There is a central frequency (ω_T) each with two envelopes $I(t)$ and $Q(t)$, controlling the amplitude and phase of each channel.

$$I(t)\cos(\omega_T t) + Q(t)\sin(\omega_T t) \tag{4.14}$$

Figure 4.18 outlines all the main components required for the microwave setup. The description shows just one channel, for simplicity. A synthesizer provides the central frequency (ω_T) while an AWG provides the envelopes for the $I(t)$ and $Q(t)$ control. The IQ mixer combines these three signals, which splits the ω_T into two signals, then phase shifts one by 90°. These two signals are then multiplied by each I and Q and summed together to resemble the equation outlined in equation 4.14. Following the IQ mixer, there is a switch controlled by the AWG which has a good isolation between ON and OFF, before being sent through an amplifier and finally to the PCB board housing the sample.

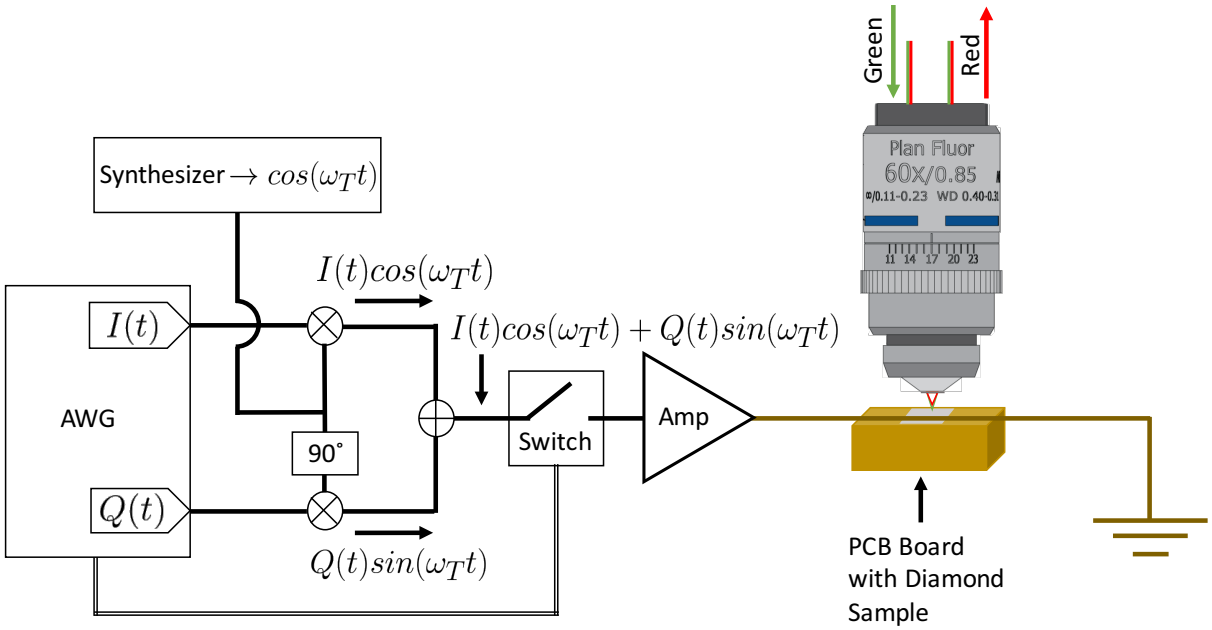

Figure 4.18: A simplified version of a single microwave channel indicates the critical components required for the microwave control of the NV centers. The frequency synthesizer provides the central frequency at ω_T and the AWG, the I and Q signals. The IQ mixer, which splits ω_T into two signals, phase shifting one by 90°, multiplying by the I(t) and Q(t) signals and summing together to create the total signal $I(t)\cos(\omega_T t) + Q(t)\sin(\omega_T t)$. The switch provides good isolation between the power between the ON and OFF state, while the amplifier boosts the amplitude for the NVs. The switch is placed before the amplifier in this case so as to not exceed the operating power threshold of the switch after the signal is amplified.

A dual-channel setup is in essence, two single-channel control setups, one each controlled by their own I and Q values from a four-channel AWG, so the total signal heading to the NVs is outlined below in equation 4.15. This equation shows an ideal case, assuming there are no phase differences between the two channels and both IQ mixers are behaving ideally.

$$(I_1(t) + I_2(t))\cos(\omega_T t) + (Q_1(t) + Q_2(t))\sin(\omega_T t) \tag{4.15}$$

Expanding from the simplified model in figure 4.18, the full picture of the microwave circuit is provided in figure 4.19 and the parts listed in table 4.11. The frequency synthesizer provides the center frequency, at 2.87 GHz. This signal splits into two with a power splitter, and sent into two IQ mixers. The IQ mixers take the central frequency and signal envelopes from the four AWG control channels, shown as the $I_{1/2}$ and $Q_{1/2}$ signals, and outputs the total microwave signal.

Just as with the single-channel setup, the IQ mixers gather the signals from the frequency synthesizer and AWG controls, multiplies and sums together so that each output from each of the IQ mixers is $I(t)\cos(\omega_T t) + Q(t)\sin(\omega_T t)$. Again, a switch follows each IQ mixer, used for extra isolation between the ON and OFF. The combination of both the IQ mixer and switch yields (-40 dB) isolation from ON and OFF. The switch is followed by an amplifier on each channel to amplify the signal in each channel by 45 dB. In this case, the switch is placed before the amplifier because its maximum acceptable power threshold would be exceeded if placed after the amplifier. A circulator follows the amplifier, which reduces the reflected power from the sample board back to the amplifier.

Both sides of the microwave circuit are recombined on the sample board via two cables of identical length. This sample board is interchangeable on this circuit setup, allowing for various field control of the NV ensembles. Following the sample board, the signal is terminated by two 30 dB attenuators and then into two 50 Ω terminators to minimize power reflection. A number of low pass filters, DC blocks and attenuators may also be seen simply there to clean up the signal and to ensure no power thresholds are exceeded for any devices.

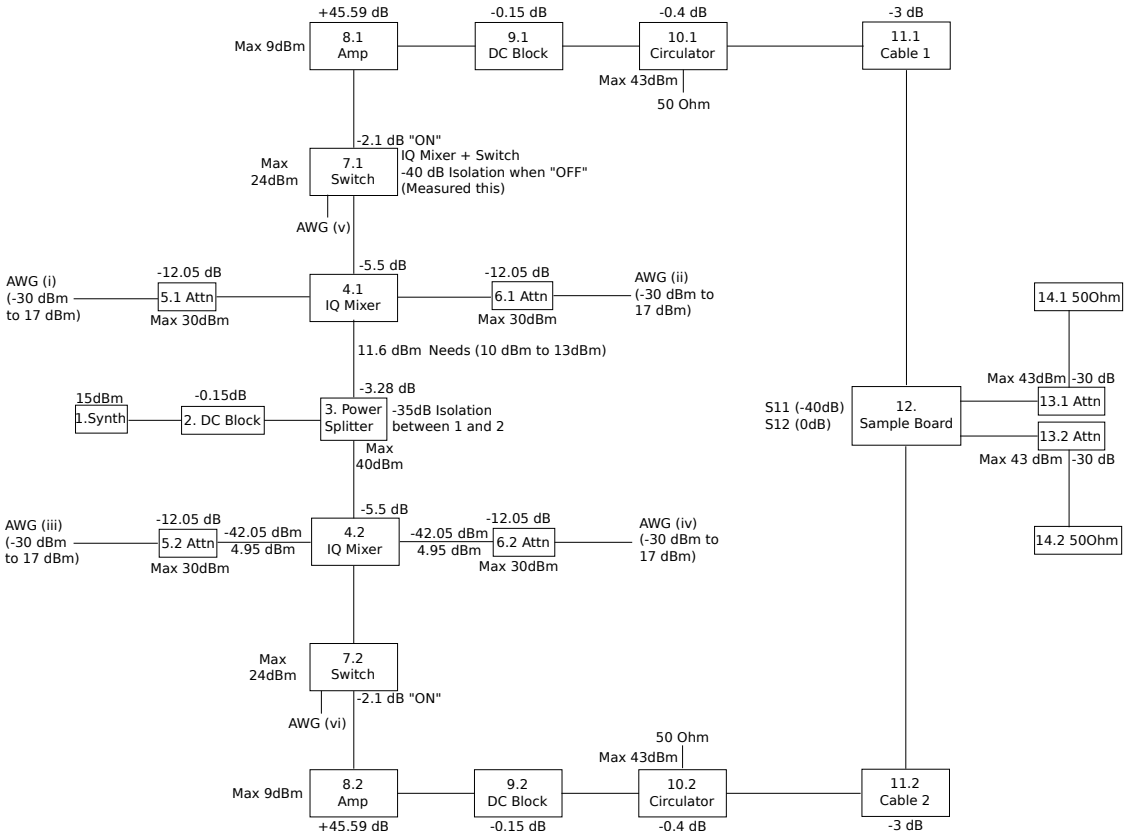

Figure 4.19: Like the single-channel case, the frequency synthesizer provides the central frequency of ω_T. In most experimental cases, since these are preformed at zero field, this will be set to 2.87 GHz. A power splitter splits the signal into the two channels, sending the central frequency into two IQ mixers, followed by two switches, two amplifiers and sent toward the sample, and terminated by two attenuators before being sent to ground. In addition to the basic components mentioned above, there are a few DC blocks, attenuators and circulators added in order to clean up the incoming signal and prevent any power levels from being exceeded. For the best success of these dual-channel setups, identical components were used in order to minimize any differences between the two channels. For each component, the figure indicates the output power [dBm] and any relevant power losses affecting the output power [dB].

Table 4.11: Microwave components corresponding to fig 4.19. Note that some components. have been listed multiple times (ex. AWG) to indicate where the connections are. The sub labels .1 or .2 represent channel 1 and 2

List of Components By Block			
Label	**Component**	**Description**	**Part No.**
1	Frequency Synthesizer	Provides Center Frequency	**Phase Matrix Inc.** FSW-0010 S/N 13201-10153
2	DC Block	Cleans up signal	**Mini-circuits** BLK-18-S+
3	Power Splitter	Splits the central frequency into the two microwave channels	**Mini-circuits** ZAPD-4-S+ (2-2.4 GHz)
4.1	IQ Mixer	Mixes IQ signals from AWG with central frequency	**Marki-microwave** IQ0255LMP
5.1(6.1)	Attenuators	Attenuates AWG signal from I(Q) by -12 dB	**Mini-circuits** VAT-12+
AWG (i)/(ii)	AWG	4 Channel AWG Channels providing the I and Q envelopes.	**Tektronix** 5014C AWG
7.1	Switch	Increases isolation for "ON" and "OFF"	**Mini-circuits** ZYSW-2-50DR
AWG (v)	AWG	transistor-transistor logic (TTL) Signal to Switch to control "ON" and "OFF"	**Tektronix** 5014C AWG
8.1	Amplifier	Amplifies Total Signal by 45 dB	**Mini-circuits** ZHL-16W-43-S+
9.1	DC Block	Cleans up signal	**Mini-circuits** BLK-18-S+
10.1	Circulator	Prevents reflected power from going back to the Amplifier	**Ditom Microwave Inc.** D3C2040
11.1	6 ft. Cable	Connects from Amplifier to Sample Board	**Pasternack** PE3369LF-72

Continuation of Table 4.11			
Label	**Component**	**Description**	**Part No.**
12	Sample PCB Board	Dual Stripline PCB Board to delivery microwaves to sample	**Rogers Corporation** Laminate: TMM10i (0.76 mm)
12	Sample PCB Board Pins	Connects microwave inputs to board via SMA connectors	**Amphenolrf** 132432
13.1	Attenuator	Attenuates signal by -30 dB	**Mini-circuits** BW-530W20+
14.1	50Ω terminator	Terminates output, 50 Ω matched	**ATM INC** RT0516
4.2	IQ Mixer	Mixes IQ signals from AWG with central frequency	**Marki-microwave** IQ0255LMP
5.2(6.2)	Attenuators	Attenuates AWG signal from I(Q) by -12 dB	**Mini-circuits** VAT-12+
AWG (iii)/(iv)	AWG	AWG Channels providing the I and Q envelopes.	**Tektronix** 5014C AWG
7.2	Switch	Increases isolation for "ON" and "OFF"	**Mini-circuits** ZYSW-2-50DR
AWG (vi)	AWG	TTL Signal to Switch to control "ON" and "OFF"	**Tektronix** 5014C AWG
8.2	Amplifier	Amplifies Total Signal by 45 dB	**Mini-circuits** ZHL-16W-43-S+
9.2	DC Block	"	"
10.2	Circulator	Prevents reflected power from going back to the Amplifier	**Ditom Microwave Inc.** D3C2040
11.2	6 ft. Cable	Connects from Amplifier to Sample Board	**Pasternack** PE3369LF-72
13.2	Attenuator	Attenuates signal by -30 dB	**Mini-circuits** BW-530W20+
14.2	50Ω terminator	Terminates output, 50 Ω matched	**ATM INC** RT0516

4.3.2 Power Characterization

It is important to understand what the amplitude at the site of the NV will be, given the control amplitude sent by the AWG. While this is not as critical for experiments like optically-detected magnetic resonance (ODMR)-continuous wave (CW), mapping of amplitude is essential for more complex pulses. The main components influencing the overall output amplitude are the AWG, IQ mixer, switch, and amplifier.

The IQ mixer has three inputs; the local oscillator local oscillator (LO), and two intermediate frequency (IF) inputs, I and Q. These combine to the output radio frequency (RF) port. For this configuration, the LO input is fed by an input power between 10 dBm and 13 dBm. The input to each IQ mixer can be seen in figure 4.19. To achieve the desired input power to the LO, a frequency synthesizer provides the center frequency at 15±2 dBm. This signal then passes through a DC block with a power loss of 0.16 dB, followed by a power splitter with power loss -3.28±0.01 dB. The total power reaching the LO input from the synthesizer is then 11.6 dBm, satisfying the 10 dBm to 13 dBm range. The output power from the IQ mixer is adjusted by changing the amplitude of each of the IF inputs, while the LO input is kept constant.

The AWG provides the envelopes for the I and Q channels. The total output power from the IQ mixer is calculated as such:

1. The AWG can output a maximum of 17±0.3 dBm and minimum of -30±0.3 dBm for each I and Q channel.

2. An attenuator reduces this signal by 12±0.1 dB. These values are attenuated such that the total maximum power emerging from the IQ mixer does not exceed any maximum power thresholds for any devices in the circuit if the AWG outputs the maximum amplitude.

3. Recall that inside the IQ mixer, the input from the local oscillator is split, with one channel being phase shifted 90° so we have a cosine and a sine signal at the center frequency determined by the frequency synthesizer. This is then multiplied by the I and Q envelopes and summed again to make an output RF signal:
   $I(t)\cos(\omega_T t) + Q(t)\sin(\omega_T t)$.

4. There is a conversion loss of -5.5±0.3 dB between the IF inputs (I and Q) and the output RF signal for each channel. In addition, to ensure there is no leakage from the LO to the RF amplitude, there is a 42±0.3 dB isolation between the LO input and RF output, recalling that the LO power is only responsible for driving the diodes in the mixer.

5. The total power from the IQ mixer is calculated in voltage, assuming there is a 50 Ω load.

The above description is summarized in the following equations below. The output from the AWG ($I_{\text{AWG}}(Q_{\text{AWG}})$), converting from [dBm] to [V] is shown below, assuming a 50 Ω load. These voltage values (peak-to-peak) were also confirmed with a voltage measurement to ensure their accuracy.

$$I_{\text{AWG}}(Q_{\text{AWG}})\ [\text{V}] = 2 \times 10^{\left(\frac{I(Q)\ [\text{dBm}]-10}{20}\right)} \tag{4.16}$$

Before heading to the $I_{\text{mixer}}(Q_{\text{mixer}})$, the signal is attenuated by 12±0.1 dB. Then the conversion loss of -5.5±0.3 dB from the IF to the RF channel is accounted for, so the output for each I(t) and Q(t) channel from the mixer ($I_{\text{mixer}}(Q_{\text{mixer}})$) is:

$$I_{\text{mixer}}(Q_{\text{mixer}})\ [\text{V}] = I_{\text{AWG}}(Q_{\text{AWG}})\ [\text{V}] 10^{\left(\frac{-12\ [\text{dB}]-5.5\ [\text{dB}]}{20}\right)} \tag{4.17}$$

The total output voltage from the IQ mixer sums the signal from each of the I(t) and Q(t):

$$\text{Mixer Amp}\ [\text{V}] = \sqrt{I_{\text{mixer}}\ [\text{V}]^2 + Q_{\text{mixer}}\ [\text{V}]^2} \tag{4.18}$$

Finally, this Mixer Amp [V] (peak-to-peak voltage) is converted back to dBm, as the rest of the specs for power loss and gain for each subsequent component are given in dB.

$$\text{Mixer Amp}\ [\text{dBm}] = 10 + 20 \times Log_{10}\left(\frac{\text{Mixer Amp}\ [\text{V}]}{2}\right) \tag{4.19}$$

Following the IQ mixer, the loss through the switch, amplifier gain, DC Block loss, circulator loss and cable loss are accounted for, which total -2.1 dB + 45.59 dB - 0.16 dB -0.4 dB for a total gain of 42.93 dB.

Summarizing the above mapping, the overall power from the AWG I and Q controls to the sample board for each channel is as follows:

$$\text{AWG}_{\text{to}}\text{Sample [dBm]} = 53 + 10\log_{10}\left(10^{\frac{I\ \text{[dBm]}-27.5}{20}} + 10^{\frac{Q\ \text{[dBm]}-27.5}{20}}\right) \tag{4.20}$$

This can be easily expressed in Watts as well:

$$\text{AWG}_{\text{to}}\text{Sample [W]} = 10^{\frac{\text{AWG}_{\text{to}}\text{Sample [dBm]}-30}{10}} \tag{4.21}$$

$$\text{AWG}_{\text{to}}\text{Sample [W]} = 10^{\frac{I\text{[dBm]}-4.5}{10}} + 10^{\frac{Q\text{[dBm]}-4.5}{10}} \tag{4.22}$$

With the total mapping of the AWG controls, the expected power from the AWG to the sample board can be calculated. Recall the AWG may emit a maximum of 17±0.3 dBm and minimum of -30±0.3 dBm for each $I_{1/2}$ and $Q_{1/2}$. If the AWG is emitting the maximum amount of power for I and Q, the maximum at the sample board is 45.5 dBm (35.5 W) for each channel 1 and 2. If the AWG emits the minimum amount of power for each I and Q, the power delivered to the sample board for each channel is -1.5 dBm (0.709 mW). In practice, each amplifier for both channels saturates, resulting in the measured maximum value of ≈ 38 dBm or 6.30 W.

4.3.3 PCB Board for NV Ensemble Control

The two independently controlled microwave sources are realized in this setup as a PCB board with two microstrips. This is not the only design which allows for circularly polarized microwave control of NV centers. Previous experimental results have been completed with four parallel resonators, ring structures, and perpendicular microstrips, [31, 68, 121, 125]. Figure 4.20 shows the rendering of the design of the PCB. A picture of the sample mounted to the PCB is shown in figure 4.8. The main design of the PCB was completed by Madelaine Liddy, and supporting simulations, dimensions and schematic was completed by Hamid Mohebbi (Microwave engineer, High Q technologies).

The PCB board is a 5 cm $\times$ 5 cm board cut from 0.76 mm TMM10i Laminate (Rogers Co.), fabricated in the QNF lab at the University of Waterloo campus by Jose Roberto Romero, (IQC - Technical Services Lab Supervisor, Senior Electronics Engineering Technologist, C.E.T.). It consists of two lines of identical length, centered in parallel segments of 7.5 mm, spaced 150 μm apart, 127 μm wide and 17.5 μm thick. All segments were milled with the LPKF ProtoMat S103 circuit board plotter, with tolerances of $\pm$0.5 μm for all cuts. The microwave inputs are connected such that current travels through the microstrips in the same direction, on the two outside connectors, numbered ports 2 and 4, respectively. The two inside connectors on ports 1 and 3 are the outputs leading to 30 dB attenuators and then terminated into 50 Ω loads. The PCB board was designed to terminate in this fashion to reduce the amount of reflected power back to the amplifier.

In addition to the microstrips at the site of the diamond, there were other design characteristics taken into account. Each total path length was determined to be equal in order to reduce phase errors. To accommodate the mounting setup on the stage, all inputs and outputs had to be placed on one side of the PCB, which dictated the microstrips require to follow a curved pattern to fit on the board. A gradual curve was used rather than hard turns, to reduce any corner acting as an antenna. In addition, the thickness of the lines were reduced from 720 μm to 127 μm over a distance of 43 μm in order to impedance match to the incoming 50 Ω load and therefore minimize the reflected signal back to the amplifier. The lines were reduced in thickness at the site of the sample to radiate as much power as possible into the sample. They were then expanded before and after to match the 50 Ω impedance of the rest of the microwave setup. The length of the microstrips at the site of the diamonds was chosen to minimize the impedance between each microstrip induced on each other, but also to accommodate precise placement of larger diamond samples of up to 4 mm in length and width.

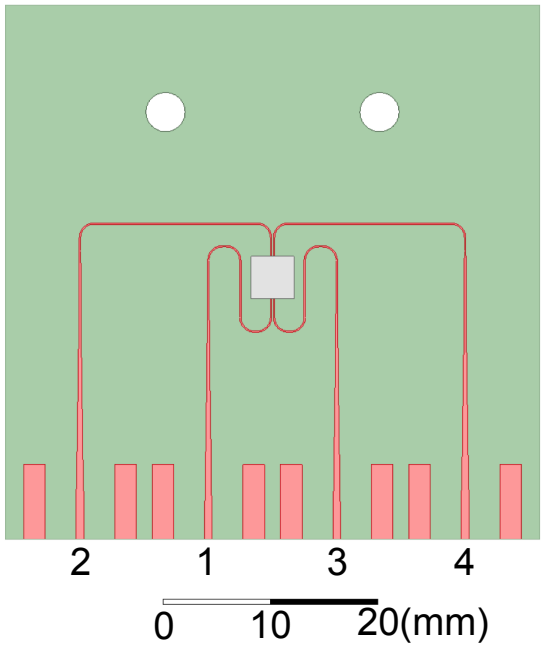

Figure 4.20: The schematic of the dual-channel PCB board with a diamond mounted. The board was designed to have two inputs (ports 2 and 4) and two outputs (ports 1 and 3), and terminating with external 50 Ω loads. The ports are labeled on the schematic above. The two microstrips are 150 μm apart, 127 μm wide, 17.5 μm thick and 7.5 mm long to accommodate diamond samples of larger size. The diamond sits on top of both microstrip, shown in the figure as a 4×4 mm diamond sample in the schematic. **Image Source:** Schematic courtesy of Hamid Mohebbi

The pins connecting the SMA connectors are isolated from ground, while the larger mounting pads on either side of the pins connect the SMA connectors to the grounding plane on the back of the board. The two white circles seen in the figure are through holes for mounting the board to the sample stage via (3/32) threaded screws.

S-parameters

The PCB was designed to have minimal power reflected back to the amplifier. The S-parameters will indicate the success of this. The two main points of interest here are the reflected power back from the output of both ports back on themselves, S(1,1), and S(3,3) and the leaked power from S(3,1), which is the isolation between the two microstrips. The reflected power at 2.87 GHz for both was -18 dB, which is small enough that the isolation of the circulator (-20 dB) will prevent damage on the return to the amplifier.

The transmitted power leaked from each microstrip to the other is also important for the function of the PCB board. This was measured to be -10 dB of isolation. The other values S(2,1), indicated the transmission through one of the microstrips from the input to the output, which showed very little loss of -2 dB, and last the backwards transmission from the input of one of the microstrips to the output of the other, S(4,1) which is -25 dB.

Moving to Experiments

Chapter three outlined the theoretical model of the Hamiltonian for an ensemble of NVs (section 3.1.6). Key examples were also shown for the (100) diamond and the capabilities of this diamond given a chosen microwave field configuration (section 3.2.2, 3.2.3 and 3.3.1).

Chapter four then detailed the optical and microwave layout, functions and characterization for an NV ensemble setup. The basic functions of each were tested outside of use on a diamond sample. Chapter five demonstrates the use of the system for NV ensemble measurements. The early parts of the chapter will outline the basic experiments confirming the presence of an ensemble of NVs and characterization of the sub-ensembles found in the (100) diamond. It will end by demonstrating the OCT experiments implemented on this sample.

Chapter 5

Experimental Results

Chapter five details the main experiments conducted with this system. Single and dual-channel optically-detected magnetic resonance (ODMR)-continuous wave (CW) experiments confirm the presence of nitrogen vacancy (NV) ensembles, and allow for the correct optical polarization to be set for all tests moving forward. The laser initialization shows the initialization and readout time for the NV ensemble, acting as a blueprint for all other experiments undertaken. The single-channel Rabi and spinlock give early insight into the understanding and control of the sub-ensembles present in the sample. A relative microwave phase experiment analyzes the response of the ensemble to the change in the relative and absolute phase between the two channels. This informs the dual-channel Rabi experiment, analyzing the amplitude response with a varying control phase. The parameters gathered from the dual-channel Rabi experiment inform the optimal control theory (OCT) experiments.

The following experiments were conducted with a (100) diamond, the $DNV - B1$ diamond manufactured by Element-Six, [99, 100]. No treatments were done on the sample, except for a mild ultrasonic bath for 10mins in each Acetone and IPA.

5.1 Single-Channel ODMR-CW

NVs are measured using ODMR techniques, [37, 92]. NVs are initialized and read out optically, while the ground state spin is controlled with microwaves. The first two tests to conduct are the ODMR-CW experiments with a single-channel, measuring the response from each channel, followed by measuring the response with both microwave channels exciting the NVs simultaneously.

The single-channel ODMR-CW experiments are looking for the signature dip at the zero field splitting (2.87 GHz). This indicates that NVs are present in the sample and is an early indicator that both the optics and microwaves are operating cooperatively. Following the confirmation of this early litmus test, the optical polarization is adjusted such that each orientation within the sample emits the same amount of fluorescence.

5.1.1 Single-Channel ODMR-CW

The ODMR-CW experiment measures the steady-state response of the photon counts from the $|0\rangle$ bright state, and $|\pm 1\rangle$ dark state in the absence and presence of a sweeping microwave frequency, respectively [37]. If NV centers are present, the ODMR-CW experiment yields a signature dip in the photon counts, normalized to the reference bright state counts, equal to the zero field splitting frequency centered about 2.87 GHz in the absence of a magnetic field.

ODMR-CW Pulse Diagram

The ODMR-CW experiment differs from all the other experiments performed, in that all the measurements are a steady-state response. Figure 5.1 shows the pulse sequence required for a ODMR-CW experiment. First, the laser pumps continuously while the detector measures the bright state photons in the absence of an applied microwave field. Second, this is repeated including a square pulse of microwaves at one frequency at the same time as the laser and detector. Each of these two sections occurs over the timescale of milliseconds, as opposed to the microsecond timescale for all other experiments conducted.

The microwaves are swept over a range of values, and each sequence repeated (n=50) times to acquire enough photons for signal analysis. Typically, microwaves are swept over a range of tens of MHz, centered about 2.87 GHz. To remove the influence of possible laser intensity drift, once the microwave range has been selected, each value of frequency is selected randomly rather than sequentially. Once all values of microwaves have been used, the entire sequence is repeated for (N=8) averages.

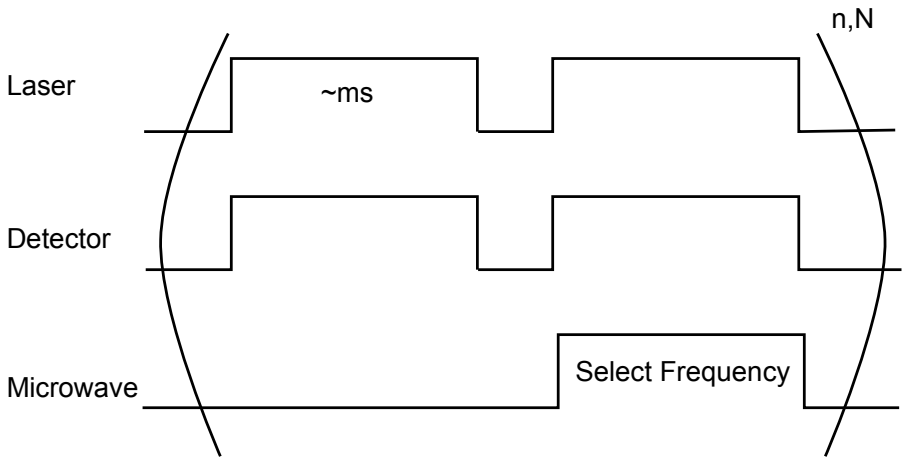

Figure 5.1: The pulse diagram for an ODMR-CW experiment. To measure the bright state ($|0\rangle$) photons, the laser and detector are pulsed simultaneously for tens of milliseconds. To measure the dark state ($|\pm 1\rangle$) photons, the laser detector and microwaves are all pulsed for tens of milliseconds simultaneously. For each sequence, the microwave is pulsed at one frequency, and repeated (n=50) times. The microwave frequency is then changed, and the entire sequence is repeated again until all the values of microwave spectrum are acquired. Once all the values of microwaves have been acquired, the process is repeated (N=8) times for averaging.

ODMR-CW Experimental Data

Figure 5.2 shows the experimental ODMR-CW results from each of the microstrips. Comparing these early experiments is a good indicator of the response of the NV ensemble from each of microstrip. For all the following experiments, each microstrip will be referred to as Channel 1 (CH1) and Channel 2 (CH2), respectively. This is done recalling that the microstrips may be exchanged with any microwave source, including coils, resonators etc.

This experiment was conducted with no intentional external static magnetic field added, and microwaves swept from 2800 MHz to 2940 MHz, centered about 2870 MHz. The figure shows only the points from 2860 MHz to 2880 MHz to highlight the central dip more clearly. Outside this range, the photon count remain at a normalized output value of 1. Each experiment was conducted at the same input microwave power of 32 dBm (1.6 W). The input power was measured in an oscilloscope at the entrance of the PCB board into the sample. The input phase was zero from each of the microwave sources, channel 1 and channel 2. For both experiments, each frequency data point was repeated for (n=50) times and then the entire spectra was averaged (N=8) times. The error bars for each ODMR-CW plot are given by the standard deviation of the normalized photon counts for each N average, subtracted from the total averaged normalized photon counts. Essentially, it shows the spread of the normalized photon counts away from the average normalized photon count.

There is a similar response from each channel. The horizontal grey line represents half of the maximum, and the vertical grey lines are the width at the half maximum value. For both microstrips the full width half maximum (FWHM) value is 8.5 MHz. In each case, the photons are normalized so the value of 1 represents the $|0\rangle$ bright state and the dip represents the $|\pm 1\rangle$ state. The contrast between the bright and dark states were $\approx 5\%$ for each channel. In both channels, the dip is centered about the expected zero field splitting of 2870 MHz, but is split by 2.75 MHz and 3 MHz for channel 1 and 2, respectively. Each dip corresponds to the $|+1\rangle$ and $|-1\rangle$ states. The equal contrast measured between each of the dips states indicates there is no preference to either the $|+1\rangle$ or $|-1\rangle$ states of the NVs.

This splitting may originate from a combination of stray magnetic fields, interactions with other impurities within the diamond crystal, crystal strain and charge inhomogeneity. As there was no shielding used in this setup, some external stray magnetic fields are not unexpected. In addition, with a high density diamond sample which has had no treatments completed, effects from crystal strain and other spin interactions within the crystal is not unexpected. Further investigation of the causes of this splitting could be included in future experiments, but in this case, it is small enough to proceed with the next experiments without further study.

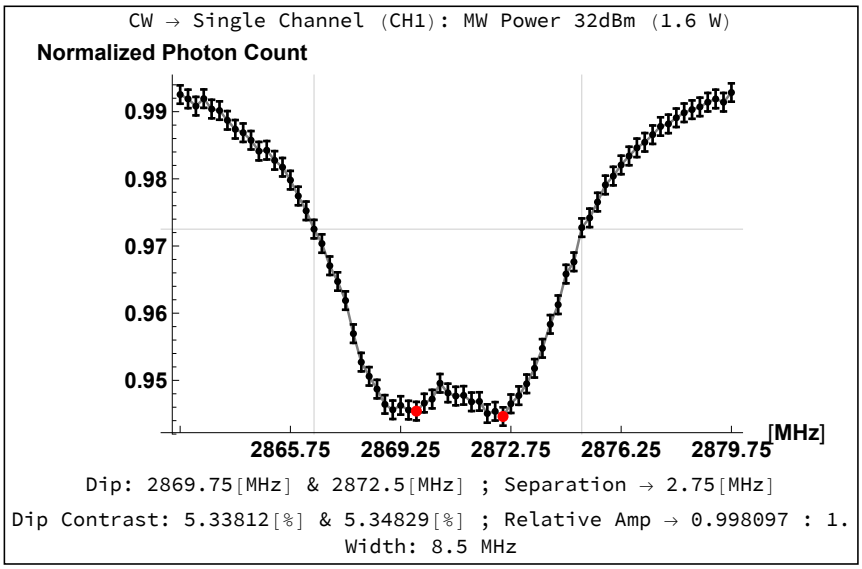

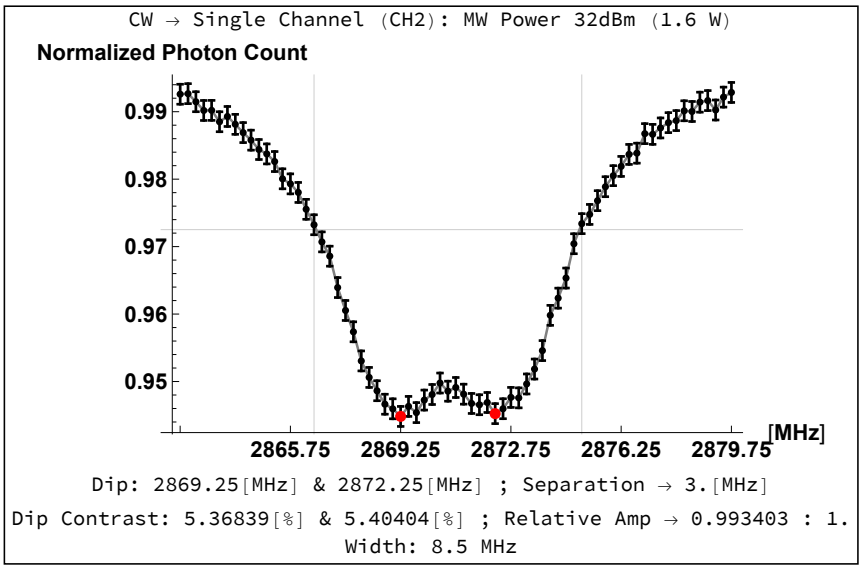

Figure 5.2: ODMR-CW for each stripline, channel 1 (CH1) **(Top)** and channel 2 (CH2) **(Bottom)** in the absence of a static magnetic field. Both channels show similar results. The linewidth from both channel 1 and channel 2 are 8.5 MHz. The average contrast from each channel 1 and channel 2 are also similar at $\approx 5.3\%$. Each of the spectra is centered around 2870 MHz, corresponding to the zero field splitting (ZFS) of the NV center. There is also a small splitting of 2.75(3) MHz ($\approx 1\ G$) centered about the ZFS for each channel, likely originating from the combination of a stray field, crystal strain, interactions with other impurities and charge inhomogeneity. Equal contrast between each of the dips in the split indicate there is no preference of state population to either the $|+1\rangle$ or $|-1\rangle$ states.

5.1.2 Selecting the Optical Polarization for NV Ensembles

Description of the Molecular Orbitals and Electronic Configuration of the NV Center

NVs are sensitive to not only the polarization of the microwaves, but the optical polarization of the incoming light as well. To understand the relationship between optical polarization and the NV center, the wavefunction of the NV center needs to be described. Figure 5.3 shows the electron configuration for an NV^- center and the higher energy molecular orbitals. Recall the NV^- is formed by the contribution of six electrons, two from the surrounding Nitrogen, three Carbons and one electron in the vacancy. These electrons form the molecular orbitals, $a_{1'}$, a_1, e_x and e_y. The $a_{1'}$ orbital lies below the valance band of the diamond, but a_1 and the higher energy orbitals are found in the band gap, [5, 27, 28, 92]. These molecular orbitals form a $C3_v$ symmetry, which has its three high energy orbitals, a_1, e_x and e_y oriented 120° apart from each other, symmetrical about the vertical axis. The vertical axis aligns with the principle axis system (P.A.S) of the NV center, the bond between the Nitrogen and the Vacancy.

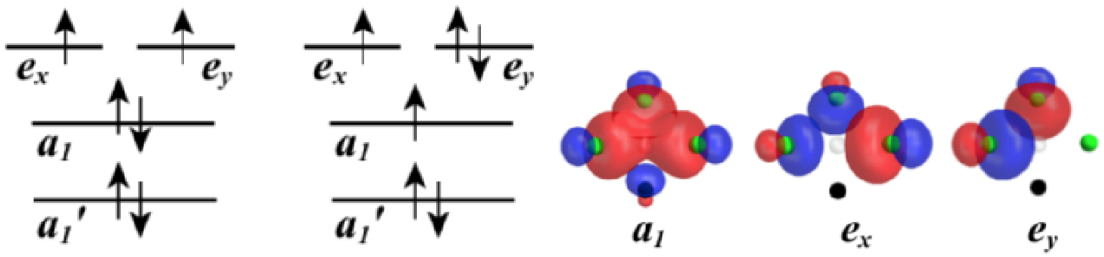

Figure 5.3: The higher energy molecular orbitals and electronic configuration of the NV center. **(Left)** The electronic configuration of the NV^- center, consisting of six electrons. The left configuration shows the ground state and the right, the excited state. When excited from the ground state, an electron may be promoted from the a_1 orbital to the e_x or e_y orbital. The a_1' orbital lies below the valance band of the diamond and is not included in electron promotion. **(Right)** The molecular orbital configuration of the three higher energy orbitals of the NV center, labelled a_1, e_x and e_y. Following a $C3_v$ symmetry, these orbitals are oriented 120° from each other, about the vertical axis (the P.A.S). Image sourced from: [5]

The unpaired electrons form the wavefunction of the NV center. In the ground state, the wavefunction is made from the two unpaired e_x and e_y orbitals and in the excited state are a_1 and either e_x or e_y, depending on where the electron gets promoted to. The description of the ground and exited triplet wave functions are shown below in equations 5.1 and 5.2, respectively, with the orbital configuration and spin state indicated. The $+, 0, -$ refers to the spin state of $m_s = (+1, 0, -1)$ for a spin-1 particle. There are singlet states as well, but are not shown in the equation below, [5, 106].

$$\begin{aligned} |^3A_2^+\rangle &= |e_x e_y\rangle \\ |^3A_2^0\rangle &= |e_x\overline{e_y}\rangle + |\overline{e_x}e_y\rangle \\ |^3A_2^-\rangle &= |\overline{e_x e_y}\rangle \end{aligned} \tag{5.1}$$

And the excited triplet state:

$$\begin{aligned} |^3E_{X/Y}^+\rangle &= |a_1 e_{x/y}\rangle \\ |^3E_{X/Y}^0\rangle &= |a_1\overline{e_{x/y}}\rangle + |\overline{a_1}e_{x/y}\rangle \\ |^3E_{X/Y}^-\rangle &= |\overline{a_1 e_{x/y}}\rangle \end{aligned} \tag{5.2}$$

NV Center Dependency on Polarization - Simulated Results

The allowed dipole transitions from the ground to excited states are satisfied when $\langle\psi_f|\vec{d}\cdot\vec{E}|\psi_i\rangle \neq 0$, where $\psi_{i/f}$ are the initial and final wavefunction, $\vec{d}$ is the NVs dipole and $\vec{E}$ is the incoming electric field vector. In short, if the NV is excited with linearly polarized light whose electric field lies along the NVs "x" axis, the electron will be promoted from the ground state, A_2 to E_x and A_2 to E_y if the NV is excited with light along the "y" axis, [73].

$$\begin{aligned} &\langle^3E_x|\hat{x}|^3A_2\rangle \\ &\langle^3E_y|\hat{y}|^3A_2\rangle \end{aligned} \tag{5.3}$$

Recalling that the vector between the Nitrogen and the Vacancy forms the "Z" axis, and this "Z" axis may be oriented in four different directions within each diamond crystal, the same incoming polarization of light will project in four different orientations associated with the four NV axes, as the xy plane for each NV lies perpendicular to the "z" axis.

Figure 5.4 shows the projection of Horizontally polarized light propagating along the lab frame "z" axis on each of the four orientations of NVs in the (100) diamond. The NVs axes are also shown, NVx, NVy and NVz, recalling that NVz is the P.A.S. The figure is clear to show that for the same incoming polarization of light, the propagation axis projects differently along each of the NV "z" axis, and the polarization projects differently for each of the "x" and "y" axes.

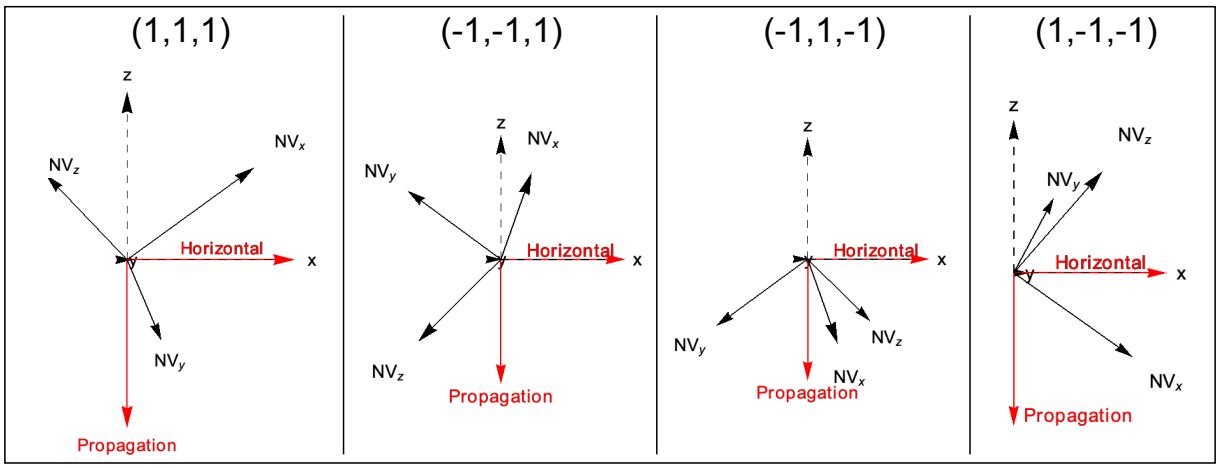

Figure 5.4: A model demonstrating the relative geometries of all the NV orientations in the (100) diamond with the same incoming horizontal polarization. The light propagates along the z optical axis, with a linear, horizontal polarization, having its electric field along the "x" axis in the lab frame. Each NV is shown in the lab frame, to show how the NVs "x", "y" and "z" axis is oriented relative to the common lab-frame. The maximum intensity output from an NV occurs when the electric field of the incoming light aligns with the NVx or NVy axis.

To promote an electron from the ground to excited state, it must do so with only the allowed dipole transitions. When a photon is released, it decays from the same dipole transition, $E_{x/y}$ state to A_2 state. For maximum excitation and therefore fluorescence from the NV, the polarization of the light would align with the NVx or NVy axis. This is shown below, where θ is the angle between the NVs P.A.S (z) and the propagation (optical) axis of the incoming beam, ϕ is the angle between the NVs "x" axis and the polarization of the incoming beam, and $IE_{x/y}$ are the intensities of emission from E_x and E_y. $ITot$ is the total intensity, the linear combination of the two, [110]. As E_y is maximized, E_x is minimized and vice versa, reflected in $ITot$.

$$\begin{aligned} IE_y(\phi) &= \sin(\phi)^2 \\ IE_x(\theta,\phi) &= \cos(\theta)^2\cos(\phi)^2 \\ ITot(\theta,\phi) &= \sin(\phi)^2 + \cos(\theta)^2\cos(\phi)^2 \end{aligned} \tag{5.4}$$

As the sample orientation and propagation axis of the beam are fixed, the "z" axis of the NV may not be adjusted, and therefore θ is fixed for all experiments. Only ϕ may be adjusted. The symmetry of the (100) diamond results in all orientations sharing a common θ value, that is, their angle away from the lab frame "z" axis is equal. As ϕ is changed, the intensity oscillates in pairs between two of the NVs, the (1,1,1), (-1,1,-1) and (-1,-1,1), (1,-1,-1). While there is not one common value which maximizes all NVs, there is a value which allows for equal fluorescence output from each. This is very valuable in an experiment, as there should be no preferential emission from any NV orientation.

The (110) diamond and (111) diamonds have unique responses for each of the NVs as there is no symmetry about the "z" axis like there is observed for the (100) diamond. As such, there is no one polarization which results in an equal fluorescence from each NV. An interesting result is shown in the (111) diamond with the (1,1,1) NV, which lies along the "z" axis, therefore of course it would always emit with maximum intensity and would be invariant with polarization. As a result of not being able to find one value for equal fluorescence for the (110) and (111) diamonds, the (100) diamond was chosen to be used these experiments, as an equal fluorescence from all NVs is preferred.

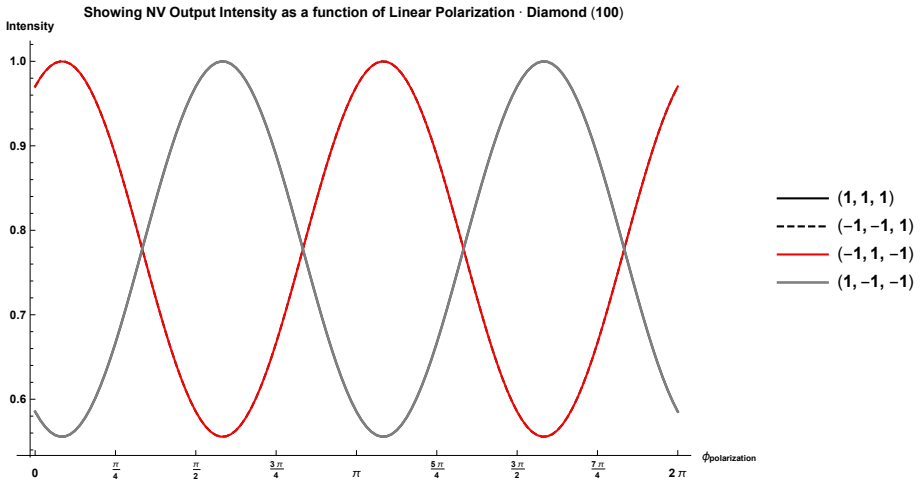

Figure 5.5: The simulated results for output fluorescence from the NV center. The symmetry present with the NV orientations in the (100) diamond results in pairs of NVs showing identical polarization responses. There does exist one polarization which results in equal fluorescence to be emitted from all NV centers in the (100) diamond.

NV Center Dependency on Polarization - Experimental Results

The ODMR-CW spectra of the (100) diamond as a function of the incoming polarization is shown in figure 5.6. The data at each frequency is repeated (n=50) times, and the entire frequency range averaged (N=10) times. The error bars are given by the same technique as with the single-channel ODMR-CW experiments. A static magnetic field was added to split the spectra into eight peaks, with a maximum separation of $\approx$ 500 MHz. The eight peaks correspond to the $|\pm 1\rangle$ ground states of the four orientations of NVs within the diamond crystal. To change the incoming polarization, the half wave plate (HWP) in the mode shaping arm was rotated by a relative value of 0° to 160°, the values of 0° to 60° are shown in the figure. Note that as the polarization entering the half-wave plate was unknown, these values of 0° $\rightarrow$ 160° are not absolute, and dependent on the optical setup. An absolute value of polarization may be determined using a half-wave plate and linear polarization to rotate and then filter the polarization until a known polarization value is set. This was not required for these experiments; a relative polarization value to reach equal fluorescence from all NVs is sufficient. In accordance with the simulations shown above, as the polarization changes, the direction of the electric field aligns with different NV orientations, changing the output fluorescence. Additionally, the enhancement and suppression of the fluorescence occurs in pairs, as was seen in the simulations.

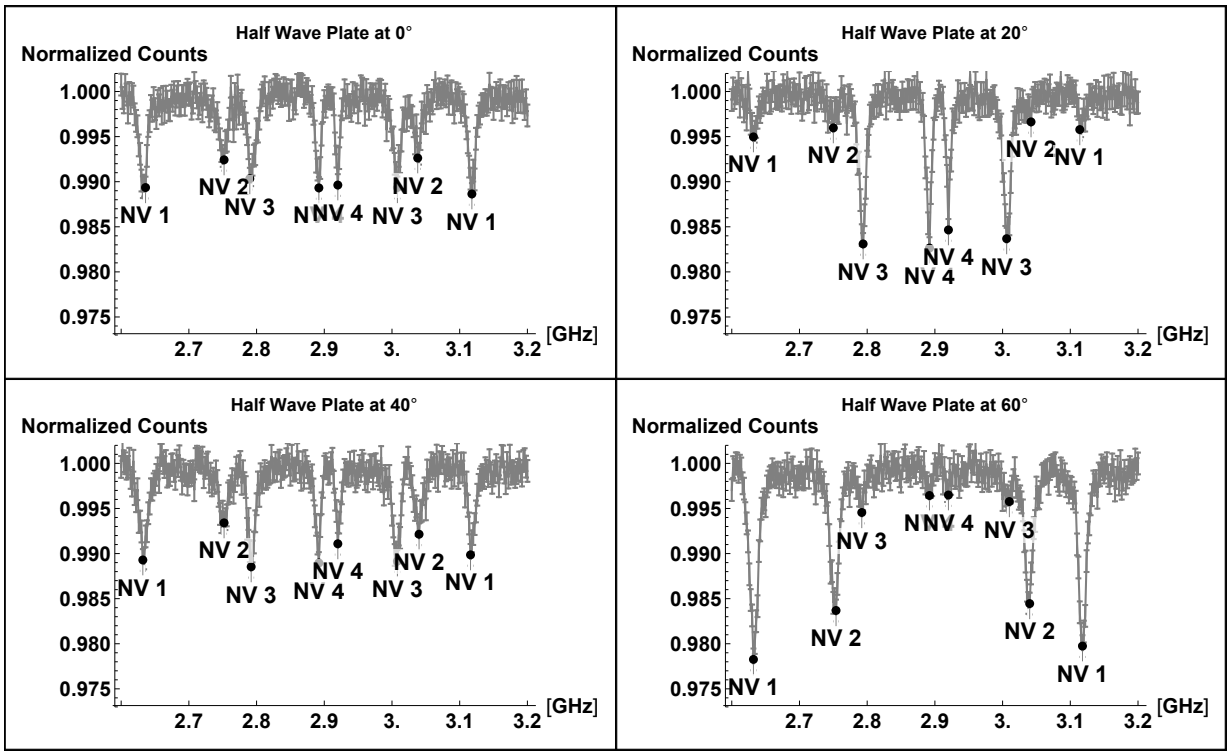

Figure 5.6: The ODMR-CW spectra as a function of the incoming optical polarization. A static magnetic field of unknown orientation was added to split the spectra, revealing eight peaks, corresponding to the $|\pm 1\rangle$ ground states of the four different orientations of the NV centers present within the (100) diamond. As the incoming polarization changes to align the electric field along the electric dipole of the NV orientation, fluorescence is favoured in some orientations over others.

For the experiments being conducted, all NVs should output the same intensity of fluorescence. Large changes in the polarization indicated that an experimental value nearing 40° showed similar fluorescence of all NV orientations. This experiment was duplicated with smaller changes in the polarization. A value of 42° was determined to be the optimal value for achieving equal fluorescence from the NVs. The variance in fluorescence at 42° is 0.016%.

5.2 Dual-Channel ODMR-CW Experiment

The dual-channel ODMR-CW experiment gives early indications that the NV ensemble responds to the phase difference between the two channels. Response to difference in phase is necessary for the success of the OCT experiments.

The pulse sequence is the same as the single-channel ODMR-CW experiment, with the exception that instead of having one channel irradiating microwaves, both irradiate simultaneously. As with the single-channel ODMR-CW, there is first a steady-state collection of the bright states without microwaves, and then a steady-state collection of the photons with both channels on while the microwave frequency sweeps incrementally until all values have been gathered. This experiment was performed in the absence of an external static magnetic field.

Figure 5.7 shows the results from a dual-channel ODMR-CW experiment. The incoming amplitude from each channel was set to be equal at a relative value of $\Omega_1 = \Omega_2 = 1$ and equal incoming phase of $\theta_1 = \theta_2 = 0°$. To gather the data, consistent with the ODMR-CW experiments, the data at each frequency is repeated (n=50) times, and the entire range averaged (N=8) times. The contrast is greater than the single-channel ODMR-CW, at 8.3% and width also greater at 10.25 MHz. The error bars are given by the same method as for the single-channel ODMR-CW for each ODMR-CW, the standard deviation of the normalized photon counts for each N average, subtracted from the total averaged normalized photon counts. The increased peak width nearly covers the split centered about the zero field splitting value at 2.87 GHz, showing a separation of 2.5 MHz. As with the single-channel ODMR-CW, there is no preference given to either the $|+1\rangle$ or $|-1\rangle$ state with this combination of phase values.

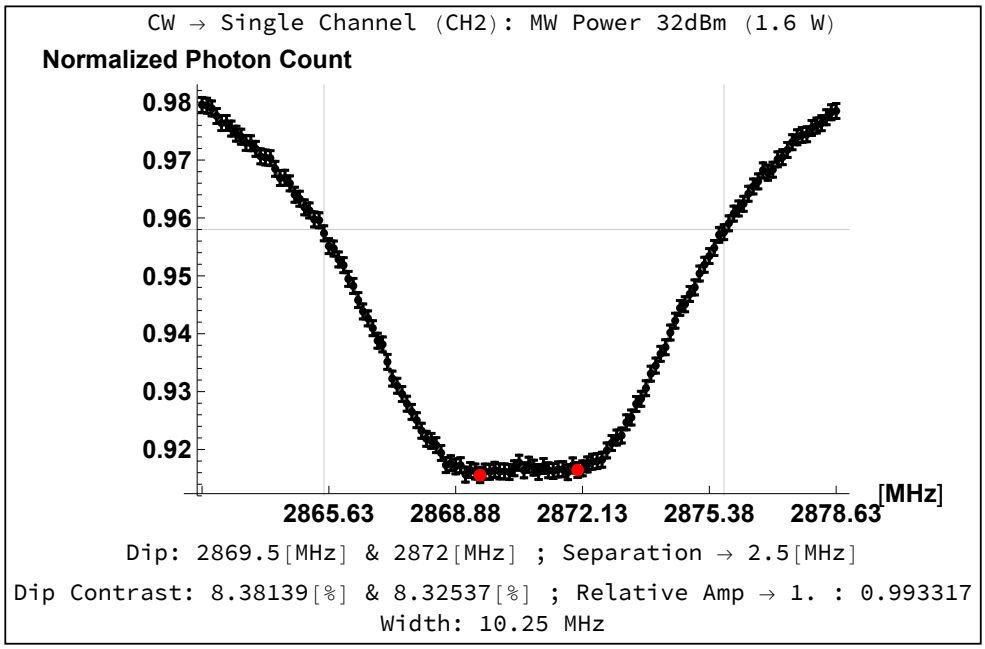

Figure 5.7: ODMR-CW for ensembles of NVs with two microstrips. Comparing to the single stripline experiment, the peaks have broadened from the increased total power, nearly losing the ability to distinguish between the $|+1\rangle$ and $|-1\rangle$ states. The distinction between the two peaks is still measured to be 2.5 MHz, centered about 2.87 GHz. The FWHM is indicated with the single horizontal line and two vertical lines, giving a width of 10.25 MHz. Compared to the single-channel experiment, the width has increased, but also has the contrast to $\approx 8\%$.

Circularly polarized microwaves allow for single transitions on the NV ensembles. The ODMR-CW experiment may be used as an early indicator for the ensembles' sensitivity to the phase. As there is a small stray field present, which splits the degeneracy between the $|\pm 1\rangle$ states, by 2.5 MHz, monitoring the results of changing the phase between the two channels can indicate early phase control.

Figure 5.8 shows the results of having channel 1 phase at $\theta_1 = 0°$ and $\theta_2 = 90°$, while the amplitude from each channel was kept at $\Omega_{1/2} = 1$. Each data point was repeated for (n=50) times and then the entire spectra was averaged (N=8) times. The figure shows the amplitude of the $|+1\rangle$ state is $\approx 7\%$ less than the amplitude for the $|-1\rangle$ state, and the separation between the two peaks is clear.

The contrast is also less than the CW experiment with both phases at zero, at only 5.5%. The purpose of this experiment is not to show optimal selection between the two transitions, but to simply show the sensitivity to the change in phase between the two channels, which is clear.

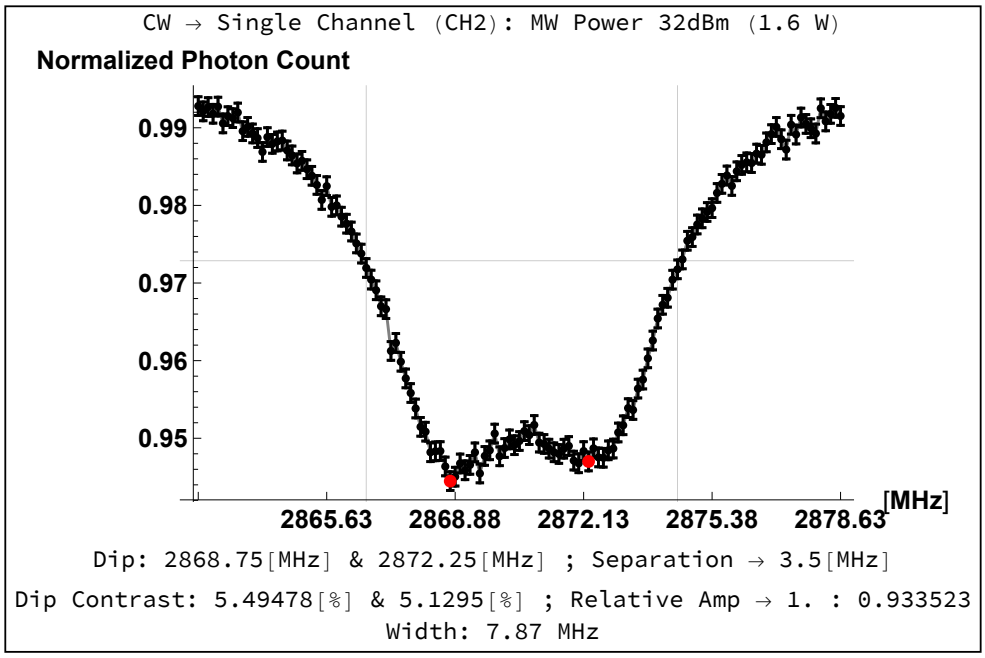

Figure 5.8: Dual-Channel ODMR-CW for ensembles of NVs with phase variation. By changing the phase between the two channels, the distinction between the $|+1\rangle$ and $|-1\rangle$ states re-appear, and additionally, one of the transitions is favoured over the other. This shows preliminary single transition selectivity with a low magnetic field ($\approx$1 G of stray field). In the total absence of any static field, selectivity cannot be shown with a ODMR-CW experiment, even with two independently controlled microstrips. This stray field totalling $\approx$3 MHz separation is convenient to be used for these preliminary selection experiments.

Both the single-channel and dual-channel ODMR-CW experiments allowed for early indication that the NV ensemble is behaving as intended. The single-channel ODMR-CW experiment did address the optical polarization that is set for the remainder of the experiments. The dual-channel ODMR-CW experiment indicated that each of the channels behave similarly so no immediate adjustments were required to be made on the setup.

5.3 Laser Initialization

Unlike the CW experiment, the following experiments do not measure a steady-state difference between the bright and dark states. They use the same base pulse sequence; initialization of the NVs, count the bright states, followed by the experiment and then counting the states as a result of the experiment. The same length of initialization and counter window is used for each experiment.

The laser initialization experiment first determines the length of time required to initialize all NVs within the focal volume. Despite the best efforts to produce a planar beam across the back of the objective to give the most uniform beam intensity, the intensity of the incoming beam across the volume of NVs will not be identical. If the initialization is too short, some NVs within the excitation volume will not be fully initialized before the experiment begins. Having an initialization time that is too long simply adds time to the experiment.

This experiment may also be used to determine the optimal length to collect photons from the NVs. If the detection window is too short, it will not collect enough photons, however if it is too long, the signal-to-noise ratio with be reduced.

This experiment also corrects for the laser delay of being switched on and off. While the optical switch has switching times on the order of nanoseconds, the signal to control the switch is controlled by a transistor-transistor logic (TTL) from the arbitrary waveform generator (AWG), and so a delay for this signal can be measured and corrected.

5.3.1 Laser Initialization Pulse Diagram

The pulse sequence for the laser initialization is shown in figure 5.9. The laser is pulsed in two windows with a π pulse given by the microwaves in between, so the photon collection for bright and dark counts may be compared. In the first instance, the π pulse may be estimated, but later refined once the π pulse has been determined from a Rabi experiment. The starting and stopping time of the laser are also controlled to determine the starting delay and window length.

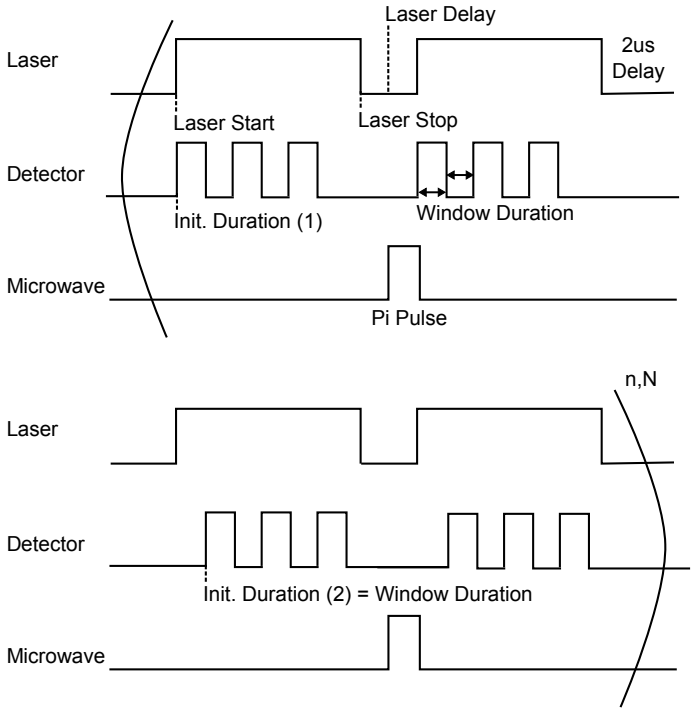

Figure 5.9: Laser initialization pulse sequence. The laser is pulsed two times for each detection train, separated by a π pulse. The starting and stopping point of the laser determine the laser start delay and length of time the laser is pulsed for. The detector collects the photons from the bright and dark states, given by the π pulse. To increase the resolution of finding the optimal detection window, the detection windows are broken into trains and the photons accumulated from each during signal processing. There are two detection trains, given two initial start times and window length, and repeated for (m) windows.

The detector is pulsed (m) times in two trains, each given an initial duration time (1 and 2) and window length. The initial duration time of the second train (2) is equal to the window length. There are two detector trains, with delays between each window so that the photon collection from each discrete window may be added up to prevent switching delays in the detector from inducing an error. For this experiment, the window length was 200 ns, while the number of windows was (m=200). Dividing the detection windows into a train of discrete windows yields higher resolution when finding the optimal detection window length, by accumulating the photons from each successive window.

The entire pulse sequence repeats (n=50 000) times to accumulate enough photons per experiment, and then averaged (N) times. For the laser initialization experiment (N=100) averages. Each experiment following the laser initialization uses the same number of (n) repeats, as the window length and initialization time is dependent upon (n). However, each following experiment can vary in the number of averages (N).

To determine the delay for the laser to turn on, the laser start is delayed from the detection start. The experiment shows the moment the photons are detected by the detector. This laser on delay is a hardware delay and not experiment specific. Once it has been found, this does not need to be adjusted again unless the laser or detector are changed. This process is also repeated to see when the laser turns off, so a delay for this may also be accounted for in experiments. For this optical setup, the laser delay is 800 ns.

5.3.2 Initialization Time for the NV Ensemble

The initialization time of the laser is determined by the time it takes the NV ensemble to reach the $|0\rangle$ steady-state, [92]. Figure 5.10 shows the bright (black) and dark (red) counts by total length of time. There are no error bars shown here as this is raw data. The initialization time is determined when the bright and dark counts become indistinguishable. This initialization time is determined by the incoming power of the laser. A higher incoming intensity will give a shorter initialization time. For an incoming laser power of ≈ 0.4 mW, the initialization time is 60 μs. Unless the incoming power is changed to the setup, the initialization time will stay the same for all experiments.

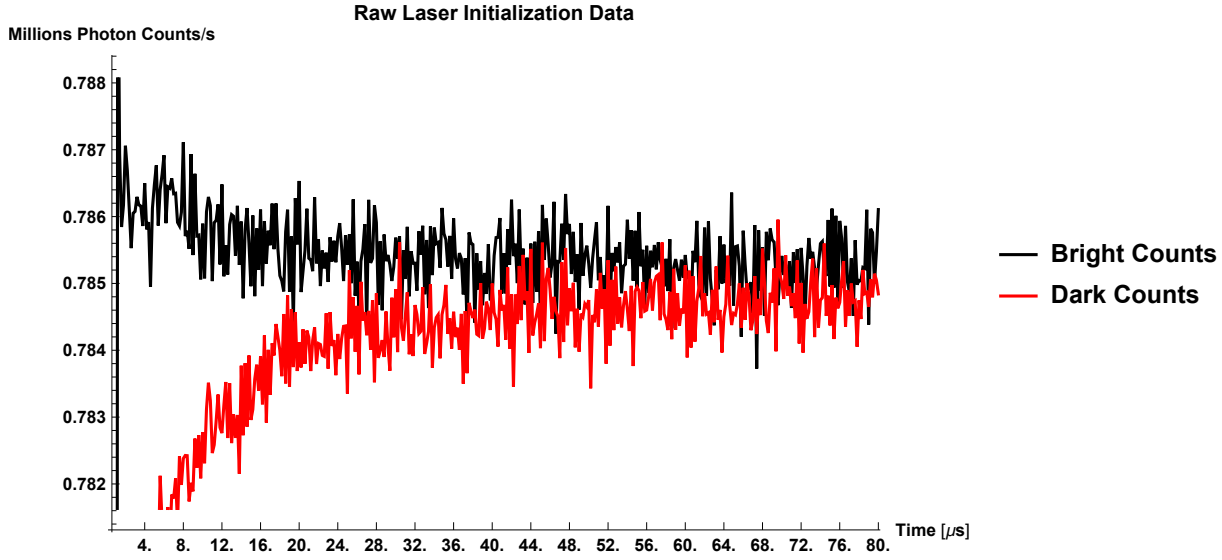

Figure 5.10: The bright (black) and dark (red) counts for the laser initialization experiment. The point at which the bright and dark counts become indistinguishable indicates the length of time the NVs require to be initialized. For an incoming laser power of ≈ 0.4 mW, the initialization time is 60 μs.

5.3.3 Determining the Optimal Detection Window Length

The optimal readout length may be inferred from the same data used to gather the initialization time. As this time also depends on the incoming laser power, once set, this is kept consistent for all of the following experiments.

Figure 5.10 shows the raw bright and dark counts for the laser initialization experiment. Qualitatively, it can be seen that at short times, there is a large contrast between the bright and dark counts, but a low number of total accumulated photons. As the detection window length is increased, the contrast between the bright and dark cases decreases until they become indistinguishable. To determine the optimal window length, first the bright and dark state counts are subtracted to find the contrast value. Then the average of the contrast is divided by its standard deviation over the length of time. Figure 5.11 shows how this relationship changes with time, processing the data from figure 5.10 to find the optimal detection window length. The optimal detection window is 1 μs, given by the maximum.

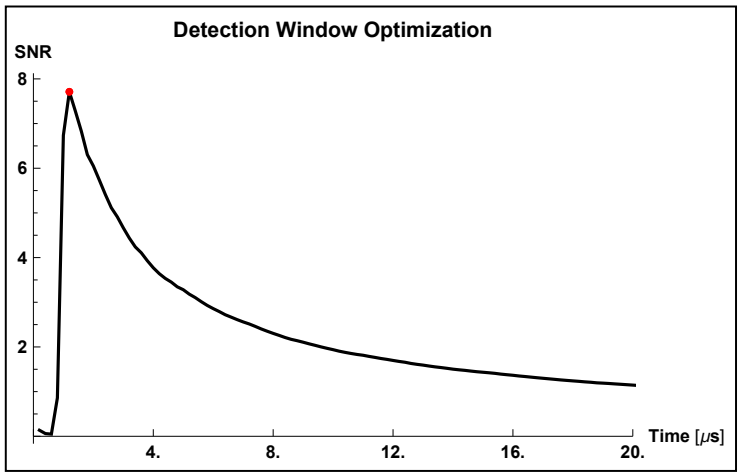

Figure 5.11: The length of the optimal detection window is determined by dividing the average accumulated contrast by the standard deviation of the accumulated contrast. The optimal detection window is 1 μs, at the maximum.

The laser initialization is used to determine the base experimental sequence for all of the following experiments. In all cases, the same hardware delays are included, as well the same initialization and readout time.

5.4 Single-Channel Rabi

The Rabi experiment gives the amplitude of each microwave source relative to the NV ensemble, length of $\frac{\pi}{2}$, and π pulses. The Fourier transform of the Rabi shows the presence of the sub-ensembles, and may inform the geographic location of the NV ensemble relative to the microstrips.

5.4.1 Single-Channel Rabi Pulse Diagram

The basic structure of the Rabi experiment is broken into two segments, the initialization and bright state count followed by the experiment and dark count detection. Figure 5.12 shows the experimental sequence for the Rabi experiment conducted with this setup.

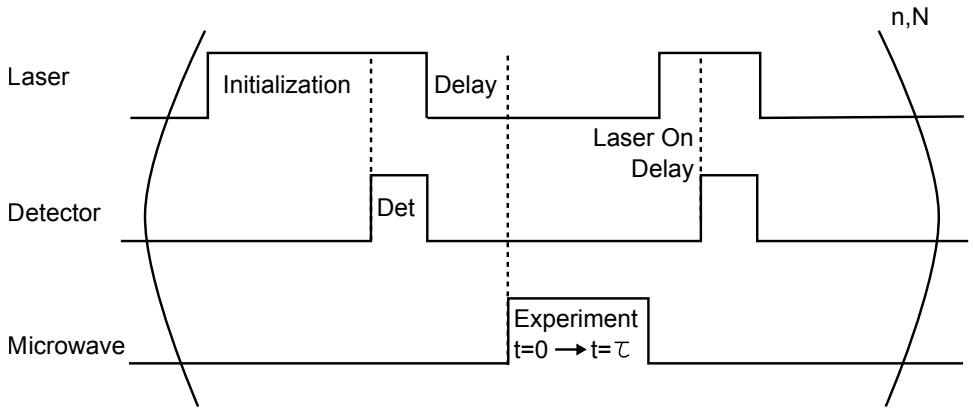

Figure 5.12: Rabi pulse sequence. The laser, detector and microwave sequences are shown, which together create the Rabi experiment. There are two main stages, the initialization and bright count detection and second, the experiment and dark state count. First, the laser initializes the states and the detector is then turned on to count the bright states. A short delay following the initialization gives time for the laser to turn off. The microwaves are applied with a square pulse which is incremented from time $t = 0 \rightarrow t = \tau$. Following the square pulse, the laser and detector are turned back on to detect the dark counts. To reduce the error from laser drift intensity, the values of (t) are chosen randomly until all values from $0 \rightarrow \tau$ have been used. Each value of square pulse (t) is repeated (n=50 000) times to gather enough photons per experiment. Once all the values of (t) have been used, the entire sequence is repeated for (N) averages.

In the first step, the laser is turned on for the length of time determined by the laser initialization experiment. Following the initialization, the counter is turned on to detect the base bright counts of the $|0\rangle$ state. A delay is left after this to allow the laser to turn off, a time also determined by the laser initialization experiment, 800 ns.

Following this, the microwaves are applied in a simple square pulse. For the Rabi experiment, the time of the microwave is incremented from $t = 0 \rightarrow t = \tau$. Following the microwave pulse, a delay of $\tau - t$ was added so each experiment would be the same length, no matter the value of t. Following the square pulse, there is again a small delay of 800 ns to allow the laser to turn on, and then the laser and detector are turned on to collect the counts from the experiment. To process the data, the experimental counts are normalized against the bright counts.

For each value of (t) chosen for the square pulse, the experiment is conducted for (n=50 000) repeats to acquire enough photons. Further, as a best practice to prevent errors from laser intensity drift, the values of t are randomly selected over the values from $0 \rightarrow \tau$. Once all the values of (t) have been used, the entire sequence is repeated for (N) averages. For a typical Rabi experiment, N=100 to 200 averages.

This pulsing sequence is used for both single-channel experiments with no deviations. The same initialization time, readout time, microwave power and pulse lengths were used.

5.4.2 Single-Channel Rabi Time Data

The Rabi time data may inform the contrast between the bright and dark states and indicate the lifetime of the NVs. Figures 5.13 and 5.14 show the Rabi time data for each of the microstrips, Channel 1 and Channel 2. The time data shows the photons normalized to the bright state, where a value of 1 would be $|0\rangle$ and deviation from that indicates the dark state. These experiments were done in the absence of a magnetic field, so the expected dark states are a mixture of the $|\pm 1\rangle$ state.

The results from both microstrips share common features. At first, the states are seen to be in the $|0\rangle$ at t=0. In a short time, there is a very fast decay away from the $|0\rangle$ state, decaying to the dark state with a contrast of $\approx 3\%$. This large dampening from the initial state has been observed for diamonds with a larger concentration of NVs, [18]. For both channels, looking beyond 0.5 μs, the data shows a far more steady-state solution. Both channels show a similar contrast, transient response, lifetime and beating patterns, giving an early indication that the NV ensemble would be located at similar distances away from each stripline. For both single-channel Rabi experiments, each data point at t was repeated (n=50 000) times, and the whole experiment averaged (N=140) times. The error bars were gathered in the same fashion as for the ODMR-CW experiments, given by the standard deviation of the normalized photon counts.

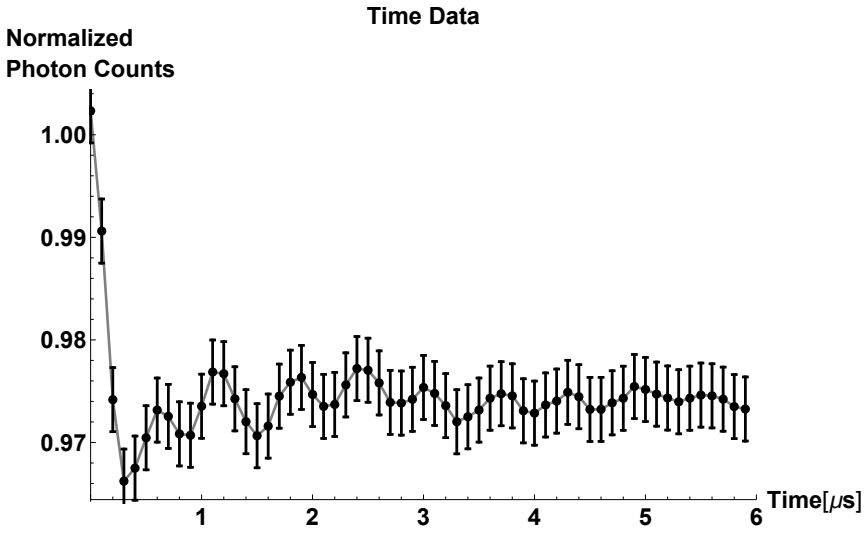

Figure 5.13: The Rabi time data for channel 1. There is a clear difference between the transient response and steady-state response of the data. For time ≤ 0.5 μs, there is a sharp dip of $\approx 3\%$ contrast. The steady-state response shows a more consistent contrast at $\approx 0.5\%$. It is evident from the time data there are two oscillations occurring, from the two pairs of NV orientations found within the diamond crystal.

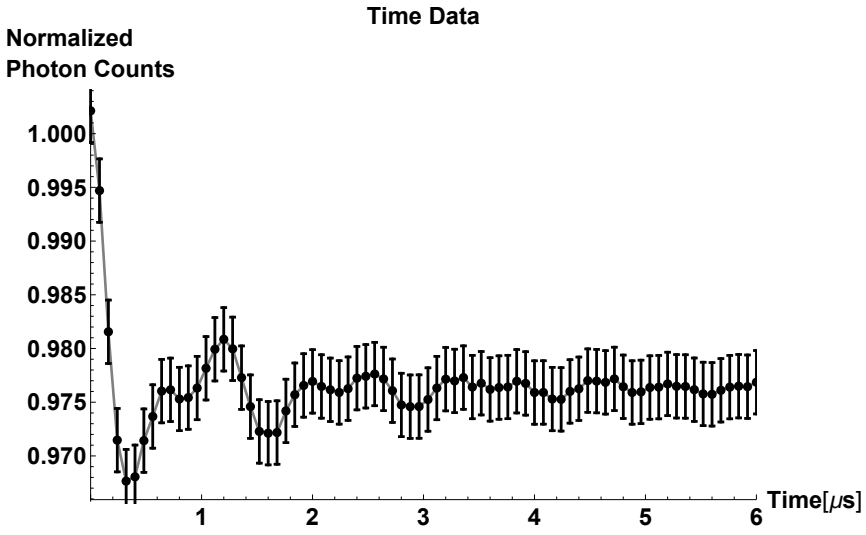

Figure 5.14: The Rabi time data for channel 2. This data shows a very similar response to the channel 1 stripline. A large sharp dip at the beginning of the data, followed by a more consistent steady-state response. The similarities in contrast, beating and transient vs. steady-state solutions between each stripline indicate the NV ensembles is a similar distance away from each of the microstrips.

For both channels, it is evident from the time data that there are two frequencies seen here, as the Rabi experiment shows two oscillations. This will be more evident in the frequency spectra of the data. These two oscillations come from the two pairs of NV orientations within this diamond crystal. This is expected for the crystal and microwave field configuration.

5.4.3 Simulating the Fourier Response

The time data offers initial insight into the behaviour of the NV ensemble and the relative response to each channel. Transforming to the Fourier domain yields more information into the response of the NV ensembles with each channel. Before looking at the experimental data in the Fourier domain, a few simulations of NV ensembles in the (100) with this microwave field configuration can be shown to understand the general behaviours and interpret the experimental data more easily.

There are three main effects on the Fourier response in a single-channel Rabi experiment, which may be simulated. First is simulating the effect of NV orientation on the Fourier response. The (100) diamond shows two peaks, separated by a ratio of (0.57:1) without including geometric effects. Second, the effect of geometry must be included in the Fourier response. Changing the distance between the stripline and NVs, or adjusting the incoming amplitude, simply translates the peaks, but the ratio is unaffected. However, changing the angle between the microstrips and NV (ϕ), will change the ratio between the two peaks. Last, inhomogeneities are introduced into the simulation to mimic more experimental like conditions.

Estimating the Fourier Response without including the NV geometry

The Hamiltonian is dependent upon the geometric location of the NV relative to the microwave source and the rotation parameters defined by each NV orientation in the crystal. As explored in chapter three, with a microwave field aligned along the "x" and "z" axes, it is expected that for a (100) diamond like the sample being used, there would be only two distinct sub-ensembles (section 3.2.2).

Removing the geometric factor from the Hamiltonian, the frequency spectra of a Rabi experiment may be simulated to understand the response dependent on only the NV orientation. A single-channel Rabi experiment was simulated and shown, in figure 5.15. As expected, the dispersive Fourier response indicates only two separate sub-ensembles, separated by a ratio of (0.57:1). This simulation was repeated for multiple Rabi amplitudes, and this ratio did not change. The ringing shown in this figure is the Gibbs phenomenon, a result of truncating the acquisition in time with no decay, [41].

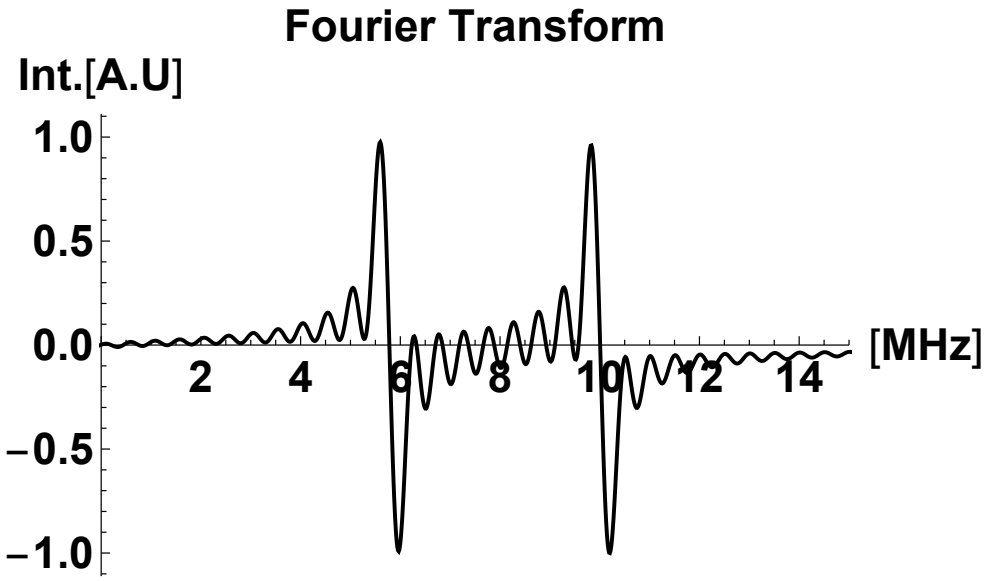

Figure 5.15: Dispersive Fourier Response of a simulated Rabi with no geometry included in the Hamiltonian. Removing the geometry from the Hamiltonian and only including the rotation factors from each NV orientation shows only two pairs of NV orientations, with the ratio between the peaks in the Fourier space being (0.57:1). This serves as the base response for the NV frequency spectra when the field is set along the "x" and "z" axes for a (100) diamond.

Simulating the Fourier Response while changing the relative angle between the NV and the stripline

The Fourier response is dependent on the relative angle between the NV and the stripline, the ϕ value. For the same distance to the wire, as ϕ is changed, the ratio between the peaks will change from their largest distance of (0.57:1) to (1:1). Figure 5.16 below shows how the relative peak ratio between the two detected frequencies changes with moving the location of the NV about ϕ around the stripline. In this case ϕ was changed from $0^\circ \rightarrow 190^\circ$. There is a pattern repeated, where at increments of 45°, the ratio between the peaks is maximized as (0.57:1), and at integers of 90°, the ratio is minimized and the peaks collapse into one frequency response.

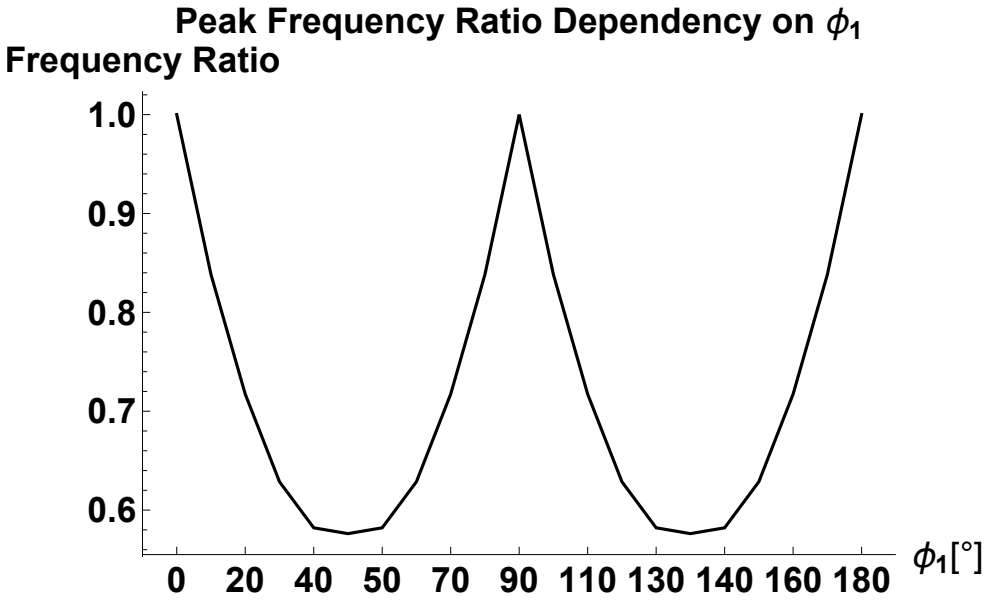

Figure 5.16: Fourier Response dependency on ϕ for a single-channel Rabi experiment. The ratio between the peaks are shown with the dependency on the angle to the microstrips, ϕ. At odd increments of 45°, the ratio is maximized, and in increments of 90°, the ratio is minimized to (0.57:1) where the peaks collapse into the same frequency.

Including Inhomogeneities in the simulated Fourier Response

The previous section saw how the ratio between the peaks changes with the relative angle between the stripline and the site of the NV center ensembles. This is not the only experimental factor to take into account when analyzing the experimental frequency spectra. The previous examples showed both cases where the linewidth of the peaks was ideal, but in experiment, the peaks would be broadened from an ideal value.

Figure 5.17 indicates the results of a simulated frequency spectra when a generic amplitude inhomogeneity is introduced. In the absence of an amplitude inhomogeneity, a change in amplitude, induced by a change in the distance between the stripline and the NVs would result in translating the peaks to a higher or lower frequency, but the effect on the ratio between the peaks does not change. Introducing an amplitude inhomogeneity results in the response to each amplitude becoming averaged, resulting in a broadened response to each.

The left part of the figure shows the dispersive response for the frequency spectra without inhomogeneities **(solid)** compared to the frequency response with a 50% amplitude inhomogeneity included **(dashed)**. Although there are still two peaks and two minima observed with the inhomogeneity, there are no longer two zero crossings as seen without inhomogeneities. To understand this further, the bottom figure shows the dispersive Fourier response of each pair of NV orientation **(dashed)**, and the mean result of each **(solid)**. Looking at each individual response, the inhomogeneity simply broadens each peak, but there is still a zero crossing for each individual pair. When the average response is taken, the spectra overlap so only the mean between the crossings appears. In experimental results, only the average of the frequency spectra is available, so it is important to take great care when analyzing and make sure information is not lost.

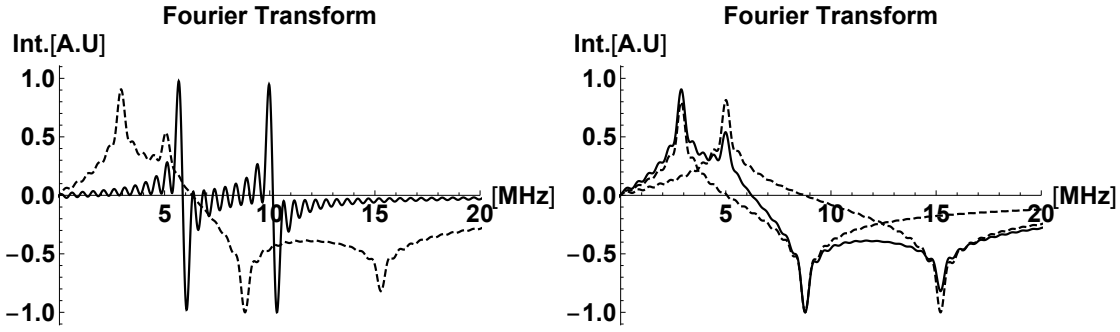

Figure 5.17: **(Left)** The dispersive frequency spectra without inhomogeneities **(solid)** overlaid with frequency spectra with a 50% amplitude inhomogeneity included **(dashed)**. Without inhomogeneities, two distinct peaks are shown, with the ratio between the zero crossings being (0.57:1). With the inhomogeneities, the peaks each broaden, overlapping such that there is only one zero crossing present. **(Right)** The Fourier response of each of the pairs of NV orientations **(dashed)** with the average **(solid)** shown overlapped. This is clear to demonstrate that the response from each peak is still centered about the original Fourier response without amplitude inhomogeneities, but each are broadened. The overlapped spectra will give the average spectra seen in the left figure.

5.4.4 Experimental Fourier Response

The three main trends seen in the Fourier domain pertain to the sub-ensembles of NV orientations, the response to the angle relative to the stripline and last, including inhomogeneities which broaden the linewidth of each response. The experimental results from each of the channels, show much of the same trends. Note that, for both experiments, the focal volume was not moved, so each reflect the response from each stripline to the same geometric location of NVs.

Fourier Response for Channel 1

Figure 5.18 shows the absorptive frequency spectra for channel 1 corresponding to the time data in figure 5.13. The sharp decay in the transient portion of the data contributes a large broad background feature, and indicates four peaks in the spectra. Referring back to the simulations conducted including inhomogeneities, this type of behaviour is not unexpected. The inhomogeneities shown in the transient data split the response to each sub-ensemble, resulting in four peaks present. These four peaks are at 0.39 MHz, 0.78 MHz, 0.97 MHz and 1.6 MHz. It's difficult to speculate which peaks belong to which orientation, without looking at the steady-state response and performing further experiments.

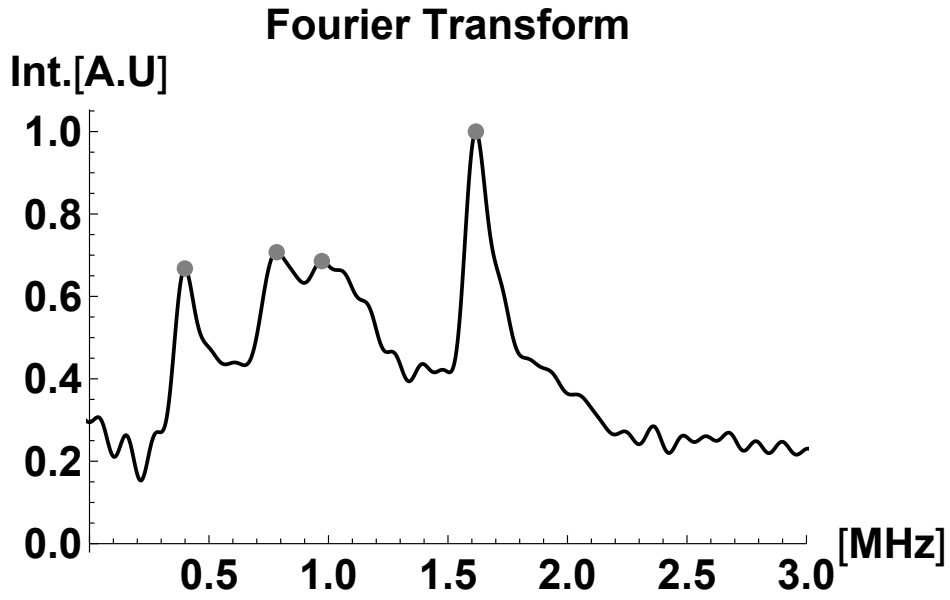

Figure 5.18: Fourier transform of CH1. Full-time data in figure 5.13. The absorptive frequency spectrum shows a large broad background signal, with four peaks, twice what is expected for this orientation of diamond crystal and microwave source. The four peaks are located at 0.39 MHz, 0.78 MHz, 0.97 MHz and 1.6 MHz. These are likely two NV peaks split by inhomogeneities as was seen in the simulated data with inhomogeneities.

To remove the large broad background, a Goldman-Shen experiment is performed, which delays the starting capture time to only capture the steady-state response. The absorptive frequency spectra of the steady-state response shown in figure 5.19 only takes the time data of CH1 (figure 5.13) after the large initial transient response. Removing the transient solution removed the large, broad background feature and reduced the response to the two competing frequencies as expected. When delaying the data to a later time, the two base frequencies become out of phase, with a 90° phase shift, resulting in the higher frequency showing an absorptive spectrum and the lower dispersive. The frequency for the dispersive signature is taken at the zero crossing (0.66 MHz), and the frequency for the absorptive frequency is at 1.58 MHz. The ratio between the two peaks is (0.46:1), well within the expected range of these NV orientations with the addition of inhomogeneities.

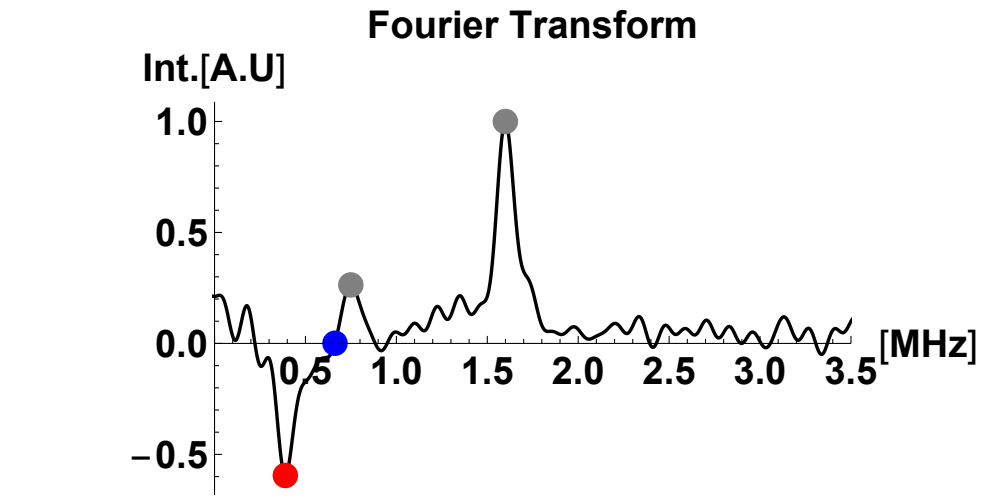

Figure 5.19: Steady-state Fourier transform of CH1, taken from the steady-state time data shown in figure 5.13. Performing a Goldman-Shen experiment by delaying the data collection removes the large broad feature, and sharpens the existing peaks. Taking the data at a delayed time captured a phase difference of 90° between the two frequencies, showing a dispersive response for the lower frequency and an absorptive curve in the higher frequency peak. The zero crossing is taken for the lower frequency, 0.66 MHz. The absorptive frequency is 1.59 MHz, and the ratio between the two peaks are (0.46:1).

Fourier Response for Channel 2

More insight to the location of the NVs relative to the microstrips may be gained with looking at the Fourier response in the second channel. The same technique is used here, taking only the steady-state response, shown in figure 5.20. As with Channel 1, analyzing the steady-state response removed a large background feature. Additionally, as the starting time was delayed, there is also a phase difference observed between the two frequencies. In this case, both show an absorptive response, but with a 180° phase difference between them. The two frequencies corresponding to the two pairs of NV orientations are at 0.81 MHz and 1.45 MHz, with a ratio of (0.56:1).

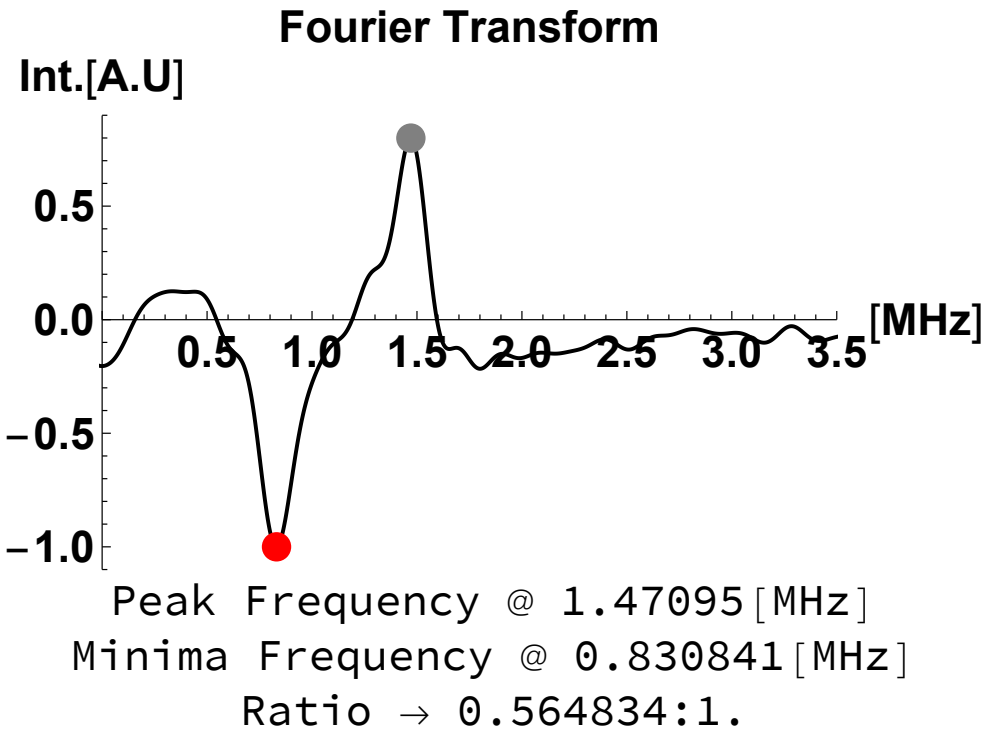

Figure 5.20: Steady-state Fourier transform of the CH2 steady-state time data in figure 5.14. Analyzing the steady-state response removes the broad baseline from the spectra. As with channel 1, taking the starting time at a delayed value yields a phase difference between the two frequencies at that time, in this case, 180°. The two frequencies for channel 2 are 0.81 MHz and 1.45 MHz at a ratio of 0:56:1.

The frequency spectra of Channel 1 and 2 show similar responses, with the maxima and minima frequencies of Channel 1 being 0.66 MHz and 1.6 MHz and 0.8 MHz and 1.4 MHz for channel 2. The ratio between the maximum values for each channel, 1.4 MHz and 1.6 MHz, (0.875:1), may be used as an approximation for the difference in radial distance from the NV ensemble to each stripline. The ratio between the peaks is a good indicator of the angle between each stripline and the NV ensemble. The ratio for channel 1 was (0.46:1) and the ratio for channel 2 is (0.56:1). This indicates the ϕ angle for CH2 is closer to an odd integer of 45° than CH1.

5.4.5 Estimating the Location of the NV Ensemble

The location of the NV ensemble relative to each stripline may be estimated given the response from each channel. In future iterations of this setup, it would be a good step to include a method for knowing the precise location of the NVs relative to the microstrips, as the geometric location is a factor included in the Hamiltonian for OCT experiments.

Modelling the microstrips as infinite wires, the magnitude of the field can be estimated with Biot-Savart, $B = \frac{\mu_o I}{2\pi r}$. $\mu_o = 4\pi \times 10^{-7}\ \frac{N}{A^2}$ is the magnetic permeability of free space, I [A] is the current at the stripline source, and r [m] is the radial distance away from the stripline.

First, the magnitude of the field strength B [T] for each stripline may be estimated for each stripline using the angular frequency (ω). The angular frequency ω $[\frac{Rad}{s}]$ of the Rabi data is related with $\omega = \gamma B$, where $\gamma = 2\pi \times 28024 \times 10^6\ \frac{Rad}{T \cdot s}$ is the gyromagnetic ratio of the NV and B [T] is the magnitude of the field. The Rabi frequency (ω) may be estimated by taking the point of the first dip in each of the single-channel experiments as a π rotation. Twice this time can be estimated as a full rotation, so $\omega = \frac{2\pi}{t}$. For channel one, the first dip occurs at 0.3 μs and channel two at 0.32 μs. These values also correspond to the π rotation values for the maximum frequency values recorded for each of the channels.

To estimate the radial distance, the field strength and current through each source stripline is required. The current in Amperes I [A] is given by the measured power in decibels at the stripline for each channel and assuming the resistance is a 50 Ω load. The measured power from channel 1 and channel 2 with the addition of the transmission loss through each stripline yields $P_1 = 29.8$ dBm and $P_2 = 30.8$ dBm, which may be used to find the current through each stripline.

$$\begin{aligned} I\ [A] &= \sqrt{\frac{P\ [W]}{R\ [\Omega]}} \\ I\ [A] &= \sqrt{\frac{10^{\frac{P\ [\mathrm{dBm}]-30}{10}}}{50\ [\Omega]}} \end{aligned} \tag{5.5}$$

Taking the Rabi frequency, current and field strength into account, the radial distance is shown in the equation below:

$$r_{(1/2)} = \frac{\gamma \mu_o I_{(1/2)} t_{(1/2)}}{(2\pi)^2}\ [\mathrm{m}] \tag{5.6}$$

Using the current and time values for each stripline, an estimate of the radial distance from each stripline can be found to be $r_1 = 463$ μm and $r_2 = 554$ μm. With these two values, and accounting for the 150 μm spacing between the two microstrips, there is only one point of intersection, marked by the site of the NV point in **(blue)**, shown in figure 5.21. The microstrips are marked with **(black)** and **(red)** circles, with arrows indicating the respective radial values, and field direction at the site of the NV. The direction of the field is consistent with the handiness given by the direction of the flow of current in the experimental setup, travelling out of the page.

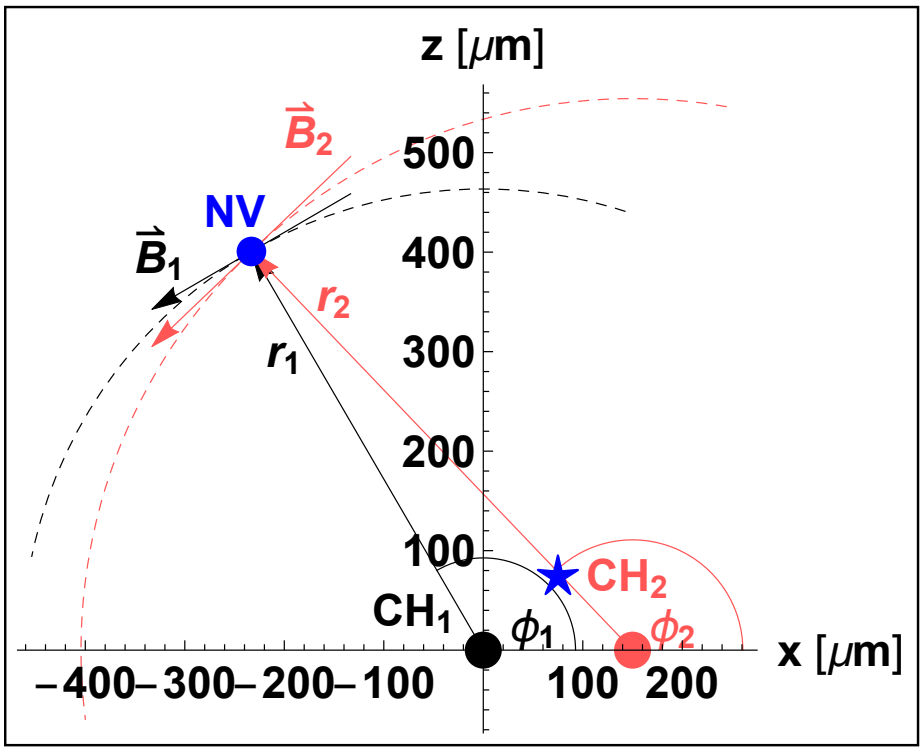

Figure 5.21: A plot of the estimated NV ensemble position relative to the microstrips. Using the Rabi data from each channel, an estimated radius from channel 1 and 2 are $r_1 = 463$ μm and $r_2 = 554$ μm. Plotting these distances, there is only one intersection point, marked at the site of the NV center **(blue)**. The handiness of the magnetic field is indicated, consistent with flow of current through the microstrips in the experimental setup. The radial distances may be used to solve for the "x" and "z" distances as well as the angle ϕ relative to each channel. The ideal position of the NV ensemble is marked with the **blue star**.

The distance in x and z may be found using the radial distances. Equation 3.32 outlined the relationship between the radial distances and the "x" and "z" Cartesian coordinates. Re-arranging these values with a known radius for each channel, the "x" and "z" values can be solved for each stripline. Recall that the "z" value for each stripline would be the same as the NVs would be found at the same depth, and that the distance x_2 from the second stripline is the x distance from the first stripline minus the separation between the microstrips $x_2 = x_1 - l$:

$$\begin{aligned} r_1 &= \sqrt{x_1^2 + z^2} \\ r_2 &= \sqrt{(x_1 - l)^2 + z^2} \\ x_1 &= \frac{r_1^2 + r_2^2 + l^2}{2l} \\ x_2 &= x_1 - l \\ z &= \sqrt{r_1^2 - x_1^2} \end{aligned} \tag{5.7}$$

Figure 5.22 shows the results of these values.

x_1 [μm]	x_2 [μm]	z [μm]	r_1[μm]	r_2[μm]	ϕ_1[°]	ϕ_2[°]
-233.033	-383.033	400.667	463.507	554.3	120.183	133.711

Figure 5.22: Estimated relative position of NV ensemble relative to the microstrips. Using the radial values of $r_1 = 463$ μm and $r_2 = 554$ μm, the solved values of $x_{(1/2)}$, z and $\phi_{(1/2)}$ are found. These output results are consistent with physical limitations as well as other pieces of experimental evidence.

Although this is an estimated value of the position of the NV ensemble, a couple of sanity checks can be made. The maximum measured value of Rabi frequency for the first channel is greater than the second channel, so it is expected that the NV ensemble would be located closer to the first stripline than the second stripline. Additionally, the ratio between the two calculated radii (0.83:1) is close to the ratio between the maximum Rabi frequencies (0.87:1).

The calculated "z" value is consistent with the thickness of the diamond 500 μm, depth of field 160 μm of the objective, and two small gaps to account for oil between the objective and diamond on the top of the diamond and wax to hold the diamond to the microstrips.

Last, using the Cartesian values for "x" and "z", the angle from each stripline ϕ_1 and ϕ_2 can be found. These angles contribute to the ratio between the peaks of the two sub-ensembles in the frequency domain. For odd integers of $\phi = 45°$, the ratio between the peaks approaches (0.57:1). The ϕ value for channel 2 is $133° \approx 3 \times 45°$, and the ratio between peaks was (0.56:1), consistent with the relationship between ϕ and the peak frequency ratio. The value of ϕ_1 is 120°, which would indicate a ratio that is less than (0.57:1), closer to converging to one peak. However, this channel had more inhomogeneities than channel 2, so there is an expectation that the ratio would be skewed from the expected value.

The ideal location of the NV ensemble would be halfway in between the microstrips, in the "x" direction, and that equivalent distance away from the microstrips in z. With this configuration, that would yield a value of 75 μm for both "x" and "z". It is at this point that the field from the two microstrips are perpendicular to each other, $\phi_2 = \phi_1 + \frac{\pi}{2}$, being the most distinguishable. The experimental constraints of having a thicker diamond made this point unachievable with the current setup, but integrating either a thinner diamond, or microstrips which are further apart would allow for this point to be achievable. However, as was seen in chapter three, the desired target states are able to be found with OCT pulses outside of this ideal value (section 3.1.5).

These results are just an estimate of where the NV ensemble is located and is used as a visualization tool. The results are consistent with physical limitations and other experimental results. These results will be important to simulate the response for the dual-channel Rabi experiment to see if this proposed location is consistent with the simulated data.

Single-Channel Rabi to Spinlock Experiment

The single-channel Rabi experiment informed of the initial behaviour of the NV ensemble. It was confirmed that with the (100) diamond and two parallel microstrips with fields along the "x" and "z" axes, there would be not four orientations present, but two sub-ensembles. Using the amplitude of each single-channel, the position of the NV ensemble relative to each stripline can be estimated.

5.5 Single-Channel Spinlock

While the Rabi experiment informed much of the behaviour of the NV ensemble, it does nothing to control each ensemble. The Spinlock experiment is a method of isolating each of the two sub-ensembles. It is comparable to using optical polarization to suppress the response of each of the sub-ensembles and then complete a Rabi experiment to look at each of their individual responses.

5.5.1 Spinlock Pulse Diagram

The experimental sequence for the spinlock is shown in figure 5.23. The spinlock uses the same initialization and base bright count and detection sequence as the Rabi experiment. The two experiments differ in the middle portion with the microwave controls. In a spinlock experiment, a $\frac{\pi}{2}$ or $\frac{3\pi}{2}$ pulse is applied, followed by a square pulse with a phase of $\frac{(3)\pi}{2}$, incremented in length from $t = 0 \rightarrow t = \tau$. Following the square pulse, another $\frac{(3)\pi}{2}$ pulse is applied. The target $\frac{(3)\pi}{2}$ pulse rotates the chosen frequency to the effective "x"-axis. Applying the next square pulse with the same phase, maintains the chosen frequency aligned with the effective "x"-axis, suppressing its evolution, while the other frequency is able to evolve freely.

The length of the target $\frac{(3)\pi}{2}$ time is found by analyzing the two frequencies which appear in the Rabi Fourier spectra, and then extracting the time to apply a $\frac{(3)\pi}{2}$ pulse for each frequency. Typically, a $\frac{\pi}{2}$ pulse is applied to suppress the lower frequency peak while a $\frac{3\pi}{2}$ pulse is required to suppress the high-frequency peak.

As with the Rabi experiment sequence, each pulse increment for $t = 0 \rightarrow t = \tau$ is repeated for (n=50 000) times, and the values of t are randomly selected in the entire sequence to avoid errors associated with laser drift. Once the range of t values has been exhausted, the entire sequence is repeated for (N=100) averages.

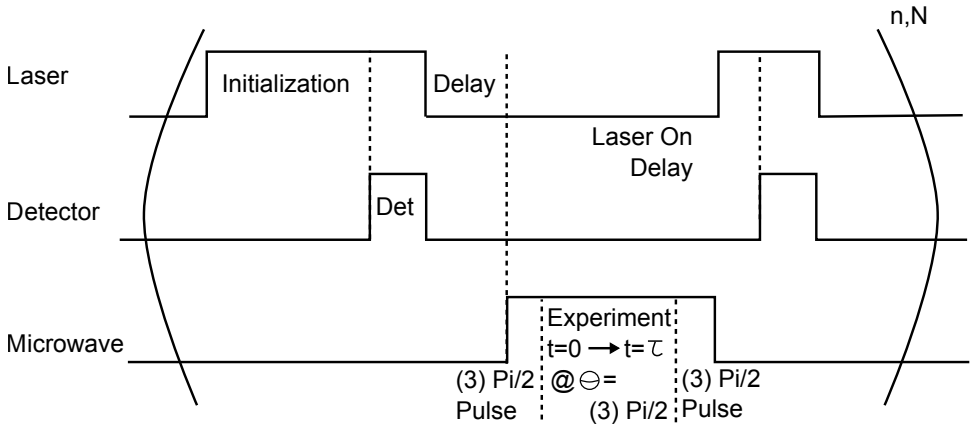

Figure 5.23: Spinlock pulse sequence. The laser and detector follow the same sequence as the Rabi sequence, initializing the spins and detecting the bright counts and detecting the experimental counts following the microwave control pulse. The Spinlock sequence suppresses one frequency by applying a target $\frac{(3)\pi}{2}$ pulse, followed by a square pulse incremented from $t = 0 \rightarrow t = \tau$ with a phase of $\frac{(3)\pi}{2}$ to maintain the suppression of the target frequency. The timing of the $\frac{(3)\pi}{2}$ pulse for each frequency is found from analyzing the Rabi Fourier spectra. During this time, the other frequency is able to evolve as it would in a Rabi experiment. Following the $\frac{(3)\pi}{2}$ pulse and square pulse, another $\frac{(3)\pi}{2}$ pulse is applied to rotate the spins back to the detection axis.

5.5.2 Proof of Concept of the Spinlock

Investigating a Spinlock Experiment with Bloch Spheres

The concept of a spinlock experiment can be further explained with Bloch sphere models. In this instance, the $|\pm1\rangle$ states have been approximated as one state, so one Bloch sphere is used to describe the evolution of the NV as an approximate spin-$\frac{1}{2}$.

To implement a spinlock experiment, first the frequencies from the low and high-frequency NV sub-ensembles are gathered from the Rabi experiment. The length of the $\frac{(3)\pi}{2}$ pulses are then calculated from those frequencies. To suppress the low-frequency sub-ensemble, a $\frac{\pi}{2}$ pulse is first applied, rotating it to the $\frac{|0\rangle+|\pm1\rangle}{\sqrt{2}}$ state (+"x"-axis), then the microwave control Hamiltonian is applied with a square pulse, at a phase along the +"x"-axis ($\theta = \frac{\pi}{2}$). When the $\frac{\pi}{2}$ pulse is applied to the low-frequency sub-ensemble, the high-frequency pair is rotated by a full π to the $|\pm1\rangle$ states, keeping it along the detection "z"-axis. As a result, when the control Hamiltonian is then applied along the (+"x"-axis), the low-frequency peak does not show evolution about the "x"-axis, but the high-frequency peak evolves similar to if it started in the $|0\rangle$ state. Following the evolution phase, another $\frac{\pi}{2}$ pulse is applied to rotate the low-frequency pair back to the detection axis, and a measurement takes place.

The spinlock experiment will measure the free evolution of the other frequency pair while the target frequency is suppressed. Figure 5.24 illustrates this full sequence for both the low and high-frequency sub-ensembles, with the suppression targeted to the low-frequency sub-ensembles.

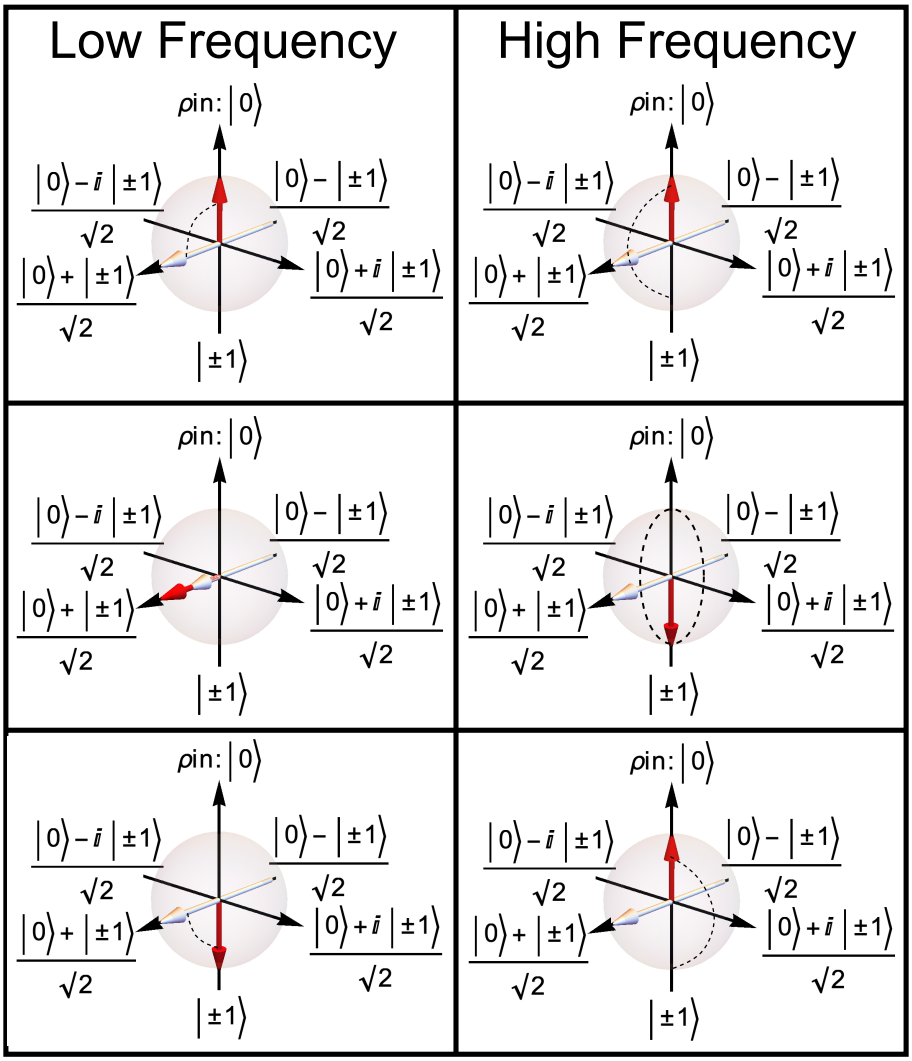

Figure 5.24: The proof of concept for a spinlock experiment shown in a Bloch Sphere representation. Both the low and high-frequency sub-ensembles from the Rabi spectra begin in the $|0\rangle$ state **(red arrows)**. A $\frac{\pi}{2}$ pulse targeted at the low-frequency pair is applied, rotating the low-frequency to the $\frac{|0\rangle+|\pm1\rangle}{\sqrt{2}}$ state (+"x" axis), and the high-frequency to the $|\pm1\rangle$ state. Applying a control Hamiltonian along the +"x" axis **(white arrow)**, will suppress the evolution of the low-frequency pair, while the high-frequency pair may evolve freely. After the evolution stage, another $\frac{\pi}{2}$ pulse is applied to rotate the low-frequency peak to the $|\pm1\rangle$ state while the high-frequency peak returns to the $|0\rangle$ state. The spinlock experiment will measure the free evolution of the high-frequency while the low-frequency is suppressed.

The high-frequency suppression can be investigated with another set of Bloch sphere figures, shown in figure 5.25. The figure illustrates why a $\frac{3\pi}{2}$ pulse is experimentally necessary to suppress the high-frequency sub-ensemble, as-opposed to a $\frac{\pi}{2}$. When a $\frac{\pi}{2}$ pulse targeted to the high-frequency pair, that target sub-ensemble is rotated to the +"x"-axis, but the low-frequency peak does not fully reach the "z"-axis. As a result, during the evolution stage when the control Hamiltonian is applied along the "x"-axis, the low-frequency pair does not evolve with full "z" components, so the experimental counts will be reduced. Combining these low contrast results with experimental noise, makes this impractical to perform. Applying a $\frac{3\pi}{2}$ pulse mitigates this problem, by rotating the high-frequency pair to the +"x"-axis, and fully rotating the low-frequency pair to the -"z"-axis, so it is able to evolve as expected.

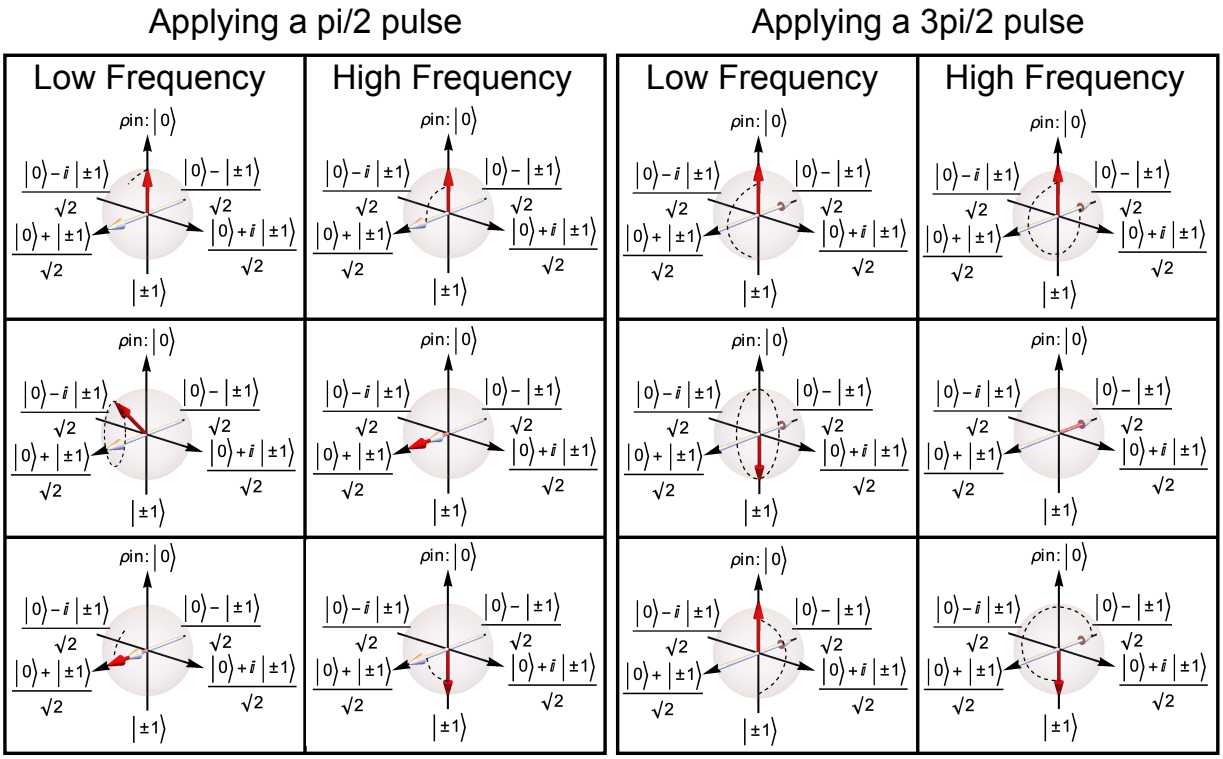

Figure 5.25: The figure compares suppression of the high-frequency pair with a $\frac{\pi}{2}$ pulse **(left)** compared to a $\frac{3\pi}{2}$ pulse **(right)**. The $\frac{\pi}{2}$ properly rotates the high-frequency NV pair to the $\frac{|0\rangle+|\pm1\rangle}{\sqrt{2}}$ state (+"x"-axis), but does not do a full π rotation of the low-frequency peak. As a result, during the evolution phase, there is lost contrast off the "z"-axis for the low-frequency peak. Applying a $\frac{3\pi}{2}$ pulse rotates the high-frequency pair to the +"x"-axis, and rotates the low-frequency peak the full π pulse, so the evolution shows a more optimal contrast with the low-frequency pair. Although a $\frac{\pi}{2}$ pulse does suppress the high-frequency pair, it makes the detection of the low-frequency pair more difficult in experiment, so a $\frac{3\pi}{2}$ pulse is applied to achieve both the suppression of the high-frequency pair and optimal detection of the evolution of the low-frequency pair.

These figures simply show the evolution of the states during the spinlock experiment so an intuition can be gained. The experimental data available would be comparing the frequency spectra of the Rabi and the spinlock experiments. In the Rabi experiment, there were two frequencies seen. If the spinlock experiment were successful, only one of those selected frequencies would evolve, while the other is suppressed.

Simulation Spinlock Results

In the ideal form, interpreting the results of a spinlock experiment is quite simple. It is easiest to analyze the results in Fourier space, overlapping the spectra of the spinlock with the initial Rabi experiment. When overlapped, the spinlock should present with one frequency suppressed while the other peak aligns with the Rabi experiment.

Figure 5.26 shows a simulation for a spinlock experiment in the Fourier space. The Rabi spectra is shown with the dashed lines, while the spinlock experiment is shown as the solid black lines. The arrows indicate which peak is being suppressed for each of the experiments. The frequency that survives the spinlocking should overlap perfectly with the remaining Rabi frequency as well in the ideal case. This simulation was done in the absence of any inhomogeneities, so the suppression is very clear in each case.

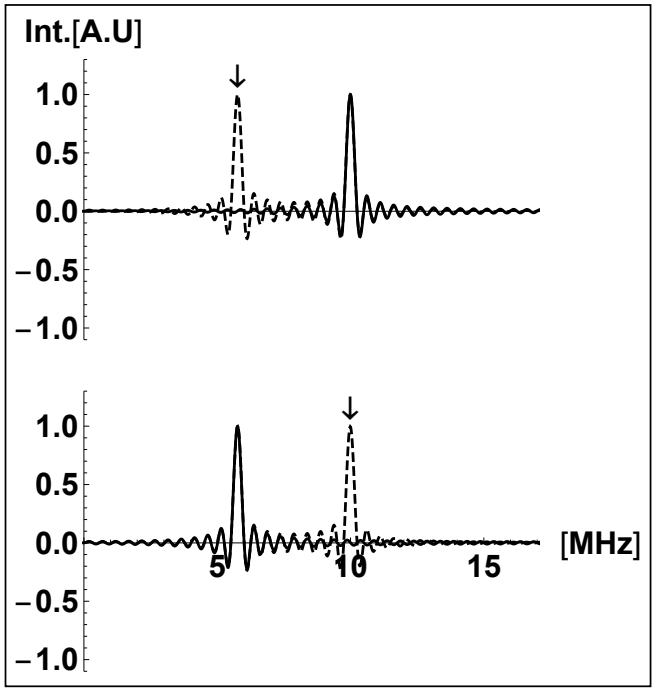

Figure 5.26: Simulation for Spinlock experiment. The absorptive Rabi spectra is shown **(Black, Dashed)** with the Spinlock experiment for suppressing each of the low and high-frequency peaks overlapped **(Black, Solid)**. The peak which is not suppressed overlaps perfectly with the Rabi peaks for this simulation. The arrows indicate which peak is being suppressed.

5.5.3 Single-Channel Spinlock - Experimental Data

Spinlock - Channel 1

Figure 5.27 shows the experimental Spinlock results for Channel 1. This data was collected with (n=50 000) repeats per data point, and averaged (N=100) times. As with the simulations, the Rabi spectra for Channel 1 is shown with black dashed lines, while the spinlock results are shown with black solid lines. The arrows indicate which peak is being suppressed for each experiment.

The Channel 1 Rabi steady-state spectra indicated two frequencies at 0.66 MHz and 1.6 MHz, shown in the dispersive and absorptive curves. The spinlock data shows a suppression of both the low and high-frequency peaks. To suppress the low-frequency peak, a $\frac{\pi}{2}$ pulse was applied, corresponding to the time for the 0.66 MHz peak (0.37 μs), followed by the Hamiltonian evolving for $t = 0 \rightarrow t = \tau$ at a phase of $\theta = \frac{\pi}{2}$.

To suppress the high-frequency peak, a $\frac{3\pi}{2}$ pulse was applied corresponding to the 1.6 MHz frequency peak (0.47 μs), followed by the Hamiltonian for $t = 0 \rightarrow t = \tau$ at a phase of $\theta = \frac{3\pi}{2}$.

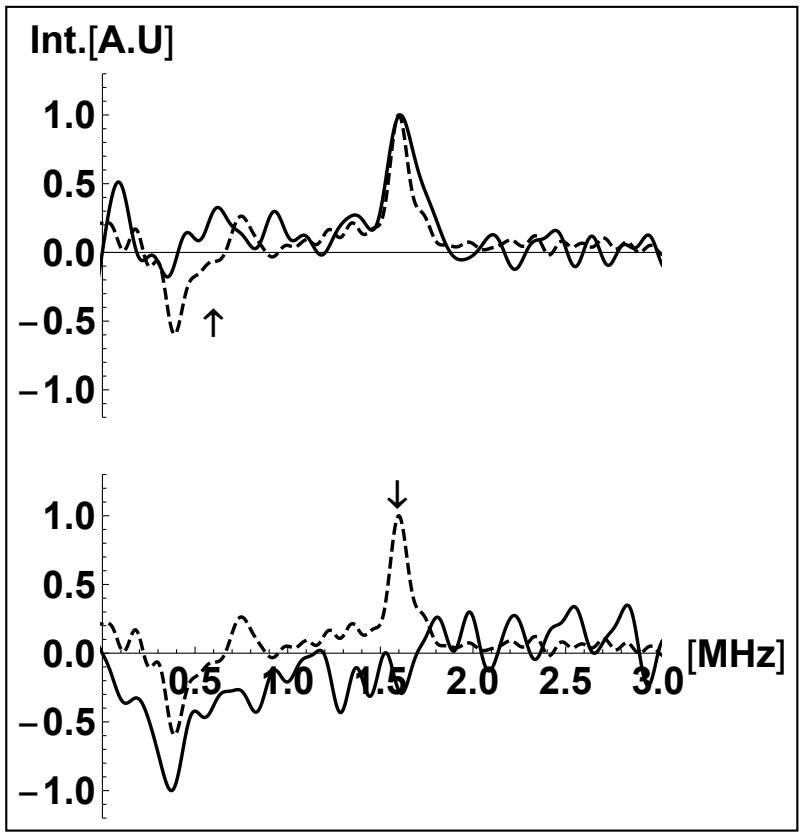

Figure 5.27: Spinlock Frequency Spectra for Channel 1. The time data is not shown here to avoid redundancy. The Rabi spectra for channel 1 is shown **(Black, Dashed)** while the results for each of the spinlocking experiments **(Black, Solid)** atop the Rabi. The arrows indicate which peak is being suppressed in the data, first the lowest frequency 0.66 MHz and then the high-frequency 1.6 MHz. To suppress the low-frequency, a $\frac{\pi}{2}$ pulse targeted to the 0.66 MHz was applied, followed by pulsing the Hamiltonian at a phase of $\theta = \frac{\pi}{2}$. To suppress the high-frequency peak at 1.6 MHz, a $\frac{3\pi}{2}$ pulse was applied corresponding to the 1.6 MHz frequency, and Hamiltonian evolved at $\theta = \frac{3\pi}{2}$.

Spinlock - Channel 2

Figure 5.28 shows the spinlocking results from channel 2. As with channel 1, this data was collected with (n=50 000) repeats per data point, and averaged (N=100) times. The same procedures are followed to suppress the low-frequency minimum at 0.83 MHz and high-frequency maximum at 1.47 MHz. A $\frac{\pi}{2}$ pulse corresponding to the frequency of 0.83 MHz (0.31 μs) is used to suppress the low-frequency peak. A $\frac{3\pi}{2}$ pulse corresponding to the frequency of 1.47 MHz (0.51 μs) is used to suppress the high-frequency peak. As with channel 1, the square pulse following the $\frac{(3)\pi}{2}$ pulse was done so at a phase of $\theta = \frac{(3)\pi}{2}$, respectively.

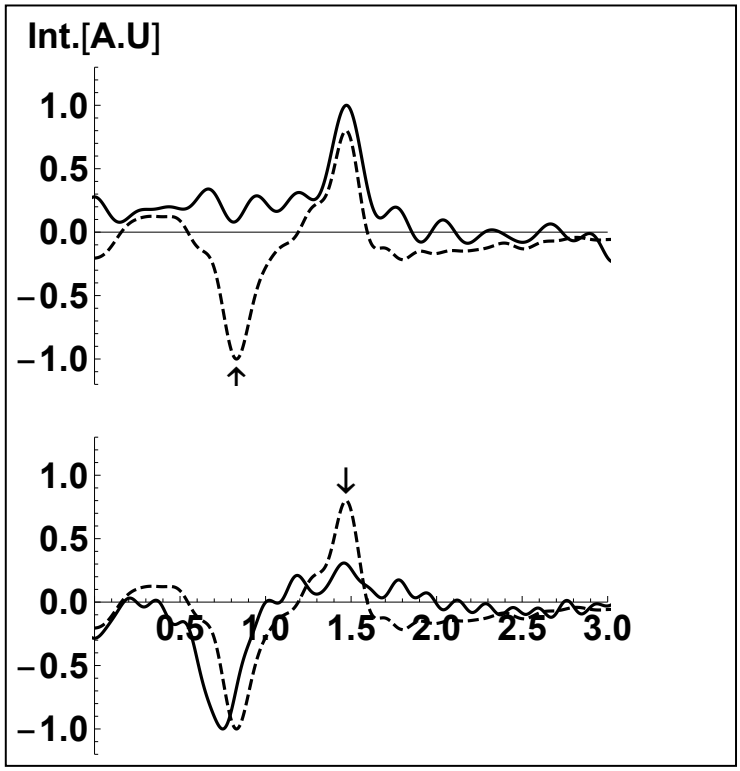

Figure 5.28: Spinlock Frequency Spectra for Channel 2, with corresponding time data in figure 5.29. The Rabi data for channel 2 is the **(Black, Dashed)** line, while the results from the spinlock data are shown as the **(Black, Solid)** lines. In each of the spectra, an arrow indicates which peak is being suppressed with the spinlock. A $\frac{(3)\pi}{2}$ pulse was used to suppress the targeted low(high)-frequency peak. There is a clear suppression of both the low and high-frequency peak for each experiment.

The results are very clearly shown, for each case, suppressing the low and high-frequency peaks. There is a small frequency shift observed in the low-frequency peak when the high-frequency peak is suppressed. As with the channel 1 spinlock, the Rabi data is shown in dashed lines behind the spinlock results.

The experimental results showed that both channels were able to suppress both the low and high-frequency peaks. With a cleaner Rabi to start, the results from channel 2 were closer to the ideal behaviour of a spinlock experiment, but channel 1 still indicated the same behaviours. The Fourier data shows that each of the frequencies may be suppressed, a preliminary control on each of the sub-ensembles.

5.5.4 Analyzing the Time Data of each Sub-Ensemble

The previous section analyzed the Fourier response of the spinlock experiment. This section will look at the time data. In the time domain, suppressing each of the sub-ensembles shows what the evolution of each sub-ensemble looks like individually. This can yield more information about each pair of orientations. Figure 5.29 below shows the time evolution of spinlock experiment for each of the sub-ensembles in channel 2.

Looking at the time evolution of the two sub-ensembles individually, while the other frequency is suppressed, yields more information about the lifetime of each sub-ensemble. Looking at the figure below, it appears the low-frequency peaks have a much shorter lifetime than the high-frequency peaks.

Looking at the lifetimes for the individual frequencies is useful for when the frequency spectra are gathered by taking only the steady-state response of the data. The delay cannot be so large that it removes the low-frequency peak all together. For example, delaying the starting time to 2 μs would remove most of the signal from the low-frequency peak. However, taking the steady-state response at a shorter time, 0.5 μs, removes the large inhomogeneity, and broad baseline without removing the signal from the low-frequency peak. The error bars are gathered with the same methods as the ODMR-CW and Rabi experiments, using the standard deviation of the normalized photon counts. As the contrast for the spinlock experiment is much lower than the Rabi experiment, these appear larger.

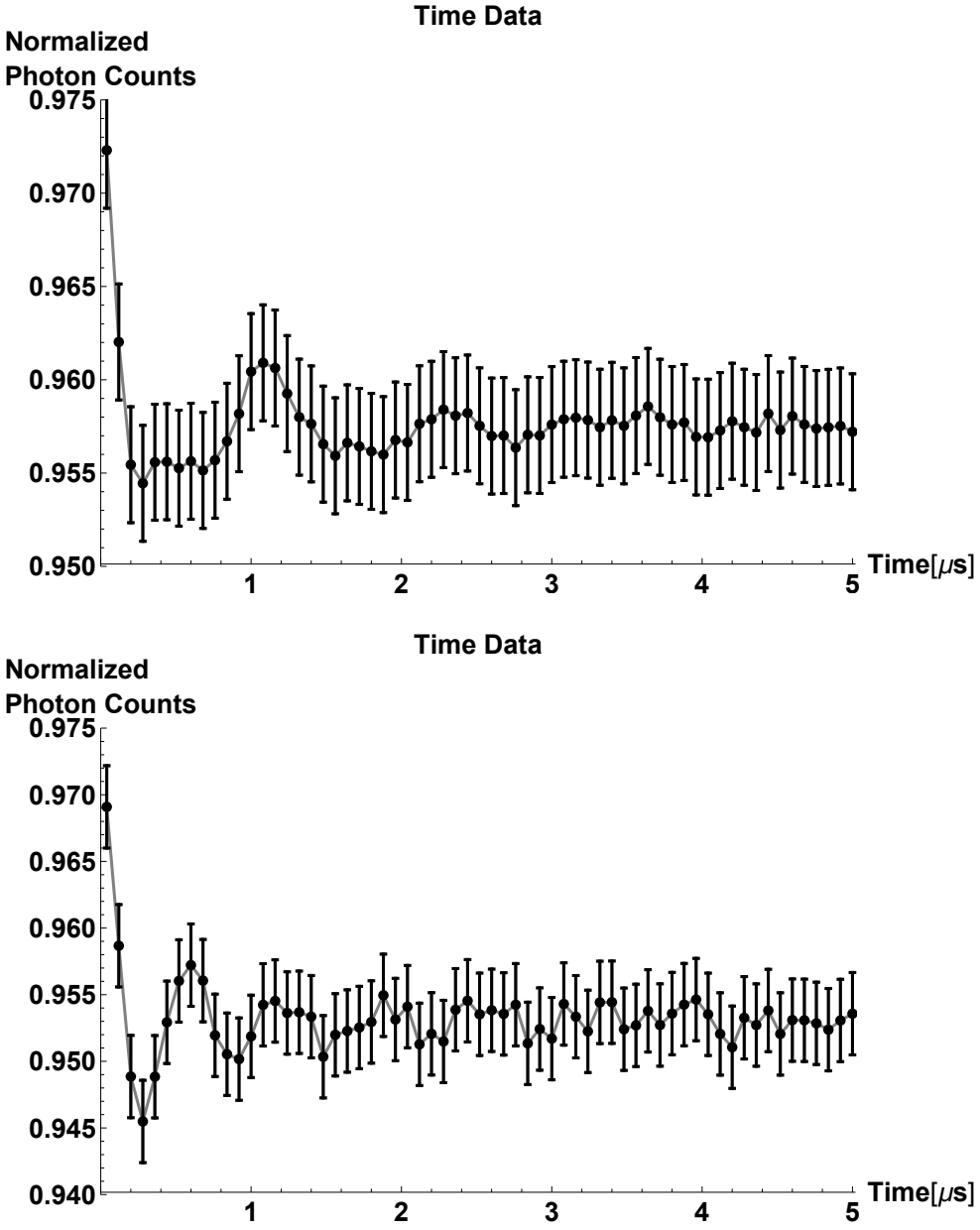

Figure 5.29: Spinlock Time Data for Channel 2. The **(Top)** data shows the time data when the high-frequency is suppressed (low-frequency remains), and **(Bottom)** shows the time data when the low-frequency is suppressed (high-frequency remains). The high-frequency data has a much longer lifetime than the low-frequency data, the low-frequency data only lasting about 3 μs, while the high-frequency data looks to extend to 5 μs.

The spinlock experiment shows early control on each of the sub-ensembles. If the evolution of each wanted to be investigated individually without changing the optical polarization of the incoming light, this experiment offers a method of doing so. Analyzing the response of each sub-ensemble through the spinlock experiment offered more insight than investigating with the Rabi experiment.

This concludes the experiments completed with the channels acting individually. Single-channel experiments confirmed the presence of the sub-ensembles in the (100) diamond, and offered a method of suppressing each of the sub-ensembles so the individual behaviour could be analyzed. The following experiments use both channels together either sequentially or simultaneously. Beginning first with the relative microwave phase experiment, this experiment will show the response of the NV ensemble to changing the relative and absolute phase between the two microstrips.

5.6 Relative Microwave Phase Experiment

The relative microwave phase experiment uses both channels, pulsed sequentially. While the single-channel experiments offer insight into amplitude response to each of the channels, it does not offer information on the phase response. The relative microwave phase experiment is used to measure the spin response to changing both the absolute and relative phase values between each of the channels. In this experiment, two $\frac{\pi}{2}$ pulses are run sequentially for channel 1 and channel 2 at a set $\theta_{1/2}$ value. The length of time for each $\frac{\pi}{2}$ is found by analyzing the Rabi experiment for each individual channel. The value of θ_1 is fixed, while the value of θ_2 varies from $0° \rightarrow 720°$. The relative microwave experiment is used to inform the dual Rabi experiment of any large discrepancies between the NV ensembles for each channel or unexpected results from the high and low-frequency peaks, as was seen in the single-channel Rabi experiments.

As the phase of θ_2 is changed, the output value of counts varies. The point of maximum counts corresponds to when a total $\mathbb{1}$ pulse is performed, this is a $\frac{\pi}{2}$ for Channel 1 and a $-\frac{\pi}{2}$ pulse for Channel 2. At this point, $\theta_2 = -\theta_1$. The point of minimum counts corresponds to when two $\frac{\pi}{2}$ pulses have been performed, forming a π pulse in total. At this point, $\theta_1 = \theta_2$.

As the single-channel Rabi experiments yielded two sub-ensembles, the relative microwave experiment was conducted in two segments. The first regime was using the frequency data from the lowest frequency sub-ensemble and second, the highest frequency sub-ensemble.

5.6.1 Relative Microwave Phase Pulse Sequence

Figure 5.30 shows the relative microwave pulse sequence. Both the laser initialization, bright count detection and experimental count detection use the same sequence and parameter as the single-channel Rabi experiment. In this experiment, both channels pulse individually with square pulses for the length of time equivalent to a $\frac{\pi}{2}$ pulse acquired from the single-channel Rabi experiment. The phase for Channel 1 is fixed at a set value of θ_1, while the phase of Channel 2 is varied from $0° \rightarrow 720°$. The phase value of θ_2 is randomly incremented to avoid errors associated with laser drift, and each phase value sequence is repeated (n=50 000) times to acquire enough photons. Once all the values of θ_2 have been used, the entire sequence is repeated for (N=10) averages.

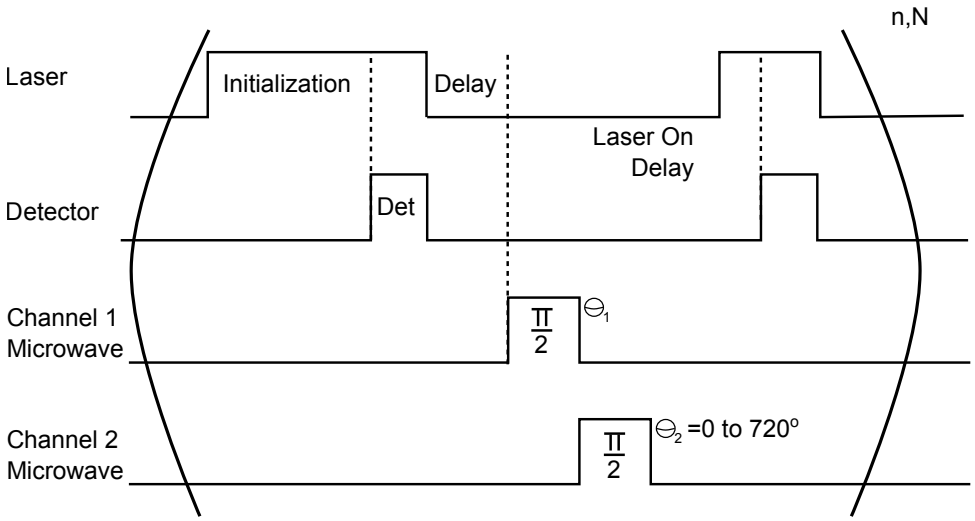

Figure 5.30: Relative microwave pulse sequence. The laser initialization, bright count detection and experimental count detection is all the same as the Rabi experiment. In this experiment, each channel is pulsed for a length of time equivalent to a $\frac{\pi}{2}$ pulse, as determined by the Rabi experiment. Channel 1 has a constant phase set to θ_1, while the phase of Channel 2, θ_2 is incremented from $0° \rightarrow 720°$. The values of θ_2 are chosen randomly to avoid laser drift affecting the results. Each increment of θ_2 is repeated (n=50 000) times, to gather enough photons. Once all the values of θ_2 have been acquired, the entire sequence is repeated for (N=10) averages.

5.6.2 Experimental Data for Fixed Channel One Phase

This section will now analyze the results from the experimental data, first for the low-frequency pair and then the high-frequency pair. Recalling from the Rabi experiments, that for each of the single-channels, there were two peaks, associated with relative low and high-frequency sub-ensemble. As this was the case, the relative microwave phase experiment was performed for two instances, using $\frac{\pi}{2}$ pulses associated with the pair of low-frequency peaks and the high-frequency peaks for each channel 1 and channel 2.

To find the length of the $\frac{\pi}{2}$ pulses for the low-frequency data, first the Rabi experiments for both channel 1 and channel 2 were analyzed. The lower frequency was taken from each data set of channel 1 and channel 2. Then from the frequency, the length of time for a $\frac{\pi}{2}$ was taken. The same procedure was repeated for the high-frequency pair.

Relative Microwave Phase Experimental Time Data with Fit - Low-Frequency Data

First, the results from the low-frequency data will be investigated. Figure 5.31 shows the results of having $\theta_1 = 0°$ and θ_2 swept from $0° \rightarrow 720°$. For all relative microwave phase experiments, the data collected at ach value of θ_2 was repeated (n=50 000) times, and then the entire experiment was averaged for (N=10) times. The $\frac{\pi}{2}$ pulses were obtained from the low-frequency peaks of each channel, corresponding to a $\frac{\pi}{2}$ pulse time of 0.64 μs for Channel 1 and 0.30 μs for Channel 2. The data shows a regular oscillation pattern over the values of θ_2, with the minima and maxima repeating every 180°. A cosine function was fit to the data, and the maxima, minima and zero crossings are extracted from the fit. In this instance, the maxima, corresponding to $\mathbb{1}$, occur at 319° and 679°, while the minima, corresponding to a π pulse, occur at 138° and 499°. The error bars are given by the standard deviation of the normalized photon counts, in the similar vein as the ODMR-CW, Rabi and Spinlock experiments.

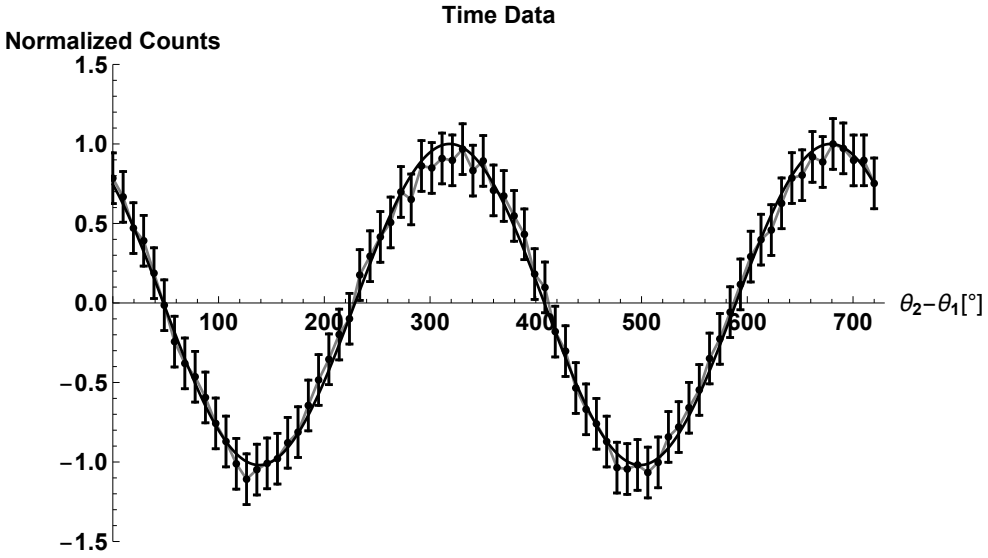

Figure 5.31: Relative microwave data set for the low-frequency NV ensemble pair. The "y" axis corresponds to the normalized photon count, while the "x" axis is $\theta_2 - \theta_1$. θ_1 is set to 0° in this instance, while θ_2 is varied from $0° \rightarrow 720°$. The minima and maxima repeat every 180°, as are the associated zero crossings. In this instance, the maxima, corresponding to $\mathbb{1}$, occur at 319° and 679°, while the minima, corresponding to a π pulse, occur at 138° and 499°.

Relative Microwave Phase Experimental Time Data with Fit - High-Frequency Data

The low-frequency data showed a regular cosine pattern for a fixed phase of channel 1 and varying channel 2 data. Recall that at the maxima, is when the two channels combine to act as an $\mathbb{1}$ pulse, with a $\frac{\pi}{2}$ from channel 1, then a $-\frac{\pi}{2}$ from channel 2, while at the minima, they form a π pulse, with two sequential $\frac{\pi}{2}$ pulses.

Figure 5.32 is the complementary data set to the low-frequency data, but with the high-frequency peaks selected. The $\frac{\pi}{2}$ pulses selected here were 0.156 μs for Channel 1 and 0.168 μs for Channel 2. An immediate difference between the slow and fast data can be seen where they appear to be offset by nearly 135°, indicating there is a clear difference in the spin response for the low and high-frequency NV pairs. This data also shows a regular oscillation, with the maxima and minima separated by 180°, with the minima, corresponding to $\mathbb{1}$, occurs at 93° and 456°, while the minima, corresponding to a π pulse occur at 275° and 638°.

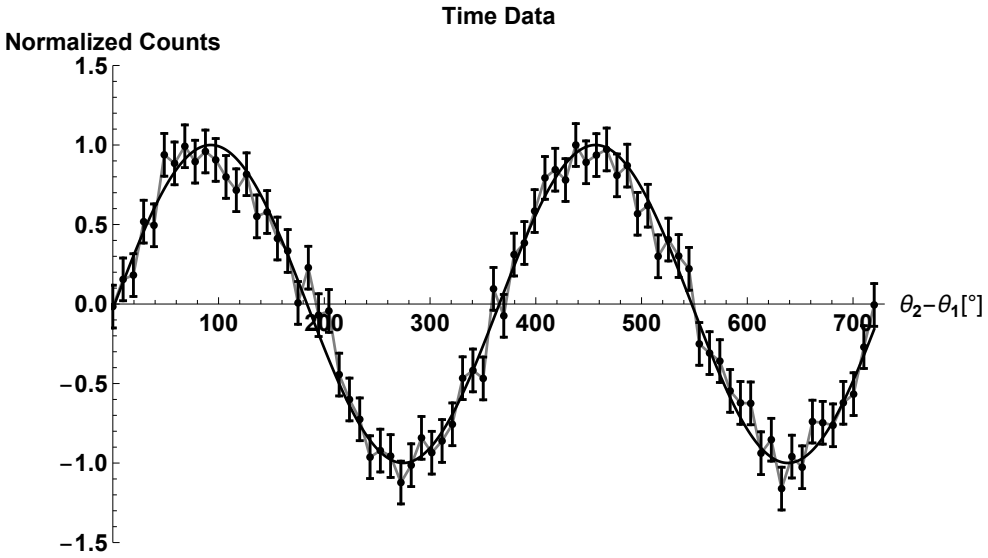

Figure 5.32: Relative microwave data set for the high-frequency NV ensemble pair. θ_1 is set to 0° in this instance, while θ_2 is varied from 0° $\rightarrow$ 720°. Like the results for the low-frequency pair, the minima and maxima are seen to repeat every 180°, as are the associated zero crossings. In this instance, the maxima, corresponding to $\mathbb{1}$, occur at 93° and 456°, while the minima, corresponding to a π pulse, occur at 275° and 638°. Comparing to the low-frequency pair, the data appears to be offset by nearly 180°.

The results of this experiment show that with a fixed phase for channel 1, the total acting pulse on the NV ensemble varies with the change in phase of the second channel. This is expected, as the spins would of course be sensitive to a relative phase difference between the two channels. From here, the response to varying the absolute phase between the channels will be investigated. This is done by changing the phase of channel 1, and then repeating the same experiment above, varying channel 2 from $0° \rightarrow 720°$.

5.6.3 Experimental Data for Varying Channel One Phase

The previous results indicated the NV ensemble is sensitive to a relative phase difference between the two channels. This was repeated with varying values of θ_1 to see if the sub-ensembles respond to only a relative difference between the phase of Channel 1 and Channel 2 or if the absolute values between the phases as well. In each instance, a regular oscillation between the maxima and minima was seen, as shown with the results above for each fixed value of the phase of the first channel, θ_1. If the spins are not reactive to the absolute values of Channel 1 and Channel 2, the value of θ_1 should not impact where the maxima, minima and zero crossings occur at.

The following results show how the position of the first zero crossing changes with varying the phase of Channel 1 (θ_1). The position of the first minima, or maxima may also be used interchangeably with the zero crossing to see the response to changing θ_1.

Varying θ_1 for the low-frequency pair

Figure 5.33 shows the results from varying θ_1 and measuring the point of the first zero crossing for the low-frequency pair of NVs. There is some variation seen here, with a total spread of 20°, with most of the deviation occurring when the value of θ_1 is $\leq 60°$. This indicates that the low-frequency pair do not have a huge sensitivity to changing absolute values of the phase for each channel, but mostly the relative phase between each channel.

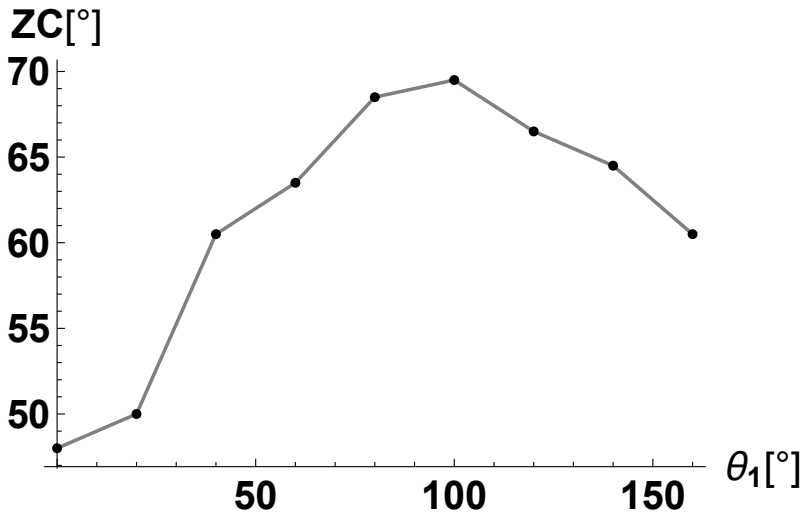

Figure 5.33: Measuring the first zero crossing for the low-frequency data with varying θ_1. The relative microwave was repeated, changing θ_1 at 20° increments, and the point of where $\theta_2 - \theta_1$ crosses zero was measured. If the spins are only sensitive to the relative phase between channel 1 and 2, the site of the zero crossing should not change when θ_1 is changed. With the low-frequency pair of orientations, there is a 20° difference in where the zero crossing occurs, with most of that spread occurring when θ_1 is $\leq 60°$.

Varying θ_1 for the high-frequency pair

Figure 5.34 shows the results for repeating the experiment with the high-frequency NV pairs. There is a linear response seen when θ_1 is varied, as shown in the location of the zero crossing. As the controls between each of the two experiments between the slow and fast NV pairs is consistent, this indicates that the high-frequency peaks are far more sensitive to a change in phase than the low-frequency peaks. The fast oscillating NV pair is sensitive not only to the relative phase value between channels 1 and 2, but the absolute values as well.

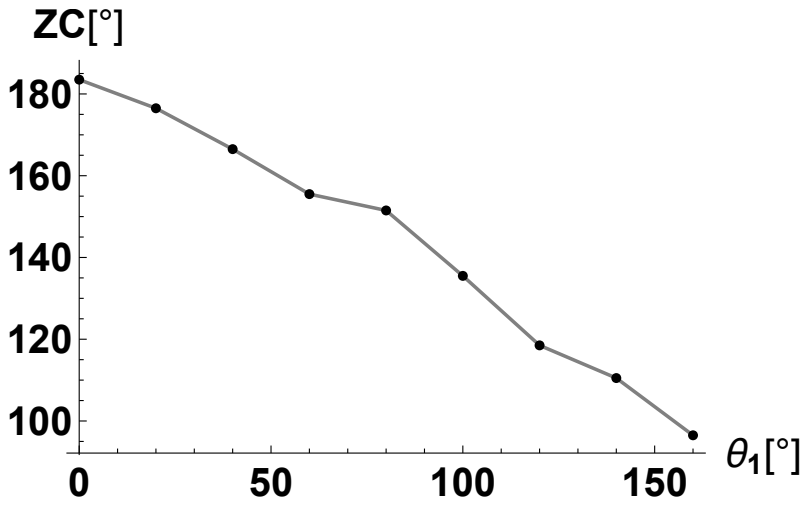

Figure 5.34: Measuring the first zero crossing for the high-frequency data with varying θ_1. This variation in the zero crossing was repeated for the high-frequency orientation pair. Unlike the low-frequency orientation pair, the response to the high-frequency pair was nearly linear. As the hardware and controls are consistent between each of the experiments performed for the experiment, this indicates an interesting spin response from the high-frequency pair. If control of the high-frequency pair is desired, it must be noted specifically which phase values of θ_1 and θ_2 are used as the spin response is unique for each pair.

The relative microwave experiment showed some early phase response behaviour for each of the low and high-frequency peaks. The high-frequency peaks appear to be far more sensitive to changes in the absolute phase than the low-frequency peaks. This note is important for designing OCT experiments, because it indicates that the ensemble will not behave in the same manner if the absolute and relative values are changed for each Channel 1 and Channel 2.

5.7 Dual-Channel Rabi Experiment

The single-channel Rabi experiment showed that there are two sub-ensembles associated with this diamond sample and microwave field configuration. The spinlock experiment showed each of these sub-ensembles may be suppressed and provided insight to the life-times and expected contrast for each. The relative microwave phase experiment then used $\frac{\pi}{2}$ pulses taken from the two lowest frequencies and two highest frequencies and investigated how each of those responded to the absolute and relative phase values between the two channels. From this experiment, it was evident that the high-frequency peaks are far more sensitive to the difference in phase than the low-frequency peaks.

The Dual Rabi channel experiment uses all the information gathered from the previous experiments, and in turn its results can inform the parameters for the OCT experiments. The response of the ensembles to phase variation between the two channels is a key factor to include in the Hamiltonian model for the OCT experiments.

The dual-channel Rabi follows the same pulse diagram as the single-channel Rabi experiment, with the exception that both microwaves channels are pulsed simultaneously, varying from $t = 0 \rightarrow t = \tau$. For all experiments, the phase of channel 1 was set to $\theta_1 = 0°$, while the phase of Channel 2 was varied for each set of data taken. As with the single-channel Rabi experiments, each data point gathered was repeated for (n=50 000) times, and averaged for (N=100) times.

5.7.1 Dual-Channel Rabi Time Data

The time data shows the dual-channel Rabi response of two select phase pairs, as an example of how varying the phase affects the Rabi amplitudes. These two phase pair values are chosen from the relative microwave experiment. The first condition appeals to the low-frequency regime. With $\theta_1 = 0°$, this was minimized, when $\theta_2 = 138°$. For the high-frequency regime, the conditions where $\theta_1 = \theta_2$ were reached when $\theta_1 = 0°$ and $\theta_2 = 275°$. These phase conditions were chosen as a starting point for the dual Rabi experiment, as they should have clear differences between them, as indicated by the relative microwave experiment.

The time data for each of the phase conditions outlined above are shown below in figure 5.35 and 5.36, respectively. For both sets of data, each data point was repeated for (n=50 000) times, and the set averaged for (N=100) times. It is clear, for these phase conditions, that they represent different frequency regimes, the first figure appearing to show a much lower frequency regime than the second figure. The error bars for both plots are given by the standard deviation of the normalized photon counts as with the previous data shown for ODMR-CW, Rabi, Relative Microwave Phase and Spinlock Experiments.

The first piece to notice between the two experiments are the contrast levels. The low-frequency data has a contrast of only about 3.5%, while the high-frequency data shows data about 8%. Like the single-channel Rabi experiment, both signals still show a large dip in the first piece of the data. Again, when analyzing the Fourier spectra, only the steady-state responses after 0.5 μs will be taken.

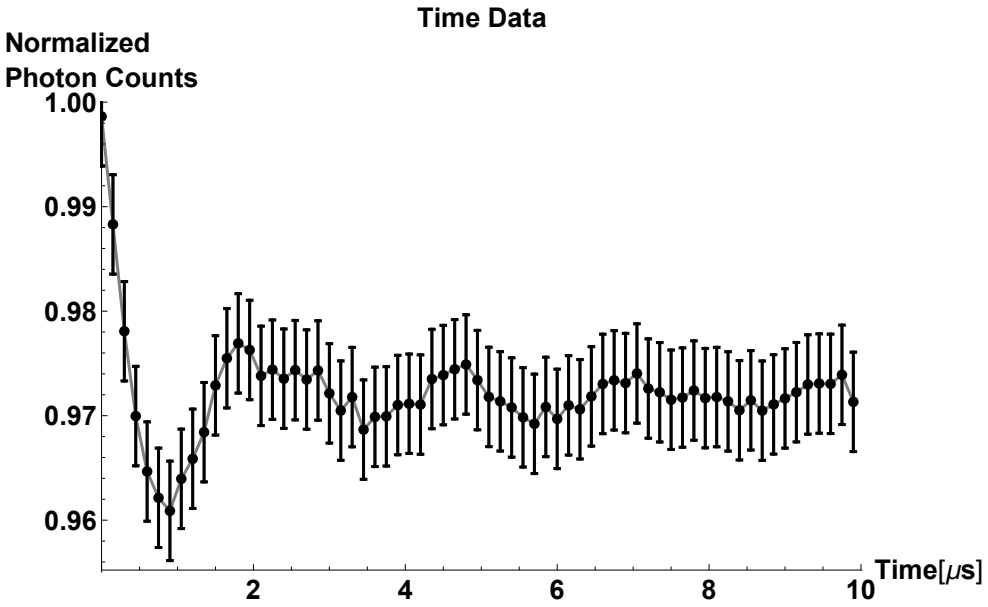

Figure 5.35: Rabi Time Data - Dual-Channel - Low Frequency. Dual Rabi Channel Time Data with $t = 0 \rightarrow t = \tau$ and $\theta_1 = 0°$ and $\theta_2 = 138°$. The steady-state contrast here is 3.5%, with a lifetime that lasts about 6 μ s. Like the single Rabi channel experiment, there is a large dip present in the transient data. The Fourier data will take the signal beginning at $t = 0.5$ μs.

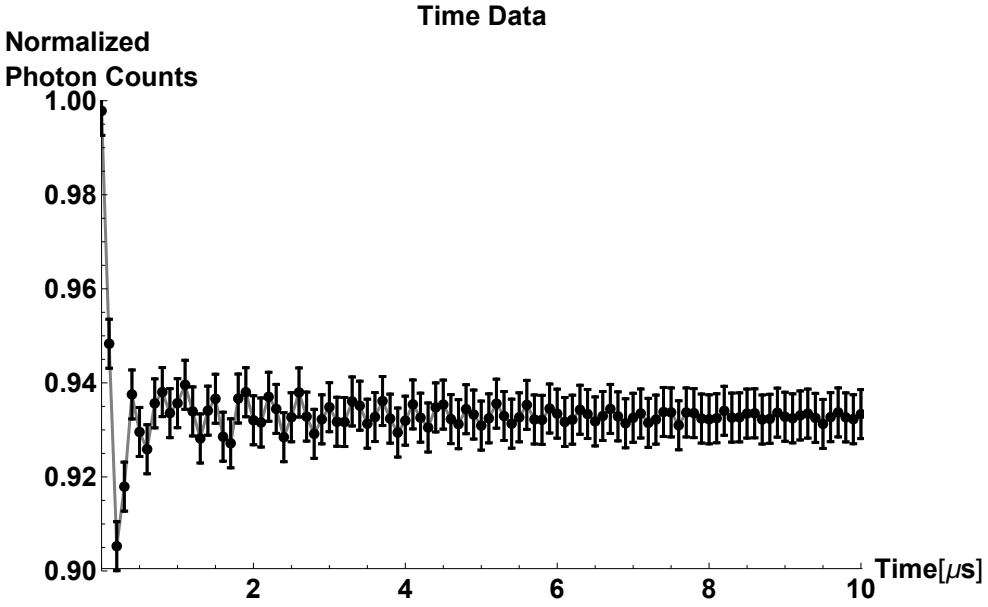

Figure 5.36: Rabi Time Data - High Frequency. Dual Rabi Channel Time Data with $t = 0 \rightarrow t = \tau$ and $\theta_1 = 0°$ and $\theta_2 = 275°$. The steady-state contrast here is $\approx 8\%$, with a lifetime that lasts about 6 μs. Like the single Rabi channel experiment, there is a large dip present in the transient data. The Fourier data will take the signal beginning at $t = 0.5$ μs.

The time data yields that there is an obvious response to the Rabi frequency when the phase of the two channels has been changed. There is a clear high and low-frequency response that can be oscillated between. To understand this relationship more clearly, this experiment is repeated with multiple phase values.

5.7.2 Simulating the Response with a Varying Phase

The time data showed an early indication that the Rabi results confirm the trends indicated by the relative microwave experiment, that there is significant dependence on the Rabi frequency with a change in phase. To analyze this change fully, a Rabi experiment for incremental values of θ_2 must be taken, with a fixed θ_1.

The simulation below uses the Hamiltonian modelled in chapter three in equation 3.31. From this, the geometric values to account for the different NV P.A.S for a (100) diamond are added, and the microwave geometry estimated from the single-channel Rabi results are used for the NV position. Recall, the estimated geometry is shown in figure 5.21. No inhomogeneities were added in these simulations, so just the dependency on the geometric values and NV orientations could be investigated.

To gather the simulated results shown below, a Rabi experiment was simulated with equal amplitude for each channel, but having the phase vary for each experiment. The phase of channel 1 was fixed at $\theta_1 = 0°$, while the phase of the second channel was incremented from $\theta_2 = 0° \rightarrow \theta_2 = 360°$ by ten degrees for each individual simulation. For each, the Fourier response was gathered and the frequency of the sub-ensembles recorded.

The frequencies from each Rabi experiment are summarized in figure 5.37 to show how they scale with changing the phase of the second channel. As the phase of the second channel is swept from 0° to 360°, the absolute values of the frequencies of the two sub-ensembles change, minimizing at 180°. They do not have the same dependency on the phase change, so as the phase is changed, the ratio between the two peaks changes as well. The maximum of the peak separation is (0.59:1) and at minimum, the peaks converge to (1:1). The phase response is symmetrical about 180°. The convergence point is not at the minimum, but slightly away from the minimum at 170° and 190°. When the two peaks collapse into one, the sub-ensembles may be treated as one orientation.

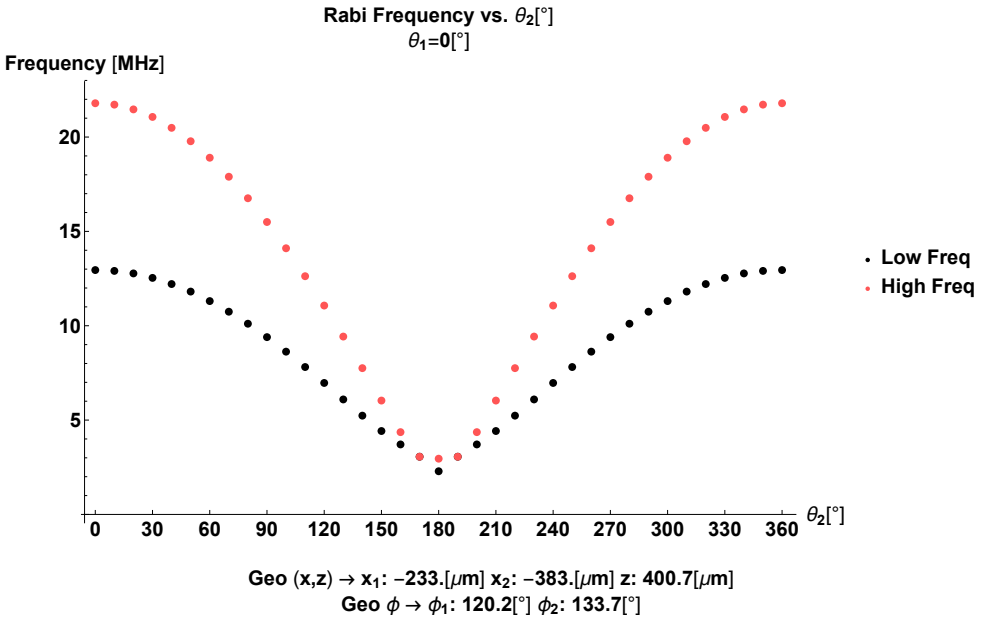

Figure 5.37: The simulated dual-channel Rabi results with varying the phase of the second channel (θ_2). For each simulation, a Rabi experiment was conducted, the Fourier response acquired and the frequencies from each gathered, and summarized in the figure above. The results show the two sub-ensembles, the low **(black)** and high **(red)** and their response to the change in phase. As the phase is swept from $0° \rightarrow 360°$, the frequencies are at their largest absolute values and then minimize at 180°. The ratio between the peaks also changes, where they are maximally separated at (0.59:1) and then converge to (1:1) near the minima point. The response to the phase may be used to indicate the geometric location of the NV ensemble relative to the microstrips.

This simulation was repeated for a few different NV geometry sites to see how the relationship changes with different locations of the NV ensemble relative to the microstrips. As the NV ensemble gets closer to the center point between the two microstrips, the ratio between the two frequencies diminishes. At the center point, there is no distinction between the two sub-ensembles. This is because at the center point, the "z" portion from each stripline cancel from being projected in the opposite direction. At this point, this leaves only the contribution from the "x" portion of the control field. As there are only two sub-ensembles, removing one portion of the field removes the distinction between them, resulting in only one peak. At the center point, as the control phase between the two channels is swept, the frequency of the peak moves in magnitude, but not does split.

At the other extreme, the pieces where the "x" and "z" portion of the control field contribute equally, there will be a maximal distinction between the two sub-ensembles. Recall that the base separation between the two peaks is (0.57:1), when the geometric factor on the Hamiltonian is removed. In the absence of inhomogeneities, this is the largest ratio between the two peaks that can be expected.

As the geometric location of the NV moves closer to the center of the microstrips from the largest extreme, the ratio between the peaks decreases, as does the rate of change of the ratio when the phase of the θ_2 is varied. The place where the two sub-ensembles converge also changes. At the center of the microstrips, the sub-ensembles are indistinguishable, while away when the contributions from the "x" and "z" control field are equivalent, the convergence occurs closer to the 180° point, and for less instances of θ_2.

No matter the geometry, given the handiness of the field and this model of Hamiltonian and microwave field configuration, the simulation results were always symmetric about 180° in simulation.

The response to how the absolute value and ratio between the two frequencies changes is a key indicator to the geometry of the location of the NV ensemble. Now the experimental results will be investigated, to see how closely these mimic the simulated results. If they are exactly matched, this indicates the estimated value of the NVs is correct and may be used for designing the OCT experiments. If the results do not match the simulated results, it still provides valuable information for how the amplitude of the Rabi response varies with changing the phase between the two channels.

5.7.3 Experimental Results - Varying the Phase

The experimental data for the dual-channel Rabi were gathered using the same procedure as the simulated results. A Rabi experiment was conducted with the phase of the first channel fixed to $\theta_1 = 0°$, while the phase of the second channel θ_2 was incremented, by a difference of 30° for each experiment. The same input amplitude for each stripline was used. Each experiment followed the same signal averaging procedure, collecting each data point (n=50 000) times and averaging for (N=100) times.

In each case, the Fourier response was gathered, and the location of the frequencies were recorded. As was seen in the time data shown, when analyzing the frequency data, the time was taken starting from 0.5 μs to remove the large inhomogeneity. The contrast between the low and high-frequency peaks were not equal, as was also evident from the time data, where the low-frequency data showed $\approx 3.5\%$ contrast and the high-frequency peak 8% contrast.

The summary of the location of the frequencies for each Rabi experiment are summarized in figure 5.38 below. The "x"-axis is the phase of the second channel, while the first channels phase was set to 0°. The "y"-axis, are the recorded Rabi frequencies for each sub-ensemble at those two set channel phases. Each set of data represents a separate experiment, which has been summarized into one plot so the change in frequency of the sub-ensembles as dependent on the phase of the channels may be analyzed. The error bars are given by the average linewidth of each peak for all experiments (0.25 MHz). The maximum separation between the peaks is (0.42:1), while the minimum is (0.68:1). There is an overlap seen of the linewidths at the minima, but the peaks are still distinguishable in these cases.

As the ratio between the peaks begin large at (0.42:1) and the change between the minima and maxima is also large (0.42:1) to (0.64:1), this further supports the NV ensembles are in the expected geometric location. If they were close to the center of the microstrips, the response to the change in phase would be much less emphasized. The contributions from the "x" and "z" fields are close to equal.

The experiment results follow the same trends seen in the simulations. The difference between the maximum and minimum separation between the peaks occur 180° apart. At the maximum separation, the absolute values of the frequencies are largest, and converge to the smallest values of the frequencies at the minimum.

Unlike the simulation, the minimum frequencies in the experimental results do not occur at 180°, but at 135°. This is due to a 45° difference in the hardware between the two channels, confirmed by measuring the phase difference through an oscilloscope for multiple combinations of phases. This behaviour was also seen in the following work, the minima changing with a difference in the channel length, [60]. For this reason, the phase of the second channel was expanded beyond 0° and 360° so the symmetry about the minima point could be seen. The maxima between the two peaks corresponds to 315° and −45°, symmetric about the minima, separated by 360°.

The absolute values for the Rabi frequency for this setup is observed. The range of frequencies is at minima 0.4 MHz and at maximum 2.9 MHz. These amplitude values should be taken into account as parameters for the OCT experiment. Recall the OCT experiment takes the absolute values of the frequencies into account.

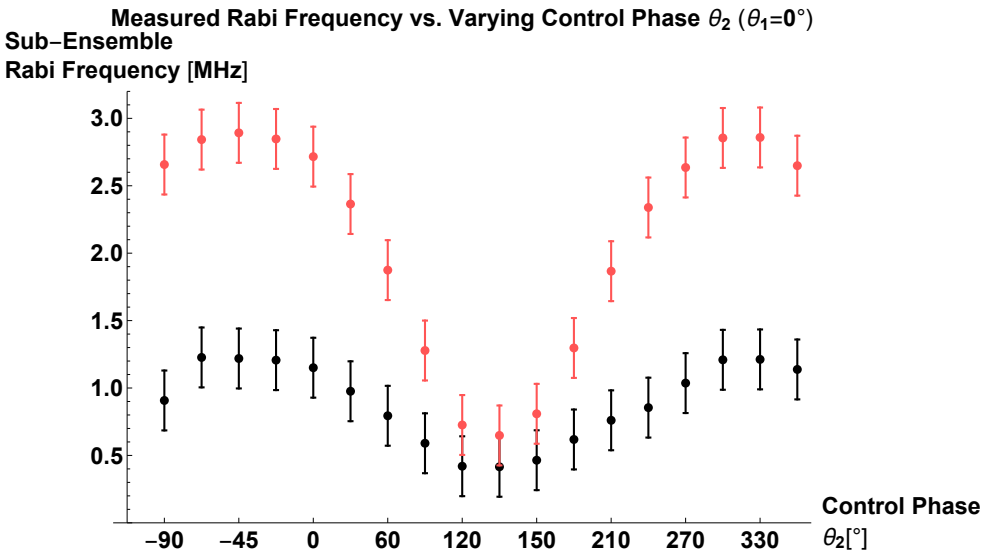

Figure 5.38: The experimental results for a dual-channel Rabi experiment with varying phase. The experimental results are closely matched with the simulation results. The low and high-frequency peaks both have their absolute maxima values at $-45°$ and $315°$, and converge to the minima at $135°$. The ratio between the peaks is maximized at (0.42:1) and changes to (0.68:1) over the same phase values.

The relative microwave phase and dual-channel Rabi experiment both show phase dependency, and consistently showed the high-frequency sub-ensembles is far more sensitive to the change in phase, compared to the low-frequency. Additionally, there were some key phase conditions outlined in the relative microwave phase experiment. When looking at the low-frequency NV pair for $\theta_1 = 0°$, the maximum and minimum points were given when $\theta_2 = 315°$ and $\theta_2 = 138°$. On the dual-channel Rabi experiment, these same phases corresponded to the maximum and minimum separation between the sub-ensemble Rabi frequencies. Performing the relative microwave phase experiment would allow for fast analysis of the maximum and minima absolute measured Rabi frequency and separation between the sub-ensembles before completing the more rigorous dual-channel Rabi.

While the experimental results of the dual-channel Rabi show much of the same trends as the simulated data with the proposed Hamiltonian model, the results do not match exactly. This indicates there are more parameters that have not been included in the *a priori* Hamiltonian model shown in chapter three. These unknown experimental parameters may still be gathered with a phenomenological Hamiltonian for the OCT experiments.

5.8 Implementation of OCT Pulses for NV Ensembles

Thus far, the intention of the experiments has been to collect data on the behaviour of the NV ensemble under the microwave field configuration and diamond crystal. In this final experimental section, the parameters gathered from the previous experiments will be used to implement OCT pulses. Chapter three simulated OCT controls with a general *a priori* Hamiltonian model. Experimentally, there are two options for implementing the Hamiltonian, the first is with an *a priori* Hamiltonian demonstrated in chapter three (section 3.1.3). A complete knowledge of the NV orientation, and location relative to the microstrips forms the *a priori* Hamiltonian. The second option is to use the experimental parameters gathered and form a phenomenological model of a Hamiltonian which uses only measured values.

The first experiments attempted were with the *a priori* Hamiltonian, the same model used in chapter three and the geometric location estimated from the single-channel Rabi experiments (section 5.4.5). While the results did qualitatively show the desired trends, the final resulting states were inconsistent, and target final state overlaps were much lower than expected. This is not a surprise as the experimental Rabi results did not match the simulated results exactly. As a result, a phenomenological Hamiltonian model was developed using only measured values gathered from the previous experiments.

The *a priori* results will be shown to reveal the qualitative improvements, then the phenomenological Hamiltonian model will be explained, outlining any differences between the two Hamiltonians. This will be followed by how the pulses are created and implemented experimentally. This is very similar to the methods used in chapter three (section 3.2.1), but will detail more of how the pulses are created and adjusting for the experimental values. The pulse sequence for these experiments will then be shown, and last, end with the OCT experiments implemented.

5.8.1 A Phenomenological Hamiltonian for OCT Experiments

Summary of results from an *a priori* Hamiltonian model

The Hamiltonian model used in chapter three, using the estimated geometry in chapter five did show successful qualitative results. This Hamiltonian model confirmed two major pieces. First is that optimizing pulses using a state-to-state transfer as opposed to a unitary target was more successful. Second was that optimizing a pulse over two of the four orientations of NVs was the most optimal.

This experiment compared the success of an identity pulse first comparing a unitary target vs. a state-to-state target. All experiments were repeated for (n=50 000) times for each data point and then averaged for (N=30 times). The unitary pulse was given the target $\mathbb{1}$, while the state-to-state transfer was given the target $|0\rangle\langle 0| \rightarrow |0\rangle\langle 0|$. Second, each of these was optimized over one, two or four orientations. It was clear that optimizing for a state-to-state transfer vs. a unitary pulse was more successful. It was also confirmed that for each of these cases, optimizing over the two pairs of NVs was most successful. This is reflected in table 5.1.

For the following experiments, the NVs are distinguished by their pairs. NV pair A is defined as the pair of NVs with the higher frequency Rabi response (-1,-1,1) and (1,-1,-1). NV pair B are the lower frequency pair (1,1,1) and (-1,1,-1). If a pulse is designed for pair A, it is designed for the (-1,-1,1) NV, and pair B, the (1,1,1) NV, while the others are left to evolve freely. If a pulse is designed for pair AB, it is designed for the (-1,-1,1) and (1,1,1) NV. The experiments labelled "All", are designed for all four orientations. The uncertainty on the population of the zero state was gathered by running the same experiment multiple times and measuring the change in recorded population of zero. For all experiments, this was consistent at 1.5%.

Table 5.1: Identity Pulse Results for an *A priori* Hamiltonian. Results compare optimizing an identity pulse for a target unitary $\mathbb{1}$ and a target state-to-state transfer, $|0\rangle \rightarrow |0\rangle$. For each of these, the pulses are also optimized for 1, 2 or 4 NV orientations. The starting state for all experiments was $|0\rangle$, a photon value of 1, so the ideal final state is also 1 for those pulses optimizing over 2 or 4 NV orientations. The state-to-state transfers showed more success than the identity pulse, and for both cases, optimizing over two orientations was the most successful. The best result was a photon count of 0.93, corresponding to a population of the $|0\rangle$ state of 30%.

Experiment	$\mathbb{1}_A$	$\mathbb{1}_{AB}$	$\mathbb{1}_{All}$	$\|0\rangle \rightarrow \|0\rangle_A$	$\|0\rangle \rightarrow \|0\rangle_{AB}$	$\|0\rangle \rightarrow \|0\rangle_{All}$
Normalized Counts	0.90(3)	0.91(8)	0.91(9)	0.91(6)	0.93(0)	0.92(5)
Population of $\|0\rangle$	$3 \pm 1.5\%$	$18 \pm 1.5\%$	$19 \pm 1.5\%$	$16 \pm 1.5\%$	$30 \pm 1.5\%$	$25 \pm 1.5\%$

While these results showed the desired qualitative results, there is room for improvement. The starting state for all experiments was the $|0\rangle$ state. An ideal identity pulse would have therefore have a final photon count reach a value of 1, (100% population of $|0\rangle$), matching the bright state, showing a full recovery of the population back to the $|0\rangle$ state. The dark state sits at 0.9, (0% population of $|0\rangle$). It is encouraging to see that there is a significant improvement from the worst result which barely discernible from the dark state ($\mathbb{1}_A$), to the best result with up to 30% population ($|0\rangle \rightarrow |0\rangle_{AB}$), indicating the spin system is responding to the optimization.

Likely the major source of error for this Hamiltonian is an inaccurate representation of the location of the NVs. It is for this reason, a phenomenological model for the Hamiltonian is formed, which uses only experimentally collected values.

Forming a phenomenological Hamiltonian model

The phenomenological Hamiltonian takes a different approach to the *a priori* model. Using only experimental values, it simplifies the Hamiltonian and leaves only one unknown parameter from those already collected.

To form the Hamiltonian, first the signal from the first stripline is chosen to align with the NVs "x"-axis. The experimental phase (η) captures the phase difference between the first and second stripline, including things but not limited to the difference in field direction.

This experimental phase is represented in the control Hamiltonian shown below, where the signal from the first stripline contains only an amplitude Ω_1 with the S_x operator, while the second stripline contains components from both S_x, and S_y, offset by the phase η. The amplitude of the second wire at the site of the NVs is Ω_2. The frequency ω_T is the transmitter frequency of the microwaves.

Last, there are two phases present, the first ($\Delta\theta$), represents the difference in control phase between the two microstrips. This phase may be controlled for experimental purposes. The second phase (η) represents the experimental phase between the two wires at the site of the NVs.

$$\mathcal{H} = \Omega_1 \cos(\omega_T t) S_x + \Omega_2 \cos(\omega_T t + \Delta\theta)\cos(\eta) S_x + \Omega_2 \sin(\omega_T t + \Delta\theta)\sin(\eta) S_y \tag{5.8}$$

Following the same procedure as was outlined in chapter three (section 3.1.3), the effective Hamiltonian is reached for one of the NV P.A.S:

$$\begin{aligned}\tilde{\mathcal{H}} =& \frac{\Omega_1}{2} S_x + \frac{\Omega_2}{2}\cos(\Delta\theta)\cos(\eta) S_x + \frac{\Omega_2}{2}\cos(\Delta\theta)\sin(\eta) S_y \\ &+ i\frac{\Omega_2}{2}\sin(\Delta\theta)\cos(\eta)[S_x, S_z^2] + i\frac{\Omega_2}{2}\sin(\Delta\theta)\sin(\eta)[S_y, S_z^2]\end{aligned} \tag{5.9}$$

A quick analysis of this Hamiltonian can give some intuition for the experimental control. There are four base operators present, $S_x, S_y, [S_x, S_z^2]$ and $[S_y, S_z^2]$, as was seen in the general form of the *a priori* Hamiltonian. The Hamiltonian may also be written in the pseudo spin-$\frac{1}{2}$ operators. In this case, the Hamiltonian has been simplified such that the control phase $\Delta\theta$, oscillates the Hamiltonian between $S_{x(y)}$ and $[S_{x(y)}, S_z^2]$, while the experimental phase η oscillates the control between x and y operators.

The experimental phase cannot be chosen, except for by changing the location of the NVs relative to the microstrips and other physical aspects of the system, but it may be found through experiments. The advantage of this Hamiltonian over the *a priori* Hamiltonian is it may measure the unknown experimental parameter through experiments, rather than rely on an estimated value.

5.8.2 Designing Pulses for Experimental Purposes

This section will show how the pulses are implemented in the experimental setup. Like chapter three, the GRAPE algorithm is used to implement the pulses. Very little differs from chapter three to generate the pulses. Any differences will be highlighted, and more information will be provided on how the different control Hamiltonians for each orientation are implemented.

Control Hamiltonians and Targets for Experimental Implementation

Chapter three demonstrated a few examples of OCT pulses. Chapter three focused mainly on the output from the pulses, detailing how the target state-to-state transfer is shown and the abilities of implementing pulses in the (100) diamond with this experimental microwave configuration (section 3.2.2, 3.2.3 and 3.3.1). In this section, a more detailed explanation of how the pulses are implemented in the experimental setup will be shown.

The pulses are found with the GRAPE algorithm, implemented with the *Quantum Utils* program designed for Mathematica, [114]. The pulse design accepts a target state-to-state transfer, target state overlap, control parameters, a control Hamiltonian, an internal Hamiltonian, a resolution of each time step, number of time steps and initial guess for the pulse.

Chapter three already showed examples of using these inputs for simulations. In this chapter, the real values will be shown for each input, detailing the changes between simulation and experimental values. Remaining unchanged are the state-to-state transfer and target state overlap. The state-to-state transfer is experiment specific and for each experiment, the target state overlap is 0.99.

As the control Hamiltonian is expressed in the effective frame of the P.A.S for each NV orientation, the internal Hamiltonian is a (3x3) matrix of zeros. If a static field or hyperfine interaction with the Nitrogen were to be added into the experiments, these are added into the internal Hamiltonian.

The first experiments performed with the *a priori* Hamiltonian used four control Hamiltonians to represent the four NV orientations. As the best results were seen with only two orientations, and the previous experiments showed the presence of only two sub-ensembles, the following experiments were performed using only two control Hamiltonians, and with only two control parameters. Each control Hamiltonian is labelled $\mathcal{H}_{NVA}$ and $\mathcal{H}_{NVB}$, respectively. As the effective Hamiltonians for each NV orientation are independent, the total control Hamiltonian is given by the direct sum for each orientation, as shown in equation 5.10 below:

$$\mathcal{H}_{control} = \alpha\mathcal{H}_{NVA} + \beta\mathcal{H}_{NVB} \tag{5.10}$$

The parameters α and β allow for individual targets to be set on each effective Hamiltonian. With the OCT pulses, two targets, T_A and T_B, are implemented for each control Hamiltonian representing the two sub-ensembles. Each target may be given the same target instructions or an individual target, for collective or selective control as was seen in chapter three. The total target is shown in equation 5.11:

$$\text{target} = \alpha T_A + \beta T_B \tag{5.11}$$

To implement the target, the distribution of the parameters $\alpha \to \beta$ are set. The value of the distribution must add to one. For example, if the pulse was designed to target NV_B while the other sub-ensemble were left to evolve freely, $\beta \to 1$, while $\alpha \to 0$. If a total target was designed for both, the distribution would be $\beta \to \frac{1}{2}, \alpha \to \frac{1}{2}$. While the total distribution of the parameters must add to one, the split between each orientation may vary.

Controls Parameters for Experimental Implementation

As only two control Hamiltonians are necessary to find OCT pulses for this diamond configuration, only two control parameters are required to design the pulses. As the sub-ensembles showed sensitivity to both the relative and absolute phase of the microstrips, seen in the relative microwave phase experiment and dual-channel Rabi experiment, the phase is fixed and only the amplitudes of each channel were used to find the control pulses.

The amplitude and phase of the channels are simply the polar coordinates of the four control parameters, I_1, I_2, Q_1, Q_2, with $\Omega_{(1/2)} = \sqrt{I_{(1/2)} + Q_{(1/2)}}$ and $\theta_{(1/2)} = \arctan\left(\frac{Q_{(1/2)}}{I_{(1/2)}}\right)$. With a fixed phase, only amplitude control is required for the control parameters.

In addition to changing from four control parameters to two, the units for the parameters were also changed from simulation to experimental implementation. Recall in chapter three, figure 3.10 showed a sample of the control parameters used for a simulated pulse, where the controls were restricted by an amplitude in the units of frequency. This was a convenient method to use, which shows the proof of concept of pulses without having to consider unknown experimental parameters given by the microwave field configuration.

The same concept is applied here, but since the frequency at the site of the NVs is known, the controls are determined by scaling the amplitude by a unitless $0 \rightarrow 1$, and then multiplying by the measured frequency. Recall the dual-channel Rabi experiment revealed two measured amplitudes for each sub-ensemble, found by setting the amplitude of the microstrips each to 1. To find the pulses for each control Hamiltonian, the values of Ω_1 and Ω_2 are varied between $0 \rightarrow 1$, optimizing the pulses for the measured Hamiltonian values for each sub-ensemble.

In addition to using only amplitude control with a fixed phase, the time step resolution is also adjusted from simulation to the implemented pulses. When the pulses are implemented by the AWG, there are hardware distortions which will change the pulse from the intended shape, [43]. In general, pulses which resemble much closer to a smooth pulse will have less resulting errors. To create a smoother pulse, the time step resolution should be adjusted to accommodate a different Rabi amplitude. As the measured Rabi amplitude was much lower than the simulated pulse amplitude (≈1-3 MHz vs. 50 MHz), a more coarse time step resolution was chosen, (40 ns vs. 2 ns). Figure 5.39 shows the pulses produced with a 2 ns vs. a 40 ns time step resolution using the overall Rabi amplitude frequency of 1.6 MHz and 2.8 MHz for NV pair A and B. Recall the Hamiltonian is multiplied by the measured Rabi frequency, and the pulses are found by allowing the amplitudes to oscillate within a range of $0 \rightarrow 1$.

To implement a pulse, the AWG will receive a list, given by the Ω_1, Ω_2 values as shown above in the control pulses for each time step. Each of these amplitudes will be multiplied by a constant chosen phase to produce the four-channel I_1, I_2, Q_1, Q_2 configuration the AWG desires. The list the AWG receives are values ranging from $-1 \rightarrow 1$, which are then scaled by the same peak-to-peak voltage as with the dual Rabi channel experiment so the measured frequency value at the site of the NV matches.

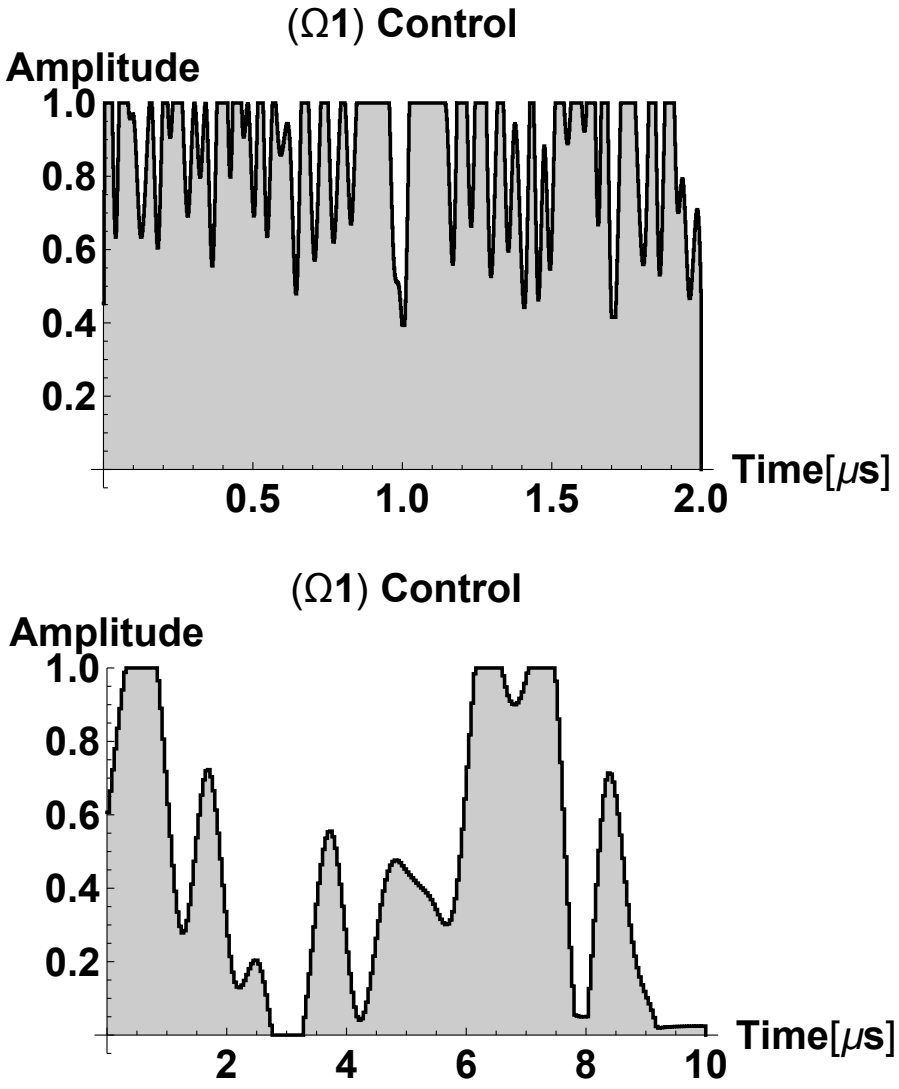

Figure 5.39: Sample pulse comparing time step resolution. Comparing the pulses produced using a 2 ns **(Top)** and 40 ns **(Bottom)** time step resolution with the same measured Rabi frequency envelope of 1.6 MHz and 2.8 MHz for NV pair A and B. To avoid hardware distortion issues, the pulses should be as smooth as possible. With such a low measured Rabi frequency, a time step resolution of 2 ns greatly over samples, and creates a pulse which is prone to hardware distortion. A more coarse time step resolution of 40 ns is more appropriate for the lower Rabi amplitude, creating a smoother pulse. Only the Ω_1 controls are shown, but the Ω_2 show similar trends.

Pulse Diagram for OCT experiments

The pulse diagram for the OCT experiments is shown in 5.40. As with the Rabi like experiments, the same basic sequence is followed. First, the laser initializes the NV ensemble, and the bright states are read out. This is followed by the OCT pulse, and the dark states read out. The OCT pulse is unique to the pulse implemented for the each experiment. For each pulse, the sequence is repeated (n=50 000) times to collect enough photons, then the next pulse is implemented. For each set of experiments, any number of OCT pulses may be implemented and the states compared after each one. Between each, the NVs are re-initialized. After all the experiments in the set have been tested, the entire sequence is repeated for (N=30) averages.

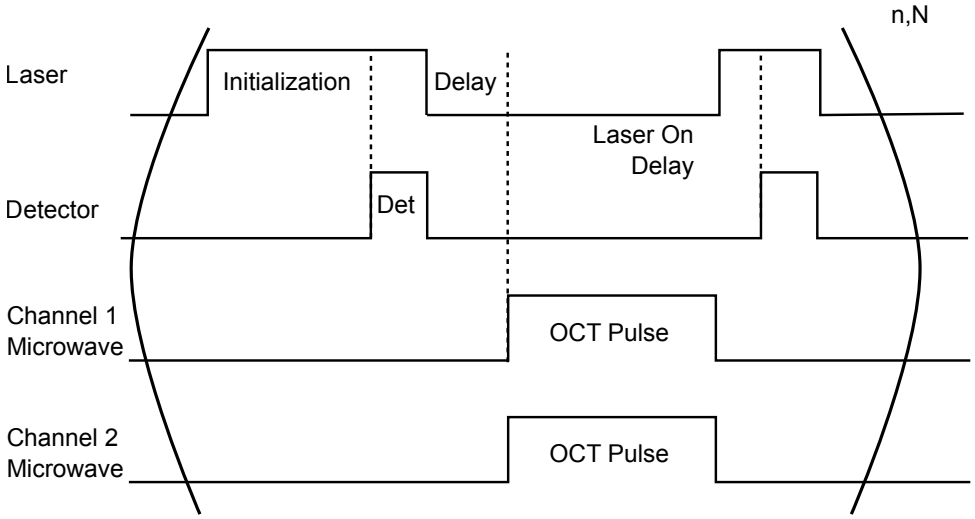

Figure 5.40: Pulse Diagram for OCT experiments. The initialization and readout of the NV state follow the same procedure as was seen with the Rabi experiment. The microwaves follow the controls given by the OCT experiments and the state is read out after the length of the pulse. As with the previous experiments, this is repeated (n=50 000) times to acquire enough photons. The sequence is then repeated for as many OCT pulses is required, re-initializing in between each one. Once the list of OCT experiments has been completed, the entire sequence is averaged (N=30) times.

5.8.3 Phenomenological Hamiltonian Results

The phenomenological Hamiltonian model contains one unknown parameter, an experimental phase factor (η) which includes the relative fields from the microstrips and any channel phase differences. For this model, the field representing the first stripline is chosen to be the "x"-axis. The field from the second wire is distinguished by the experimental phase factor η from the first wire. To find the value η, multiple $\mathbb{1}$ and π_+ pulses for NV pair A were optimized over a range of η values. Recall that the $\mathbb{1}$ pulse is really a state-to-state transfer from $|0\rangle\langle 0| \rightarrow |0\rangle\langle 0|$ and the π_+ a transfer of $|0\rangle\langle 0| \rightarrow |+1\rangle\langle +1|$. For these experiments, the control phases were fixed at $\theta_1 = 0°$ and $\theta_2 = 275°$.

The OCT pulses were optimized over a range of η values, ranging from $5° \rightarrow 175°$ in increments of 5°. While each pulse was able to be optimized, the experiments were more or less successful when implemented on the experimental setup depending on the input η value. Over this optimized range, the pulses with an experimental phase value of $\eta = 115°$ were the most successfully implemented. The success criteria was defined by how distinguishable the results of the $\mathbb{1}$ and π_+ pulses were.

Following the sweep, the more pulses were optimized for the NV B pair, and then again for both pairs.

The results for optimizing an Identity and a single transitions π pulse are shown in table 5.2. In accordance with the pulse diagram, the NVs are first initialized, then the complete control pulse implemented and the output photon counts measured. The NVs are re-initialized before the next pulse is run. The results show the output from six experiments, $\mathbb{1}_A, \pi_{+A}, \mathbb{1}_B, \pi_{+B}, \mathbb{1}_{AB}, \pi_{+AB}$.

Table 5.2: The results show the final photon count collected following six OCT experiments, and their corresponding population of the $|0\rangle$ state, $\mathbb{1}_A, \pi_{+A}, \mathbb{1}_B, \pi_{+B}, \mathbb{1}_{AB}, \pi_{+AB}$. These experiments represent an Identity ($|0\rangle\langle 0| \rightarrow |0\rangle\langle 0|$) and single transition π pulse ($|0\rangle\langle 0| \rightarrow |+1\rangle\langle +1|$) optimized for NV pair (A), (B) and both pairs (AB). The Identity results are consistent, optimizing to ≈ 0.94, and the π_+ results to ≈ 0.92. For an identity pulse the ideal result would be a value of 1, and for the π pulse, 0.9.

Experiment	$\mathbb{1}_A$	π_{+A}	$\mathbb{1}_B$	π_{+B}	$\mathbb{1}_{AB}$	π_{+AB}
Normalized Counts	0.94(0)	0.91(7)	0.94(0)	0.91(9)	0.93(9)	0.92(5)
Population of $\|0\rangle$	$40 \pm 1.5\%$	$17 \pm 1.5\%$	$40 \pm 1.5\%$	$19 \pm 1.5\%$	$39 \pm 1.5\%$	$25 \pm 1.5\%$

For a population of $|0\rangle$ of 100%, the Identity pulse would show a photon count of 1, while the π_+ pulse would show a result close to 0.9. First, the results of the identity pulses. While the best case of the identity pulse results at 40% population, it is a significant improvement from the results run with the previous Hamiltonian model. In the previous model, optimizing over one NV pair gave a best result of 0.903, over NV pair A, while here a value of 0.940 was achieved, improving the population from 3% to 40%. Additionally, comparing the results to optimizing over both pairs of NVs, the previous best result was a population value of 30% and 39% in this case. Further, this shows obvious improvement over the previous results as these pulses were only optimized using amplitude, so the instinct to restrict the phase because of the phase sensitivity was correct.

The π_+ results are consistent for optimizing over NV pair A and B, with a value just less than 0.92, and optimizing for both sub-ensembles a value just above 0.92. At first glance, it would appear the π_+ pulses are closer to their desired photon count value of (0.9), which is a much better population value of 17% and 19% for NV pair A and B respectively, compared with the identity pulses. Recall that for the π_+ pulses, the population of the $|0\rangle$ should be 0 in the ideal case, so a low population value is desired.

Optimizing over a static field inhomogeneity

While the phenomenological Hamiltonian has shown improvement compared with using the *a priori* Hamiltonian, there are still obvious improvements that may be made. To accommodate a lower Rabi frequency, not only was a more coarse time step resolution necessary, but the pulse required more time to optimize, extending the length of the pulse to 10 μs. With an extended pulse length, there is competition with decoherence occurring from field gradients and other local spins including C^{13} to name a few examples.

As an exercise, the experiments were repeated, optimizing over a small static field inhomogeneity equivalent to $\pm 150\ kHz$. The static field inhomogeneity is implemented as an offset value in the internal Hamiltonian proportional to δS_z, where δ =150 kHz. The pulses were then optimized over a uniform distribution of $-\delta \rightarrow \delta$ in steps of $\approx$ 14 kHz. This was tested for optimizing the $\mathbb{1}$ and π_+ pulses for NV pair A. The results of the optimization on the final state overlap are shown in table 5.3.

Table 5.3: Final State Overlap Comparison for NV Pair A with and without optimizing over a field inhomogeneity, labelled as (Field Opt).

Experiment	$\mathbb{1}_A$	$\mathbb{1}_A$ (Field Opt.)	π_{+A}	π_{+A} (Field Opt.)
Normalized Counts	0.94(0)	0.95(3)	0.91(7)	0.92(1)
Population of $\|0\rangle$	$40 \pm 1.5\%$	$53 \pm 1.5\%$	$17 \pm 1.5\%$	$21 \pm 1.5\%$

Optimizing over this distribution improved the previous population value of the $\mathbb{1}$ pulse, optimized over NV pair A by $13 \pm 1.5\%$. The π_+ results declined slightly, from $17 \pm 1.5\%$ to $21 \pm 1.5\%$, recalling that for these experiments, the best desired result is a population of 0. The $\mathbb{1}$ results are more sensitive to static field inhomogeneities than π_+ pulses due to the refocusing nature of π pulses, so the identity results being more sensitive to this optimization is expected.

The large improvement on the $\mathbb{1}$ pulse with optimizing over only an inhomogeneity of $\approx \pm 150$ kHz supports the theory that the main source of population loss is due to the pulse length.

The optimization performed is just a proof of principle to see how the OCT results respond to including robustness over some small arbitrary static field inhomogeneity. The low experimental Rabi-frequency is unable to optimize over larger field inhomogeneities while maintaining the same pulse length, but this population improvement over a small sample field shows the potential of this type of optimization. A more rigorous next step would be to measure the experimental field inhomogeneities, and compare to the simulated data. The ODMR-CW results indicated the experimental inhomogeneities to be larger than the sample static field of 150 kHz.

To optimize over these larger field inhomogeneities, a higher Rabi frequency is required. Increasing the Rabi frequency would allow for shorter pulses and optimization over larger field inhomogeneities, closer to the measured experimental inhomogeneities indicated by the ODMR-CW experiments.

OCT Summary

Optimizing pulses with state-to-state transfers rather than unitaries yielded more successful results. Further, each of these was tried with the *a priori* Hamiltonian, optimizing over one NV pair, the two sub-ensembles, or all four orientations. The best results were found with optimizing over the two sub-ensembles of NVs, with a final population value of 30% for the $|0\rangle \rightarrow |0\rangle$ pulse on both NV sub-ensembles.

This inspired the development of a phenomenological Hamiltonian, which uses only the measured Rabi amplitudes for each NV pair given a fixed control phase. The dual-channel Rabi and relative microwave phase experiment indicated the sensitivity to phase, so this was fixed. However, since the pulses needed only to optimize over two sub-ensembles, only two amplitude controls were required.

Pulses were optimized using the phenomenological Hamiltonian over a range of experimental phases, the only unknown in this Hamiltonian. Once the optimal value was found for NV pair A, this was repeated for NV pair B and both sub-ensembles, which yielded significant improvement over the previous *a priori* Hamiltonian results. The final population value of the Identity pulses were consistent at $\approx 40\%$ and $\approx 20\%$ for the π_+ for NV pair A, B and both pairs.

The increased pulse length was proposed to be the biggest source of error and so the pulses were further optimized over a small static field offset. This again yielded a large improvement in the final population value, yielding a final result of 53% for the Identity pulse on NV pair A, and 21% for the π_+ pulse.

There are numerous further improvements to be made, but the consistency of these pulses, easily distinguishable results of the identity and π pulses and response to optimizations made here are promising.

Chapter 6

Conclusions and Future Work

6.1 Conclusion

This thesis detailed three main pieces. The first is a novel generalized Hamiltonian of each of the four NV orientations in a varying diamond crystal orientation and microwave field control configuration. This model was used to simulate OCT control for each of the (100), (110) and (111) diamonds. An experimental setup was designed and built to suit the control requirements, most notably an optical system able to detect ensembles of NV centers and able to implement the helical microwave control required for the OCT pulses. A set of characterization experiments on the NV ensembles informed the necessary parameters to implement OCT pulses. OCT experiments were demonstrated for the (100) diamond, showing a clear proof of principle of collective control of four NV orientations, distinguishing between Identity state-to-state transfers and selective π state-to-state transfers. These results also responded well to including a robustness over a small static field inhomogeneity, indicating their potential for future optimizations.

Demonstrating OCT controls without the need of a static magnetic field, and NVs at an arbitrary location relative to the microwave control source allows for the direct integration of these controls with compact devices, expanding their applications. Collective control of all four orientations of NVs in an ensemble increases the signal to noise ratio by four times. Selective control enables more precise vector magnetometry and navigation. The groundwork for implementing these control pulses has been set in this thesis and looking forward, optimizing these controls and implementing into numerous applications will lead to exciting opportunities.

6.2 Future Work

6.2.1 Improving the OCT pulses and Experimental Setup

There are numerous ways to improve the effectiveness of the OCT pulses. It was encouraging to see that adding in a small optimization over a static magnetic inhomogeneity did improve the results significantly. Improving upon this could also involve increasing the Rabi amplitude to allow for shorter pulses to be implemented, making the pulses more robust to this decay to begin with.

Following this, two pieces to optimize over are the hyperfine coupling with the nitrogen nuclear spin and the microwave inhomogeneity from the microstrips. These pulses were only optimized over the $m_s = 0$ state of the nitrogen nuclear spin. Future iterations would see these pulses optimized over the $m_s = \pm 1$ states as well. An increased Rabi power would benefit this optimization as well. A 100x objective was used to implicitly reduce the volume of interest for the NV ensemble, therefore minimizing the microwave inhomogeneity. However, designing pulses to be robust over these inhomogeneities would allow experimentalists to increase the volume of interest, and then therefore reduce the restrictions on the objective, making the hardware more adaptable to a portable device.

Improvements to the experimental setup configuration

An engineer can always see room for improvement in their experimental setup. The thickness of the diamond combined with the shallow working distance of the objective placed the NV ensemble far from the microstrips, significantly reducing the control amplitude. A simple first step would use a thinner diamond would allow for a greater amplitude. Additionally, providing visual markers on the PCB board would act as a good sanity check to confirm the location of the NV ensemble.

6.2.2 Future Experiments

Expanding to different diamond crystal orientations

The (100) diamond did provide a useful platform for first testing the OCT pulses. As the NVs presented in only two sub-ensembles, understanding the physics and designing pulses was made easier with this orientation of diamond. This symmetry also presented an advantage for creating target pulses aimed at producing the same output for all four NV orientations having only to design for two, and removed the control phase as a required parameter, optimizing over only the control amplitude. Without changing the experimental setup, a (110) diamond may be used providing selective control on each of the four orientations. This enables four unique targets for each orientation, expanding the applications.

Testing with a known field

While the OCT pulses did yield that they were able to optimize over multiple orientations of the NV ensemble, the next natural test would be to confirm its usefulness with sensing a known external magnetic field in an DC or AC capacity and compare with existing sensing techniques. Confirmation of OCTs compatibility with existing sensing techniques would allow for the applications to be broadened to chemical sensing, as was proposed in the first chapter.

Expanding to a chemical sensing scheme

Expanding beyond AC and DC field sensing would be to integrate the control with a chemical sensing scheme, sensing moieties on the diamond's surface. This thesis highlighted the capabilities of OCT control with NV ensembles, demonstrating collective control over all four orientations is possible. Two example pulses, an Identity and a selective π pulse exhibited collective control on the NV ensemble in a (100) diamond. This was accomplished without the use of a static magnetic field and with one central microwave frequency controlling all four orientations.

With a similar scheme outlined in chapter one, the diamond may be functionalized, attaching a chemical species to its surface. The first experiment would compare the signal acquired by the NVs, detecting the presence of the species controlled both with and without a collective OCT pulse. Using an OCT pulse with collective control on the NV ensemble, treating it as one effective qubit would boost the signal to noise ratio by approximately four times, using all four orientations to sense the presence of the target species. This scheme may be expanded to include conformationally changing molecules, sensitive to target moieties, and using the NV ensemble to detect the change in conformation. Looking beyond this, selectively controlling the NV orientations allows for multiplexing of multiple target species.

OCT provides the advantage of being able to easily change the application and sensing scheme without alterations to the experimental setup. Further development of these schemes, removing more hardware restrictions like a high magnification objective, moving to a thinner diamond are all steps which would allow for easier integration with a portable chemical sensing device.

Onto a compact portable sensing device

There have been numerous demonstrations of a simple, cost-effective, compact setups compatible with NV experiments, [44, 94, 104, 111, 124]. This thesis proposes a control method implemented on the NV center whilst still maintaining a microwave configuration compatible with a portable device, notably the arbitrary location of the NVs and the absence of an external magnetic field. Integration of OCT controls with these existing devices would enhance their capabilities and applications for exciting future opportunities.

References

[1] Eisuke Abe and Kento Sasaki. Tutorial: Magnetic resonance with nitrogen-vacancy centers in diamond—microwave engineering, materials science, and magnetometry. *Journal of Applied Physics*, 123(16):161101, March 2018. Publisher: American Institute of Physics.

[2] V. M. Acosta, E. Bauch, A. Jarmola, L. J. Zipp, M. P. Ledbetter, and D. Budker. Broadband magnetometry by infrared-absorption detection of nitrogen-vacancy ensembles in diamond. *Appl. Phys. Lett.*, 97(17):174104, October 2010. Publisher: American Institute of Physics.

[3] V. M. Acosta, E. Bauch, M. P. Ledbetter, A. Waxman, L.-S. Bouchard, and D. Budker. Temperature Dependence of the Nitrogen-Vacancy Magnetic Resonance in Diamond. *Phys. Rev. Lett.*, 104(7):070801, February 2010. Publisher: American Physical Society.

[4] V. M. Acosta, A. Jarmola, E. Bauch, and D. Budker. Optical properties of the nitrogen-vacancy singlet levels in diamond. *Phys. Rev. B*, 82(20):201202, November 2010. Publisher: American Physical Society.

[5] Victor Marcel Acosta. *Optical magnetometry with nitrogen-vacancy centers in diamond*. PhD thesis, University of California, Berkley, Spring 2011.

[6] Thiago P. Mayer Alegre, Charles Santori, Gilberto Medeiros-Ribeiro, and Raymond G. Beausoleil. Polarization-selective excitation of nitrogen vacancy centers in diamond. *Phys. Rev. B*, 76(16):165205, October 2007. Publisher: American Physical Society.

[7] Nithya Arunkumar, Dominik B. Bucher, Matthew J. Turner, Patrick TomHon, David Glenn, Sören Lehmkuhl, Mikhail D. Lukin, Hongkun Park, Matthew S. Rosen, Thomas Theis, and Ronald L. Walsworth. Micron-Scale NV-NMR Spectroscopy with

Signal Amplification by Reversible Exchange. *PRX Quantum*, 2(1):010305, January 2021. Publisher: American Physical Society.

[8] D.P.L. Aude Craik, P. Kehayias, A.S. Greenspon, X. Zhang, M.J. Turner, J.M. Schloss, E. Bauch, C.A. Hart, E.L. Hu, and R.L. Walsworth. Microwave-Assisted Spectroscopy Technique for Studying Charge State in Nitrogen-Vacancy Ensembles in Diamond. *Phys. Rev. Applied*, 14(1):014009, July 2020. Publisher: American Physical Society.

[9] S. Baier, C.E. Bradley, T. Middleburg, V.V. Dobrovitski, T.H. Taminiau, and R. Hanson. Orbital and Spin Dynamics of Single Neutrally-Charged Nitrogen-Vacancy Centers in Diamond. *Phys. Rev. Lett.*, 125(19):193601, November 2020. Publisher: American Physical Society.

[10] John F. Barry, Jennifer M. Schloss, Erik Bauch, Matthew J. Turner, Connor A. Hart, Linh M. Pham, and Ronald L. Walsworth. Sensitivity optimization for NV-diamond magnetometry. *Rev. Mod. Phys.*, 92(1):015004, March 2020. Publisher: American Physical Society.

[11] John F. Barry, Matthew J. Turner, Jennifer M. Schloss, David R. Glenn, Yuyu Song, Mikhail D. Lukin, Hongkun Park, and Ronald L. Walsworth. Optical magnetic detection of single-neuron action potentials using quantum defects in diamond. *PNAS*, 113(49):14133–14138, December 2016. Publisher: National Academy of Sciences Section: Biological Sciences.

[12] Michael S. J. Barson, Elmars Krausz, Neil B. Manson, and Marcus W. Doherty. The fine structure of the neutral nitrogen-vacancy center in diamond. *Nanophotonics*, 8(11):1985–1991, November 2019. Publisher: De Gruyter.

[13] Erik Bauch, Connor A. Hart, Jennifer M. Schloss, Matthew J. Turner, John F. Barry, Pauli Kehayias, Swati Singh, and Ronald L. Walsworth. Ultralong Dephasing Times in Solid-State Spin Ensembles via Quantum Control. *Phys. Rev. X*, 8(3):031025, July 2018. Publisher: American Physical Society.

[14] Erik Bauch, Swati Singh, Junghyun Lee, Connor A. Hart, Jennifer M. Schloss, Matthew J. Turner, John F. Barry, Linh M. Pham, Nir Bar-Gill, Susanne F. Yelin, and Ronald L. Walsworth. Decoherence of ensembles of nitrogen-vacancy centers in diamond. *Phys. Rev. B*, 102(13):134210, October 2020. Publisher: American Physical Society.

[15] Hannes Bernien. *Control, measurement and entanglement of remote quantum spin registers in diamond*. PhD thesis, Technische Universtiteit Delft, 2014.

[16] Dominik B. Bucher, David R. Glenn, Hongkun Park, Mikhail D. Lukin, and Ronald L. Walsworth. Hyperpolarization-Enhanced NMR Spectroscopy with Femtomole Sensitivity Using Quantum Defects in Diamond. *Phys. Rev. X*, 10(2):021053, June 2020. Publisher: American Physical Society.

[17] Filipe Camarneiro, Juanita Bocquel, Juan Gallo, Manuel Bañobre-López, Kirstine Berg-Sørensen, Ulrik Lund Andersen, Alexander Huck, and Jana B. Nieder. Magnetic Field Mapping Around Individual Magnetic Nanoparticle Agglomerates Using Nitrogen-Vacancy Centers in Diamond. *Particle & Particle Systems Characterization*, page 2100011, 2021. _eprint: https://onlinelibrary.wiley.com/doi/pdf/10.1002/ppsc.202100011.

[18] Jeson Chen, Oliver Y. Chen, and Huan-Cheng Chang. Relaxation of a dense ensemble of spins in diamond under a continuous microwave driving field. *Sci Rep*, 11(1):16278, August 2021.

[19] Joonhee Choi, Hengyun Zhou, Helena S. Knowles, Renate Landig, Soonwon Choi, and Mikhail D. Lukin. Robust Dynamic Hamiltonian Engineering of Many-Body Spin Systems. *Phys. Rev. X*, 10(3):031002, July 2020.

[20] P. Christiaens, V. Vermeeren, S. Wenmackers, M. Daenen, K. Haenen, M. Nesládek, M. vandeVen, M. Ameloot, L. Michiels, and P. Wagner. EDC-mediated DNA attachment to nanocrystalline CVD diamond films. *Biosens Bioelectron*, 22(2):170–177, August 2006.

[21] Santibáñez Cisternas and Vicente Andrés. Chemical sensor based on nitrogen-vacancy centers in diamond. Master's thesis, Pontificia Universidad Católica de Chile, 2020. Accepted: 2021-01-22T14:42:15Z.

[22] Tyler B. Coplen, John Karl Böhlke, P. De Bièvre, T. Ding, N. E. Holden, J. A. Hopple, H. R. Krouse, A. Lamberty, H. S. Peiser, K. Revesz, S. E. Rieder, K. J. R. Rosman, E. Roth, P. D. P. Taylor, R. D. Vocke, and Y. K. Xiao. Isotope-abundance variations of selected elements (IUPAC Technical Report). *Pure and Applied Chemistry*, 74(10):1987–2017, October 2002. Publisher: De Gruyter.

[23] David J. Griffiths. *Introduction to electrodynamics*. Prentice Hall, 1999.

[24] Lucas Nunes Sales de Andrade, Charlie Oncebay Segura, and Sérgio Ricardo Muniz. Measurements of spin-coherence in NV centers for diamond-based quantum sensors. In *2021 SBFoton International Optics and Photonics Conference (SBFoton IOPC)*, pages 1–4, May 2021.

[25] Stephen J. DeVience, Linh M. Pham, Igor Lovchinsky, Alexander O. Sushkov, Nir Bar-Gill, Chinmay Belthangady, Francesco Casola, Madeleine Corbett, Huiliang Zhang, Mikhail Lukin, Hongkun Park, Amir Yacoby, and Ronald L. Walsworth. Nanoscale NMR spectroscopy and imaging of multiple nuclear species. *Nature Nanotechnology*, 10(2):129–134, February 2015.

[26] M. W. Doherty, F. Dolde, H. Fedder, F. Jelezko, J. Wrachtrup, N. B. Manson, and L. C. L. Hollenberg. Theory of the ground-state spin of the nv^- center in diamond. *Phys. Rev. B*, 85:205203, May 2012.

[27] M. W. Doherty, N. B. Manson, P. Delaney, and L. C. L. Hollenberg. The negatively charged nitrogen-vacancy centre in diamond: the electronic solution. *New J. Phys.*, 13(2):025019, February 2011. Publisher: IOP Publishing.

[28] Marcus W. Doherty, Neil B. Manson, Paul Delaney, Fedor Jelezko, Jörg Wrachtrup, and Lloyd C. L. Hollenberg. The nitrogen-vacancy colour centre in diamond. *Physics Reports*, 528(1):1–45, July 2013.

[29] Y. Dumeige, M. Chipaux, V. Jacques, F. Treussart, J.-F. Roch, T. Debuisschert, V. M. Acosta, A. Jarmola, K. Jensen, P. Kehayias, and D. Budker. Magnetometry with nitrogen-vacancy ensembles in diamond based on infrared absorption in a doubly resonant optical cavity. *Phys. Rev. B*, 87(15):155202, April 2013. Publisher: American Physical Society.

[30] Andrew Mark Edmonds, Connor A. Hart, Matthew J. Turner, Pierre-Olivier Colard, Jennifer M. Schloss, Kevin Olsson, Raisa Trubko, Matthew L. Markham, Adam Rathmill, Ben Horne-Smith, Wilbur Lew, Arul Manickam, Scott Bruce, Peter G. Kaup, Jon C. Russo, Michael J. DiMario, Joseph T. South, Jay T. Hansen, Daniel J. Twitchen, and Ronald Walsworth. Characterisation of CVD diamond with high concentrations of nitrogen for magnetic-field sensing applications. *Mater. Quantum. Technol.*, January 2021. Publisher: IOP Publishing.

[31] E. R. Eisenach, J. F. Barry, L. M. Pham, R. G. Rojas, D. R. Englund, and D. A. Braje. Broadband loop gap resonator for nitrogen vacancy centers in diamond. *Review of Scientific Instruments*, 89(9):094705, September 2018. Publisher: American Institute of Physics.

[32] Ádám Gali. Ab initio theory of the nitrogen-vacancy center in diamond. *Nanophotonics*, 8(11):1907–1943, November 2019. Publisher: De Gruyter.

[33] David R. Glenn, Dominik B. Bucher, Junghyun Lee, Mikhail D. Lukin, Hongkun Park, and Ronald L. Walsworth. High-resolution magnetic resonance spectroscopy using a solid-state spin sensor. *Nature*, 555(7696):351–354, March 2018. Number: 7696 Publisher: Nature Publishing Group.

[34] David R. Glenn, Kyungheon Lee, Hongkun Park, Ralph Weissleder, Amir Yacoby, Mikhail D. Lukin, Hakho Lee, Ronald L. Walsworth, and Colin B. Connolly. Single-cell magnetic imaging using a quantum diamond microscope. *Nature Methods*, 12(8):736–738, August 2015. Number: 8 Publisher: Nature Publishing Group.

[35] Arne Götze, Nico Striegler, Alastair Marshall, Philipp Neumann, Christian Giese, Patricia Quellmalz, and Peter Knittel. Preferential Placement of Aligned NV Centers in CVD-Overgrown Diamond Microstructures. *physica status solidi (RRL) – Rapid Research Letters*, 2021. _eprint: https://onlinelibrary.wiley.com/doi/pdf/10.1002/pssr.202100373.

[36] Jeremy J. Gray. Olinde Rodrigues' Paper of 1840 on Transformation Groups. *Archive for History of Exact Sciences*, 21(4):375–385, 1980. Publisher: Springer.

[37] A. Gruber, A. Dräbenstedt, C. Tietz, L. Fleury, J. Wrachtrup, and C. von Borczyskowski. Scanning Confocal Optical Microscopy and Magnetic Resonance on Single Defect Centers. *Science*, 276(5321):2012–2014, June 1997. Publisher: American Association for the Advancement of Science Section: Report.

[38] Connor A. Hart, Jennifer M. Schloss, Matthew J. Turner, Patrick J. Scheidegger, Erik Bauch, and Ronald L. Walsworth. Nv–Diamond Magnetic Microscopy Using a Double Quantum 4-Ramsey Protocol. *Phys. Rev. Applied*, 15(4):044020, April 2021. Publisher: American Physical Society.

[39] Kan Hayashi, Yuichiro Matsuzaki, Takaki Ashida, Shinobu Onoda, Hiroshi Abe, Takeshi Ohshima, Mutsuko Hatano, Takashi Taniguchi, Hiroki Morishita, Masanori Fujiwara, and Norikazu Mizuochi. Experimental and Theoretical Analysis of Noise Strength and Environmental Correlation Time for Ensembles of Nitrogen-Vacancy Centers in Diamond. *J. Phys. Soc. Jpn.*, 89(5):054708, April 2020. Publisher: The Physical Society of Japan.

[40] A.J. Healey, L.T. Hall, G.A.L. White, T. Teraji, M.-A. Sani, F. Separovic, J.-P. Tetienne, and L.C.L. Hollenberg. Polarization Transfer to External Nuclear Spins

Using Ensembles of Nitrogen-Vacancy Centers. *Phys. Rev. Applied*, 15(5):054052, May 2021. Publisher: American Physical Society.

[41] Edwin Hewitt and Robert E. Hewitt. The Gibbs-Wilbraham phenomenon: An episode in fourier analysis. *Arch. Hist. Exact Sci.*, 21(2):129–160, 1979.

[42] Ian Hincks, Christopher Granade, and David G Cory. Statistical inference with quantum measurements: methodologies for nitrogen vacancy centers in diamond. *New J. Phys.*, 20(1):013022, January 2018.

[43] Hincks, Ian. *Exploring Practical Methodologies for the Characterization and Control of Small Quantum Systems*. PhD Thesis, UWSpace, 2018.

[44] Kun Huang, Yunlong Nie, Baixi Du, Jinlong Jiang, Zichuan Zhang, Qi Wang, and RanRan Xu. A compact two-dimensional quantum magnetometer module based on the fixed-frequency optical detection of magnetic resonance using nitrogen vacancy centers. *Appl. Phys. Lett.*, 119(11):114005, September 2021. Publisher: American Institute of Physics.

[45] Toyofumi Ishikawa, Kai-Mei C. Fu, Charles Santori, Victor M. Acosta, Raymond G. Beausoleil, Hideyuki Watanabe, Shinichi Shikata, and Kohei M. Itoh. Optical and Spin Coherence Properties of Nitrogen-Vacancy Centers Placed in a 100 nm Thick Isotopically Purified Diamond Layer. *Nano Lett.*, 12(4):2083–2087, April 2012. Publisher: American Chemical Society.

[46] A. Jarmola, V. M. Acosta, K. Jensen, S. Chemerisov, and D. Budker. Temperature- and Magnetic-Field-Dependent Longitudinal Spin Relaxation in Nitrogen-Vacancy Ensembles in Diamond. *Phys. Rev. Lett.*, 108(19):197601, May 2012. Publisher: American Physical Society.

[47] F. Jelezko and J. Wrachtrup. Single defect centres in diamond: A review. *physica status solidi (a)*, 203(13):3207–3225, 2006.

[48] Webb Jl, Troise L, Hansen Nw, Olsson C, Wojciechowski Am, Achard J, Brinza O, Staacke R, Kieschnick M, Meijer J, Thielscher A, Perrier Jf, Berg-Sørensen K, Huck A, and Andersen Ul. Detection of biological signals from a live mammalian muscle using an early stage diamond quantum sensor. *Sci Rep*, 11(1):2412–2412, January 2021.

[49] S.O. Kasap. *Optoelectronics and Photonics: Principles and Practices*. Pearson, second edition, 2013.

[50] Stefan Kaufmann, David A. Simpson, Liam T. Hall, Viktor Perunicic, Philipp Senn, Steffen Steinert, Liam P. McGuinness, Brett C. Johnson, Takeshi Ohshima, Frank Caruso, Jörg Wrachtrup, Robert E. Scholten, Paul Mulvaney, and Lloyd Hollenberg. Detection of atomic spin labels in a lipid bilayer using a single-spin nanodiamond probe. *PNAS*, 110(27):10894–10898, July 2013. Publisher: National Academy of Sciences Section: Physical Sciences.

[51] Zeeshawn Kazi, Isaac M. Shelby, Hideyuki Watanabe, Kohei M. Itoh, Vaithiyalingam Shutthanandan, Paul A. Wiggins, and Kai-Mei C. Fu. Wide-Field Dynamic Magnetic Microscopy Using Double-Double Quantum Driving of a Diamond Defect Ensemble. *Phys. Rev. Applied*, 15(5):054032, May 2021. Publisher: American Physical Society.

[52] Navin Khaneja, Timo Reiss, Cindie Kehlet, Thomas Schulte-Herbrüggen, and Steffen J. Glaser. Optimal control of coupled spin dynamics: design of NMR pulse sequences by gradient ascent algorithms. *Journal of Magnetic Resonance*, 172(2):296–305, February 2005.

[53] Sayaka Kitazawa, Yuichiro Matsuzaki, Soya Saijo, Kosuke Kakuyanagi, Shiro Saito, and Junko Ishi-Hayase. Vector-magnetic-field sensing via multifrequency control of nitrogen-vacancy centers in diamond. *Phys. Rev. A*, 96(4):042115, October 2017. Publisher: American Physical Society.

[54] Koji Kobashi. *Diamond Films: Chemical Vapor Deposition for Oriented and Heteroepitaxial Growth*. Elsevier Science, 2010.

[55] Ngoc Diep Lai, Dingwei Zheng, Fedor Jelezko, François Treussart, and Jean-François Roch. Influence of a static magnetic field on the photoluminescence of an ensemble of nitrogen-vacancy color centers in a diamond single-crystal. *Applied Physics Letters*, 95(13):133101, September 2009.

[56] J. A. Larsson and P. Delaney. Electronic structure of the nitrogen-vacancy center in diamond from first-principles theory. *Phys. Rev. B*, 77:165201, Apr 2008.

[57] D. Le Sage, K. Arai, D. R. Glenn, S. J. DeVience, L. M. Pham, L. Rahn-Lee, M. D. Lukin, A. Yacoby, A. Komeili, and R. L. Walsworth. Optical magnetic imaging of living cells. *Nature*, 496(7446):486–489, April 2013. Number: 7446 Publisher: Nature Publishing Group.

[58] D. Le Sage, L. M. Pham, N. Bar-Gill, C. Belthangady, M. D. Lukin, A. Yacoby, and R. L. Walsworth. Efficient photon detection from color centers in a diamond optical waveguide. *Physical Review B*, 85(12), March 2012.

[59] Myoengwon Lee, Jungbae Yoon, and Donghun Lee. Atomic Scale Magnetic Sensing and Imaging Based on Diamond NV Centers. *Magnetometers - Fundamentals and Applications of Magnetism*, February 2019.

[60] Till Lenz, Arne Wickenbrock, Fedor Jelezko, Gopalakrishnan Balasubramanian, and Dmitry Budker. Magnetic sensing at zero field with a single nitrogen-vacancy center. *Quantum Sci. Technol.*, 6(3):034006, June 2021. Publisher: IOP Publishing.

[61] Edlyn V. Levine, Matthew J. Turner, Pauli Kehayias, Connor A. Hart, Nicholas Langellier, Raisa Trubko, David R. Glenn, Roger R. Fu, and Ronald L. Walsworth. Principles and techniques of the quantum diamond microscope. *Nanophotonics*, 8(11):1945–1973, November 2019. Publisher: De Gruyter.

[62] Kuo Kan Liang. Efficient conversion from rotating matrix to rotation axis and angle by extending Rodrigues' formula. *arXiv:1810.02999 [cs]*, October 2018. arXiv: 1810.02999.

[63] Stephen G Lipson. Polarization and scattering. In *Optics Experiments and Demonstrations for Student Laboratories*, 2053-2563, pages 3–1 to 3–18. IOP Publishing, 2020.

[64] Robin Lofgren. *A Theoretical Investigation of The Nitrogen-Vacancy Center In Diamond As A Single Molecule Sensor And Qubit.* PhD thesis, Luleä University of Technology, 2021.

[65] I. Lovchinsky, A. O. Sushkov, E. Urbach, N. P. de Leon, S. Choi, K. De Greve, R. Evans, R. Gertner, E. Bersin, C. Müller, L. McGuinness, F. Jelezko, R. L. Walsworth, H. Park, and M. D. Lukin. Nuclear magnetic resonance detection and spectroscopy of single proteins using quantum logic. *Science*, 351(6275):836–841, February 2016.

[66] B. J. Maertz, A. P. Wijnheijmer, G. D. Fuchs, M. E. Nowakowski, and D. D. Awschalom. Vector magnetic field microscopy using nitrogen vacancy centers in diamond. *Appl. Phys. Lett.*, 96(9):092504, March 2010. Publisher: American Institute of Physics.

[67] N. B. Manson, J. P. Harrison, and M. J. Sellars. Nitrogen-vacancy center in diamond: Model of the electronic structure and associated dynamics. *Phys. Rev. B*, 74(10):104303, September 2006. Publisher: American Physical Society.

[68] Giacomo Mariani, Shuhei Nomoto, Satoshi Kashiwaya, and Shintaro Nomura. System for the remote control and imaging of MW fields for spin manipulation in NV centers in diamond. *Scientific Reports*, 10(1):4813, March 2020. Number: 1 Publisher: Nature Publishing Group.

[69] Ferenc Marki and Christopher Marki. *A Tutorial for RF & Microwave Mixers*, 2010.

[70] Mason C. Marshall, Reza Ebadi, Connor Hart, Matthew J. Turner, Mark J.H. Ku, David F. Phillips, and Ronald L. Walsworth. High-Precision Mapping of Diamond Crystal Strain Using Quantum Interferometry. *Phys. Rev. Applied*, 17(2):024041, February 2022. Publisher: American Physical Society.

[71] Mason C. Marshall, David F. Phillips, Matthew J. Turner, Mark J. H. Ku, Tao Zhou, Nazar Delegan, F. Joseph Heremans, Martin V. Holt, and Ronald L. Walsworth. Scanning X-Ray Diffraction Microscopy for Diamond Quantum Sensing. *Phys. Rev. Applied*, 16(5):054032, November 2021. Publisher: American Physical Society.

[72] Minsky Marvin. Microscopy apparatus, December 1961.

[73] J R Maze, A Gali, E Togan, Y Chu, A Trifonov, E Kaxiras, and M D Lukin. Properties of nitrogen-vacancy centers in diamond: the group theoretic approach. *New J. Phys.*, 13(2):025025, feb 2011.

[74] Daniel J. McCloskey, Nikolai Dontschuk, David A. Broadway, Athavan Nadarajah, Alastair Stacey, Jean-Philippe Tetienne, Lloyd C. L. Hollenberg, Steven Prawer, and David A. Simpson. Enhanced Widefield Quantum Sensing with Nitrogen-Vacancy Ensembles Using Diamond Nanopillar Arrays. *ACS Appl. Mater. Interfaces*, 12(11):13421–13427, March 2020. Publisher: American Chemical Society.

[75] Benjamin Rocco Moss. Nitrogen Vacancy Diamond Quantum Sensing Applied to Mapping Magnetic Fields of Bacteria. Master's thesis, University of Massachusetts Boston, United States – Massachusetts, 2021. ISBN: 9798516097881.

[76] Osama Moussa, Ian Hincks, and David G. Cory. Preparing and preserving the double quantum coherence in NV^- centers in Diamond at low fields. *Journal of Magnetic Resonance*, 249:24–31, December 2014.

[77] M. Mrózek, J. Mlynarczyk, D. S. Rudnicki, and W. Gawlik. Circularly polarized microwaves for magnetic resonance study in the GHz range: Application to nitrogen-vacancy in diamonds. *Appl. Phys. Lett.*, 107(1):013505, July 2015. Publisher: American Institute of Physics.

[78] Shintaro Nomura, Koki Kaida, Hideyuki Watanabe, and Satoshi Kashiwaya. Near-field radio-frequency imaging by spin-locking with a nitrogen-vacancy spin sensor. *Journal of Applied Physics*, 130(2):024503, July 2021. Publisher: American Institute of Physics.

[79] Razvan Nutiu and Yingfu Li. Structure-Switching Signaling Aptamers. *J. Am. Chem. Soc.*, 125(16):4771–4778, April 2003. Publisher: American Chemical Society.

[80] Michael F. O'Keeffe, Lior Horesh, John F. Barry, Danielle A. Braje, and Isaac L. Chuang. Hamiltonian engineering with constrained optimization for quantum sensing and control. *New J. Phys.*, 21(2):023015, February 2019. Publisher: IOP Publishing.

[81] Giulia Petrini, Ekaterina Moreva, Ettore Bernardi, Paolo Traina, Giulia Tomagra, Valentina Carabelli, Ivo Pietro Degiovanni, and Marco Genovese. Is a Quantum Biosensing Revolution Approaching? Perspectives in NV-Assisted Current and Thermal Biosensing in Living Cells. *Advanced Quantum Technologies*, page 2000066, 2020. _eprint: https://onlinelibrary.wiley.com/doi/pdf/10.1002/qute.202000066.

[82] L. M. Pham, N. Bar-Gill, D. Le Sage, C. Belthangady, A. Stacey, M. Markham, D. J. Twitchen, M. D. Lukin, and R. L. Walsworth. Enhanced metrology using preferential orientation of nitrogen-vacancy centers in diamond. *Phys. Rev. B*, 86(12):121202, September 2012. Publisher: American Physical Society.

[83] L. M. Pham, D. Le Sage, P. L. Stanwix, T. K. Yeung, D. Glenn, A. Trifonov, P. Cappellaro, P. R. Hemmer, M. D. Lukin, H. Park, A. Yacoby, and R. L. Walsworth. Magnetic field imaging with nitrogen-vacancy ensembles. *New J. Phys.*, 13(4):045021, April 2011. Publisher: IOP Publishing.

[84] F. Poggiali, P. Cappellaro, and N. Fabbri. Optimal control for one-qubit quantum sensing. *Phys. Rev. X*, 8(2):021059, June 2018. Publisher: American Physical Society.

[85] Matteo Pompili, Sophie L. N. Hermans, Simon Baier, Hans K. C. Beukers, Peter C. Humphreys, Raymond N. Schouten, Raymond F. L. Vermeulen, Marijn J. Tiggelman, Laura dos Santos Martins, Bas Dirkse, Stephanie Wehner, and Ronald Hanson. Realization of a multi-node quantum network of remote solid-state qubits. *Science*, 372(6539):259–264, April 2021.

[86] Andreas F. L. Poulsen, Joshua D. Clement, James L. Webb, Rasmus H. Jensen, Kirstine Berg-Sørensen, Alexander Huck, and Ulrik Lund Andersen. Optimal control of a nitrogen-vacancy spin ensemble in diamond for sensing in the pulsed domain. *arXiv:2101.10049 [physics, physics:quant-ph]*, January 2021. arXiv: 2101.10049.

[87] Adarsh D. Radadia, Courtney J. Stavis, Rogan Carr, Hongjun Zeng, William P. King, John A. Carlisle, Aleksei Aksimentiev, Robert J. Hamers, and Rashid Bashir. Control of Nanoscale Environment to Improve Stability of Immobilized Proteins on Diamond Surfaces. *Adv Funct Mater*, 21(6):1040–1050, March 2011.

[88] K. Rama Koteswara Rao and Dieter Suter. Level anti-crossings of a nitrogen-vacancy center in diamond: decoherence-free subspaces and 3D sensors of microwave magnetic fields. *New J. Phys.*, 22(10):103065, October 2020. Publisher: IOP Publishing.

[89] Phila Rembold, Nimba Oshnik, Matthias M. Müller, Simone Montangero, Tommaso Calarco, and Elke Neu. Introduction to quantum optimal control for quantum sensing with nitrogen-vacancy centers in diamond. *AVS Quantum Sci.*, 2(2):024701, June 2020. Publisher: American Vacuum Society.

[90] Lucio Robledo, Hannes Bernien, Toeno van der Sar, and Ronald Hanson. Spin dynamics in the optical cycle of single nitrogen-vacancy centres in diamond. *New J. Phys.*, 13(2):025013, February 2011. Publisher: IOP Publishing.

[91] L Rondin, J-P Tetienne, T Hingant, J-F Roch, P Maletinsky, and V Jacques. Magnetometry with nitrogen-vacancy defects in diamond. *Rep. Prog. Phys.*, 77(5):056503, May 2014.

[92] Romana Schirhagl, Kevin Chang, Michael Loretz, and Christian L. Degen. Nitrogen-vacancy centers in diamond: nanoscale sensors for physics and biology. *Annu Rev Phys Chem*, 65:83–105, 2014.

[93] Jennifer M. Schloss, John F. Barry, Matthew J. Turner, and Ronald L. Walsworth. Simultaneous Broadband Vector Magnetometry Using Solid-State Spins. *Phys. Rev. Applied*, 10(3):034044, September 2018. Publisher: American Physical Society.

[94] Vikas K. Sewani, Hyma H. Vallabhapurapu, Yang Yang, Hannes R. Firgau, Chris Adambukulam, Brett C. Johnson, Jarryd J. Pla, and Arne Laucht. Coherent control of NV^- centers in diamond in a quantum teaching lab. *American Journal of Physics*, 88(12):1156–1169, December 2020. Publisher: American Association of Physics Teachers.

[95] James F. Shackelford. *Introduction to Materials Science for Engineers*. Pearson Prentice Hall, seventh edition, 2009.

[96] Shinich Shikata, Takenori Tanno, Tokuyuki Teraji, Hisao Kanda, Takatoshi Yamada, and Jun ichi Kushibiki. Precise measurements of diamond lattice constant using bond method. *Japanese Journal of Applied Physics*, 57(11):111301, oct 2018.

[97] Jeong Hyun Shim, Seong-Joo Lee, Santosh Ghimire, Ju Il Hwang, Kwang-Geol Lee, Kiwoong Kim, Matthew J. Turner, Connor A. Hart, Ronald L. Walsworth, and Sangwon Oh. Multiplexed sensing of magnetic field and temperature in real time using a nitrogen vacancy spin ensemble in diamond. *Phys. Rev. Applied*, 17(1):014009, January 2022. Publisher: American Physical Society.

[98] David S Simon. *Gaussian beams and lasers*. 2053-2571. Morgan and Claypool Publishers, 2016.

[99] Element Six. DNV-B1 3.0x3.0mm, 0.5mm thick, June 2020.

[100] Element Six. Unlocking next generation quantum technologies, June 2020.

[101] P. L. Stanwix, L. M. Pham, J. R. Maze, D. Le Sage, T. K. Yeung, P. Cappellaro, P. R. Hemmer, A. Yacoby, M. D. Lukin, and R. L. Walsworth. Coherence of nitrogen-vacancy electronic spin ensembles in diamond. *Phys. Rev. B*, 82(20):201201, November 2010. Publisher: American Physical Society.

[102] Courtney Stavis, Tami Lasseter Clare, James E. Butler, Adarsh D. Radadia, Rogan Carr, Hongjun Zeng, William P. King, John A. Carlisle, Aleksei Aksimentiev, Rashid Bashir, and Robert J. Hamers. Surface functionalization of thin-film diamond for highly stable and selective biological interfaces. *PNAS*, 108(3):983–988, January 2011. Publisher: National Academy of Sciences Section: Research Articles.

[103] S. Steinert, F. Dolde, P. Neumann, A. Aird, B. Naydenov, G. Balasubramanian, F. Jelezko, and J. Wrachtrup. High sensitivity magnetic imaging using an array of spins in diamond. *Review of Scientific Instruments*, 81(4):043705, April 2010. Publisher: American Institute of Physics.

[104] Felix M. Stürner, Andreas Brenneis, Thomas Buck, Julian Kassel, Robert Rölver, Tino Fuchs, Anton Savitsky, Dieter Suter, Jens Grimmel, Stefan Hengesbach, Michael Förtsch, Kazuo Nakamura, Hitoshi Sumiya, Shinobu Onoda, Junichi Isoya, and Fedor Jelezko. Integrated and Portable Magnetometer Based on Nitrogen-Vacancy Ensembles in Diamond. *Advanced Quantum Technologies*, 4(4):2000111, 2021.

[105] A. O. Sushkov, N. Chisholm, I. Lovchinsky, M. Kubo, P. K. Lo, S. D. Bennett, D. Hunger, A. Akimov, R. L. Walsworth, H. Park, and M. D. Lukin. All-Optical

Sensing of a Single-Molecule Electron Spin. *Nano Lett.*, 14(11):6443–6448, November 2014.

[106] Gergő Thiering and Adam Gali. Theory of the optical spin-polarization loop of the nitrogen-vacancy center in diamond. *Phys. Rev. B*, 98(8):085207, August 2018. Publisher: American Physical Society.

[107] Moeta Tsukamoto, Kensuke Ogawa, Hayato Ozawa, Takayuki Iwasaki, Mutsuko Hatano, Kento Sasaki, and Kensuke Kobayashi. Vector magnetometry using perfectly aligned nitrogen-vacancy center ensemble in diamond. *Appl. Phys. Lett.*, 118(26):264002, June 2021. Publisher: American Institute of Physics.

[108] Matthew J. Turner, Nicholas Langellier, Rachel Bainbridge, Dan Walters, Srujan Meesala, Thomas M. Babinec, Pauli Kehayias, Amir Yacoby, Evelyn Hu, Marko Lončar, Ronald L. Walsworth, and Edlyn V. Levine. Magnetic Field Fingerprinting of Integrated-Circuit Activity with a Quantum Diamond Microscope. *Phys. Rev. Applied*, 14(1):014097, July 2020. Publisher: American Physical Society.

[109] Matthew James Turner, Edlyn Victoria Levine, Pauli Kehayias, Daniel T. Walters, Ronald L. Walsworth, Marko Loncar, and Nicholas Ryan Langellier. High-resolution magnetic field fingerprinting of integrated circuit activity with a quantum diamond microscope, August 2021.

[110] Amir Waxman. *Sensitive Magnetometry Based on NV Centers in Diamonds*. PhD thesis, University of the Negev, 2014.

[111] James L. Webb, Joshua D. Clement, Luca Troise, Sepehr Ahmadi, Gustav Juhl Johansen, Alexander Huck, and Ulrik L. Andersen. Nanotesla sensitivity magnetic field sensing using a compact diamond nitrogen-vacancy magnetometer. *Appl. Phys. Lett.*, 114(23):231103, June 2019. Publisher: American Institute of Physics.

[112] Timo Benjamin Weggler. *Paving the Way for Structure Mapping Measurements of Biological Macromolecules Using a Single Quantum Sensor*. PhD thesis, Ulm university, April 2021.

[113] Thomas Wolf, Philipp Neumann, Kazuo Nakamura, Hitoshi Sumiya, Takeshi Ohshima, Junichi Isoya, and Jörg Wrachtrup. Subpicotesla Diamond Magnetometry. *Phys. Rev. X*, 5(4):041001, October 2015.

[114] Christopher Wood, Ian Hincks, and Christopher Granade. Quantumutils for mathematica, 2014.

[115] Ralf Wunderlich, Robert Staacke, Wolfgang Knolle, Bernd Abel, Jürgen Haase, and Jan Meijer. Robust nuclear hyperpolarization driven by strongly coupled nitrogen vacancy centers. *Journal of Applied Physics*, 130(10):104301, September 2021. Publisher: American Institute of Physics.

[116] Mouzhe Xie, Xiaofei Yu, Lila V. H. Rodgers, Daohong Xu, Ignacio Chi-Durán, Adrien Toros, Niels Quack, Nathalie P. de Leon, and Peter C. Maurer. Biocompatible surface functionalization architecture for a diamond quantum sensor. *PNAS*, 119(8), February 2022. Publisher: National Academy of Sciences Section: Physical Sciences.

[117] Tianyu Xie, Zhiyuan Zhao, Maosen Guo, Mengqi Wang, Fazhan Shi, and Jiangfeng Du. Identity Test of Single NV- Centers in Diamond at Hz-Precision Level. *Phys. Rev. Lett.*, 127(5):053601, July 2021. Publisher: American Physical Society.

[118] Jing-Yan Xu, Yang Dong, Shao-Chun Zhang, Yu Zheng, Xiang-Dong Chen, Wei Zhu, Guan-Zhong Wang, Guang-Can Guo, and Fang-Wen Sun. Room-temperature Composite-pulses for Robust Diamond Magnetometry. *arXiv:1811.00191 [quant-ph]*, October 2018. arXiv: 1811.00191.

[119] Ken Yahata, Yuichiro Matsuzaki, Shiro Saito, Hideyuki Watanabe, and Junko Ishi-Hayase. Demonstration of vector magnetic field sensing by simultaneous control of nitrogen-vacancy centers in diamond using multi-frequency microwave pulses. *Appl. Phys. Lett.*, 114(2):022404, January 2019. Publisher: American Institute of Physics.

[120] Tatsuma Yamaguchi, Yuichiro Matsuzaki, Soya Saijo, Hideyuki Watanabe, Norikazu Mizuochi, and Junko Ishi-Hayase. Control of all the transitions between ground state manifolds of nitrogen vacancy centers in diamonds by applying external magnetic driving fields. *Jpn. J. Appl. Phys.*, 59(11):110907, November 2020. Publisher: IOP Publishing.

[121] Xiaoying Yang, Ning Zhang, Heng Yuan, Guodong Bian, Pengcheng Fan, and Mingxin Li. Microstrip-line resonator with broadband, circularly polarized, uniform microwave field for nitrogen vacancy center ensembles in diamond. *AIP Advances*, 9(7):075213, July 2019.

[122] Heng Yuan, Xiaoying Yang, Ning Zhang, Zhiqiang Han, Lixia Xu, Jixing Zhang, Guodong Bian, Pengcheng Fan, Mingxin Li, and Yuchen Liu. Frequency-tunable and Circularly Polarized Microwave Resonator for Magnetic Sensing with NV Ensembles in Diamond. *IEEE Sensors Journal*, pages 1–1, 2020. Conference Name: IEEE Sensors Journal.

[123] Chen Zhang, Heng Yuan, Ning Zhang, Lixia Xu, Jixing Zhang, Bo Li, and Jiancheng Fang. Vector magnetometer based on synchronous manipulation of nitrogen-vacancy centers in all crystal directions. *J. Phys. D: Appl. Phys.*, 51(15):155102, March 2018. Publisher: IOP Publishing.

[124] Haimei Zhang, Carina Belvin, Wanyi Li, Jennifer Wang, Julia Wainwright, Robbie Berg, and Joshua Bridger. Little bits of diamond: Optically detected magnetic resonance of nitrogen-vacancy centers. *American Journal of Physics*, 86(3):225–236, March 2018.

[125] Ning Zhang, Chen Zhang, Lixia Xu, Ming Ding, Wei Quan, Zheng Tang, and Heng Yuan. Microwave Magnetic Field Coupling with Nitrogen-Vacancy Center Ensembles in Diamond with High Homogeneity. *Appl Magn Reson*, 47(6):589–599, June 2016.

[126] Yang Zhang, Zhonghao Li, Yuanyao Feng, Hao Guo, Huanfei Wen, Jun Tang, Jun Tang, Jun Liu, and Jun Liu. High-sensitivity DC magnetic field detection with ensemble NV centers by pulsed quantum filtering technology. *Opt. Express, OE*, 28(11):16191–16201, May 2020. Publisher: Optical Society of America.

[127] Huijie Zheng, Arne Wickenbrock, Georgios Chatzidrosos, Lykourgos Bougas, Nathan Leefer, Samer Afach, Andrey Jarmola, Victor M. Acosta, Jingyan Xu, Geoffrey Z. Iwata, Till Lenz, Zhiyin Sun, Chen Zhang, Takeshi Ohshima, Hitoshi Sumiya, Kazuo Nakamura, Junichi Isoya, Jörg Wrachtrup, and Dmitry Budker. Novel Magnetic-Sensing Modalities with Nitrogen-Vacancy Centers in Diamond. *Engineering Applications of Diamond*, January 2021. Publisher: IntechOpen.

[128] Huijie Zheng, Jingyan Xu, Geoffrey Z. Iwata, Till Lenz, Julia Michl, Boris Yavkin, Kazuo Nakamura, Hitoshi Sumiya, Takeshi Ohshima, Junichi Isoya, Jörg Wrachtrup, Arne Wickenbrock, and Dmitry Budker. Zero-Field Magnetometry Based on Nitrogen-Vacancy Ensembles in Diamond. *Phys. Rev. Applied*, 11(6):064068, June 2019. Publisher: American Physical Society.

[129] Hengyun Zhou, Joonhee Choi, Soonwon Choi, Renate Landig, Alexander M. Douglas, Junichi Isoya, Fedor Jelezko, Shinobu Onoda, Hitoshi Sumiya, Paola Cappellaro, Helena S. Knowles, Hongkun Park, and Mikhail D. Lukin. Quantum Metrology with Strongly Interacting Spin Systems. *Phys. Rev. X*, 10(3):031003, July 2020.

[130] Yikang Zuo, Tsukasa Hayashi, Hiroshige Deguchi, Hiromi Nakanishi, Yoshiki Nishibayahi, Natsuo Tatsumi, Minori Teramoto, and Yutaka Kobayashi. Synthetic

Diamond for Nitrogen Vacancy Sensor and Its Applicability. *Industries, Sumitomo Electric*, (92):6, April 2021.